Aus der

Radiologischen Universitätsklinik Tübingen

Abteilung Diagnostische und Interventionelle Radiologie

Quantitative analysis of flow effects on signal characteristics in volume-selective 1H spectroscopy – Theory and experiments on whole-body MRI scanners

Inaugural-Dissertation
zur Erlangung des Doktorgrades
der Medizin

der Medizinischen Fakultät
der Eberhard Karls Universität
zu Tübingen

vorgelegt von

Oberparleiter, Moritz

2024

Dekan: Professor Dr. B. Pichler

1. Berichterstatter: Professor Dr. F. Schick
2. Berichterstatter: Professor Dr. U. Klose

Tag der Disputation: 02.12.2024

Contents

List of Tables

List of Figures

List of Symbols and Acronyms

α	angle in the complex plane
χ	susceptibility
χ_{blood}	susceptibility of blood
χ_{do}	susceptibility of deoxygenated blood
χ_{st}	susceptibility of the surrounding tissue
δ	chemical shift
$\Delta\chi$	susceptibility in relation to the surrounding tissue
$\Delta\varphi_{total}$	total dephasing created by a sequence
ΔB	magnetic field inside a vein compared to the surrounding tissue
δL	edge length of a voxel in a given direction
η	dynamic viscosity
γ	gyromagnetic ratio
$\hbar$	reduced Planck constant
λ	coherence decay rate constant
$\mathbb{N}_0$	natural numbers including 0
μ	magnetic moment
μ_0	vacuum permeability
ω	angular velocity
$\omega_{\mathbf{ref}}$	reference frequency for the chemical shift
$\omega_{\mathbf{sam}}$	frequency measured in a sample
ω_L	Larmor frequency
ϕ	dephasing/phase
ρ	density
θ	angle between the main magnetic field and a vessel
θ_0	initial angle
φ_{cor}	angle used for phase correction
$\varphi_{dephase}$	dephasing angle of a spectrum
SO_2	oxygen saturation
$v/\vec{v}$	velocity

180°-pulse	180 degrees radiofrequency pulse
90°-pulse	90 degrees radiofrequency pulse
^{1}H	hydrogen-1
A	cross-sectional area
B_0	external magnetic field
B_1	magnetic field produced by a radiofrequency pulse
B_{eff}	effective magnetic field
B_{ind}	induced magnetic field
B_{loc}	local magnetic field
BOLD	blood-oxygen-level-dependent
C	complex number
cos^2	cosine-squared function
CSF	cerebrospinal fluid
D	inner diameter of a tube
D_H	hydraulic diameter
E_{mag}	magnetic energy
F(ω)	spectrum obtained by a Fourier transform
F_{cor}(ω)	phase-corrected spectrum
FID	free induction decay
fMRI	functional magnetic resonance imaging
FWHM	full width at half maximum
G/G(t)	(time-dependent) gradient
Hct	haematocrit
I	moment of inertia
Im(C)	imaginary part of a complex number
J	angular momentum quantum number
k	a constant for a set of conditions
L	angular momentum
m	mass
M	net magnetisation
M_{eq}	maximal possible longitudinal magnetisation
M_x	magnetisation along the x-axis
M_y	magnetisation along the y-axis
M_z	longitudinal magnetisation
MRI	magnetic resonance imaging
MRS	magnetic resonance spectroscopy
NbTi	niobium-titanium

ppm	parts per million
PRESS	point-resolved spectroscopy
Q	volumetric flow rate
R_{180}	R factor of a 180 degrees radiofrequency pulse
R_{90}	R factor of a 90 degrees radiofrequency pulse
Re	Reynolds number
Re(C)	real part of a complex number
RF pulse	radiofrequency pulse
S	spin
s	spin quantum number
S(ω)	spectrum acquired by MRS
s_z	spin projection/magnetic quantum number
SSG	slice selection gradient
STEAM	stimulated echo acquisition mode
SVS	single volume spectroscopy
T	tesla
T_{180}	duration of a 180 degrees radiofrequency pulse
T_1	longitudinal relaxation time constant
T_2	transverse relaxation time constant
T_2^*	effective transverse relaxation time constant
T_{90}	duration of a 90 degrees radiofrequency pulse
t_{flow}	duration of flow
t_{ramp}	ramp time
TE	echo time
TE_1	first half of the echo time
TE_2	second half of the echo time
TM	mixing time
TR	repetition time
V	volume
v_{flow}	average flow velocity

Chapter 1

Introduction

1.1 Context of the thesis

Radiology provides numerous tools to aid diagnostics and therapies in medicine. Since the discovery of X-rays and their medical application, radiology has come a long way. More sophisticated imaging modalities have been developed, such as sonography, computed tomography, and magnetic resonance imaging (MRI). Each modality has its applications, advantages, and disadvantages. MRI is an exciting imaging modality. Its ability to yield detailed images of soft tissue and internal organs benefits millions of patients annually. MRI was developed in the 1970s and 1980s, but research is still in progress to advance the abilities and accuracy of this imaging modality.

The discovery of nuclear magnetic resonance (NMR) by Isidor Isaac Rabi in the 1930s made the development of magnetic resonance spectroscopy (MRS) and later MRI possible [66, 105]. NMR describes the phenomenon that nuclei exposed to a strong, constant magnetic field generate an electromagnetic signal when a radiofrequency pulse (RF pulse) has been applied to the nuclei. This signal can be transformed into a spectrum of different frequencies mathematically. Information about the environment and chemical binding of the nuclei is accessed by spectrum analysis. This technique is called MRS. MRS was used in physics and chemistry before applications in medicine were conceived. The determination of the structure of organic molecules is one of many examples.

While MRS provides information about the nuclei's environment, it cannot produce images. However, the development of techniques, such as gradients, phase encoding, and frequency encoding, made imaging possible. Among others, Lauterbur, Mansfield, and Damadian developed those techniques in the 1970s and 1980s [25, 72, 85].

Although imaging is the main application of NMR in medicine, MRS is also used. MRS and MRI combined offer the advantage of molecular imaging since the spectrum contains information about the abundance of metabolites in cells [41]. Applications have

been extensively researched. Over the years, an enormous amount of research in MRS has been done, especially in neuroradiology, where researchers investigated diseases such as Alzheimer's disease, brain tumours, epilepsy, and motor neuron disease [10]. In addition, MRS is evaluated as a diagnostic tool in other forms of tumours, such as breast and prostate cancer [93, 94, 118, 119]. MRS aids diagnostics because it can detect abnormal concentrations of metabolites such as choline and N-acetylaspartic acid in tumour cells [41].

The signal used in MRI is primarily created by hydrogen-1 (^{1}H) nuclei found in water molecules and lipids. The ^{1}H nuclei in small organic molecules and macromolecules also contribute to the signal. However, their contribution is minute because their concentration in the tissue is small compared to water and lipids. Contrary to MRI, medical MRS research often focuses on metabolites with small concentrations. In these cases, water suppression is needed. However, water and fat signals in MR spectra are also investigated [63, 83, 108, 116].

Even before MRI scanners were developed, the possibility of differentiating between tumours and normal tissue using the water signal characteristics – not metabolites – in MRS was investigated [25]. Further examples include the investigation of water and fat signals in the leukaemic bone marrow and research about the role of intramuscular fat in diabetes mellitus [63, 83, 116].

1.2 Motivation for the thesis

Most metabolites measured in MRS reside within cells, such as brain and tumour cells. Therefore, these metabolites are stationary during MRS measurements. Because the body stores lipids mainly in adipocytes, lipids are also primarily static during measurements. In the human body, water is found in cells, blood vessels, and the extracellular space.

When an MR spectrum of human tissue containing blood vessels is acquired, the water signal is generated by stationary water (e.g., within cells) and moving water within blood vessels. Therefore, flow influences the water signal more than the signals of lipids and metabolites. Note that water within cells and the extracellular space is also subject to movement in the form of diffusion.

The directional motion of water molecules within blood vessels and the non-directional diffusion of water molecules outside blood vessels influence MRI and MRS measurements. Considerable research has been done on flow and diffusion in MRI [59, 87, 90, 142]. However, the role of flow and diffusion in MRS sequences has been largely overlooked. Although measurements of diffusion in MRS were made even before the development of MRI, few studies have linked diffusion with MRS sequences used in modern whole-

body MRI scanners [91, 125, 126]. While diffusion in MRS has attracted some research attention, the lack of studies about flow in MRS is evident [83, 91].

A study by Schick et al. concerned with MRS of bone marrow has increased the interest in the role of flow in MRS [23, 116]. Further, how exactly flow leads to the signal alterations of MR spectra has yet to be established. Since there is sustained medical interest in MRS and research about the mechanisms of flow effects in MRS is scarce, an investigation of the topic seems relevant.

1.3 Aim of the thesis

Alterations of MR spectra due to flow likely arise from several mechanisms. Firstly, MRS sequences use field gradients (supplementary magnetic fields in addition to the main magnetic field of the MRI scanner) for volume selection [92]. These gradients are one source of potential signal alterations due to flow. Another possible source for signal alterations is an effect related to the BOLD effect caused by relatively paramagnetic venous blood flowing in bent vessels.

This thesis aimed to investigate the effects that lead to signal alterations induced by flow in ^{1}H spectroscopy. Specifically, the investigation focused on the impact of gradient-induced effects and BOLD-related effects within curved venous vessels. This aim was achieved by a two-step approach. The first step was to develop mathematical frameworks to determine the significance of gradient-induced and BOLD-related effects in theory. The second step was to investigate gradient-induced effects on MR spectra experimentally.

There are several MRS sequences used in whole-body MRI scanners. This study investigated the most common MRS sequences: stimulated echo acquisition mode (STEAM) and point-resolved spectroscopy (PRESS). This thesis aimed to determine the influence of specific sequence parameters, such as echo and mixing times, on gradient-induced and BOLD-related effects in PRESS and STEAM. A comprehensive understanding of the impact of sequence parameters on flow effects enables intentional modification of these parameters to either suppress or use flow effects for diagnostic purposes.

The motion of water molecules in inhomogeneous magnetic fields created by iron, air, bone, and fat is another suspected contributor to signal alterations due to flow. Notably, bone trabeculae and iron deposits lead to relevant inhomogeneities in the magnetic field. This thesis examines these susceptibility-related effects theoretically.

1.4 Significance of the thesis

This section aims to elucidate the significance of this thesis in a broader context. Generally, the study seeks to enlarge the limited knowledge concerning flow effects in ^{1}H spectroscopy. As stated above, little research has been done on signal alterations due to flow in ^{1}H spectroscopy, and the underlying mechanisms still need to be established. This study strives to give an overview of the effects that are considered significant contributors to such signal alterations.

Further, the thesis provides a quantitative analysis of these effects to asses their magnitude and practical implications. Based on the results and insights gained, an optimisation of existing applications of MR spectroscopy is conceivable. The knowledge about the effects can be used to minimise unwanted signal alterations. Even new applications of MR spectroscopy could eventually arise due to advancements in the field. A potential application is the development of innovative methods to quantify stationary and flowing water in peripheral tissue. In theory, MRS sequences could also be used to detect increased flow velocities, a hallmark of inflammation. Therefore, detecting inflammatory changes is a potential application, especially in tissues with good vascularisation.

1.5 Overview of the thesis

This section provides a brief outline of the thesis structure. The introduction is followed by Chapter 2, which presents the background necessary to understand the methodology, underlying hypotheses, and experiments. Firstly, Chapter 2 revises the physical and technical basics of MR spectroscopy and imaging. Secondly, details of MRS and MRI sequences are presented with a particular focus on PRESS and STEAM, the two main sequence types used in the simulations and experiments. Thirdly, a review of the flow rates and the geometry of vessels in the human body is given as both factors determine the magnitude of flow effects in different tissues.

An introduction to gradient-induced and susceptibility-induced phase-shift effects follows these accounts. The explanation of the susceptibility-induced phase-shift effects entails the BOLD-related phase-shift effects occurring in bent vessels. The introductory sections concerning phase-shift effects are crucial as they explain the origins of the signal alterations due to flow.

Note that the thesis is primarily concerned with gradient-induced and BOLD-related phase-shift effects. While this study investigates BOLD-related phase-shift effects using simulations, gradient-induced phase-shift effects are investigated using simulations and experiments. The experiments seek to validate and support the developed theoretical

model. The focus on these two topics leads to a dichotomous framework of the subsequent chapters. The chapters describing the materials, methods and results begin with sections on gradient-induced phase-shift effects and continue with sections on BOLD-related phase-shift effects. Even the discussion largely follows this framework.

Chapter 3 is concerned with the materials and methods used in this study. The first section shows the methods for calculating gradient-induced phase-shift effects in PRESS and STEAM sequences. The calculations are performed with exemplary sequences to illustrate the simulation of gradient-induced phase-shift effects.

The following section outlines the experimental design of phantom measurements conducted to evaluate gradient-induced phase-shift effects. Subsequently, the experimental design of in vivo measurements evaluating gradient-induced phase-shift effects in red bone marrow is described. For the experiments, it was necessary to develop flow-sensitised PRESS and STEAM sequences. These sequences are presented in the following section. The penultimate section outlines the methods used to analyse the experimental data. The last section describes the mathematical model for calculating the BOLD-related phase-shift effects.

Chapter 4 shows the results of the simulations and experiments. The first section presents the results of the simulations of the gradient-induced phase-shift effects. Subsequently, the experimental results of the phantom measurements are outlined. The following section shows the results obtained in phantom measurements to validate the flow-sensitised sequences. Further, the results of the in vivo measurements of red bone marrow in two subjects are given. Lastly, the results of the simulations of BOLD-related phase-shift effects are delineated.

Chapter 5 represents the discussion and aims to interpret the results and their implications. The first section interprets the results obtained in the simulation of gradient-induced phase-shift effects. Specifically, the reasons for increases/decreases in the magnitude of phase-shift effects due to variations in sequence parameters are discussed. The second section discusses the results obtained by the experiments on gradient-induced phase-shift effects, while the third section debates the simulation of the BOLD-related phase-shift effects. Lastly, the conclusions drawn from this study are presented in the final section of this chapter.

A thesis summary is provided in English in Chapter 6 and German in Chapter 7. Chapter 8 provides the student contribution. The bibliography and acknowledgements follow these chapters.

Chapter 2

Background

2.1 Physical basics

This section gives an overview of the relevant physical and mathematical concepts necessary to understand the simulations and experiments of this study. In the beginning, this section will explain the basic concepts of angular momentum, spin, and magnetism because they lead to understanding MR spectroscopy. Further, the role of RF pulses in obtaining a measurable signal is introduced. The introduction of RF pulses is followed by a discussion of different forms of relaxation and how the signal is mathematically processed to yield a spectrum that can be analysed.

2.1.1 Angular momentum

Nuclear magnetic resonance is based on nuclear spin, a form of angular momentum (L) [44]. Therefore, it is vital to consider angular momentum mathematically and physically to understand spin.

Angular momentum is, in classical mechanics, a property associated with rotation. Every rotating object or particle has angular momentum. It is calculated with the rotating objects angular velocity (ω) and its moment of inertia (I) [28].

$$\vec{L} = I \cdot \vec{\omega} \tag{2.1}$$

Like momentum, angular momentum is a conserved quantity and a vector. The vector $\vec{L}$ points either parallel or antiparallel to the axis of rotation. Angular momentum measures an object's fundamental property to continue its rotational movement [28].

When considering angular momentum on a microscopic scale (molecules, atoms, elementary particles), it is essential to note that it is quantised. The quantisation means

angular momentum can only assume discrete values, which are a solution of the following equation [44, 75].

$$L = \hbar\sqrt{J(J+1)} \mid J \in \mathbb{N}_0 \tag{2.2}$$

J is called the angular momentum quantum number. J can assume half-integer values in some cases.

2.1.2 Spin

Spin (S) is a fundamental property of atoms and subatomic particles. As previously stated, spin can be considered a form of angular momentum. In classical mechanics, an object must rotate to have angular momentum. In that respect, spin behaves differently, in so far as a particle that has spin does not rotate but has angular momentum nonetheless [44]. The former is called spin angular momentum, and the latter is called orbital angular momentum to distinguish angular momentum in the form of spin from the angular momentum of a rotating system like a diatomic molecule [75].

As angular momentum is quantised on a microscopic scale, spin is also quantised. Analogous to Equation 2.2 spin angular momentum (S) can be calculated the following way [75]:

$$S = \hbar\sqrt{s(s+1)} \tag{2.3}$$

The spin quantum number (s) is a fundamental and fixed property of particles like protons, electrons, and photons. The spin quantum number can take half-integer and integer values. Particles with half-integer spin quantum numbers are called fermions, and particles with integer spin quantum numbers are called bosons [75].

All elementary particles except the Higgs boson possess spin [128]. For nuclear magnetic resonance, it is essential to notice that the electron and the proton both have a spin quantum number of $\frac{1}{2}$, the photon of 1 [44].

2.1.3 Spin orientation

As stated above, angular momentum is a vector with a magnitude and a direction. Spin is associated with a rotation axis and a direction. Since spin is based on quantum mechanics, the formalism describing the spatial orientation of spin differs from the simple vector

formalism of angular momentum in classical mechanics. This subsection will give an introduction to this formalism.

The spin projection/magnetic quantum number (s_z) is a quantum number that is useful to define spin orientation. s_z can assume the following values [75]:

$$s_z = -s, -s+1..., +s \tag{2.4}$$

The atom used in nuclear magnetic resonance imaging is ^{1}H. The nucleus of an ^{1}H atom is a single proton and thus has a spin quantum number of $\frac{1}{2}$. Using Equation 2.4 it can be determined that s_z can either be $\frac{1}{2}$ or $-\frac{1}{2}$. An ^{1}H nucleus with $s_z = \frac{1}{2}$ is said to have a spin orientation of "spin up", while a proton's spin orientation with $s_z = -\frac{1}{2}$ is called "spin down" [44].

"Up" and "down" refer to the orientation parallel or antiparallel to an externally applied electromagnetic field, respectively. If a proton is left alone, it is not forced to be in either spin-up or spin-down position [52]. Its orientation can assume any possible combination (superposition) of both [52, 75].

This changes when the proton's wave function is subject to external influences and collapses [44, 75]. A wave function collapse is usually not observed in MR imaging and spectroscopy [52].

2.1.4 Magnetism

In addition to the concept of spin, a basic understanding of magnetism is needed to make sense of MRS.

In everyday life, we experience magnetism primarily as ferromagnetism. Ferromagnetism is a form of permanent magnetism which does not depend on an externally applied magnetic field. Other forms of magnetism only arise when an external magnetic field (B_0) is present [75]. One such form of magnetism is paramagnetism. A magnetic field induces a so-called magnetic moment μ in a paramagnetic object. This object produces a second magnetic field as a response. This field points in the same direction as the externally applied field. Thus, the induced field augments the external field.

On the other hand, there is diamagnetism. A diamagnetic object also creates an induced magnetic field when subject to an external magnetic field. The field produced by diamagnetic substances points opposite to the applied field. Thereby, the induced field weakens the initially applied field [27].

Magnetism arises on a microscopic level. Electric currents of circulating electrons and the intrinsic magnetic moments of electrons are responsible for the magnetic properties of materials. Notably, the magnetic moments associated with atomic nuclei are con-

siderably smaller than those of electrons, rendering the contribution of nuclear magnetic moments neglectable. Paramagnetism arises from the magnetic moments of unpaired electrons when an external field is applied. In ferromagnetism, magnetic moments of unpaired electrons also tend to align with each other even without applying an external field. On the other hand, diamagnetism arises when an externally applied magnetic field induces electronic currents that oppose the influence of the applied field, thus overshadowing the impact of unpaired electrons.

The susceptibility (χ) is a quantitative indicator of whether a substance exhibits diamagnetic or paramagnetic properties. Diamagnetism is associated with negative susceptibility values, whereas positive values signify paramagnetism. The strength of the induced field is determined by the induced magnetic moment, which can, in turn, be related to the susceptibility [27, 75].

$$\vec{\mu} = \mu_0^{-1} V \chi \vec{B_0} \tag{2.5}$$

Here, μ_0 is the magnetic constant, and V is the object's volume under consideration.

Dia- and paramagnetic objects in an external magnetic field carry associated energies. This magnetic energy (E_{mag}) is a form of potential energy and can be calculated as [75]:

$$E_{mag} = -\vec{\mu} \cdot \vec{B_0} \tag{2.6}$$

This scalar product inherently depends on the angle between the two vectors. When both vectors are precisely parallel, E_{mag} becomes minimal because of the negative algebraic sign. Since a system wants to minimise its potential energy, the magnetic moment will try to align itself with the external field. This tendency can be seen with a compass needle. In the case of a compass needle, friction is responsible for stopping its oscillation [75].

2.1.5 Spin and magnetism

This section introduces the relationship between spin and magnetism. An ^{1}H nucleus has a magnetic moment resulting from its spin. Magnetic moments of multiple ^{1}H nuclei (e.g., in the human body) align to some degree under the influence of an external electromagnetic field (as present in an MRI scanner). The alignment is the basis for MR imaging and spectroscopy.

As mentioned above, magnetism has its origin on a microscopic scale. On the one hand, it is an inherent property of particles; on the other, it is generated by the movement

of electric charge [75]. A particle's magnetic moment is directly related to the particle's spin [44].

$$\mu = \gamma S \tag{2.7}$$

The gyromagnetic ratio (γ) relates the particle's spin with its magnetic moment [75]. The sign of γ can either be positive or negative, signifying the orientation of the magnetic moment in relation to the spin. For instance, in the case of ^{1}H nuclei, where γ is positive, the magnetic moment aligns parallel to the spin. Conversely, when γ is negative, the magnetic moment aligns in the opposite direction [75].

If a proton is subject to a magnetic field, its magnetic moment interacts with the magnetic field. Like the previously mentioned compass needle, the proton's magnetic energy will be the lowest if its magnetic moment points in the direction of B_0. Since no friction eventually stops the proton and it has a spin angular momentum, it begins to precess (Figure 2.1). During this precession, the angle between the spin axis and the magnetic field stays the same. Simultaneously, the spin axis rotates around the axis of the magnetic field [44, 75].

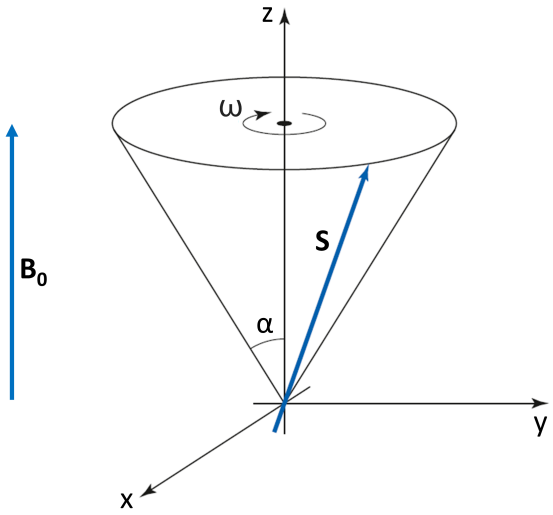

Figure 2.1: Precession produced by a magnetic field. The precession of the spin axis S of a particle due to the magnetic field $\vec{B}_0$ is shown. In this case, B_0 points along the z-axis. ω is the angular velocity and α is the angle of precession. Adapted from Griffiths [44].

2.1.6 Larmor frequency

The frequency of the particle's precession around B_0 is called Larmor frequency [14, 44]. If the Larmor frequency is given as an angular frequency, it is denoted ω_L. The value of a particle's Larmor frequency is given by [14, 44]:

$$\omega_L = -\gamma B_{loc} \tag{2.8}$$

Notably, the Larmor frequency does not depend on B_0 directly but on the local magnetic field (B_{loc}) that a particle is subject to [75]. This means that even small-scale changes in the magnetic field result in different Larmor frequencies. The gyromagnetic ratio determines the rotational direction of the precession. If ω_L is positive, the direction of the rotation is given by the right-hand rule when the thumb is aligned with the magnetic field [75].

2.1.7 Net magnetisation

While the magnetic moment of a single proton cannot be measured using an MRI scanner, the summation of multiple magnetic moments can be measured. Considering a probe of water not exposed to magnetism, the magnetic moments of the ^{1}H nuclei point equally likely in every direction; there is no bias. The numerous protons, even in a small volume of water, will average out any tendency toward a particular direction [8, 75].

Two important things will happen if a magnetic field B_0 is applied to this water sample. Firstly, since water is diamagnetic, the sample will generate an induced magnetic field opposite to B_0. Secondly, the ^{1}H nuclei's spin polarisation axes will shift to smaller angles relative to B_0, i.e., will tend to align with B_0. Subsection 2.1.8 explains the underlying mechanism. The magnetic moments of the ^{1}H nuclei are added and defined as the net magnetisation (M) to quantify this tendency. The net magnetisation vector represents the average orientation of all spin magnetic moments [8, 75].

M is not solely a theoretical quantity; it can be measured with an MRI scanner. Further, it is useful to consider M, not individual magnetic moments, when evaluating macroscopic processes or the behaviour of an ensemble of particles [8, 75].

2.1.8 Longitudinal nuclear magnetisation

This subsection explains why M arises. Consider a sample of water. The spins of the protons and, thus, the magnetic moments are uniformly distributed within the sample. This state is called isotropic distribution. This isotropic distribution must be broken to observe an effect of nuclear magnetism, meaning there must be a polarisation in one direction [75]. When B_0 is applied to such a sample, there arises a polarisation of spins and thus magnetic

moments in the direction of B_0 [112].

Since the magnetic energy diminishes when the magnetic moments are orientated towards B_0 (Subsection 2.1.4), there is a statistical tendency that smaller angles of precession will result. Due to this effect, a longitudinal polarisation arises, i.e., a polarisation of magnetic moments towards B_0. This polarisation is slight because the thermal energies at room temperature are large compared to the magnetic energies at 3 or even 7 T. Longitudinal magnetisation (M_z) is determined by a thermal equilibrium between the tendency of the ^{1}H nuclei to align with B_0 and their capability to acquire energy from the surrounding thermal environment [14]. Consequently, strong magnetic fields are necessary for MRS/MRI. Longitudinal polarisation can be understood as the build-up of M along the axis of B_0 [75].

The formation of M_z is also called spin-lattice relaxation or longitudinal relaxation. Longitudinal relaxation results from time-dependent processes. If the external magnetic field is turned on or off, M_z builds or decays exponentially, respectively [14, 75].

$$M_z = M_{eq} \cdot (1 - e^{\frac{t}{T_1}}) \tag{2.9}$$

M_{eq} is the maximal possible longitudinal magnetisation, and T_1 is the time constant that characterises how fast the process takes place. T_1 is called the longitudinal relaxation time constant and is a substance-specific property [75].

2.1.9 Transverse nuclear magnetisation

The effects of nuclear magnetic resonance must be measurable to use them. The longitudinal magnetisation (M_z) of an ensemble of ^{1}H nuclei is challenging to measure because it is small compared to the magnetic field induced by the diamagnetism of water. This induced field points precisely to the opposite direction of the longitudinal magnetisation. A way to circumvent this problem is to rotate M out of the z-axis (axis along B_0). The resulting magnetisation has a rotating component perpendicular to B_0. The rotation makes it easier to measure [75]. This component is called transverse magnetisation.

In MRS and MRI, an radiofrequency pulse (RF pulse) is used to rotate the magnetisation. The RF pulse rotates the net magnetisation by a defined angle called the flip angle. For instance, the flip angle can be 90°. In this case, the magnetisation no longer points in the direction of B_0 but is perpendicular to it, i.e., transverse [75].

The component of M that is transverse to B_0 after the RF pulse does not instantly decay after the RF pulse is turned off; it rotates about B_0 because the spins of the ensemble of ^{1}H nuclei precess with similar Larmor frequencies [112]. However, longitudinal relaxation resumes, and in addition to the transverse nuclear magnetisation, a longitudinal magneti-

sation component starts to rebuild. The transversely polarised spins eventually dephase because some spins rotate faster than others, as every nucleus experiences a slightly different magnetic field. This process is a consequence of Equation 2.8, where the frequency will change when B_{loc} is different for nuclei of an ensemble [75].

The decay of transverse magnetisation is also called transverse relaxation or spin-spin relaxation. It is abbreviated as T_2 relaxation. Again, there is a substance-specific constant called T_2 or transverse relaxation time constant. T_2 quantifies the rate of transverse relaxation. If it were not for the spin-spin relaxation, the transverse magnetisation would rotate about the z-axis indefinitely, and its x- and y-components (M_x and M_y) would fluctuate in a sinusoidal fashion. T_2 decay and the rotation of the transverse magnetisation yield the following formulae for both components in case the transverse magnetisation is aligned with the x-axis after the RF pulse [14, 75]. The equations are illustrated in Figure 2.2.

$$M_x = M_{eq} \cdot \cos(\omega_0 t) \cdot e^{\frac{-t}{T_2}} \tag{2.10}$$

$$M_y = M_{eq} \cdot \sin(\omega_0 t) \cdot e^{\frac{-t}{T_2}} \tag{2.11}$$

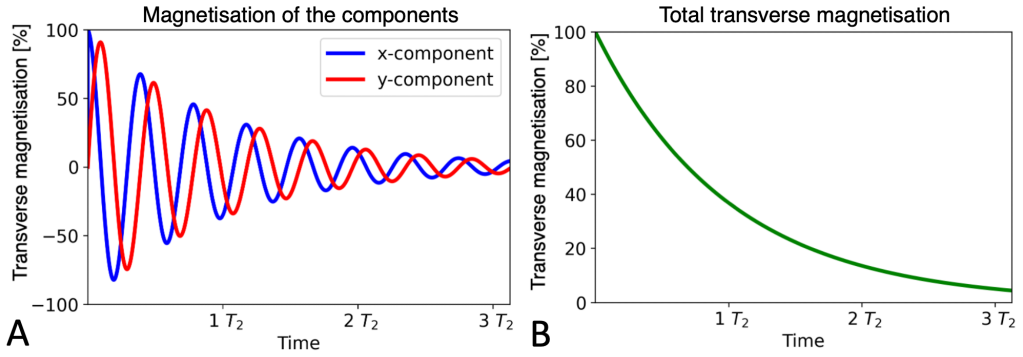

Figure 2.2: T_2-decay of transverse magnetisation. [A] Transverse relaxation of the x- and y-components over time. The x- and y-components of the transverse magnetisation fluctuate according to the Equations 2.10 and 2.11. [B] Relaxation of the total transverse magnetisation. After the time T_2, the overall transverse magnetisation will have diminished to 36.8% or e^{-1} times the initial amplitude.

2.1.10 Longitudinal relaxation

Longitudinal relaxation occurs after an RF pulse has rotated the net magnetisation out of the z-axis. The system strives to return to the lowest energy state, which is achieved when the net magnetisation is realigned with B_0. The energy that was added to the system via the excitation of the spins must be reallocated for the realignment to happen [75].

The ^{1}H nuclei transfer their energy to nearby molecules. The transfer happens, for instance, through collisions and electromagnetic interactions. The time constant that quantifies the relaxation is called longitudinal magnetisation time constant T_1 [14, 42, 75, 112]. For T_1 values of human tissues at 1.5 T, see Figure 2.3A.

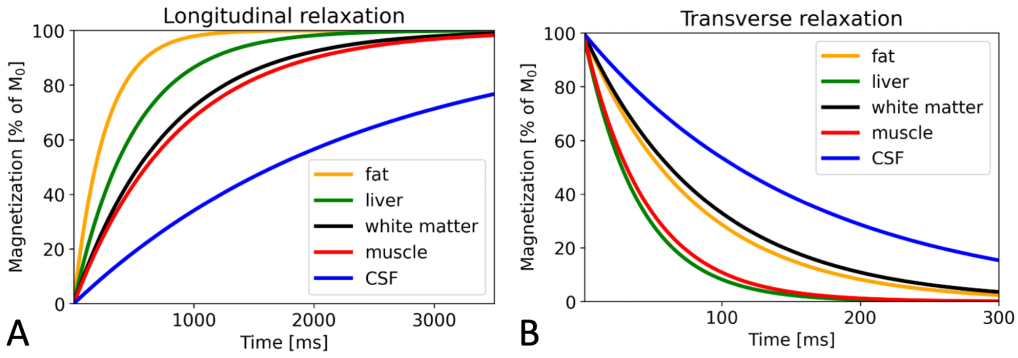

Figure 2.3: Longitudinal and transverse magnetisation of different human tissues. The values for T_1 and T_2 used here were published by Mahesh [84]. [A] The longitudinal relaxation is depicted for the following tissues at B_0 = 1.5 T: fat (T_1 = 260 ms), liver (T_1 = 500 ms), muscle (T_1 = 870 ms), white matter (T_1 = 780 ms) and cerebrospinal fluid (CDF) (T_1 = 2400 ms). [B] The transverse relaxation is depicted for the following tissues: fat (T_2 = 80 ms), liver (T_2 = 40 ms), muscle (T_2 = 45 ms), white matter (T_2 = 90 ms) and CSF (T_2 = 160 ms).

2.1.11 Transverse relaxation

The loss of transverse magnetisation over time is called transverse relaxation. Some phenomena lead only to transverse relaxation but not to longitudinal relaxation. However, longitudinal relaxation also leads to transverse relaxation [75].

The processes leading to longitudinal relaxation are associated with an energy exchange of the ^{1}H nuclei with their environment. After the exchange, the spin axis can point in any possible direction, resulting in a loss of phase with the other spins. Further, the ^{1}H nuclei are subject to B_{loc}, the sum of B_0 and magnetic fields produced by nearby atoms and molecules. Due to the motion of molecules relative to each other, B_{loc} varies over time. The slightly larger or smaller local magnetic field changes the Larmor frequency of an ^{1}H nucleus exposed to such field fluctuations. Naturally, an altered Larmor frequency leads to a loss of phase with other spins. This loss is an example of a process that leads to transverse relaxation but not longitudinal relaxation [14, 75, 112]. The time constant that quantifies the transverse relaxation is called the spin–spin relaxation constant T_2. Figure 2.3B shows typical T_2 values for human tissues at 1.5 T.

2.1.12 Susceptibility effects

In reality, the transverse magnetisation decays faster than the T_2 value would suggest. This disagreement has different reasons. In contrast to an idealised system, an MRI scanner does not have a perfectly homogeneous magnetic field since the magnets and coils used are imperfect.

Further, many tissues and molecules inside the human body are either significantly para- or diamagnetic. The induced field created by para- or diamagnetic tissues changes B_0 and leads to further field inhomogeneities. Both the imperfect magnets of the MRI scanner and the effects of para- and diamagnetism lead to local field inhomogeneities that cause differences in Larmor frequencies of individual ^{1}H nuclei.

Over time, those differences will dephase the synchronised ^{1}H nuclei and, consequently, the transverse magnetisation. For that reason, transverse magnetisation decays faster than would be expected. The time constant that denotes the effective transverse magnetisation is called effective transverse relaxation time constant (T_2^*) [21, 114].

2.1.13 Free-induction decay and signal detection

The previous subsections described how net magnetisation arises in MRS and MRI. A transverse magnetisation component occurs by applying an RF pulse. The rotating transverse magnetisation creates a changing electromagnetic field that is the key to obtaining a measurable signal.

Faraday's law of induction serves as a basis for measuring the signal. The law is commonly stated as "the electromotive force around a closed path is equal to the negative of the time rate of change of the magnetic flux enclosed by the path" [65]. This statement means that a changing magnetic field, like the one created by net magnetisation, can induce a current in a conductive loop. The changing electromagnetic field, created by the rotating transverse magnetisation, is detected by coils that act as conductive loops [50].

This electric current/signal is called free induction decay (FID). The word decay is used because the signal diminishes over time due to transverse relaxation. The FID is subsequently analysed by technical means to obtain spectra and images [75].

To acquire a vector representation of the net magnetisation, two perpendicularly arranged coils are required since a single coil can only measure the net magnetisation along the axis through its centre [75]. Using two coils enables the measurement of the net magnetisation in two different directions, which can be mathematically represented as a complex number using i, the imaginary unit.

$$C = Re(C) \cdot \cos(\alpha) + i \cdot Im(C) \cdot \sin(\alpha) \tag{2.12}$$

Here, C is a complex number, Re(C) is the real part of the complex number, Im(C) is the imaginary part, and α is the angle in the complex plane. In this example, the FID signal of the second coil (FID_2) is multiplied by i and added to the FID signal of the first coil (FID_1) to obtain a vector in the complex plane. The magnitude of the vector corresponds to the absolute strength of the net magnetisation and its angle to the phase of the net magnetisation. The zero point of the phase must be corrected later. Thus, the signal can be written as:

$$Signal(t) = FID_1(t) + i \cdot FID_2(t) \tag{2.13}$$

This notation is essential to understand how the signal is analysed subsequently [75].

2.1.14 Fourier transformation

Due to variations in B_{loc}, the nuclei precess with slightly different frequencies. The aim of MRS is to quantify the frequencies in the sample and their relative abundance. For the quantification, a spectrum in the frequency domain is desired. However, the FID is a signal in the time domain. The FID is caused by ^{1}H nuclei precessing with different frequencies. It is possible to differentiate these frequencies and obtain a frequency-domain spectrum from the time-domain signal. The mathematical procedure necessary to obtain such a spectrum is called Fourier transform [36].

The FID(t) is transformed into a continuous frequency domain function F(ω) by the Fourier transformation (Figure 2.4). This frequency domain function represents the desired spectrum and is calculated using the equation [98]:

$$F(\omega) = \int_{-\infty}^{\infty} FID(t) \cdot e^{-i\omega t} dt \tag{2.14}$$

By this means, the Fourier transform allows analysing the frequencies of the precessing ^{1}H nuclei in MRS [14, 75].

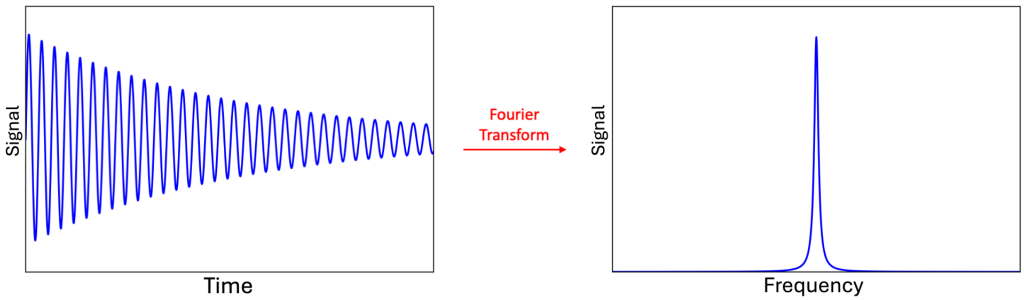

Figure 2.4: Principle of Fourier transform. A Fourier transform is a mathematical method to transform a periodic signal in the time domain, like the one shown on the left, into a spectrum (displayed to the right). For simplicity, only the real part of both the time-domain signal and the frequency-domain spectrum (phase corrected) are shown above.

2.1.15 Phase correction

As explained above, the signal FID(t) is a complex number and combines the signals of two different receiver coils positioned perpendicular to each other. The spectrum obtained by the Fourier transform F(ω) is also complex and has thus a real and an imaginary part. In Figure 2.4, only the real part of F(ω) is shown. It takes the form of an absorption mode Lorentzian. The imaginary part of F(ω) has another form called a dispersion mode Lorentzian. Figure 2.5 shows both.

The above only holds if FID(t) has no phase shift. In practice, FID(t) is often phase-shifted, and the real part of the spectrum is no longer a pure absorption mode Lorentzian but has a dispersion component, as shown in Figure 2.5. This dispersion component is detrimental to further analysis of the spectrum. A phase correction is applied to the spectrum to diminish the dispersion component [35].

The phase correction can be applied to the FID(t) and the frequency domain signal F(ω). It can be shown mathematically that the phase-corrected spectrum $F_{cor}(\omega)$ is obtained as follows [35].

$$F_{cor}(\omega) = e^{i\varphi_{cor}} \cdot F(\omega) \tag{2.15}$$

When $\varphi_{dephase}$ is the phase shift of the original spectrum F(ω), it turns out that:

$$\varphi_{dephase} = -\varphi_{cor} \tag{2.16}$$

In practice, the phase φ_{cor} is found in a trial and error fashion, adjusting the phase until

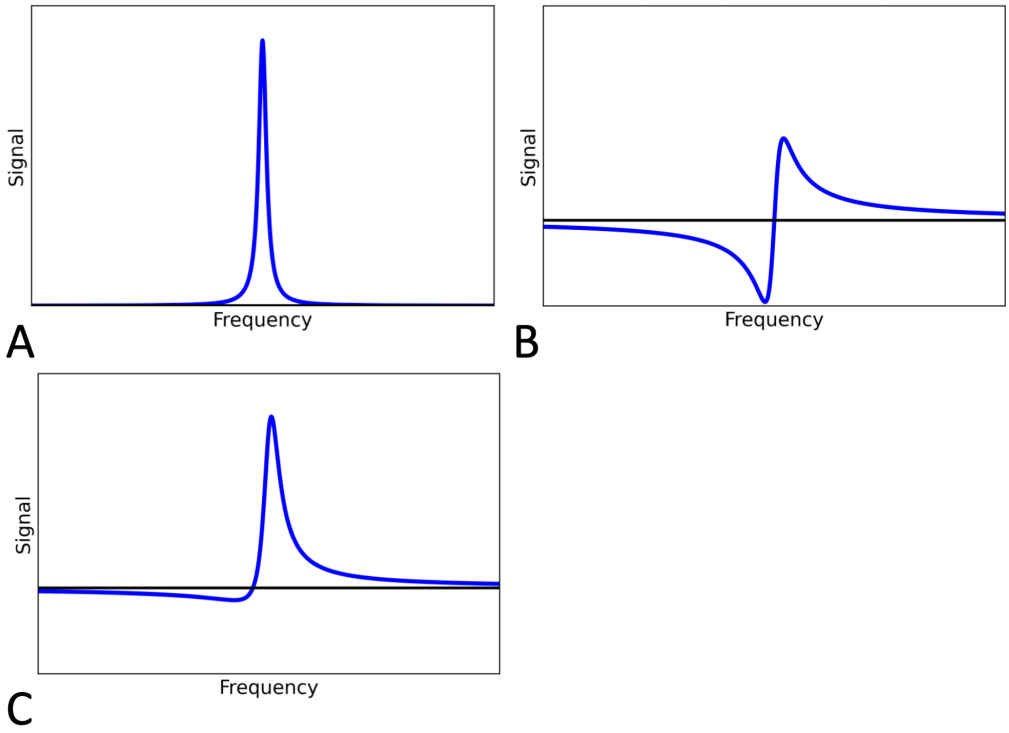

Figure 2.5: Basics of phase correction. [A] shows the real part of a spectrum with no dephasing. In this case, the real part is a perfect absorption mode Lorentzian. [B] shows the imaginary part of a spectrum with no dephasing. This line shape is called dispersion mode Lorentzian. [C] shows a spectrum that can be seen as the result of a real MRS measurement. Here, the spectrum is neither in complete absorption nor dispersion mode. It has characteristics of both. Phase correction aims to modify such a spectrum to approximate the line shape of [A].

the spectrum appears to be closest to an absorption mode.

2.2 Technical basics

This section explains how a modern MRI scanner is set up. Further, gradients are introduced as they are necessary for MRI and MRS sequences in whole-body MRI scanners. The timing of RF pulses and gradients in a measurement is called a sequence. The basic parameters of sequences will be explained as well.

2.2.1 MRI scanner

MRS is a method that researchers first used in chemistry and physics for analysing molecular properties [49]. The use of nuclear magnetic resonance in medicine is comparatively new. In the 1970s, Mansfield, Lauterbur and Damadian published papers that laid the

foundation for developing modern MRI scanners [25, 72, 85].

MRS instruments used in chemistry/physics cannot access information on the spatial distribution of the nuclei in the sample yielding the signal. However, imaging depends on being able to distinguish different locations. The basic idea that made imaging and modern MRI scanners possible was to achieve spatial resolution by applying a field gradient in addition to the main magnetic field [72]. When such a gradient is applied, nuclei experience different local magnetic fields and start to precess with varying Larmor frequencies depending on their position within the scanner [14]. Herman Carr was the first to use this technique [18].

Although applying a single gradient was a start, further technological principles and components are used in modern-day MRI scanners. The main aspects are explained below. Figure 2.6 depicts an MRI scanner and its components.

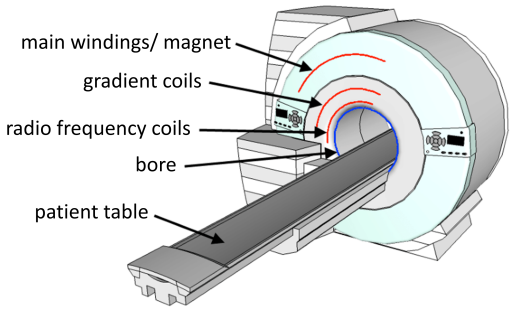

Figure 2.6: MRI scanner and its components. Adapted from Haynes et al. [55].

2.2.2 Main components and functions of an MRI scanner

Main magnet and shimming A superconducting coil creates the main magnetic field. This coil is usually made of niobium-titanium (NbTi). For NbTi to become superconducting, it must be cooled below 9.4 K. The cooling is achieved by placing the NbTi coil in liquid helium below this critical temperature. The coil and the liquid helium are placed in a cryostat to avoid heating. The coil is arranged along the length of the scanner.

In addition, shim coils are another component of the scanner. The current in the shim coils can be modified to make B_0 more homogeneous. This process is called active shimming. Pieces of metal or ferromagnetic materials are placed around the bore's opening to enhance the homogeneity of B_0. This process is called passive shimming. Modern clinical scanners operate with B_0 in the 0.3 to 7 T range.

Radiofrequency coils and pulses In addition to the coils that generate the main magnetic field and the shimming coils, radiofrequency coils are an important component of the MRI scanner. In contrast to the previously mentioned coils that operate with a direct current, radiofrequency coils operate with an alternated current. Radiofrequency coils produce the radiofrequency pulses necessary to generate transverse nuclear magnetisation. An RF pulse is a rotating electromagnetic field B_1. B_1 is far weaker than B_0 [75]. The frequency of the RF pulse is set to be resonant with the nuclei's Larmor frequencies. This resonance allows energy to be transferred to the nuclei. The RF pulse rotates the net magnetisation by a defined angle [75]. The pulse duration is correlated to the angle that it will produce [14].

Radiofrequency pulses are used to sway the net magnetisation out of the alignment with B_0 (Figure 2.7). The rotation is necessary since magnetisation can only be measured when there is some x- or y-component to the net magnetisation. In MRS, the most common RF pulse rotates the net magnetisation by 90° (usually called 90 degrees radiofrequency pulse (90°-pulse)). The signal can be detected either through the radiofrequency coil that was used to transmit the pulse or through a separate set of coils [14, 45].

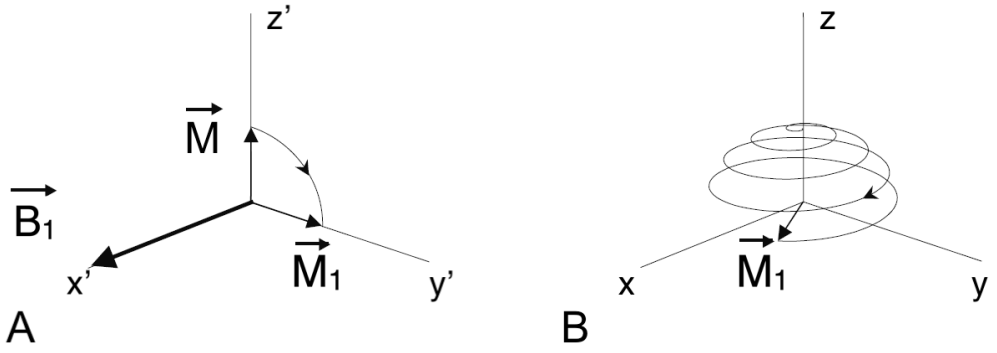

Figure 2.7: Effect of a radiofrequency pulse on the net magnetisation. [A] The effect of a 90°-pulse is shown in a rotating frame of reference. In this rotating frame of reference, the rotating magnetic field $\vec{B_1}$ caused by the RF pulse always points along the x'-axis. The effect of the 90°-pulse is to rotate the net magnetisation $\vec{M}$ by 90° so that it points along the y'-axis after the pulse is applied. $\vec{M_1}$ denotes the net magnetisation after the 90°-pulse. [B] shows the effect of the same 90°-pulse in a non-rotating frame of reference. Adapted from Brown et al. [14].

Gradient coils and gradients In general, a gradient (G) is a measure of the spatial change of a field. In MRI/MRS, the gradient is a measure of the magnetic field's change in space, for example, along the x-axis of the scanner. Consider two points x_1 and x_2 along the x-axis of the scanner with the magnetic fields $B(x_1)$ and $B(x_2)$ respectively. The gradient along the x-axis can be calculated using the distance between these points (Δx).

$$G = \frac{B(x_1) - B(x_2)}{\Delta x} \tag{2.17}$$

Gradients are necessary for spatially localised MR spectroscopy and imaging. Gradient coils of MRI scanners create such gradients along arbitrary axes. In modern scanners, there are usually three gradient coil systems installed. The first gradient coil system can produce a gradient along the z-axis, the second along the y-axis, and the third along the x-axis [62]. These coil systems can produce a gradient along every possible axis. Using gradient coil systems enables the variation of the magnetic field as a function of space [18, 72].

The local magnetic field B_{loc} determines the Larmor frequencies of the nuclei (Equation 2.8). If no gradient is applied, all nuclei precess similar Larmor frequencies and are equally excited by an RF pulse. When a gradient is applied, B_{loc} starts to vary in the sample, and an RF pulse may only excite some of the nuclei. For instance, if a gradient is applied along the z-axis (Figure 2.8), each plane perpendicular to the z-axis contains a set of nuclei with similar Larmor frequencies. These sets can be excited selectively using a sinc-shaped RF pulse [18, 72].

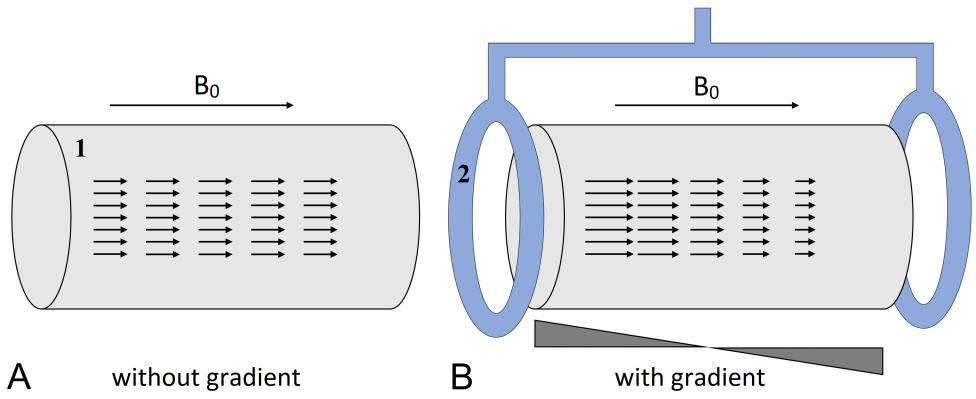

Figure 2.8: Visualisation of gradients. (1) denotes the space within the scanner. The gradient coils for generating a gradient along the z-axis are denoted by (2). [A] Situation without gradients. The magnetic field within the scanner is homogeneous and determined by B_0. [B] Under the influence of a gradient along the z-axis, the local magnetic fields B_{loc} differs according to their position along the z-axis. Differences in the local magnetic field are the prerequisite for slice-selective excitation by an RF pulse.

2.2.3 Sequence parameters and design

The following paragraphs introduce different parameters and concepts used in MRI and MRS sequences. These are necessary to understand how sequences are designed.

Repetition time (TR) and echo time (TE) TR and TE are two of the essential parameters in MRS/MRI. The repetition time is the interval between the first RF pulses of two consecutive sequences. During the repetition time, longitudinal and transverse relaxation occur. In general, longer values for TR will lead to more signal intensity because the first RF pulse of a sequence acts solely on longitudinal magnetisation, which is not fully restored after a short TR. Thus, TR determines the contrast depending on the T_1 constant [14, 62, 114].

The echo time is the interval between the excitation of the nuclei and the time when the FID is measured. The longer TE, the more the image's contrast depends on T_2, the transverse relaxation time constant. This is because the FID is caused by the transverse magnetisation, which decays with T_2 [14, 62, 114].

Spoiling Spoiling is used to get rid of unwanted signals. In the following, one application for spoiling is presented. Consider two consecutive sequences and the repetition time between them. In many image acquisition modes, the repetition time is short compared to T_2, meaning that the transverse magnetisation produced by the first sequence has not fully decayed at the start of the second sequence. The transverse magnetisation that remains after the first sequence gives rise to unwanted components in the signal. Here, spoiling can be used to get rid of the unwanted, previously generated transverse magnetisation. There are three modes of spoiling in use: long TR spoiling, gradient spoiling, and RF spoiling.

Long TR spoiling means that the repetition time is chosen to be significantly longer than T_2^* so that the coherence is lost due to natural processes. In gradient spoiling, gradients are used at the end of the sequence to dephase the nuclei before the following sequence starts. RF spoiling is achieved through variation of the phase of the RF pulses [30, 73].

Crusher gradients These are used for gradient spoiling and are essential in MRS [73]. Crusher gradients are applied to eliminate unwanted signals within a single sequence. RF pulses are imperfect as they do not lead to the same flip angle in the entire sample. In addition, the nuclei positioned at the edges of a selected slice experience flip angles smaller than the desired ones. Unwanted transverse nuclear magnetisation arises from those nuclei. Crusher gradients desynchronise this unwanted transverse nuclear magnetisation.

Multiple RF pulses are often used to excite nuclei within a single MRS sequence. Using multiple pulses leads to the formation of desired and undesired signals. The latter can

be targeted with crusher gradients as well [16].

Echoes Due to T_2^* decay and, in some cases, the deliberate use of gradients, transverse magnetisation diminishes over time. Accordingly, the signal in the FID gets smaller as well. However, there are ways to recover transverse magnetisation partially. The two ways of recovery explained below are spin echoes and gradient echoes. Such techniques cause a temporary spike in the magnitude of the FID. This spike is called echo and gives the methods their names [74].

Spin echoes During a sequence, the nuclei lose phase coherence due to the effects of T_2 decay and those that additionally contribute to T_2^* decay. The added effect of T_2^* decay is due to field inhomogeneities that are constant over time. Spin echoes can recover the part of the signal lost due to T_2^* decay. How a spin echo achieves this due to the application of a 180°-pulse is explained in the following.

The nuclei that experience an increased field due to those inhomogeneities rotate faster (Figure 2.9). The faster rotation means that the spins will gain phase compared with other nuclei. A 180°-pulse inverses the phase gains of the faster-rotating nuclei relative to other nuclei. As the sequence progresses, the faster-rotating nuclei compensate for their loss in phase and catch up with the other nuclei. The moment they catch up, all dephasing of the additional components of T_2^* is lost. The resulting signal peak is called spin echo. However, a spin echo cannot compensate for the decay of transverse magnetisation solely due to T_2 relaxation [49, 74, 113].

Gradient echoes In contrast to spin echoes, gradient echoes do not compensate for the effects of microscopic field inhomogeneities. Two equally strong, equally long gradients of opposite directions are applied after an RF pulse to produce a gradient echo. The first gradient dephases the nuclei, while the second gradient rephases the nuclei again. The rephasing only happens provided the spins do not move [86].

Gradient echo formation is a versatile tool in imaging sequences. One of the primary applications of gradient echoes is frequency encoding, an essential MRI component. In addition, diffusion- and susceptibility-weighted imaging commonly uses gradient echoes.

When a sequence contains a 180 degrees radiofrequency pulse (180°-pulse), the gradients must be set up differently to form a gradient echo. A gradient applied before a 180°-pulse must be followed by a gradient of the same direction, not the opposite, after the 180°-pulse for a gradient echo to form. This holds because the differences in phase of the spins are reversed by the 180°-pulse [74, 113].

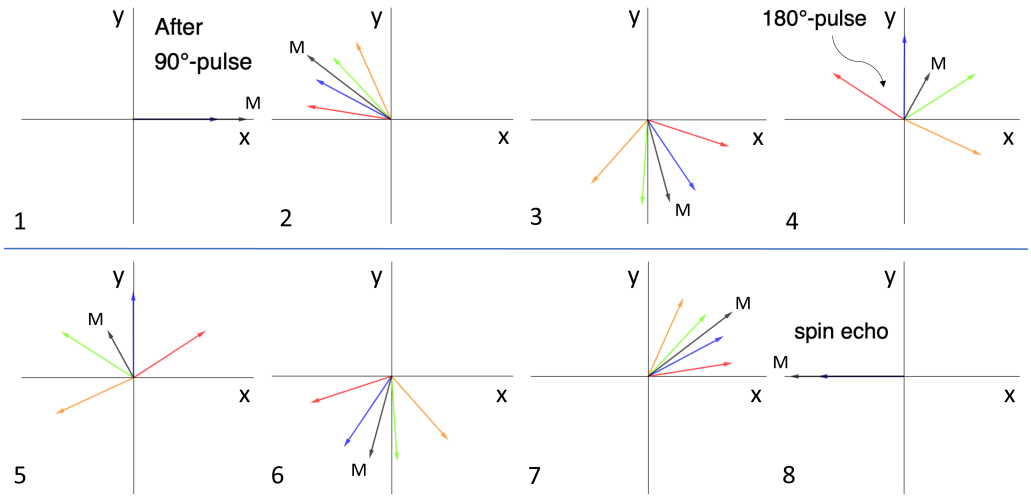

Figure 2.9: Formation of a spin echo. At first, the net magnetisation is turned in the xy-plane by a 90°-pulse and aligned with the x-axis (1). Afterwards, the transverse magnetisation (herein M) starts to rotate (clockwise). The spin axes of individual nuclei start to dephase due to T_2^* decay (2–4). Here, the spin axes of four different nuclei are depicted as blue, red, green, and yellow arrows. The net magnetisation gets smaller because of the dephasing from (2) to (4). At the moment that is depicted in (4), a 180°-pulse is applied. This pulse mirrors the spin distribution at the y-axis, meaning that the gain in the phase of the faster precessing nuclei, which occurred between (1) and (4), is reversed. The situation after the 180°-pulse is depicted in (5). The faster precessing nuclei (orange and green arrow) now lag behind the slower rotating ones. This lag gets smaller from (5) to (8) since the faster precessing nuclei catch up. Consequently, the net magnetisation reaches a second maximum at (8), called spin echo. This schematic representation neglects pure T_2 decay.

2.3 MR spectroscopy

In contrast to MRI, the purpose of MRS is not to generate images. MRS aims to analyse the distribution of the Larmor frequencies of signals from a given sample/volume. Differences in Larmor frequency occur between chemical elements since each has its specific gyromagnetic ratio. Further, differences in frequency occur in nuclei of the same element due to differences in the chemical binding of the nuclei. Local field inhomogeneities of B_0 lead to changes in Larmor frequency even in nuclei of the same element bound in the same way [32, 75].

In contrast to MRI, volume-selective MRS evaluates just one or a few voxels. The position of these voxels cannot be frequency encoded because the frequency is to be evaluated. Therefore, MRS makes use of slice-selective excitation. The signal measured in MRS is converted through Fourier transformation. The result is a spectrum of frequencies that corresponds to the precessing nuclei. When evaluating the frequencies, the chemical shift (δ) is used for analysis instead of absolute frequencies [75, 130].

2.3.1 What a spectrum shows

Consider a sample of pure water within a homogenous magnetic field. All ^{1}H nuclei are bound to oxygen similarly. The spectrum will show a single frequency peak near the Larmor frequency of ^{1}H. The chemical bindings of the ^{1}H nuclei to oxygen alter the local magnetic field at the microscopic level, resulting in an offset from the Larmor frequency. This is an elementary illustration of a spectrum. However, more intricate spectra arise from distinct molecules with varying chemical bindings of the ^{1}H nuclei within a sample. Spectral peaks representing nuclei are not infinitely sharp lines, but they are peaks with a finite height and width. The width of the spectrum is characterised by the full width at half maximum (FWHM). The FWHM is the width of the spectral peak measured at half its maximum [75].

The spectrum $S(\omega)$ has the following nature:

$$S(\omega) = \frac{\lambda}{\lambda^2 + (\omega - \omega_0)^2} \tag{2.18}$$

In this function, the constant λ determines the peak's width. Importantly, the T_2 relaxation time influences the width of the spectral peak. If T_2 is long, the peak is sharp. If T_2 is short, the peak is broad. The uncertainty principle explains this. The coherence decay rate constant λ depends inversely on T_2 and is given by [75]:

$$\lambda = \frac{1}{T_2} \tag{2.19}$$

Interestingly, FWHM is exactly 2 λ [75].

2.3.2 Chemical shift effects

As stated above, the chemical shift measures differences in Larmor frequency in MRS. Measuring a chemical shift δ between two identical nuclei exposed to the same B_0 is possible. They do not directly experience B_0 but the local magnetic field B_{loc}. B_0 and B_{loc} differ because of the diamagnetic susceptibility and effects of the electron shell. The effect of B_0 on the electron shell leads to an induced magnetic field (B_{ind}) opposed to B_0. The local magnetic field is thus the difference of B_0 and B_{ind}. This opposed magnetic field diminishes the effect of B_0 on the nuclei [54, 131].

$$B_{loc} = B_0 - B_{ind} \tag{2.20}$$

The Larmor frequency ω_{L} does not depend on B_0 but on B_{loc}, meaning that local differences in magnetic susceptibility result in different Larmor frequencies for otherwise identical nuclei.

$$\omega_L = -\gamma \cdot B_{loc} \tag{2.21}$$

MRS can measure these Larmor frequencies, usually quantified using the chemical shift δ [131]. The chemical shift is calculated as follows. Since the chemical shift δ is a measure for differences in ω_{L}, a reference frequency ω_{ref} must be defined with which the frequency of a sample ω_{sam} is to be compared. The reference frequency is measured using tetramethylsilane as a reference substance in ^{1}H spectroscopy. The chemical shift can be calculated using both frequencies [54, 131]:

$$\delta = \frac{\omega_{sam} - \omega_{ref}}{\omega_{ref}} \tag{2.22}$$

The resulting ratio is small because the differences in frequencies are minor compared to the absolute frequencies. Therefore, δ is given in ppm (parts per million). Further, it is helpful to utilise a ratio, not the absolute difference in frequencies, since the ratio is independent of B_0 [54, 131].

The extent of diamagnetic susceptibility a nucleus experiences is largely determined by the nature of its chemical binding to other nuclei and its valence electrons [75]. As a result, one can distinguish differently bound nuclei within a given sample/tissue by measuring the chemical shift.

2.3.3 MR spectroscopy sequences

Multiple MRS sequences are used in MRI scanners. One can measure a single voxel or multiple. Measuring a single voxel is called single volume spectroscopy (SVS). The two SVS methods most commonly used are point-resolved spectroscopy (PRESS) and stimulated echo acquisition mode (STEAM), which will be explained in detail. Measuring multiple voxels is called chemical shift imaging or MR spectroscopic imaging [5, 32].

Point resolved spectroscopy (PRESS) PRESS is explained in the following and illustrated in Figure 2.10A. PRESS uses three RF pulses to generate a final spin echo. This spin echo comes from a voxel within the sample, defined by slice selection (Figure 2.11).

At first, a slice selection gradient (SSG) along the z-axis is imposed. Then, a 90°-pulse

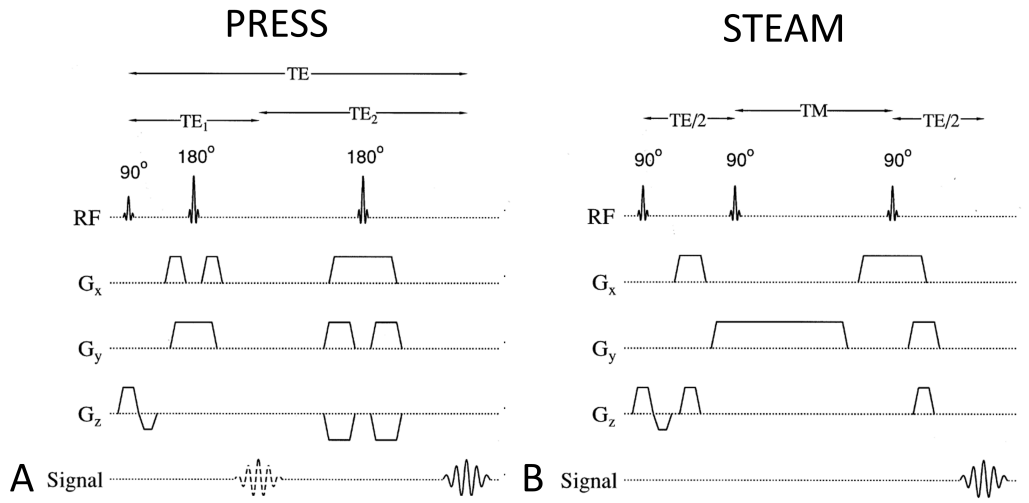

Figure 2.10: Sequence design of PRESS and STEAM. [A] In PRESS, the initial 90°-pulse is followed by a 180°-pulse, which acts to refocus the spins after TE_1 to form a spin echo. A second 180°-pulse refocuses this first spin echo to form a final spin echo after TE_2, which is recorded as the signal. [B] In a STEAM sequence, the initial 90°-pulse is followed by two other 90°-pulses to form a stimulated echo. After the second 90°-pulse, the net magnetisation is antiparallel to B_0 and, therefore, not subject to T_2 decay during TM. The final two 90°-pulses combined act like a single 180°-pulse and refocus half the nuclei after TE. Adapted from Schick [111].

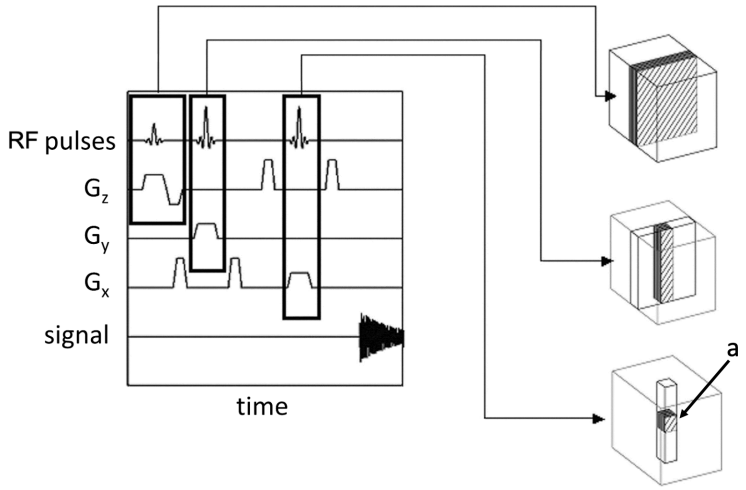

Figure 2.11: Method of slice selection in PRESS. Three SSGs are applied during a PRESS sequence to enable volume selection. The gradients are consecutively applied in the z-, y-, and x-direction. Only the small cube (a) experiences all three RF pulses. Thus, the slice selection ensures that the FID comes only from the voxel (a). Adapted from Klose [70].

excites nuclei in an xy-plane. A crusher gradient is applied before another SSG is imposed along the y-axis. This SSG and a 180°-pulse act upon the magnetisation in an xz-plane

perpendicular to the previously selected xy-plane.

A second crusher gradient is applied after the 180°-pulse. The second crusher gradient refocuses only the magnetisation affected by the 180°-pulse and the first crusher gradient. The magnetisation in the intersection of both planes undergoes a spin echo at the time TE_1.

A third crusher gradient is introduced before applying the second 180°-pulse during a third SSG along the x-direction. The second 180°-pulse affects magnetisation in a yz-plane mutually perpendicular to the two preceding planes.

Subsequently, a fourth crusher gradient refocuses the magnetisation affected by the third crusher gradient and the second 180°-pulse. Only the magnetisation in a voxel at the intersection of all three planes is refocused by all three RF pulses. The second 180°-pulse is responsible for another spin echo at the time TE_2. The total echo time is the sum of TE_1 and TE_2 [70, 111, 131].

$$TE = TE_1 + TE_2 \tag{2.23}$$

While the first spin echo is essential for the second spin echo to form, it is neither analysed nor measured. The second spin echo is measured and used for analysis. The excited nuclei are subject to T_2 relaxation during TE. Since two spin echoes must happen, TE is long. The long echo time results in the inherent weakness of PRESS when measuring substances with short T_2 relaxation times [70, 111, 131].

Stimulated echo acquisition mode (STEAM) STEAM generates a stimulated echo using three consecutive 90°-pulses. As in PRESS, the 90°-pulses are imposed during the SSGs in the x-, y-, and z-direction. The gradients ensure that the signal comes from nuclei in a voxel where the three selected planes intersect. The echo is a stimulated echo instead of a spin echo measured in PRESS [16]. As a consequence of the stimulated echo, half the signal intensity is lost compared to PRESS [92].

The sequence design is explained in the following and illustrated in Figure 2.10B. The first 90°-pulse flips the net magnetisation into the xy-plane. At first, the spins must dephase to eventually generate a stimulated echo. A dephasing/crusher gradient achieves the necessary dephasing.

Then, a second 90°-pulse flips the spins out of the xy-plane to a variable extent, meaning the information is phase-encoded and stored as longitudinal magnetisation. T_2 decay does not affect those spins until the next pulse. The third 90°-pulse flips the magnetisation back into the xy-plane. Combined, the second and third RF pulses have an effect like a 180°-pulse. Therefore, the spins will produce an echo analogous to a spin echo after a 180°-pulse [70, 111, 131].

The time between the second and the third 90°-pulse is called mixing time (TM). TM is unique because T_2 relaxation does not affect the signal during this interval. Further, TM can be varied and used for multiple purposes such as water suppression or T_1-weighting. The time between the first and the second 90°-pulse (t_{12}) is as long as the time between the third 90°-pulse and the following stimulated echo (t_{3STE}). In STEAM, the echo time is defined as the sum of t_{12} and t_{3STE} [75].

$$TE = t_{12} + t_{3STE} \tag{2.24}$$

In addition to the previously mentioned SSGs, crusher gradients (Subsection 2.2.3) must be applied. SSGs and crusher gradients between the first two 90°-pulses must be compensated by rephasing gradients after the third 90°-pulse for a stimulated echo to form. The rephasing gradients used for this purpose have the same direction as those applied between the first two 90°-pulses because the second and third 90°-pulses combined reverse the phase differences (as they act like a 180°-pulse, see Subsection 2.2.3). In addition to the stimulated echo, the three RF pulses produce four spin echoes. STEAM also uses crusher gradients to minimise the influence of the spin echoes on the signal [70, 111, 131].

2.4 Magnetic resonance imaging

While this thesis primarily concerns MRS, MRI is used in the experiments to position voxels for the MRS sequences. Therefore, this section briefly discusses the basics of MRI.

2.4.1 Making an image

A typical MR imaging sequence generates a 2D imaging series for diagnostic purposes. These images are usually oriented parallel to one another and aligned along a predefined axis [112]. The fundamental principles of MR imaging, including slice selective excitation, phase encoding, and frequency encoding, enable the creation of such images. These principles will be further elucidated in the subsequent sections.

Slice selection Slice selection is the first step in an imaging sequence. A plane perpendicular to the z-axis is selected. The image will correspond to this plane. Applying an SSG along the z-axis enables slice selection. The width of the slice depends on the magnitude of the gradient. An RF pulse generates transverse nuclear magnetisation of the nuclei in

the selected plane. This RF pulse marks the start of the sequence. Afterwards, spin or gradient echoes, frequency encoding, and phase encoding follow.

Frequency encoding Frequency encoding is necessary to separate pixels of the MR image. The whole plane contributes to the signal if solely unidirectional slice selection is used. No information about the x- or y-direction could be distinguished. The MR image is defined by a set of signals corresponding to the pixels. Frequency and phase encoding are utilised to determine a signal for each pixel.

Applying a so-called ”read-out gradient” during the measurement of the FID achieves frequency encoding. The read-out gradient is used either in the x- or y-direction. In this example, it is applied in the x-direction. The effect of the gradient is to influence the Larmor frequencies of the nuclei along the x-axis, meaning that the FID will contain signals with different frequencies. It is possible to separate these frequencies using Fourier transformation (Subsection 2.1.14) and attribute signals to rows along the x-axis of the image [14, 112].

Phase encoding In addition to phase encoding, frequency encoding is necessary to yield an image. Both are necessary because every pixel in a row created by frequency encoding along the x-axis produces a signal that is superposed with the other pixels. Introducing phase encoding to a sequence is necessary to access information about the individual pixels in the rows.

Phase encoding is achieved by applying a gradient just before recording the FID. The gradient is applied along the y-axis in this example. The gradient alters the phase of the nuclei based on their position along the y-axis. Thus, MR imaging can access information about individual pixels in each row. The number of phase encoding steps determines the number of pixels along the y-axis. Therefore, the phase encoding is repeated multiple times [14, 112].

The information gained by frequency and phase encoding is sorted into the so-called ”k-space”. The resulting raw image is then subjected to two-dimensional Fourier transformation, which yields the final image [14, 112].

2.4.2 Types of images

MRI distinguishes different tissue types like fat, muscle, or fluids. The differentiation is achieved because these tissues vary in molecular and cellular properties. Depending on the indication for the MRI scan, different imaging sequences are necessary to provide relevant information. The various sequences aim at differences in tissue properties to gain information [14, 62].

T_1-weighted images T_1-weighted images use differences in longitudinal relaxation times of different tissues. The shorter the longitudinal relaxation time constant, the more signal the tissue will contribute to the image. A T_1-weighted image is created by a sequence with a short repetition time (TR) and a short echo time (TE). A short TE is used because the longer the echo time, the more the signal will decay due to T_2 relaxation. The T_2 decay is unwanted since the image should only depend on differences in T_1 relaxation [114, 143].

A short TR is used because tissues with small T_1 constants rebuild longitudinal magnetisation faster after a previous RF pulse than those with larger T_1 constants. The longitudinal magnetisation in tissues with small T_1 constants will be converted into a larger transverse magnetisation by the following RF pulse. More transverse magnetisation means more signal intensity. Thus T_1 contrast is created [114, 143].

T_2-weighted images T_2-weighted images depend on the transverse relaxation times of tissues. A long TR and a long TE are needed in this case. The long TR ensures that T_1 relaxation has taken place, minimising its effect on image contrast. Long echo times achieve T_2-weighting as tissues with shorter T_2 constants will give rise to less signal than those tissues with longer values of T_2 [114, 143]. Additionally, spin echo formation is required to compensate for chemical shift and microscopic field inhomogeneities [114].

A problem of T_2-weighted sequences is that they demand much time since the repetition time can be several seconds. Therefore, fast or turbo spin echo sequences were developed [114, 143]. These sequences record multiple echoes after each excitation pulse, reducing the time required for signal acquisition.

Diffusion-weighted images Diffusion-weighted images show the extent of diffusion in the human body. While water in the ventricular system or the bladder diffuses freely, water in cells is trapped. Whether a structure contains free water or water confined by cells is medically helpful information. The differentiation between a tumour and a cyst is possible with such information [2, 143].

Diffusion-weighting is achieved by bipolar gradient switching. Two equally strong gradients are applied in opposite directions to dephase and then resynchronise the nuclear spins. However, not all tissues will be resynchronised to the same extent. Free water will move during the gradients due to diffusion. Due to this movement, a free water molecule experiences the second gradient differently. Thus, the signal created by the gradient echo will be smaller for free water. Where little diffusion happens, tissues will contribute more signal in diffusion-weighted images. The applied gradients are called diffusion-sensitising gradients (DGs) [2, 143].

2.5 Blood flow in the human body

The primary example of flow in the human body is blood flowing through the vasculature. In principle, larger arteries branch into smaller ones that enter different organs. Within these organs, small arteries branch further and become arterioles. These arterioles drain into a system of capillaries, which transfer oxygen and nutrients from the blood to the surrounding tissue [4, 81].

The architecture of capillaries varies depending on the organ they nourish. The bone marrow, liver, and spleen need discontinuous endothelium to function, whereas the brain depends on its tight blood-brain barrier [29]. The diameter of the capillaries is also not uniform in all tissues. These differences in architecture lead to differences in the flow patterns. The following subsections show these tissue-specific properties in bone marrow, brain, and muscle tissues [4, 81]. These tissues were chosen as they are frequently examined using MRS or represent promising targets for research. Further, this study investigated bone marrow experimentally.

Capillaries converge into venules, which collect the deoxygenated blood. Venules form small veins, which leave the organs and join larger veins. The large veins bring blood back to the heart (the exception being the portal vein). Examples of flow velocities in veins and arteries are given in the following.

2.5.1 Blood flow in large vessels

The highest blood flow velocities in the human body occur in the arteries. In contrast to small vessels like capillaries, blood flow in arteries is not continuous. In the systole, the heart pumps blood into the arteries with high pressure, and maximum flow velocities occur in arteries close to the heart. The peak flow velocities of arteries more distal from the heart occur later. The delay is due to the elasticity of arteries.

In the diastole, the large arteries contract to supply blood volume to the periphery and stabilise the peripheral blood pressure. In the aorta, peak velocities of 1–1.5 m/s were observed, with average velocities of 0.67 ± 0.22 m/s in women and 0.64 ± 0.21 m/s in men [37].

Arteries that branch directly from the aorta and larger arteries generally exhibit high flow velocities. In the renal artery, mean peak systolic velocities between 0.60 ± 0.28 and 0.66 ± 0.25 m/s were found in one study [60]. For the middle cerebral artery, average flow velocities of 0.64 ± 0.10 m/s in subjects 40 or younger and 0.55 ± 0.11 m/s in subjects above 40 years of age have been reported [26].

Peripheral arteries show slower flow velocities. For instance, the P2 segment of the posterior cerebral artery shows an average flow velocity of 0.34 ± 0.03 m/s in subjects 40

or younger and 0.30 ± 0.03 m/s in subjects above 40 years of age [26].

In veins, blood flows slower. In the inferior vena cava, average velocities between 0.26 and 0.11 m/s and between 0.10 and 0.07 m/s in the superior vena cava have been reported [140]. Large peripheral veins show even slower flow velocities. For instance, the popliteal veins of a control group showed flow velocities of between 5.27 and 7.86 cm/s in one study [79].

2.5.2 Blood flow in bone marrow

Recently, flow dynamics in bone marrow were investigated in detail by Bixel et al. using a mouse model [7]. The following is based on these results. Figure 2.12 provides an overview of the bone marrow architecture. Bone marrow has many cavities and is built similarly to a sponge. In these cavities, blood vessels are found.

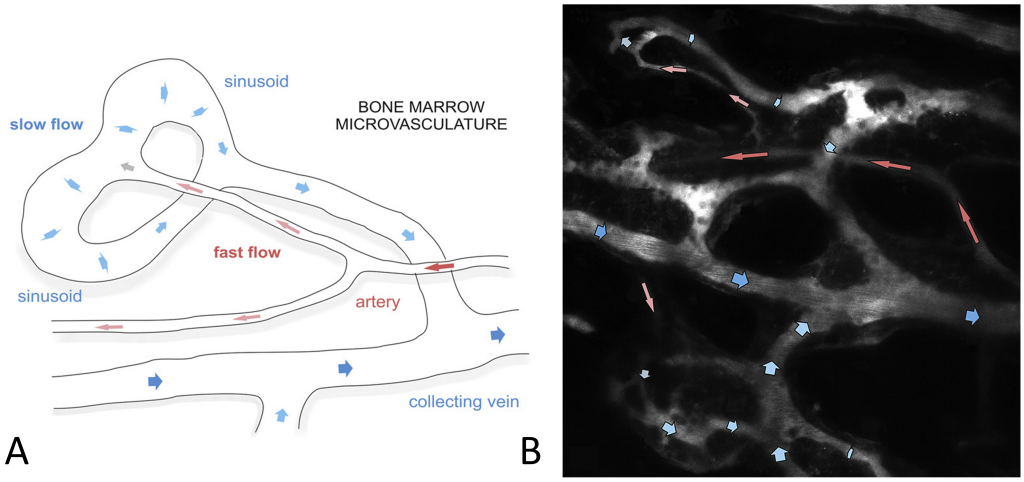

Figure 2.12: Blood flow in bone marrow. [A] A schematic representation of blood flow in the bone marrow. The flow is faster in arteries and post-arterial capillaries than in the sinusoidal capillaries and the venules. [B] Two-photon microscopy picture of bone marrow microvasculature. Red arrows indicate arterial, fast blood flow, pale blue arrows indicate slow flow within the sinusoidal capillaries, and dark blue arrows indicate intermediate flow in venules. Adapted from Bixel et al. [7].

The blood enters the bone marrow through arterioles, which branch into smaller arterioles until they meet a system of capillaries and sinusoidal vessels. In these arterioles, flow velocities of approximately 2.0 mm/s were observed [7]. Post-arterial capillaries are smaller and form the next generation of vessels. In capillaries, blood flow velocities of about 1.1 mm/s were observed [7]. Arterioles are approximately 8.0 μm in diameter, while the post-arterial capillaries are slightly smaller on average (7.8 μm) [7].

The sinusoidal vessels are larger in diameter (10 – 46 μm) than the arterioles, and their basement membrane is discontinuous [7]. They form an irregular system of inter-

connected vessels with slow blood flow. The blood flow becomes more turbulent as the erythrocytes are no longer stacked on each other, as in the thin arterioles. On average, the flow velocities in sinusoidal vessels were 0.23 mm/s [7].

The sinusoidal system drains into collecting venules. The average flow velocity in the venules increases slightly and is in the range of 0.5–0.8 mm/s [7]. Their diameter varies between 20 and 25 μm [7]. The venules combine to form larger venules and veins.

In addition, intermediate capillaries connect post-arterial capillaries to sinusoidal capillaries. Their diameter is about 11.2 μm, and the blood flow velocity is approximately 0.66 mm/s [7]. Bixel et al. also observed sinusoidal capillaries with zero or near zero flow [7]. Table 2.1 gives an overview of the velocities and diameters in different segments of the vasculature.

Table 2.1: Flow velocities and vessel diameters in bone marrow. Adapted from Bixel et al. [7]. This table lists the calculated average flow velocities and diameters of the investigated vessels. The authors do not list precise averages for the venules but mention the range of values they observed in multiple venules. Those are included in the table as well.

Segment	Velocity [$\frac{mm}{s}$]	Diameter [μm]
Arteriole	1.95 ± 0.57	8.0 ± 1.0
Post-arterial capillaries	1.10 ± 0.31	7.8 ± 1.0
Intermediate capillaries	0.66 ± 0.18	11.2 ± 1.9
Sinusoidal capillaries	0.23 ± 0.22	21.1 ± 10.7
Venules	0.5–0.8	20–25

2.5.3 Blood flow in brain tissue

Generally, the brain's microvasculature differs from the vasculature in the bone marrow. While the bone marrow has fenestrated endothelium and wide sinusoids, the cerebral capillaries have a tight endothelium due to numerous tight junctions [7, 80]. The capillaries are also narrower, with approximately 5 μm in diameter [29].

More literature is available about capillary flow in brain tissue than in bone marrow. The following values have been measured in rats. Schulte et al. [117] published an average flow velocity of the red blood cells of 0.42 mm/s and Ivanov [61] of 0.79 mm/s. Further, Villringer et al. [134] determined an average value of 0.54 mm/s. A more recent study of

mice by Gutiérrez et al. investigated how flow velocity in capillaries changes depending on the depth of the capillaries in the cortex [47]. They measured an average flow velocity of 1.37 mm/s and found that flow velocities diminish the deeper the capillaries are in the cortex. Table 2.2 gives an overview of these studies.

Table 2.2: Flow velocities in capillaries of brain tissue. This table lists the different flow velocities found in capillaries of brain tissue by different authors.

Authors	Schulte et at.	Ivanov et al.	Villringer et al.	Gutiérrez et al.
Flow velocity [$\frac{mm}{s}$]	0.42 ± 0.02	0.79 ± 0.03	0.54 ± 0.33	1.37 ± 0.05

2.5.4 Blood flow in muscle

The muscle is subject to changing demands of nutrients and oxygen due to different physical activity levels. Therefore, the blood flow through a muscle is highly variable. These demands determine the properties of its microvasculature [71].

Several studies that compare the blood flow at rest to the blood flow under contraction of muscles in animals have been published [68, 69]. Further studies have investigated the difference in blood flow through muscles in young versus old mice [67, 109]. The average diameter of the capillaries was determined to be 6 μm in one study [109] and 5 μm in another [69].

Those studies only obtained values for capillary flow. However, Ivanov et al. have determined an average blood flow velocity of 2.43 mm/s in arterioles [71]. Table 2.3 summarises the capillary flow velocities determined in the studies. Arterioles in muscle tissue were found to have a diameter of between 20 and 50 μm in rats [71].

2.6 Gradient-induced phase-shift effects in ^{1}H spectroscopy

As stated in the introduction, this thesis concerns the effects of flow in MRS. While relatively little has been published concerning flow in MRS, several methods for measuring flow in MRI exist [92].

One of these methods is phase-contrast MR angiography. This method will be introduced in this section since it is vital to understand flow effects in PRESS and STEAM measurements. Gradient-induced phase-shift effects should also occur in PRESS and STEAM due to the application of various gradients. PRESS and STEAM sequences were analysed in this study to gain insight into this. Further, experiments were performed to validate the

Table 2.3: Capillary flow velocities in muscle tissue. This table gives an overview of the flow velocities in capillaries of muscle tissue determined by different authors.

Author	Flow velocity [$\frac{mm}{s}$]	Location of measurement
Ivanov et al.	1.14 ± 0.04	rat, temporal muscle
Klitzman et al.	0.21	hamster, cremaster
Kindig et al.	0.270 ± 0.062	rat, spinotrapezius at rest
Kindig et al.	0.428 ± 0.047	rat, spinotrapezius after contraction
Russel et al.	0.219 ± 0.012	young rat, spinotrapezius
Russel et al.	0.310 ± 0.014	old rat, spinotrapezius
Kindig and Poole	0.302 ± 0.011	rat, diaphragm

theoretical findings. To understand the experiments, the theoretical insight provided in this section is necessary.

2.6.1 Phase-contrast MR angiography

This subsection will explain gradient-induced phase-shift effects based on phase-contrast MR angiography. For this purpose, a simple sequence is chosen. However, the basic principles introduced here are directly applicable to MRS sequences.

It is possible to measure flow velocities in MRI using a spin echo sequence and bipolar ”flow-encoding” gradients. The gradients lead to a phase shift when nuclei are moving or flowing. In phase-contrast MR angiography, MR angiography can only measure the velocity along the direction in which the flow-encoding gradients are applied [15, 17]. The flow-encoding gradients are usually applied perpendicular to the imaging plane.

There are several ways to build a phase-contrast MR angiography sequence. One example is explained in the following and illustrated in Figure 2.13 [15]. For this purpose, the behaviour of stationary nuclei is compared to nuclei moving or flowing along the y-axis.

The sequence design is the following. Initially, a 90°-pulse and an SSG excite the nuclei in the imaging plane, here an xz-plane. Then, the first of two flow-encoding gradients is applied along the y-axis. The first gradient leads to a gain in the phase of all nuclei,

moving or stationary, in the imaging plane. The gain occurs because the nuclei experience a magnetic field produced by the gradient coils in addition to B_0.

Afterwards, the second flow-encoding gradient is applied. This second gradient is as strong as the first but points in the opposite direction. Therefore, the gradient nullifies the phase gain of the nuclei that have been stationary during the sequence. The effects of both gradients balance each other for static nuclei.

However, the nuclei that moved along the y-axis during the sequence experienced a stronger magnetic field during the second flow-encoding gradient than during the first (Figure 2.13). This is because the further a nucleus moves along the y-axis, the stronger the gradient dephases the nucleus. The effects of both gradients do not cancel each other because the moving nucleus experienced them differently.

Consequently, moving or flowing nuclei will have gained phase due to the flow-encoding gradients compared to stationary nuclei. The velocity can be determined using the phase shift. The phase shift ($\Delta\varphi$) over the period δ is calculated the following way [15, 17]:

$$\Delta\varphi = \gamma \cdot \int_{t}^{t+\delta} G(t) \cdot r(t) dt \tag{2.25}$$

Here, r(t) is a nucleus's position as a time function. The phase shift should be between $+180^\circ$ and -180° for phase-contrast MR angiography because one cannot differentiate between +270° and -90° and so on. Imaging sequences can show the phase differences in phase maps, where every pixel has a grey value representing the phase shift [15, 17].

Figure 2.14 shows another phase-contrast sequence. It differs from the one explained above since the second phase-encoding gradient points in the same direction as the first. Further, an additional 180°-pulse is added. The 180°-pulse acts to invert the initial dephasing created by the first phase-encoding gradient. The second phase-encoding gradient balances the previously created and reversed dephasing for stationary nuclei.

Although the first phase-contrast sequence explains gradient-induced phase-shift effects adequately, the second phase-contrast sequence was introduced because the underlying mechanism is encountered when dealing with phase-shift effects in PRESS and STEAM.

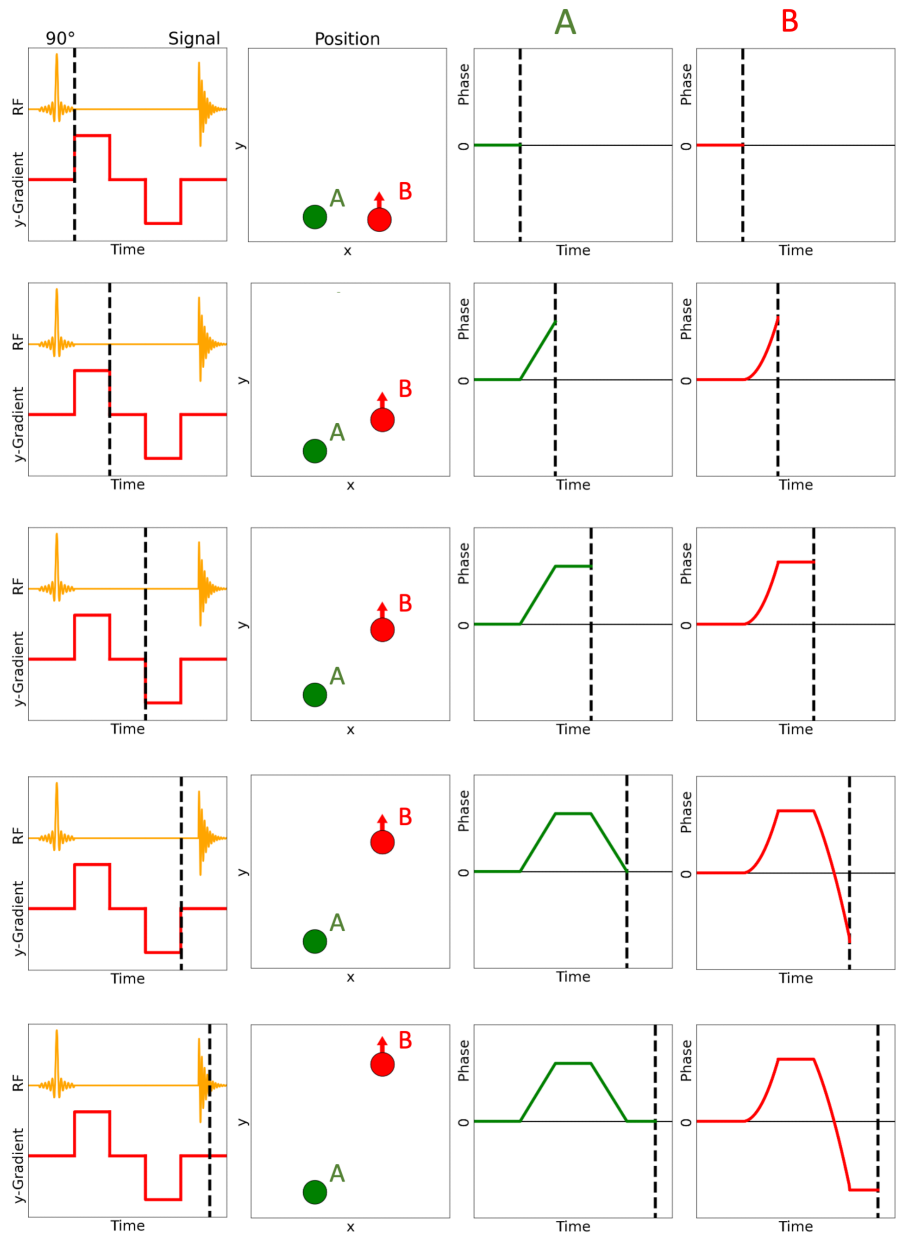

Figure 2.13: Phase contrast in gradient echo sequences. The first column shows the sequence plot. It is a gradient echo sequence with two gradients applied along the y-axis. For simplicity, the diagram does not show SSGs. The way the sequence acts upon two protons labelled (A) and (B) is shown. The second column of the diagram depicts their positions. The proton (A) is stationary and experiences a temporary gradient-induced phase shift. However, a net phase shift during the measurement does not occur because the second gradient cancels the phase shift produced by the first gradient, as they are equally strong but have different algebraic signs. The third column illustrates this. The proton (B) moves along the y-axis. Because of the increasing displacement along the y-axis during the sequence, (B) experiences a stronger dephasing during the second gradient than during the first, leading to a net phase gain at the measurement time. The fourth column shows this graphically.

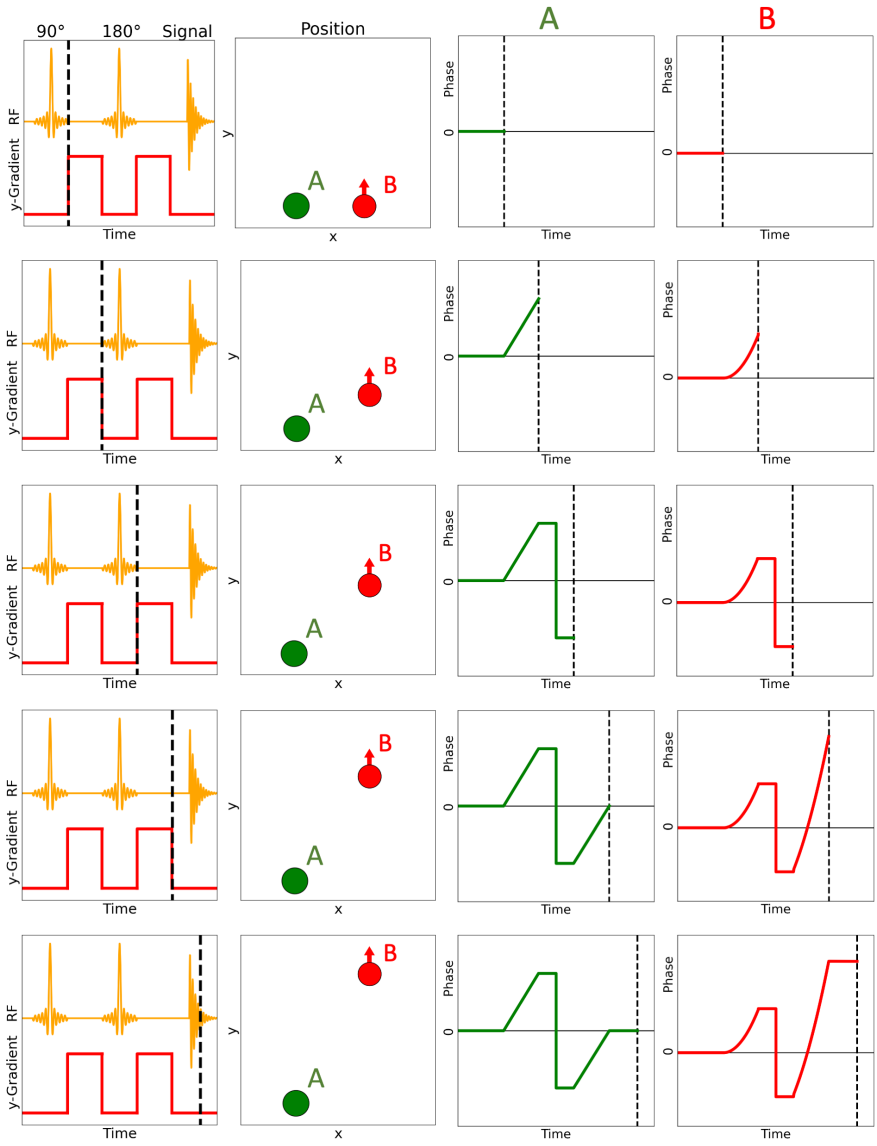

Figure 2.14: Phase contrast in spin echo sequences. The first column shows the sequence plot of the spin echo sequence with two gradients applied along the y-axis. The progression of the sequence is illustrated from top to bottom. The slice selection gradients are omitted from the diagram to maintain clarity. The behaviour of two labelled protons, (A) and (B), under the influence of the sequence is depicted. The second column of the diagram depicts their position in an xy-plane. Notably, the magnetic field induced by the gradients is more potent at the top of the xy-plane shown in the second column compared to the bottom. Proton (A) is stationary and experiences a temporary gradient-induced phase shift. However, a net phase shift during the measurement does not occur. The third column illustrates this. The reason is that the phase shift produced by the first gradient is cancelled by the second gradient when considering the inversion produced by the 180°-pulse. Proton (B) experiences a stronger dephasing during the second gradient than during the first because (B) moves to the top, where the magnetic field is stronger, leading to a net phase gain at the measurement time. The fourth column shows this graphically.

2.7 Susceptibility-induced phase-shift effects in ^{1}H spectroscopy

This section delves into the basics of phase-shift effects in ^{1}H spectroscopy arising from variations in the human body's susceptibilities. In addition to the previously mentioned gradient-induced phase-shift effects, susceptibility-induced phase-shift effects constitute the second important group of causes for changes in signal characteristics in ^{1}H spectroscopy related to flow.

It is beneficial to divide susceptibility-induced phase-shift effects into two distinct groups within the context of this thesis to provide clarity. Firstly, there are phase-shift effects primarily originating outside of vessels, attributable to substances such as air, fat, bone, and iron deposits. When these substances are close to vessels, they can induce phase-shift effects on flowing ^{1}H nuclei, thereby influencing the characteristics of MR spectra. Secondly, there are susceptibility-induced phase-shift effects associated with the BOLD effect, which are defined as the second group.

The BOLD effect originates in veins, venules and terminal capillaries, where deoxygenated blood accumulates. The deoxygenated blood leads to phase-shift effects of flowing ^{1}H nuclei inside these vessels. While extravascular mechanisms contribute to the BOLD effect, this thesis primarily focuses on intravascular mechanisms. This section will provide a more detailed introduction to the BOLD effect.

The background and underlying principles of the first group of susceptibility-induced phase-shift effects will be elucidated in the Subsections 2.7.1 to 2.7.4. The group of phase-shift effects related to the BOLD effect (BOLD-related phase-shift effects) will be explored in greater depth within the scope of this thesis. Section 3.5 introduces models developed for quantifying these BOLD-related phase-shift effects, while Section 4.5 presents the corresponding results obtained through these models.

The quantification of BOLD-related phase-shift effects represents the core of this thesis, in addition to the theoretical and experimental study of gradient-induced phase-shift effects. The necessary theoretical background to comprehend the BOLD-related phase-shift effects is given in the Subsections 2.7.6 to 2.7.8.

Magnetic field inhomogeneities due to dia- and paramagnetic substances

The following paragraphs provide background information for the first group of susceptibility-induced phase-shift effects, facilitating a deeper understanding of the following subsections. The fundamental concept of susceptibility was introduced in Subsection 2.1.4.

On average, the human body is slightly diamagnetic, with a susceptibility similar to that of water. However, naturally occurring substances such as air, fat, iron, blood, and bone differ significantly in their susceptibility compared to water. The presence of these substances generates inhomogeneous magnetic fields within the body. Nuclei near paramagnetic substances (compared to water) will experience a stronger magnetic field and precess faster. Nuclei near diamagnetic substances (compared to water) will experience a weaker magnetic field and precess slower.

In gradient echo sequences, this reduces signal intensity due to the phase shift of nuclei close to these substances. However, spin echo sequences can compensate for these effects, provided the spins remain stationary throughout the sequence. This scenario changes when dealing with moving or flowing nuclei, as their local magnetic field and Larmor frequency change during the sequence due to their motion relative to dia- or paramagnetic substances, and phase-shift effects arise (Figure 2.15). As mentioned above, these phase-shift effects can cause signal alterations in ^{1}H spectroscopy. The following subsections will highlight the roles of these substances in producing inhomogeneous magnetic fields in the human body.

2.7.1 Magnetic field inhomogeneities due to air

Air is mainly present in the lungs and other parts of the respiratory system. More broadly, gas is found inside the bowel, where its molecular composition differs from the air. Air is found elsewhere in pathologic conditions such as bowel wall necrosis, air embolism, and pneumomediastinum. In MRI, the lungs are the most critical location of air.

Air is weakly paramagnetic and has a volume susceptibility of $3.7 \cdot 10^{-7}$ [133]. This paramagnetic value is due to its oxygen content. However, when air is breathed in, it is saturated with diamagnetic water molecules, and the oxygen content drops inside the alveolar space due to the oxygenation of haemoglobin. Therefore, the air inside the lung has a lower volume susceptibility of about $1.8 \cdot 10^{-7}$ [133].

MR imaging of the lung is complex for different reasons. Apart from the low proton density of the lung and the significant motion during breathing, the susceptibility of air is another reason. The countless air-tissue boundaries inside the lung represent locations of sudden changes in susceptibility. These changes lead to microscopic field gradients. A highly inhomogeneous magnetic field inside the lung is the consequence. T_2^* relaxation times as short as 2 ms (at 1.5 T) occur. However, new imaging techniques such as ultrashort echo time imaging led to an advance in the MRI of the lung [6, 141].

For this study, it is relevant that the pulmonary vessels are very close to the air-tissue boundaries. Thus, the blood flowing inside the arterioles, capillaries, and venules is subject to the highly inhomogeneous magnetic field produced by the susceptibility differences

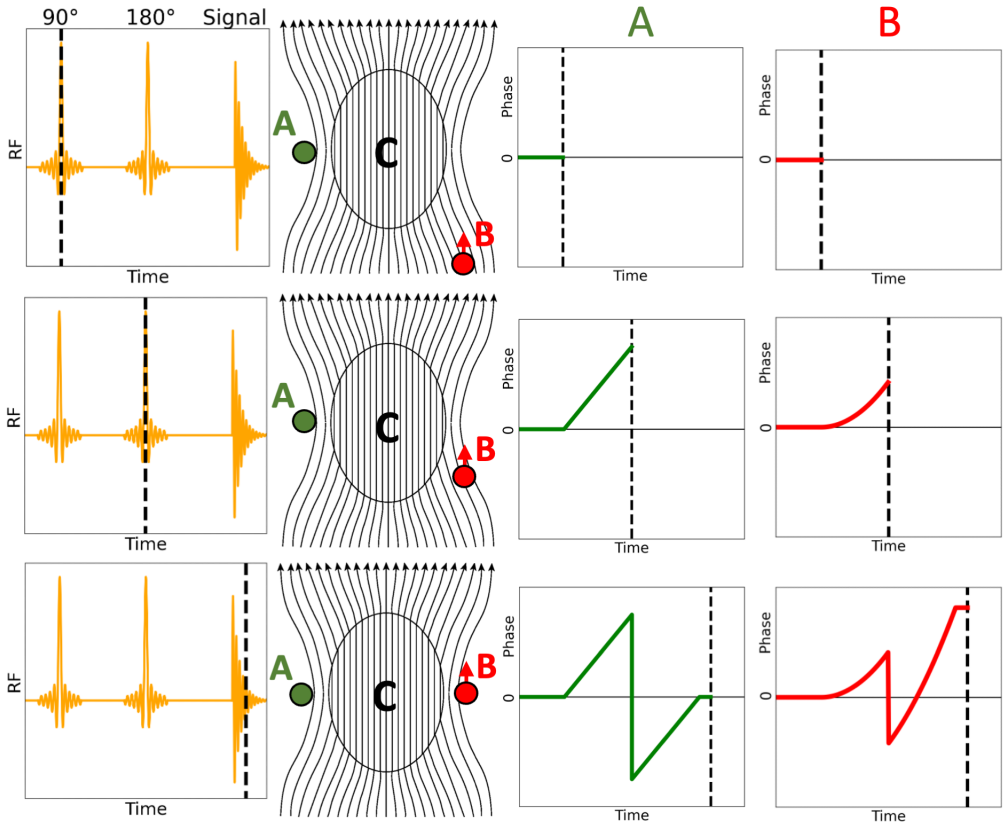

Figure 2.15: Susceptibility and motion. The first column shows a spin echo sequence plot with a refocusing 180°-pulse. The progression of the sequence is illustrated from top to bottom. The second column shows the position of the ^{1}H nuclei (A) and (B) relative to a paramagnetic object (C) shown as an oval. (A) is close to (C) and experiences a local magnetic field stronger than B_0. (B) moves closer to (C) during the sequence and is subject to an increasing local magnetic field due to (C). The third column shows that (A) gains phase during the sequence due to its proximity to (C) and that the 180°-pulse inverts the phase shift so that (A) has a net zero phase at the end of the sequence. In contrast, (B) experiences increasing field strengths, and the 180°-pulse is not able to resynchronise (B) with (A) at the end of the sequence. The fourth column of the diagram illustrates this. The field map displayed in the second column is adapted from Levitt [86].

of tissue and air. The hydrogen nuclei flowing through the vessels are expected to experience faster dephasing than the stationary hydrogen nuclei in the lung parenchyma due to their motion in the inhomogeneous magnetic field. Therefore, the lung is an organ where flow effects are relevant in MRI and MRS.

2.7.2 Magnetic field inhomogeneities due to fat

Fat is less diamagnetic than water. Human fat has a volume susceptibility of $-8.47 \cdot 10^{-6}$, while water has a volume susceptibility of $9.05 \cdot 10^{-6}$ [58, 110]. Therefore, regions where

fat and water-rich tissue border each other represent locations of susceptibility gradients. Fat, haematopoietic tissue, and vessels are close to each other in the bone marrow. Fat vacuoles are also near blood vessels in the liver, especially in steatohepatitis. Figure 2.16 shows both examples.

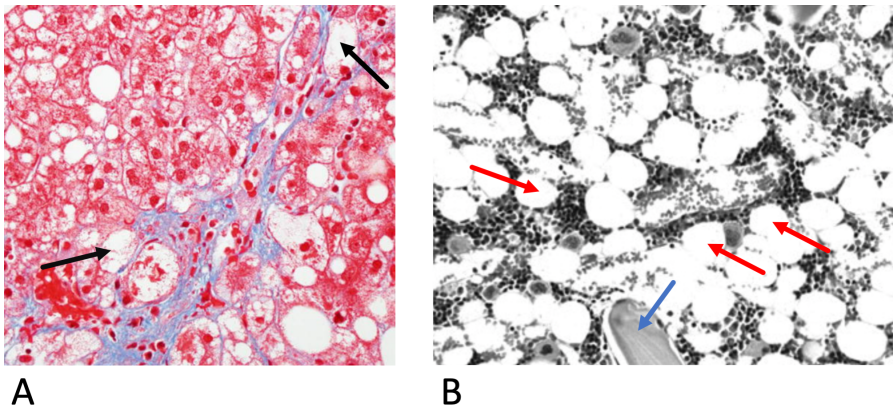

Figure 2.16: Proximity of fat and blood vessels. [A] shows fat vacuoles (indicated by black arrows) inside liver parenchyma close to sinusoids and small vessels. The image depicts a liver biopsy of a patient with non-alcoholic steatohepatitis. Adapted from Brown et al. [13]. [B] Bone marrow of the distal femur of a rat. The red arrows indicate fat vacuoles near the sinusoids. The blue arrow shows a bone trabecula. Adapted from Peci et al. [102].

Therefore, bone marrow and the liver provide instances where flow inside vessels occurs close to susceptibility gradients created by borders between water-rich tissues and fat. The influence of the susceptibility of fat inside bone marrow on signal characteristics has already been acknowledged [46, 58, 82].

2.7.3 Magnetic field inhomogeneities due to bone

Here, the effects of the susceptibility of cortical bone and bone trabeculae are discussed. One study showed cortical bone (bovine) to have a susceptibility of $11.3 \cdot 10^{-6}$ [58]. This value means compact bone is more diamagnetic than other tissues and water. While compact bone yields no signal in MRI due to very short relaxation times, the diamagnetic effects of compact bone are measurable [82]. The bone trabeculae are close to sinusoids and haematopoietic tissue in the red bone marrow. The blue arrow in Figure 2.16 indicates the proximity. At the borders of the trabeculae to surrounding tissue, susceptibility gradients arise [33]. These gradients contribute to the short echo times of bone marrow [33, 138]. The movement of ^{1}H nuclei inside the vessels close to trabeculae is a further example of flow in proximity to inhomogeneous magnetic fields.

2.7.4 Magnetic field inhomogeneities due to iron

As described above, magnetic field inhomogeneities arise from atoms, molecules, and structures with susceptibilities differing from the surrounding tissue. Iron atoms, found abundantly in the human body, occurring in various molecules and proteins, contribute to inhomogeneities. The extent to which an iron atom causes inhomogeneity depends on its chemical bonds and micro-environment. While iron in diamagnetic molecules creates weak inhomogeneities, iron-containing molecules can also be paramagnetic, ferromagnetic, and ferrimagnetic, resulting in substantial field disturbances.

Iron atoms are predominantly found in the blood (70%), where they bind to haemoglobin, with each haemoglobin subunit containing a pocket with a haem group holding a central iron atom. Oxygen binds to this iron atom to facilitate oxygen transportation in the human body [107]. Although oxygenated haemoglobin is diamagnetic, deoxygenated haemoglobin becomes paramagnetic, leading to measurable and relevant field inhomogeneities [107]. This effect, known as the blood-oxygen-level-dependent (BOLD) effect, will be discussed in more detail later in this chapter [43].

In addition to haemoglobin, iron is found in ferritin, transferrin, haemosiderin, myoglobin, iron-sulphur proteins, cytochromes, mitochondria, and foreign bodies (such as pacemakers, orthopaedic implants or projectiles) [24, 107].

Functions and metabolism of iron

Iron is transported to tissues and cells by the transferrin. The bone marrow is an essential destination for iron transportation since haematopoiesis needs iron. Here, the haem group is synthesised. Additionally, iron is bound to ferritin, a water-soluble protein that serves as an intracellular iron storage system. In the cytoplasm, iron atoms are integrated into enzymes like cytochromes. Similar to haemoglobin, iron binds oxygen in myoglobin.

Although iron recycling is effective, some iron atoms end up in haemosiderin, a conglomerate of denatured proteins, remnants of ferritin, and lipids. Haemosiderin is found inside cells and aged lysosomes. While the bulk of iron is found in erythrocytes, the fraction of iron stored in ferritin and haemosiderin is the second largest [106, 110]. As a result, the magnetic properties of ferritin and haemosiderin are examined next.

Ferritin

Ferritin, a polymer of 24 subunits and two polypeptides, measures 12 nm (Figure 2.17) [24]. It has a globular form and holds a crystallite of ferrihydrite (5–7 nm in diameter) containing iron in its centre [24]. The magnetic properties of the core are complex. While the iron atoms close to the surface are unordered and paramagnetic, the inner crystallite is su-

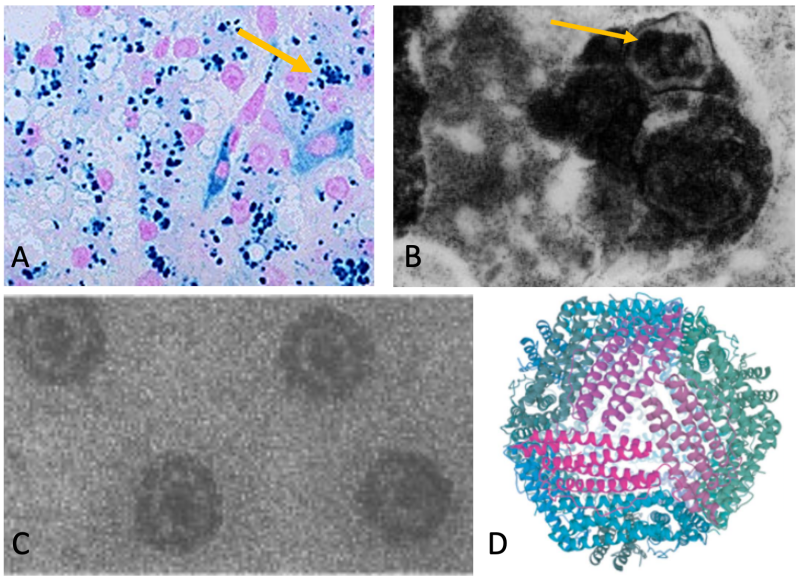

Figure 2.17: Haemosiderin and Ferritin. [A] Prussian blue stain of liver cells. The arrow indicates a group of haemosiderin conglomerates that are intensely stained due to their iron content. The picture is a courtesy of Allen D. Elster, MRIquestions.com. [B] An electron micrograph of a human spleen. The arrow points at haemosiderin inside a cell. Adapted from Crichton [24]. [C] An electron micrograph of ferritin sourced from a human spleen. The image displays four ferritin molecules, with a visible outer protein shell and inner iron core. Adapted from Crichton [24]. [D] The globular structure of apoferritin (ferritin without iron) is depicted. Adapted from Plays et al. [103].

perparamagnetic [1, 24, 107]. Although superparamagnetism is related to ferromagnetism, the behaviour of superparamagnetic structures is akin to strongly paramagnetic structures. Therefore, ferritin can create strong local magnetic field inhomogeneities. While the liver is the primary site of ferritin storage, the mononuclear phagocyte system cells in the bone marrow and spleen also contain ferritin [95]. Abnormally high ferritin levels are found in iron deposition diseases such as haemochromatosis [48].

Haemosiderin

The iron stored in haemosiderin is not readily accessible for physiological processes. It can be considered a waste product of ferritin and other proteins. The composition of haemosiderin varies, but it contains more iron than ferritin. Haemosiderin can become larger than ferritin [107]. Further, compared to ferritin, the resulting field inhomogeneities are even stronger [135]. Haemosiderin is found alongside ferritin in the liver, bone marrow and spleen. However, after acute or chronic haemorrhages, haemosiderin is also found at the bleeding site [144].

Furthermore, increased concentrations of haemosiderin are observed in conditions

such as hemochromatosis, sickle cell anaemia, and thalassemia [107]. More research is needed to clarify the magnetic properties of haemosiderin [107]. One study found human spleen haemosiderin to be paramagnetic, while another found an animal (Dugong dugon) liver sample to be superparamagnetic [1].

Iron in the brain

In addition to the organs mentioned above, the brain has iron-rich regions as well [107, 144]. Iron in the brain serves in cellular respiration as in other tissues but also for neurotransmitter synthesis and myelin production [89].

The highest concentration of iron is found in the globus pallidus, putamen, substantia nigra, red nucleus, and dentate nucleus [51]. Especially oligodendrocytes, microglial cells, pericapillary astrocytes, and endothelial cells contain iron [89]. Microglial cells belong to the mononuclear phagocyte system, which is known to store iron [144]. Oligodendrocytes show the highest concentration of iron and are responsible for myelination [89].

In the context of this thesis, it is interesting that high levels of iron are also present in pericapillary astrocytes and endothelial cells since the blood flowing through the capillaries might be affected by the field inhomogeneities produced by iron. On a subcellular level, the iron concentration is highest in the mitochondria and lysosomes [89].

Ferromagnetism

Usually, ferromagnetism does not occur in the human body. Although ferromagnetic particles have been found in various tissues, they are assumed to be of external origin [144]. Further, foreign bodies such as implants or even projectiles sometimes contain ferromagnetic iron or other ferromagnetic materials [120, 127]. Foreign bodies lead to safety concerns and strong inhomogeneities, creating artefacts in MR imaging [115, 124].

Flow and iron

As explained above, haemosiderin and ferritin are found in the liver, the spleen, and red bone marrow. Both of these molecules create strong magnetic field disturbances. All three organs have dense vasculature. Therefore, the flow of water molecules in vessels of these organs in the proximity of haemosiderin and ferritin should lead to the dephasing of the protons inside the water molecules. In diseases like haemochromatosis, the effects of the inhomogeneous magnetic fields produced by haemosiderin and ferritin have already been demonstrated. Further, the proximity of iron atoms to vessels inside the brain hints at the potential dephasing of spins inside the flowing blood.

2.7.5 Magnetic field inhomogeneities due to blood and the BOLD effect

When considering the field inhomogeneities produced by blood, it is essential to notice that blood susceptibility depends on the oxygenation level. Interestingly, blood in arteries is more diamagnetic than in veins because deoxygenated haemoglobin has four unpaired electrons in each of the four haem groups. In contrast, oxygenated haemoglobin has no unpaired electrons [100, 101]. The unpaired electrons make deoxygenated haemoglobin paramagnetic [43]. Therefore, the level of oxygenation of the blood directly determines its susceptibility. This phenomenon is called blood-oxygen-level-dependent (BOLD). Seiji Ogawa described the BOLD first [96, 97].

In research, the BOLD effect is used for functional magnetic resonance imaging (fMRI). FMRI is an imaging modality aiming to visualise brain activity. When neurons are activated, the surrounding arterioles dilate, and more blood flows through the nearby microvasculature [34]. However, the brain tissue's oxygen demand does not increase as much as the blood flow through the tissue [34, 43]. Therefore, venous blood in active brain regions has higher oxygen saturation levels (SO_2) than in inactive brain regions. Thus, a susceptibility change of the blood within veins after the activation of neurons in their surroundings occurs [14].

FMRI can visualise the difference in susceptibility because it leads to the dephasing of ^1H nuclei in the veins and their surroundings. This dephasing shortens the T_2 and the T_2^* constants of brain tissue, which means that T_2-sensitive sequences can identify the difference [14].

The following subsection explains the BOLD effect in more detail. This explanation is crucial for this thesis because the BOLD effect is suspected to cause susceptibility-induced phase-shift effects in flowing blood. As stated earlier, the evaluation and analysis of these effects are presented in the subsequent chapters, representing an integral part of this thesis.

2.7.6 Origins of the BOLD effect

As stated above, the change in susceptibility of the blood due to deoxygenated haemoglobin leads to field inhomogeneities and, therefore, dephasing of the nuclei in and outside of veins [43, 57]. This happens due to different mechanisms [12, 57]. While the BOLD effect encompasses extravascular and intravascular mechanisms, the subsequent explanations will focus on the two intravascular mechanisms relevant to this study.

Here, the first intravascular mechanism is explained. A cylinder that is paramagnetic compared to its surroundings creates a magnetic field inside the cylinder by induction when an external magnetic field B_0 is applied. The induced magnetic field inside the

cylinder augments B_0 [3, 14].

In MRI, a vein containing deoxygenated haemoglobin behaves like a cylinder [3, 14, 43]. Therefore, the nuclei inside the vein experience a stronger magnetic field than elsewhere (Figure 2.18) [3, 14]. This leads to phase-shift effects in gradient echo sequences [57]. However, since the stronger magnetic field inside a vein represents a temporally invariant field disturbance, it can be compensated for by spin echo sequences, as long as the nuclei are stationary [43]. If the nuclei are not stationary, phase shifts arise even in spin echo sequences.

In the existing literature, this effect is commonly called "susceptibility-induced phase shift of blood" [57]. However, in the context of this thesis, it will be referred to more concisely as the "BOLD-related phase-shift effect" as it is the sole contributor to the BOLD effect discussed in the following chapters.

Further, the diffusion of water molecules close to deoxygenated haemoglobin contributes to the BOLD as well [78, 129]. It is the second intravascular mechanism. On a microscopic scale, water molecules in the blood diffuse near deoxygenated haemoglobin. Deoxygenated haemoglobin creates a strong, inhomogeneous magnetic field. Therefore, ^{1}H nuclei experience different magnetic fields in short periods, leading to random dephasing and signal decay [129]. Since this happens chaotically, the signal decay is a form of T_2 decay and cannot be compensated by spin echo sequences [78]. In other words, blood's T_2 constant depends on the oxygenation level. This second effect is called "oxygenation-dependence of transverse relaxation of blood".

2.7.7 BOLD-related phase-shift effect

As mentioned above, the simulation of the BOLD-related phase-shift effect in ^{1}H spectroscopy constitutes one of two significant parts of this thesis. The previous subsection explained the origins of this effect. This subsection gives the corresponding formulae describing the magnetic field inside the vein and the susceptibility of venous blood. These formulae are crucial for the simulations shown in later chapters. The following subsection will provide more context and explain the mechanisms responsible for the BOLD-related phase-shift effect in ^{1}H spectroscopy.

Susceptibility of venous blood The susceptibility of venous blood can be determined if the oxygen saturation (SO_2) is known. In MRS, it is convenient to calculate the difference between the susceptibility of the blood χ_{blood} and its surrounding tissue χ_{st} instead of the absolute susceptibility.

$$\Delta\chi = \chi_{blood} - \chi_{st} \tag{2.26}$$

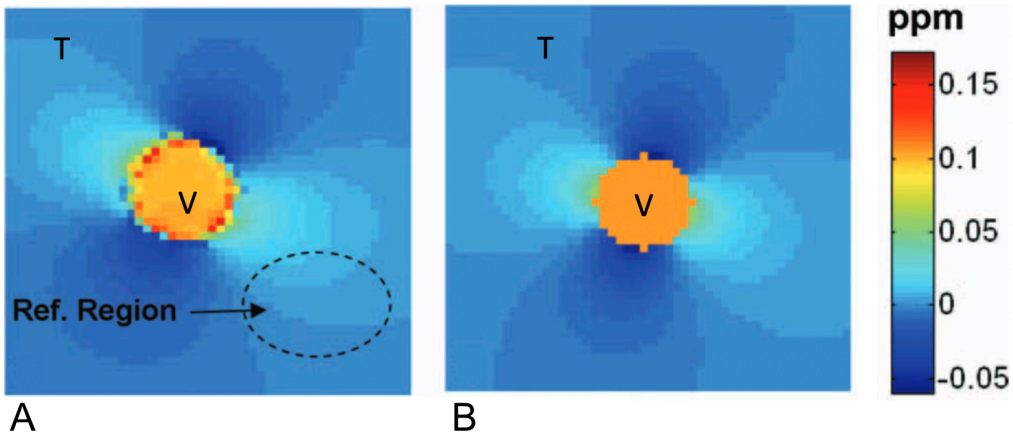

Figure 2.18: Susceptibility-induced phase shift inside and outside a vein. Here, V denotes the vein and T the surrounding tissue. [A] A field map of the cross-section of the femoral vein. The colours represent the variation of the magnetic field according to the scale on the right side. The figure shows that the magnetic field inside the vein is stronger than outside. However, the nuclei outside the vein are also affected by and contribute to the BOLD. The field map represents a computation that uses the anatomical geometry of the femoral vein. [B] For comparison, a field map has been computed assuming the vein is infinitely long. Adapted from Li et al. [77].

This difference $\Delta\chi$ is more relevant for imaging/spectroscopy purposes than the absolute susceptibility of blood. $\Delta\chi$ can be evaluated as follows [77, 88, 137]:

$$\Delta\chi = \chi_{do}\, Hct\, (1 - SO_2) \tag{2.27}$$

The haematocrit (Hct) is the fraction of the blood volume taken by erythrocytes. The constant χ_{do} corresponds to the susceptibility of fully deoxygenated blood assuming a haematocrit of one (like $\Delta\chi$, it is defined based on the susceptibility of the surrounding tissue).

Magnetic field inside the vein It is possible to evaluate the magnetic field inside a vein using the susceptibility of the partly deoxygenated blood within the vein. In this thesis, volume susceptibility is used exclusively. The magnetic field inside a vein will be stronger than the magnetic field in the surrounding tissue. This difference is called ΔB. When the angle between the vein and B_0 is θ, then ΔB is [77, 88]:

$$\Delta B = \frac{\Delta\chi}{2}\left(\cos^2(\theta) - \frac{1}{3}\right) B_0 \tag{2.28}$$

This equation is based on a few assumptions that lead to limitations of the developed model. It assumes that the vein is an infinitely long, straight cylinder. Secondly, the equation

assumes that the susceptibility within the cylinder is distributed perfectly homogeneously. However, a study has shown that the equation is sufficiently valid [77].

2.7.8 Flow and BOLD-related phase-shift effects in MRS

As mentioned above, this subsection will elaborate on why the BOLD-related phase-shift effect in flowing blood is relevant in PRESS and STEAM measurements of peripheral tissue. Understanding this mechanism is essential as it is suspected to be one of the principal sources for signal alterations in ^{1}H spectroscopy due to flow. For this explanation, two scenarios are considered. In both scenarios, an ^{1}H nucleus flows through veins during an MRS sequence. However, in the second scenario, a net phase shift occurs.

Scenario 1 Consider the MR spectrum of tissue containing a straight (linear) vein. An ^{1}H nucleus in a water molecule inside the vein will experience a stronger magnetic field than an ^{1}H nucleus in the surrounding tissue due to the BOLD effect [96, 97, 137]. The angle of the vein relative to B_0 determines the strength of the magnetic field inside the vein (Subsection 2.7.7). The stronger magnetic field inside the vein leads to higher Larmor frequencies and, thus, a phase shift of nuclei inside the vein relative to the nuclei outside the vein over time. This consideration also applies to terminal capillaries and venules with a high percentage of deoxygenated blood.

The phase shift relative to the surrounding tissue will lead to a signal loss in gradient echo sequences. However, the phase shift of the nucleus inside the vein can be compensated by spin and stimulated echo sequences in Scenario 1 because the magnetic field inside the vein does not change (the angle of the vein relative to B_0 is constant, Figure 2.19). PRESS and STEAM are spin and stimulated echo sequences, respectively [40, 99, 104]. Therefore, BOLD-related phase-shift effects in straight veins do not affect spectra acquired with PRESS and STEAM sequences.

Scenario 2 Consider the MR spectrum of human tissue containing a curved vein changing the angle relative to B_0 along its path through the tissue. The vein is aligned with B_0 in a voxel's lower half but bends 90° in the upper half (Figure 2.20). Since the magnetic field inside this vein is determined by the angle between B_0 and the vein (Equation 2.28), the magnetic field inside the vein is not homogenous. The part of the vein parallel to B_0 has a different magnetic field than the part of the vein after the 90°-bend.

In Scenario 2, an ^{1}H nucleus in a water molecule inside the vein is initially in the voxel's lower half and the section of the vein parallel to B_0. An MRS sequence is applied, and at the same time, the nucleus flows through the 90°-bend and into the voxel's upper half before the signal is recorded. During the sequence, the nucleus experienced a

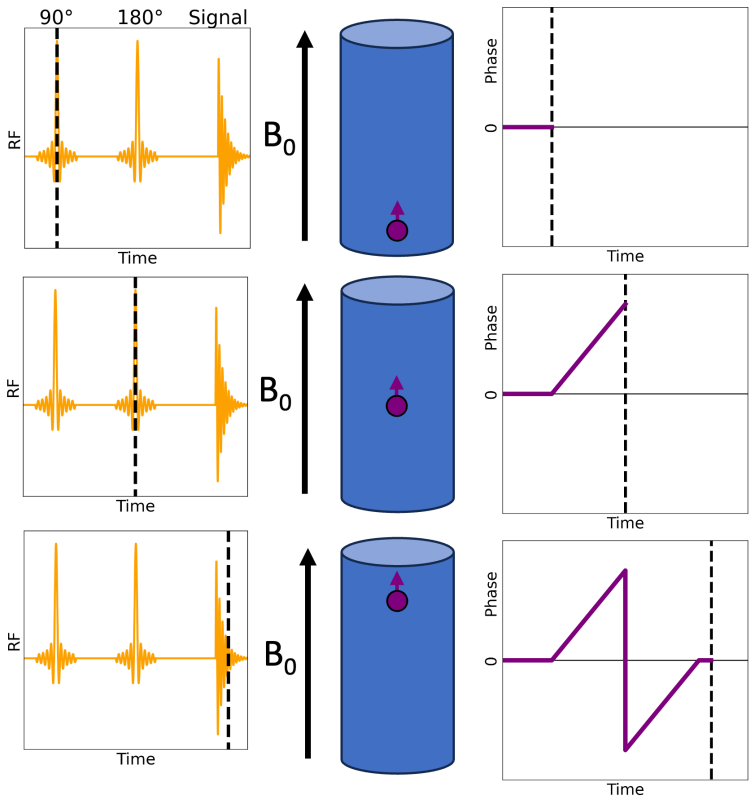

Figure 2.19: Flow and BOLD-related phase-shift effects in MRS, illustration of Scenario 1. The first column shows a spin echo sequence plot with a refocusing 180°-pulse. The progression of the sequence is illustrated from top to bottom. The second column shows the position of the ^{1}H nucleus (purple dot) within the vein. The nucleus moves from the bottom to the top of the vein during the sequence. The third column shows the phase shift of the nucleus compared to a nucleus outside the vein during the sequence. Initially, the nucleus gains phase relative to a nucleus outside the vein due to the stronger magnetic field inside the vein. Then, the refocusing 180°-pulse inverts the phase shift. At the end of the sequence, the phase shift is completely mitigated because the nucleus inside the vein still experiences a stronger magnetic field. In short, for a straight vein, no phase shift is observed in spin or stimulated echo sequences.

changing magnetic field due to its movement through the bend because the magnetic field inside the vein depends on the angle of the vein relative to B_0. In Scenario 2, the Larmor frequency of the nucleus and its phase shift relative to a nucleus outside the vein is not constant during the sequence.

Comparison of both scenarios For a linear vein (Scenario 1), a spin or stimulated echo sequence can compensate for the phase shift experienced by nuclei inside a vein compared to the nuclei outside the vein as the Larmor frequency remains constant over time. For a curved vein (Scenario 2), spin and stimulated echo sequences fail to refocus the nuclei because the Larmor frequencies of the flowing nuclei change during the sequences. Conse-

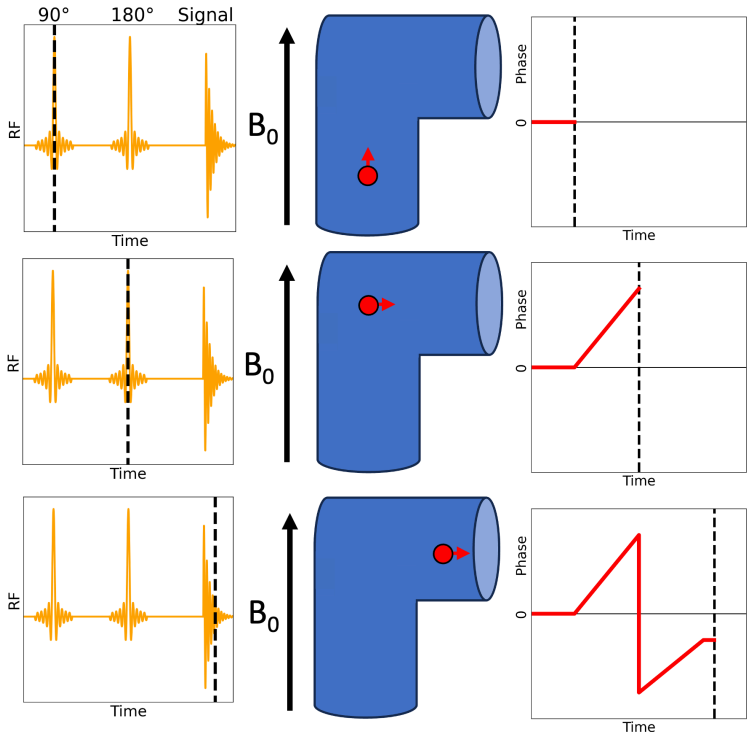

Figure 2.20: Flow and BOLD-related phase-shift effects in MRS, illustration of Scenario 2. The first column shows a spin echo sequence plot with a refocusing 180°-pulse. The progression of the sequence is illustrated from top to bottom. The second column shows the position of the ^{1}H nucleus (red dot) within a curved vein. The vein is aligned with B_0 in the lower part of the diagram/voxel. In the upper part of the diagram, the vein takes a 90°-bend. The third column shows the phase shift of the nucleus compared to a nucleus outside the vein during the sequence. Initially, the nucleus gains phase while it flows through the part of the vein aligned with B_0. Then, the refocusing 180°-pulse inverts the phase shift. During the second half of the sequence, the nucleus changes direction and flows in the part of the vein that is not aligned with B_0. The phase shift is not mitigated (third column) because the nucleus experiences a weaker magnetic field in the upper part of the vein compared to the lower part. In short, a net phase shift is observed in spin or stimulated echo sequences for flowing nuclei in a curved vein.

quently, a phase shift of the nuclei inside the vein relative to those outside occurs, resulting in a corresponding loss of signal even in spin and stimulated echo sequences. Therefore, PRESS and STEAM sequences should exhibit BOLD-related phase-shift effects.

Building on this argument, Section 3.5 presents mathematical models to quantify the phase shift in PRESS and STEAM measurements due to nuclei flowing through a curved vein.

Chapter 3

Materials and Methods

3.1 Simulation of gradient-induced phase-shift effects in ^{1}H spectroscopy

As described in Section 2.6, measuring flow with MRI sequences using phase-shift methods is possible. However, gradient-induced phase-shift effects are not limited to MRI. The gradients used in PRESS and STEAM can also produce phase-shift effects [92]. In PRESS and STEAM, the prominent contributors to gradient-induced phase-shift effects arising from flow are the bipolar crusher gradients. They are stronger than the slice select gradients that contribute only weakly to the phase-shift effects.

Gradient-induced phase-shift effects due to flow are thought to change signal characteristics in ^{1}H spectroscopy. Therefore, investigating gradient-induced phase-shift effects in PRESS and STEAM sequences constitutes a significant part of this thesis. Simulations and experiments were conducted to evaluate these effects.

This section lays the groundwork for understanding the simulations and experiments. For this purpose, the following subsections introduce exemplary PRESS and STEAM sequences and their parameters. Subsequently, it is shown how formulae can represent those sequences. The obtained formulae are used to calculate the gradient-induced phase-shift effects exhibited by exemplary sequences to facilitate an understanding of the simulations. These calculations serve illustrative purposes and show the principles behind the general approach. Further, an understanding of the interplay between sequence design and the resulting gradient-induced phase-shift effects in ^{1}H spectroscopy is conveyed. However, the general results obtained by the simulations are systemically presented in Chapter 4 and discussed in Chapter 5.

3.1.1 Exemplary PRESS sequence

This subsection details the calculation of gradient-induced phase-shift effects using an exemplary PRESS sequence. Similar to the phase-contrast sequence introduced in Section 2.6, the gradient-induced phase-shift effects in PRESS depend on the magnitude and timing of the gradients. In order to analyse the gradients, it is necessary to express them as mathematical formulae. Since the gradients along the x-, y-, and z-axes differ, a set of formulae describing the gradients for each axis has to be determined. In Figure 3.1, the gradients of the exemplary PRESS sequence are illustrated. The exemplary sequence is a PRESS sequence for the 3 T Magnetom Prisma Fit whole-body MRI scanner (used in the experiments of this study).

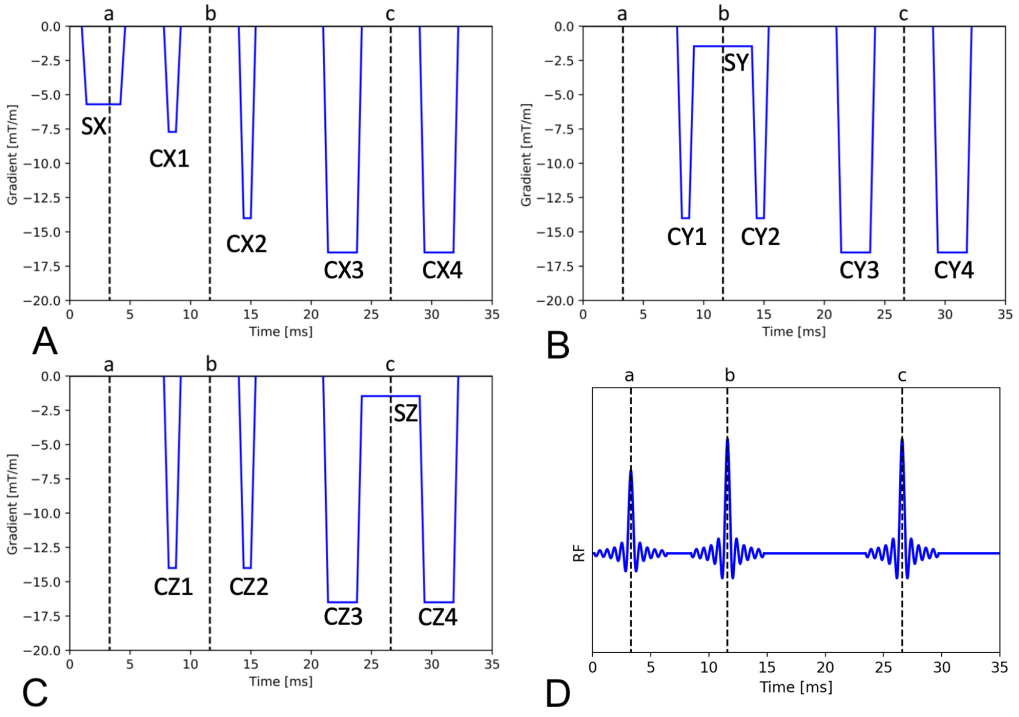

Figure 3.1: Illustration of the exemplary PRESS sequence. Sequence parameters: δL (edge length of the voxel) = 20 mm, TE = 30 ms. [A] Gradients of the sequence along the x-axis. [B] Gradients of the sequence along the y-axis. [C] Gradients of the sequence along the z-axis. [D] Plot of the three RF pulses. (a) Timing of the initial 90°-pulse. (b) Timing of the first 180°-pulse. (c) Timing of the second 180°-pulse. (CX1/CY1/CZ1) First half of the crusher gradient during TE_1 along the corresponding axis. (CX2/CY2/CZ2) Second half of the crusher gradient during TE_1 along the corresponding axis. (CX3/CY3/CZ3) First half of the crusher gradient during TE_2 along the corresponding axis. (CX4/CY4/CZ4) Second half of the crusher gradient during TE_2 along the corresponding axis. (SX/SY/SZ) Slice selection gradient along the corresponding axis.

Firstly, several parameters necessary to determine the formulae for the slice selection gradients of the PRESS sequence are presented. Although the contribution of the slice

selection gradients to the phase-shift effects is small compared to the crusher gradients, the simulations take them into account. The strength of the slice selection gradient (SSG_a) along an arbitrary axis "a" is determined by the following formula:

$$SSG_a = \frac{2 \cdot \pi \cdot n \cdot R}{\delta L \cdot T \cdot \gamma} \tag{3.1}$$

Table 3.1 lists the sequence-specific technical parameters n, R, δL, and T. Importantly, δL is the edge length of the voxel along a given axis of the spectroscopy sequence. Therefore, δL can differ in the x-, y-, and z-direction. Notably, Equation 3.1 also applies to STEAM sequences. For PRESS sequences, SSG_x (the strength of the slice selection gradient along the x-axis) is calculated differently from the strength of the slice selection gradients along the y- and z-axis ($SSG_{y,z}$).

Table 3.1: Parameters of the exemplary PRESS sequence.

Parameter	Acronym	Value, (Range)
Voxel length/height/width	δL	20mm, (3–40mm)
Duration of the 90°-pulse	T_{90}	1.8 ms
R factor of the 90°-pulse	R_{90}	1.75
n of the 90°-pulse	n_{90}	5
Duration of the 180°-pulse	T_{180}	4.8 ms
R factor of the 180°-pulse	R_{180}	1.5
n of the 180°-pulse	n_{180}	4
Ramp time of gradients	t_{ramp}	0.4 ms

Table 3.1 shows that the parameters differ depending on whether a 90°-pulse or a 180°-pulse is considered. Since the RF pulse applied during the slice selection gradient along

the x-axis is a 90°-pulse, the corresponding parameters are used to calculate SSG_x.

$$SSG_x = \frac{2 \cdot \pi \cdot n \cdot R}{\delta L \cdot T \cdot \gamma} \tag{3.2}$$

$$SSG_x = \frac{2 \cdot \pi \cdot rad \cdot 5 \cdot 1.75}{2.0 \cdot 10^{-2}\, m \cdot 1.8 \cdot 10^{-3}\, s \cdot 2.675 \cdot 10^{8}\, \frac{rad}{T \cdot s}} \tag{3.3}$$

$$SSG_x = 5.71 \cdot 10^{-3}\, \frac{T}{m} \tag{3.4}$$

For the calculation of $SSG_{y,z}$, the parameters corresponding to the 180°-pulse are used.

$$SSG_{y,z} = \frac{2 \cdot \pi \cdot n \cdot R}{\delta L \cdot T \cdot \gamma} \tag{3.5}$$

$$SSG_{y,z} = \frac{2 \cdot \pi \cdot rad \cdot 4 \cdot 1.5}{2.0 \cdot 10^{-2}\, m \cdot 4.8 \cdot 10^{-3}\, s \cdot 2.675 \cdot 10^{8}\, \frac{rad}{T \cdot s}} \tag{3.6}$$

$$SSG_{y,z} = 1.47 \cdot 10^{-3}\, \frac{T}{m} \tag{3.7}$$

Gradients of the exemplary PRESS sequence along the x-direction

Using the values for SSG and information provided by Siemens Healthcare, a set of functions describing the gradients along the x-axis was determined. These formulae are listed below. It can be seen in Figure 3.1 that five gradients are applied along the x-axis in total. Two pairs of crusher gradients follow the first slice selection gradient. The sequence considered here has an echo time of 30 ms, and δL is 20 mm along each axis. The time the gradients need to build up is called ramp time (t_{ramp}) and is 0.4 ms.

An alternative term for crusher gradient is spoiler gradient. The term crusher gradient is used here because it simplifies the terminology of the formulae below. The names given to the gradients correspond to the names used in Figure 3.1.

The slice selection gradient in the x-direction (SX) is described by the three formulae $SX_1(t)$, $SX_2(t)$, and $SX_3(t)$. $SX_1(t)$, and $SX_3(t)$ are the ramps of the gradient. $SX_2(t)$ corresponds to the plateau of the gradient. The same nomenclature is used for all following gradients.

$$SX_1(t) = -14.27\, \frac{mT}{m \cdot ms}\, (t - 1\, ms) \qquad | \, 1.0\, ms < t < 1.4\, ms \tag{3.8}$$

$$SX_2(t) = -5.71\, \frac{mT}{m} \qquad | \, 1.4\, ms < t < 4.2\, ms \tag{3.9}$$

$$SX_3(t) = 14.27\, \frac{mT}{m \cdot ms}\, (t - 4.6\, ms) \qquad | \, 4.2\, ms < t < 4.6\, ms \tag{3.10}$$

The crusher gradient CX1 is described by the three formulae $CX1_1(t)$, $CX1_2(t)$, and $CX1_3(t)$.

$$CX1_1(t) = -19.30\,\frac{mT}{m \cdot ms}\,(t - 7.8\,ms) \qquad | \, 7.8\,ms < t < 8.2\,ms \qquad (3.11)$$

$$CX1_2(t) = -7.72\,\frac{mT}{m} \qquad | \, 8.2\,ms < t < 8.8\,ms \qquad (3.12)$$

$$CX1_3(t) = 19.30\,\frac{mT}{m \cdot ms}\,(t - 9.2\,ms) \qquad | \, 8.8\,ms < t < 9.2\,ms \qquad (3.13)$$

The crusher gradient CX2 is described by the three formulae $CX2_1(t)$, $CX2_2(t)$, and $CX2_3(t)$.

$$CX2_1(t) = -35\,\frac{mT}{m \cdot ms}\,(t - 14\,ms) \qquad | \, 14.0\,ms < t < 14.4\,ms \qquad (3.14)$$

$$CX2_2(t) = -14\,\frac{mT}{m} \qquad | \, 14.4\,ms < t < 15.0\,ms \qquad (3.15)$$

$$CX2_3(t) = 35\,\frac{mT}{m \cdot ms}\,(t - 16.0\,ms) \qquad | \, 15.0\,ms < t < 15.4\,ms \qquad (3.16)$$

The crusher gradient CX3 is described by the three formulae $CX3_1(t)$, $CX3_2(t)$, and $CX3_3(t)$.

$$CX3_1(t) = -41.25\,\frac{mT}{m \cdot ms}\,(t - 21.0\,ms) \qquad | \, 21.0\,ms < t < 21.4\,ms \qquad (3.17)$$

$$CX3_2(t) = -16.5\,\frac{mT}{m} \qquad | \, 21.4\,ms < t < 23.8\,ms \qquad (3.18)$$

$$CX3_3(t) = 41.25\,\frac{mT}{m \cdot ms}\,(t - 24.2\,ms) \qquad | \, 23.8\,ms < t < 24.2\,ms \qquad (3.19)$$

The crusher gradient CX4 is described by the three formulae $CX4_1(t)$, $CX4_2(t)$, and $CX4_3(t)$.

$$CX4_1(t) = -41.25\,\frac{mT}{m \cdot ms}\,(t - 29.0\,ms) \qquad | \, 29.0\,ms < t < 29.4\,ms \qquad (3.20)$$

$$CX4_2(t) = -16.5\,\frac{mT}{m} \qquad | \, 29.4\,ms < t < 31.8\,ms \qquad (3.21)$$

$$CX4_3(t) = 41.25\,\frac{mT}{m \cdot ms}\,(t - 32.2\,ms) \qquad | \, 31.8\,ms < t < 32.2\,ms \qquad (3.22)$$

Gradients of the exemplary PRESS sequence along the y-direction

Here, all formulae are listed that describe the gradients of the PRESS sequence along the y-direction.

The slice selection gradient in the y-direction is described by the formula SY(t).

$$SY(t) = -1.47\frac{mT}{m} \qquad | \, 9.2\,ms < t < 14.0\,ms \qquad (3.23)$$

The crusher gradient CY1 is described by the three formulae $CY1_1(t)$, $CY1_2(t)$, and $CY1_3(t)$.

$$CY1_1(t) = -35\,\frac{mT}{m \cdot ms}\,(t - 7.8\,ms) \qquad | \, 7.8\,ms < t < 8.2\,ms \qquad (3.24)$$

$$CY1_2(t) = -14\,\frac{mT}{m} \qquad | 8.2\,ms < t < 8.8\,ms \qquad (3.25)$$

$$CY1_3(t) = 31.33\,\frac{mT}{m \cdot ms}\,(t - \ 9.25ms) \qquad | \, 8.8\,ms < t < 9.2\,ms \qquad (3.26)$$

The crusher gradient CY2 is described by the three formulae $CY2_1(t)$, $CY2_2(t)$, and $CY2_3(t)$.

$$CY2_1(t) = -31.33\,\frac{mT}{m \cdot ms}\,(t - 13.95\,ms) \qquad | \, 14.0\,ms < t < 14.4\,ms \qquad (3.27)$$

$$CY2_2(t) = -14\,\frac{mT}{m} \qquad | \, 14.4\,ms < t < 15.0\,ms \qquad (3.28)$$

$$CY2_3(t) = 35\,\frac{mT}{m \cdot ms}\,(t - 15.4\,ms) \qquad | \, 15.0\,ms < t < 15.4\,ms \qquad (3.29)$$

The crusher gradient CY3 is described by the three formulae $CY3_1(t)$, $CY3_2(t)$, and $CY3_3(t)$.

$$CY3_1(t) = -41.25\,\frac{mT}{m \cdot ms}\,(t - 21.0\,ms) \qquad | \, 21.0\,ms < t < 21.4\,ms \qquad (3.30)$$

$$CY3_2(t) = -16.5\,\frac{mT}{m} \qquad | \, 21.4\,ms < t < 23.8\,ms \qquad (3.31)$$

$$CY3_3(t) = 41.25\,\frac{mT}{m \cdot ms}\,(t - 24.2\,ms) \qquad | \, 23.8\,ms < t < 24.2\,ms \qquad (3.32)$$

The crusher gradient CY4 is described by the three formulae $CY4_1(t)$, $CY4_2(t)$, and $CY4_3(t)$.

$$CY4_1(t) = -41.25\,\frac{mT}{m \cdot ms}\,(t - 29.0\,ms) \qquad | \, 29.0\,ms < t < 29.4\,ms \qquad (3.33)$$

$$CY4_2(t) = -16.5\,\frac{mT}{m} \qquad | \, 29.4\,ms < t < 31.8\,ms \qquad (3.34)$$

$$CY4_3(t) = 41.25\,\frac{mT}{m \cdot ms}\,(t - 32.2\,ms) \qquad | \, 31.8\,ms < t < 32.2\,ms \qquad (3.35)$$

Gradients of the exemplary PRESS sequence along the z-direction

Here, all formulae are listed that describe the gradients of the PRESS sequence along the z-direction.

The slice selection gradient in the z-direction is described by the formula SZ(t).

$$SZ(t) = -1.47\frac{mT}{m} \qquad | \, 24.2\,ms < t < 29\,ms \qquad (3.36)$$

The crusher gradient CZ1 is described by the three formulae $CZ1_1(t)$, $CZ1_2(t)$, and $CZ1_3(t)$.

$$CZ1_1(t) = -35\,\frac{mT}{m \cdot ms}\,(t - 7.8\,ms) \qquad | \, 7.8\,ms < t < 8.2\,ms \tag{3.37}$$

$$CZ1_2(t) = -14\,\frac{mT}{m} \qquad | \, 8.2\,ms < t < 8.8\,ms \tag{3.38}$$

$$CZ1_3(t) = 35\,\frac{mT}{m \cdot ms}\,(t - 9.2\,ms) \qquad | \, 8.8\,ms < t < 9.2\,ms \tag{3.39}$$

The crusher gradient CZ2 is described by the three formulae $CZ2_1(t)$, $CZ2_2(t)$, and $CZ2_3(t)$.

$$CZ2_1(t) = -35\,\frac{mT}{m \cdot ms}\,(t - 14.0\,ms) \qquad | \, 14.0\,ms < t < 14.4\,ms \tag{3.40}$$

$$CZ2_2(t) = -14\,\frac{mT}{m} \qquad | \, 14.4\,ms < t < 15.0\,ms \tag{3.41}$$

$$CZ2_3(t) = 35\,\frac{mT}{m \cdot ms}\,(t - 15.4\,ms) \qquad | \, 15.0\,ms < t < 15.4\,ms \tag{3.42}$$

The crusher gradient CZ3 is described by the three formulae $CZ3_1(t)$, $CZ3_2(t)$, and $CZ3_3(t)$.

$$CZ3_1(t) = -41.25\,\frac{mT}{m \cdot ms}\,(t - 21.0\,ms) \qquad | \, 21.0\,ms < t < 21.4\,ms \tag{3.43}$$

$$CZ3_2(t) = -16.5\,\frac{mT}{m} \qquad | \, 21.4\,ms < t < 23.8\,ms \tag{3.44}$$

$$CZ3_3(t) = 37.58\,\frac{mT}{m \cdot ms}\,(t - 24.24\,ms) \qquad | \, 23.8\,ms < t < 24.2\,ms \tag{3.45}$$

The crusher gradient CZ4 is described by the three formulae $CZ4_1(t)$, $CZ4_2(t)$, and $CZ4_3(t)$.

$$CZ4_1(t) = -37.58\,\frac{mT}{m \cdot ms}\,(t - 28.96\,ms) \qquad | \, 29.0\,ms < t < 29.4\,ms \tag{3.46}$$

$$CZ4_2(t) = -16.5\,\frac{mT}{m} \qquad | \, 29.4 < t < 31.8 \tag{3.47}$$

$$CZ4_3(t) = 41.25\,\frac{mT}{m \cdot ms}\,(t - 32.2\,ms) \qquad | \, 31.8\,ms < t < 32.2\,ms \tag{3.48}$$

3.1.2 Calculation of gradient-induced phase-shift effects in PRESS

This subsection shows how gradient-induced phase-shift effects are calculated in PRESS sequences. The PRESS sequence discussed above will serve as an example. Gradient-induced phase-shift effects due to flow in MR spectroscopy depend on the flow direction since the gradients differ in the x-, y-, and z-direction. Therefore, the formulae deducted here depend on the flow velocity and direction. The following calculations show the mathematical approach. Chapter 4 presents more general results.

Considering the algebraic signs associated with each gradient is crucial because, after each 180°-pulse (or two consecutive 90°-pulses), the effect of the previous gradients is

inverted. When such an inversion is considered in the calculations, a negative algebraic sign is applied to the corresponding formulae.

Gradient-induced phase-shift effects in PRESS along the x-direction

The following general formula for calculating the gradient-induced phase shift is used as the basis for the calculations (Subsection 2.6.1).

$$\Delta\varphi = \gamma \int_{t}^{t+\delta} G(t) \cdot r(t) dt \tag{3.49}$$

Here, r(t) is substituted with v(t) · t. In this model, the velocity of the moving/flowing nucleus is assumed to be constant during the sequence (v(t) = const.). It follows that:

$$\Delta\varphi = \gamma \cdot v \int_{t}^{t+\delta} G(t) \cdot t \cdot dt \tag{3.50}$$

The gyromagnetic ratio γ for ^{1}H nuclei is:

$$\gamma = 2.675 \cdot 10^8 \cdot \frac{rad}{s\,T} \tag{3.51}$$

The total dephasing of an ^{1}H nucleus moving along the x-axis depending on its velocity v is called $\Delta\varphi_{total,x}(v)$. $\Delta\varphi(CX1)$ is the dephasing of the nucleus caused by the first crusher gradient CX1. This nomenclature is applied to all other gradients as well. $\Delta\varphi_{total,x}(v)$ is the sum of the effect of all individual gradients. Figure 3.2 shows the gradients responsible for the phase-shift effects.

$$\Delta\varphi_{total,x}(v) = \Delta\varphi(SX) + \Delta\varphi(CX1) + \Delta\varphi(CX2) + \Delta\varphi(CX3) + \Delta\varphi(CX4) \tag{3.52}$$

Calculation of $\Delta\varphi$(SX) The 90°-pulse excites the nucleus 3.3 ms after the start of the sequence. Therefore, the effect of the gradient starts at 3.3 ms. $\Delta\varphi(SX_2)$ represents the dephasing due to the plateau of the gradient described by the formula for SX_2(t) and $\Delta\varphi(SX_3)$ represents the dephasing due to the latter ramp of the gradient described by the formula SX_3(t). For conciseness, γ is written with its numeric value only in the first example. The contribution of the dephasing due to the slice selection gradient is calculated

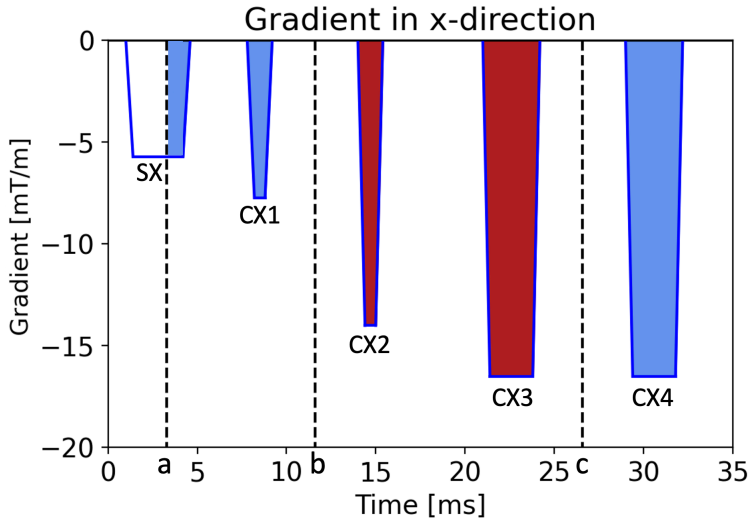

Figure 3.2: PRESS gradients in the x-direction and their impact on phase-shift effects. Sequence parameters: δL = 20 mm, TE = 30 ms. (a) Timing of the initial 90°-pulse. (b) Timing of the first 180°-pulse. (c) Timing of the second 180°-pulse. (CX1) First half of the crusher gradient during TE_1. (CX2) Second half of the crusher gradient during TE_1. (CX3) First half of the crusher gradient during TE_2. (CX4) Second half of the crusher gradient during TE_2. (SX) Slice selection gradient. Notably, the pale blue colour of CX1, CX4, and the latter part of SX (after the initial 90°-pulse) signifies their negative algebraic contribution to the gradient-induced phase shift. Conversely, the reddish colour of CX2 and CX3 represents their positive algebraic contribution to the gradient-induced phase shift. An important observation is that the initial part of SX does not contribute to the phase shift since no transverse magnetisation has been generated up to that point.

using Equation 3.50:

$$\Delta\varphi(SX_2) = 2.675 \cdot 10^8 \cdot \frac{rad}{s\,T} \cdot v \cdot \int_{0.0033s}^{0.0042s} -0.00571 \frac{T}{m} \cdot t \cdot dt \tag{3.53}$$

$$\Delta\varphi(SX_3) = \gamma \cdot v \cdot \int_{0.0042s}^{0.0046s} 14.275 \cdot \frac{T}{m \cdot s} \cdot (t - 0.0046s) \cdot t \cdot dt \tag{3.54}$$

Here, $\Delta\varphi(SX)$ is the sum of both components. Calculating the above integrals yields the following formula for the contribution of the slice selection gradient.

$$\Delta\varphi(SX) = \Delta\varphi(SX_2) + \Delta\varphi(SX_3) \tag{3.55}$$

$$\Delta\varphi(SX) = -6.48 \frac{rad \cdot s}{m} \cdot v \tag{3.56}$$

Note that the dephasing caused by the gradient is inverted twice by the two following 180°-pulses. However, the twofold inversion has a net zero effect on the dephasing.

Calculation of $\Delta\varphi$(CX1) The first crusher gradient along the x-axis is described by the three formulae $CX1_1$(t), $CX1_2$(t), and $CX1_3$(t). Their contributions to the dephasing of the nucleus are called $\Delta\varphi(CX1_1)$, $\Delta\varphi(CX1_2)$, and $\Delta\varphi(CX1_3)$ respectively. Here, Equation 3.50 is used again to determine the contributions of the components.

$$\Delta\varphi(CX1_1) = v \cdot \gamma \cdot \int_{0.0078s}^{0.0082s} -19.30\frac{T}{m \cdot s}(t - 0.0078s) \cdot t \cdot dt \tag{3.57}$$

$$\Delta\varphi(CX1_2) = v \cdot \gamma \cdot \int_{0.0082s}^{0.0088s} -0.00772\frac{T}{m} \cdot t \cdot dt \tag{3.58}$$

$$\Delta\varphi(CX1_3) = v \cdot \gamma \cdot \int_{0.0088s}^{0.0092s} 19.30\frac{T}{m \cdot s} \cdot (t - 0.0092s) \cdot t \cdot dt \tag{3.59}$$

The value of $\Delta\varphi(CX1)$ is the sum of the above components. The effect of this crusher gradient is inverted twice by the following 180°-pulses. However, the twofold inversion has no net effect.

$$\Delta\varphi(CX1) = \Delta\varphi(CX1_1) + \Delta\varphi(CX1_2) + \Delta\varphi(CX1_3) \tag{3.60}$$

$$\Delta\varphi(CX1) = -17.56\ \frac{rad \cdot s}{m} \cdot v \tag{3.61}$$

Calculation of $\Delta\varphi$(CX2) The second crusher gradient along the x-axis is described by the three formulae $CX2_1$(t), $CX2_2$(t), and $CX2_3$(t). Their contributions to the dephasing of the nuclei are called $\Delta\varphi(CX2_1)$, $\Delta\varphi(CX2_2)$, and $\Delta\varphi(CX2_3)$ respectively. Here, Equation 3.50 is used again to determine the contributions of the components.

$$\Delta\varphi(CX2_1) = v \cdot \gamma \cdot \int_{0.0140s}^{0.0144s} -35.0\frac{T}{m \cdot s} \cdot (t - 0.0140s) \cdot t \cdot dt \tag{3.62}$$

$$\Delta\varphi(CX2_2) = v \cdot \gamma \cdot \int_{0.0144s}^{0.0150s} -0.014\frac{T}{m} \cdot t \cdot dt \tag{3.63}$$

$$\Delta\varphi(CX2_3) = v \cdot \gamma \cdot \int_{0.0150s}^{0.0154s} 35.0\frac{T}{m \cdot s} \cdot (t - 0.0154s) \cdot t \cdot dt \tag{3.64}$$

The value of $\Delta\varphi(CX2)$ is the inverse of the sum of the above components because the second crusher gradient is followed by only one 180°-pulse that acts to invert the contribution of the gradient.

$$\Delta\varphi(CX2) = -(\Delta\varphi(CX2_1) + \Delta\varphi(CX2_2) + \Delta\varphi(CX2_3)) \tag{3.65}$$

$$\Delta\varphi(CX2) = 55.06\ \frac{rad \cdot s}{m} \cdot v \tag{3.66}$$

Calculation of $\Delta\varphi$(CX3) The third crusher gradient along the x-axis is described by the three formulae $CX3_1$(t), $CX3_2$(t), and $CX3_3$(t). Their contributions to the dephasing of the

nuclei are called $\Delta\varphi(CX3_1)$, $\Delta\varphi(CX3_2)$, and $\Delta\varphi(CX3_3)$ respectively. Here, Equation 3.50 is used again to determine the contributions of the components.

$$\Delta\varphi(CX3_1) = v \cdot \gamma \cdot \int_{0.0210s}^{0.0214s} -41.25\frac{T}{m \cdot s} \cdot (t - 0.0210s) \cdot t \cdot dt \tag{3.67}$$

$$\Delta\varphi(CX3_2) = v \cdot \gamma \cdot \int_{0.0214s}^{0.0238s} -0.0165\frac{T}{m} \cdot t \cdot dt \tag{3.68}$$

$$\Delta\varphi(CX3_3) = v \cdot \gamma \cdot \int_{0.0238s}^{0.0242s} 41.25\frac{T}{m \cdot s} \cdot (t - 0.0242s) \cdot t \cdot dt \tag{3.69}$$

The value of $\Delta\varphi(CX3)$ is the inverse of the sum of the above components because the third crusher gradient is followed by only one 180°-pulse that acts to invert the contribution of the gradient.

$$\Delta\varphi(CX3) = -(\Delta\varphi(CX3_1) + \Delta\varphi(CX3_2) + \Delta\varphi(CX3_3)) \tag{3.70}$$

$$\Delta\varphi(CX3) = 279.33\,\frac{rad \cdot s}{m} \cdot v \tag{3.71}$$

Calculation of $\Delta\varphi$(CX4) The fourth crusher gradient along the x-axis is described by the three formulae $CX4_1(t)$, $CX4_2(t)$, and $CX4_3(t)$. Their contributions to the dephasing of the nuclei are called $\Delta\varphi(CX4_1)$, $\Delta\varphi(CX4_2)$, and $\Delta\varphi(CX4_3)$ respectively. Here, Equation 3.50 is used again to determine the contributions of the components.

$$\Delta\varphi(CX4_1) = v \cdot \gamma \cdot \int_{0.0290s}^{0.0294s} -41.25\frac{T}{m \cdot s} \cdot (t - 0.029s) \cdot t \cdot dt \tag{3.72}$$

$$\Delta\varphi(CX4_2) = v \cdot \gamma \cdot \int_{0.0294s}^{0.0318s} -0.0165\frac{T}{m} \cdot t \cdot dt \tag{3.73}$$

$$\Delta\varphi(CX4_3) = v \cdot \gamma \cdot \int_{0.0318s}^{0.0322s} 41.25\frac{T}{m \cdot s} \cdot (t - 0.0322s) \cdot t \cdot dt \tag{3.74}$$

The value of $\Delta\varphi(CX4)$ is the sum of the above components. No inversion of the phase takes place since no 180°-pulse follows.

$$\Delta\varphi(CX4) = \Delta\varphi(CX4_1) + \Delta\varphi(CX4_2) + \Delta\varphi(CX4_3) \tag{3.75}$$

$$\Delta\varphi(CX4) = -378.20\,\frac{rad \cdot s}{m} \cdot v \tag{3.76}$$

Calculation of $\Delta\varphi_{total,x}$ The value of $\Delta\varphi_{total,x}$ is given by the sum of the contribution of the gradients mentioned above.

$$\Delta\varphi_{total,x}(v) = \Delta\varphi(CX1) + \Delta\varphi(CX2) + \Delta\varphi(CX3) + \Delta\varphi(CX4) + \Delta\varphi(SX) \tag{3.77}$$

$$\Delta\varphi_{total,x}(v) = -67.85\,\frac{rad\cdot s}{m}\cdot v \approx -3887°\frac{s}{m}\cdot v \tag{3.78}$$

This formula can be utilised to determine the dephasing of an ^{1}H nucleus flowing or moving with the velocity v along the x-axis for the exemplary PRESS sequence.

Gradient-induced phase-shift effects in PRESS along the y-direction

Calculating the dephasing of a nucleus moving along the y-axis is similar to the above calculation. Figure 3.3 shows the gradients responsible for the phase-shift effects. The total dephasing along the y-axis is called $\Delta\varphi_{total,y}(v)$. Again, $\Delta\varphi(CY1)$ denotes the dephasing caused by the first crusher gradient along the y-axis CY1 and so on.

$$\Delta\varphi_{total,y}(v) = \Delta\varphi(CY1) + \Delta\varphi(SY) + \Delta\varphi(CY2) + \Delta\varphi(CY3) + \Delta\varphi(CY4) \tag{3.79}$$

Calculation of $\Delta\varphi$(CY1) The first crusher gradient along the y-axis is described by the three formulae $CY1_1$(t), $CY1_2$(t), and $CY1_3$(t). Their contributions to the dephasing of the nuclei are called $\Delta\varphi(CY1_1)$, $\Delta\varphi(CY1_2)$, and $\Delta\varphi(CY1_3)$ respectively. Here, Equation 3.50 is used again to determine the contributions of the components.

$$\Delta\varphi(CY1_1) = v\cdot\gamma\cdot\int_{0.0078s}^{0.0082s} -35.0\frac{T}{m\cdot s}\cdot(t-0.0078s)\cdot t\cdot dt \tag{3.80}$$

$$\Delta\varphi(CY1_2) = v\cdot\gamma\cdot\int_{0.0082s}^{0.0088s} -0.014\frac{T}{m}\cdot t\cdot dt \tag{3.81}$$

$$\Delta\varphi(CY1_3) = v\cdot\gamma\cdot\int_{0.0088s}^{0.0092s} 31.33\frac{T}{m\cdot s}\cdot(t-0.00925s)\cdot t\cdot dt \tag{3.82}$$

The dephasing caused by this first crusher gradient is inverted twice by the two following 180°-pulses, resulting in a net zero effect.

$$\Delta\varphi(CY1) = \Delta\varphi_{CY1,1} + \Delta\varphi_{CY1,2} + \Delta\varphi_{CY1,3} \tag{3.83}$$

$$\Delta\varphi(CY1) = -32.55\,\frac{rad\cdot s}{m}\cdot v \tag{3.84}$$

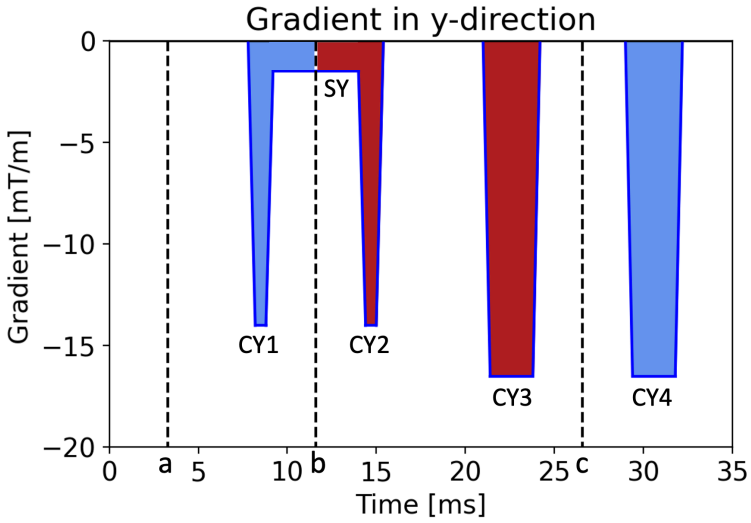

Figure 3.3: PRESS gradients in the y-direction and their impact on phase-shift effects. Sequence parameters: δL = 20 mm, TE = 30 ms. (a) Timing of the initial 90°-pulse. (b) Timing of the first 180°-pulse. (c) Timing of the second 180°-pulse. (CY1) First half of the crusher gradient during TE_1. (CY2) Second half of the crusher gradient during TE_1. (CY3) First half of the crusher gradient during TE_2. (CY4) Second half of the crusher gradient during TE_2. (SY) Slice selection gradient. Notably, the pale blue colour of CY1, CY4, and the first half of SY signifies their negative algebraic contribution to the gradient-induced phase shift. Conversely, the reddish colour of CY2, CY3, and the second half of SY represents their positive algebraic contribution to the gradient-induced phase shift.

Calculation of $\Delta\varphi$(SY) During the slice selection gradient along the y-axis, a 180°-pulse is applied, meaning that the effect of the first half of the gradient is effectively inverted. The dephasing caused by the first half is called $\Delta\varphi(SY_1)$, and the second half is called $\Delta\varphi(SY_2)$ here.

$$\Delta\varphi(SY_1) = v \cdot \gamma \cdot \int_{0.0092s}^{0.0116s} -0.00147\frac{T}{m} \cdot t \cdot dt \tag{3.85}$$

$$\Delta\varphi(SY_2) = v \cdot \gamma \cdot \int_{0.0116s}^{0.014s} -0.00147\frac{T}{m} \cdot t \cdot dt \tag{3.86}$$

$\Delta\varphi(SY_2)$ is followed by a single 180°-pulse. Therefore, a negative algebraic sign is added to account for the inversion of the phase. Since the dephasing $\Delta\varphi(SY_1)$ is followed by two 180°-pulses and thus inverted twice, its contribution is denoted with a positive algebraic sign.

$$\Delta\varphi(SY) = -\Delta\varphi(SY_2) + \Delta\varphi(SY_1)) \tag{3.87}$$

$$\Delta\varphi(SY) = 2.26\,\frac{rad \cdot s}{m} \cdot v \tag{3.88}$$

Calculation of $\Delta\varphi$(CY2) The second crusher gradient along the y-axis is described by the three formulae $CY2_1$(t), $CY2_2$(t), and $CY2_3$(t). Their contributions to the dephasing of the nuclei are called $\Delta\varphi(CY2_1)$, $\Delta\varphi(CY2_2)$, and $\Delta\varphi(CY2_3)$ respectively. Here, Equation 3.50 is used again to determine the contributions of the components.

$$\Delta\varphi(CY2_1) = v \cdot \gamma \cdot \int_{0.0140s}^{0.0144s} -31.325\frac{T}{m \cdot s} \cdot (t - 0.01395s) \cdot t \cdot dt \tag{3.89}$$

$$\Delta\varphi(CY2_2) = v \cdot \gamma \cdot \int_{0.0144s}^{0.0150s} -0.014\frac{T}{m} \cdot t \cdot dt \tag{3.90}$$

$$\Delta\varphi(CY2_3) = v \cdot \gamma \cdot \int_{0.0150s}^{0.0154s} 35.0\frac{T}{m \cdot s} \cdot (t - 0.0154s) \cdot t \cdot dt \tag{3.91}$$

The second crusher gradient is followed by a single 180°-pulse. Therefore, the contribution to the dephasing is inverted using a negative algebraic sign.

$$\Delta\varphi(CY2) = -(\Delta\varphi(CY2_1) + \Delta\varphi(CY2_2) + \Delta\varphi(CY2_3)) \tag{3.92}$$

$$\Delta\varphi(CY2) = 56.17\,\frac{rad \cdot s}{m} \cdot v \tag{3.93}$$

Calculation of $\Delta\varphi$(CY3) The third crusher gradient along the y-axis is described by the three formulae $CY3_1$(t), $CY3_2$(t), and $CY3_3$(t). Their contributions to the dephasing of the nuclei are called $\Delta\varphi(CY3_1)$, $\Delta\varphi(CY3_2)$, and $\Delta\varphi(CY3_3)$ respectively. Here, Equation 3.50 is used again to determine the contributions of the components.

$$\Delta\varphi(CY3_1) = v \cdot \gamma \cdot \int_{0.0210s}^{0.0214s} -41.25\frac{T}{m \cdot s} \cdot (t - 0.0210s) \cdot t \cdot dt \tag{3.94}$$

$$\Delta\varphi(CY3_2) = v \cdot \gamma \cdot \int_{0.0214s}^{0.0238s} -0.0165\frac{T}{m} \cdot t \cdot dt \tag{3.95}$$

$$\Delta\varphi(CY3_3) = v \cdot \gamma \cdot \int_{0.0238s}^{0.0242s} 41.25\frac{T}{m \cdot s} \cdot (t - 0.0242s) \cdot t \cdot dt \tag{3.96}$$

The third crusher gradient is followed by a single 180°-pulse. Therefore, the contribution to the dephasing is inverted using a negative algebraic sign.

$$\Delta\varphi(CY3) = -(\Delta\varphi(CY3_1) + \Delta\varphi(CY3_2) + \Delta\varphi(CY3_3)) \tag{3.97}$$

$$\Delta\varphi(CY3) = 279.33\,\frac{rad \cdot s}{m} \cdot v \tag{3.98}$$

Calculation of $\Delta\varphi$(CY4) The fourth crusher gradient along the y-axis is described by the three formulae $CY4_1$(t), $CY4_2$(t), and $CY4_3$(t). Their contributions to the dephasing of the nuclei are called $\Delta\varphi(CY4_1)$, $\Delta\varphi(CY4_2)$, and $\Delta\varphi(CY4_3)$ respectively. Here, Equa-

tion 3.50 is used again to determine the contributions of the components.

$$\Delta\varphi(CY4_1) = v \cdot \gamma \cdot \int_{0.0290s}^{0.0294s} -41.25\frac{T}{m \cdot s} \cdot (t - 0.029s) \cdot t \cdot dt \tag{3.99}$$

$$\Delta\varphi(CY4_2) = v \cdot \gamma \cdot \int_{0.0294s}^{0.0318s} -0.0165\frac{T}{m} \cdot t \cdot dt \tag{3.100}$$

$$\Delta\varphi(CY4_3) = v \cdot \gamma \cdot \int_{0.0318s}^{0.0322s} 41.25\frac{T}{m \cdot s} \cdot (t - 0.0322s) \cdot t \cdot dt \tag{3.101}$$

$$\tag{3.102}$$

The fourth crusher gradient is not followed by another pulse. Therefore, $\Delta\varphi(CY4)$ is calculated as follows.

$$\Delta\varphi(CY4) = \Delta\varphi(CY4_1) + \Delta\varphi(CY4_2) + \Delta\varphi(CY4_3) \tag{3.103}$$

$$\Delta\varphi(CY4) = -378.2\ \frac{rad \cdot s}{m} \cdot v \tag{3.104}$$

Calculation of $\Delta\varphi_{total,y}$ The value of $\Delta\varphi_{total,y}$ is given by the sum of the contribution of the above gradients.

$$\Delta\varphi_{total,y}(v) = \Delta\varphi(CY1) + \Delta\varphi(SY) + \Delta\varphi(CY2) + \Delta\varphi(CY3) + \Delta\varphi(CY4) \tag{3.105}$$

$$\Delta\varphi_{total,y}(v) = -73.00\ \frac{rad \cdot s}{m} \cdot v \approx -4183°\frac{s}{m} \cdot v \tag{3.106}$$

This formula can be utilised to determine the dephasing of an ^{1}H nucleus flowing or moving with the velocity v along the y-axis for the exemplary PRESS sequence.

Gradient-induced phase-shift effects in PRESS along the z-direction

The calculation of the dephasing of a nucleus moving along the z-axis is shown here. Figure 3.4 shows the gradients responsible for the phase-shift effects. The total dephasing along the z-axis is called $\Delta\varphi_{total,z}(v)$. Again, $\Delta\varphi(CZ1)$ denotes the dephasing caused by the first crusher gradient along the z-axis CZ1 and so on.

$$\Delta\varphi_{total,z}(v) = \Delta\varphi(CZ1) + \Delta\varphi(CZ2) + \Delta\varphi(CZ2) + \Delta\varphi(SZ) + \Delta\varphi(CZ4) \tag{3.107}$$

Calculation of $\Delta\varphi$(CZ1) The first crusher gradient along the z-axis is described by the three formulae $CZ1_1$(t), $CZ1_2$(t), and $CZ1_3$(t). Their contributions to the dephasing of the nuclei are called $\Delta\varphi(CZ1_1)$, $\Delta\varphi(CZ1_2)$, and $\Delta\varphi(CZ1_3)$ respectively. Here, Equation

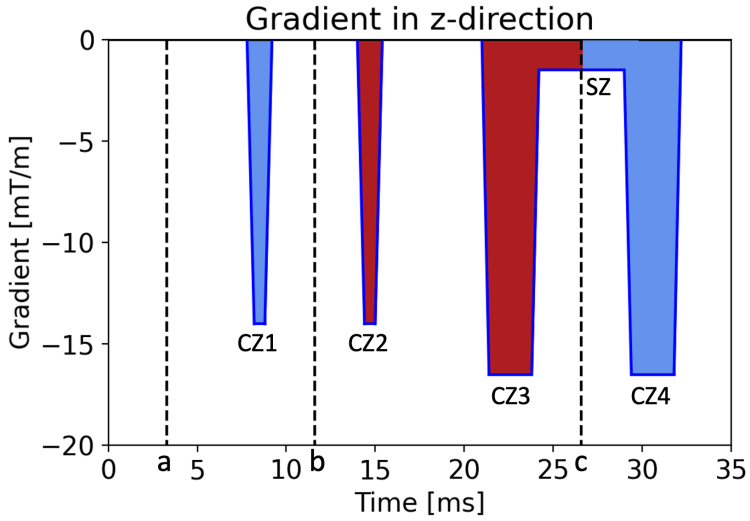

Figure 3.4: PRESS gradients in the z-direction and their impact on phase-shift effects. Sequence parameters: δL = 20 mm, TE = 30 ms. (a) Timing of the initial 90°-pulse. (b) Timing of the first 180°-pulse. (c) Timing of the second 180°-pulse. (CZ1) First half of the crusher gradient during TE_1. (CZ2) Second half of the crusher gradient during TE_1. (CZ3) First half of the crusher gradient during TE_2. (CZ4) Second half of the crusher gradient during TE_2. (SZ) Slice selection gradient. Notably, the pale blue colour of CZ1, CZ4, and the second half of SZ signifies their negative algebraic contribution to the gradient-induced phase shift. Conversely, the reddish colour of CZ2, CZ3, and the first half of SZ represents their positive algebraic contribution to the gradient-induced phase shift.

3.50 is used again to determine the contributions of the components.

$$\Delta\varphi(CZ1_1) = v \cdot \gamma \cdot \int_{0.0078s}^{0.0082s} -35.0\frac{T}{m \cdot s} \cdot (t - 0.0078s) \cdot t \cdot dt \tag{3.108}$$

$$\Delta\varphi(CZ1_2) = v \cdot \gamma \cdot \int_{0.0082s}^{0.0088s} -0.014\frac{T}{m} \cdot t \cdot dt \tag{3.109}$$

$$\Delta\varphi(CZ1_3) = v \cdot \gamma \cdot \int_{0.0088s}^{0.0092s} 35.0\frac{T}{m \cdot s} \cdot (t - 0.0092s) \cdot t \cdot dt \tag{3.110}$$

The dephasing caused by this first crusher gradient is inverted twice by the two following 180°-pulses, resulting in no net effect.

$$\Delta\varphi(CZ1) = \Delta\varphi(CZ1_1) + \Delta\varphi(CZ1_2) + \Delta\varphi(CZ1_3) \tag{3.111}$$

$$\Delta\varphi(CZ1) = -31.84\,\frac{rad \cdot s}{m} \cdot v \tag{3.112}$$

Calculation of $\Delta\varphi$(CZ2) The second crusher gradient along the z-axis is described by the three formulae $CZ2_1$(t), $CZ2_2$(t), and $CZ2_3$(t). Their contributions to the dephasing of the nuclei are called $\Delta\varphi(CZ2_1)$, $\Delta\varphi(CZ2_2)$, and $\Delta\varphi(CZ2_3)$ respectively. Here, Equa-

tion 3.50 is used again to determine the contributions of the components.

$$\Delta\varphi(CZ2_1) = v \cdot \gamma \cdot \int_{0.0140s}^{0.0144s} -35.0\frac{T}{m \cdot s} \cdot (t - 0.0140s) \cdot t \cdot dt \tag{3.113}$$

$$\Delta\varphi(CZ2_2) = v \cdot \gamma \cdot \int_{0.0144s}^{0.0150s} -0.014\frac{T}{m} \cdot t \cdot dt \tag{3.114}$$

$$\Delta\varphi(CZ2_3) = v \cdot \gamma \cdot \int_{0.0150s}^{0.0154s} 35.0\frac{T}{m \cdot s} \cdot (t - 0.0154s) \cdot t \cdot dt \tag{3.115}$$

The second crusher gradient is followed by a single 180°-pulse. Therefore, the contribution to the dephasing is inverted using a negative algebraic sign.

$$\Delta\varphi(CZ2) = -(\Delta\varphi(CZ2_1) + \Delta\varphi(CZ2_2) + \Delta\varphi(CZ2_3)) \tag{3.116}$$

$$\Delta\varphi(CZ2) = 55.06\ \frac{rad \cdot s}{m} \cdot v \tag{3.117}$$

Calculation of $\Delta\varphi$(CZ3) The third crusher gradient along the z-axis is described by the three formulae $CZ3_1$(t), $CZ3_2$(t), and $CZ3_3$(t). Their contributions to the dephasing of the nuclei are called $\Delta\varphi(CZ3_1)$, $\Delta\varphi(CZ3_2)$, and $\Delta\varphi(CZ3_3)$ respectively. Here, Equation 3.50 is used again to determine the contributions of the components.

$$\Delta\varphi(CZ3_1) = v \cdot \gamma \cdot \int_{0.0210s}^{0.0214s} -41.25\frac{T}{m \cdot s} \cdot (t - 0.0210s) \cdot t \cdot dt \tag{3.118}$$

$$\Delta\varphi(CZ3_2) = v \cdot \gamma \cdot \int_{0.0214s}^{0.0238s} -0.0165\frac{T}{m} \cdot t \cdot dt \tag{3.119}$$

$$\Delta\varphi(CZ3_3) = v \cdot \gamma \cdot \int_{0.0238s}^{0.0242s} 37.58\frac{T}{m \cdot s} \cdot (t - 0.02424s) \cdot t \cdot dt \tag{3.120}$$

The third crusher gradient is followed by a single 180°-pulse. Therefore, the contribution to the dephasing is inverted using a negative algebraic sign.

$$\Delta\varphi(CZ3) = -(\Delta\varphi(CZ3_1) + \Delta\varphi(CZ3_2) + \Delta\varphi(CZ3_3)) \tag{3.121}$$

$$\Delta\varphi(CZ3) = 281.22\ \frac{rad \cdot s}{m} \cdot v \tag{3.122}$$

Calculation of $\Delta\varphi$(SZ) During the slice selection gradient along the z-axis, a 180°-pulse is applied. This means that the effect of the first half of the gradient is effectively inverted. The dephasing caused by the first half is called $\Delta\varphi(SZ_1)$, and the second half

is called $\Delta\varphi(SZ_2)$ here.

$$\Delta\varphi(SZ_1) = v \cdot \gamma \cdot \int_{0.0242s}^{0.0266s} -0.00147\frac{T}{m} \cdot t \cdot dt \tag{3.123}$$

$$\Delta\varphi(SZ_2) = v \cdot \gamma \cdot \int_{0.0266s}^{0.0290s} -0.00147\frac{T}{m} \cdot t \cdot dt \tag{3.124}$$

$\Delta\varphi(SZ_2)$ is not followed by a pulse. Therefore, its contribution is denoted with a positive algebraic sign. Since the dephasing $\Delta\varphi(SZ_1)$ is followed by a 180°-pulse and thus inverted, its contribution is denoted with a negative algebraic sign.

$$\Delta\varphi(SZ) = -\Delta\varphi(SZ_1) + \Delta\varphi(SZ_2) \tag{3.125}$$

$$\Delta\varphi(SZ) = -2.26\ \frac{rad \cdot s}{m} \cdot v \tag{3.126}$$

Calculation of $\Delta\varphi$(CZ4) The fourth crusher gradient along the z-axis is described by the three formulae $CZ4_1$(t), $CZ4_2$(t), and $CZ4_3$(t). Their contributions to the dephasing of the nuclei are called $\Delta\varphi(CZ4_1)$, $\Delta\varphi(CZ4_2)$, and $\Delta\varphi(CZ4_3)$ respectively. Here, Equation 3.50 is used again to determine the contributions of the components.

$$\Delta\varphi(CZ4_1) = v \cdot \gamma \cdot \int_{0.0290s}^{0.0294s} -37.58\frac{T}{m \cdot s} \cdot (t - 0.02896s) \cdot t \cdot dt \tag{3.127}$$

$$\Delta\varphi(CZ4_2) = v \cdot \gamma \cdot \int_{0.0294s}^{0.0318s} -0.0165\frac{T}{m} \cdot t \cdot dt \tag{3.128}$$

$$\Delta\varphi(CZ4_3) = v \cdot \gamma \cdot \int_{0.0318s}^{0.0322s} 41.25\frac{T}{m \cdot s} \cdot (t - 0.0322s) \cdot t \cdot dt \tag{3.129}$$

The fourth crusher gradient is not followed by another pulse. Therefore, $\Delta\varphi(CZ4)$ is calculated as follows.

$$\Delta\varphi(CZ4) = \Delta\varphi(CZ4_1) + \Delta\varphi(CZ4_2) + \Delta\varphi(CZ4_3) \tag{3.130}$$

$$\Delta\varphi(CZ4) = -380.49\ \frac{rad \cdot s}{m} \cdot v \tag{3.131}$$

Calculation of $\Delta\varphi_{total,z}$ The value of $\Delta\varphi_{total,z}$ is given by the sum of the contribution of the above gradients.

$$\Delta\varphi_{total,z}(v) = \Delta\varphi(CZ1) + \Delta\varphi(CZ2) + \Delta\varphi(CZ2) + \Delta\varphi(SZ) + \Delta\varphi(CZ4) \tag{3.132}$$

$$\Delta\varphi_{total,z}(v) = -78.32\ \frac{rad \cdot s}{m} \cdot v \approx -4487°\frac{s}{m} \cdot v \tag{3.133}$$

This formula can be utilised to determine the dephasing of an ^{1}H nucleus flowing or moving with the velocity v along the z-axis for the exemplary PRESS sequence.

3.1.3 Exemplary STEAM sequence

The STEAM sequence utilised by the 3 T Magnetom Prisma Fit whole-body MRI scanner is used here. The same sequence was used in the experiments of this study. Therefore, the parameters provided by Siemens Healthcare were used here. Figure 3.5 shows the exemplary STEAM sequence, and Table 3.2 the corresponding parameters. Firstly, the strength of the slice selection gradient (SSG) must be calculated.

$$SSG = \frac{2 \cdot \pi \cdot n \cdot R}{\delta L \cdot T \cdot \gamma} \tag{3.134}$$

$$SSG = \frac{2 \cdot \pi \cdot rad \cdot 5 \cdot 1.75}{2.0 \cdot 10^{-2} m \cdot 1.8 \cdot 10^{-3} s \cdot 2.675 \cdot 10^{8} \frac{1}{T \cdot s}} \tag{3.135}$$

$$SSG = 5.71 \cdot 10^{-3} \frac{T}{m} \tag{3.136}$$

Table 3.2: Parameters of the exemplary STEAM sequence.

Parameter	Acronym	Value, (Range)
Voxel length/height/width	δL	20mm, (3–40mm)
Duration of the 90°-pulse	T_{90}	1.8 ms
R factor of the 90°-pulse	R_{90}	1.75
n of the 90°-pulse	n_{90}	5
Ramp time of gradients	t_{ramp}	0.8 ms

Gradients of the exemplary STEAM sequence along the x-direction

Here, a set of functions describing the gradients along the x-axis is determined. It can be seen in Figure 3.5 that four gradients are applied along the x-axis in total. The first is the slice selection gradient, followed by a pair of crusher gradients, one before the second 90°-pulse and the other after the third 90°-pulse. Another crusher gradient is applied during

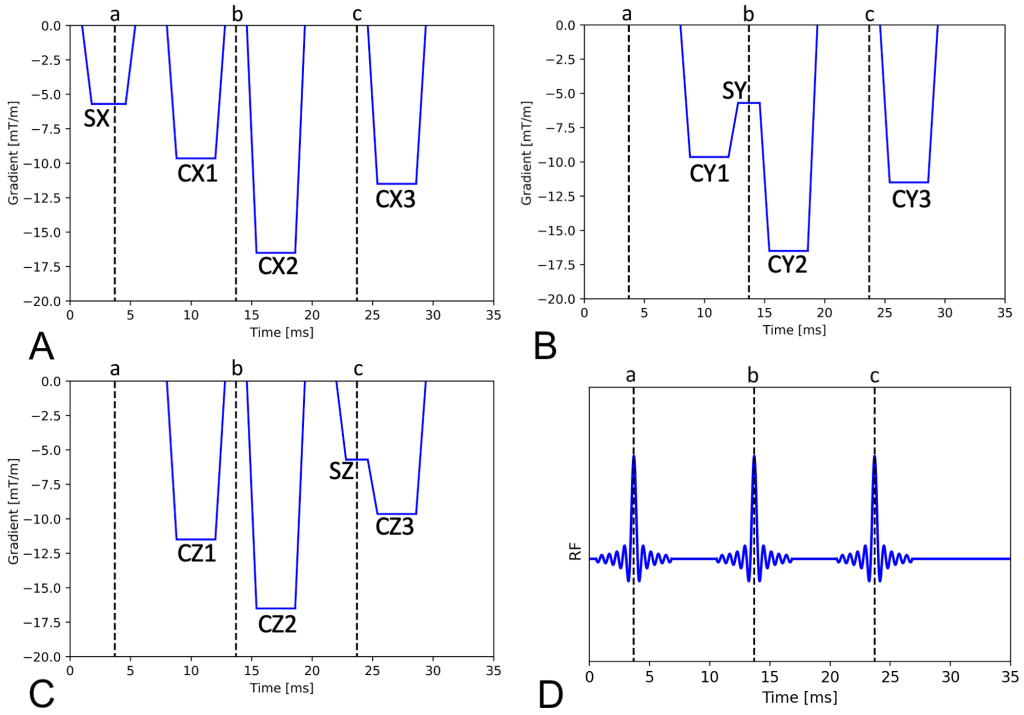

Figure 3.5: Illustration of the exemplary STEAM sequence. Sequence parameters: δL = 20 mm, TE = 20 ms, TM = 10 ms. [A] Gradients of the sequence in the x-direction. [B] Gradients of the sequence in the y-direction. [C] Gradients of the sequence in the z-direction. [D] Plot of the three RF pulses. (a) Timing of the initial 90°-pulse. (b) Timing of the second 90°-pulse. (c) Timing of the final 90°-pulse. (CX1/CY1/CZ1) Crusher gradient during the first half of TE along the corresponding axis. (CX2/CY2/CZ2) Crusher gradient during TM along the corresponding axis. (CX3/CY3/CZ3) Crusher gradient during the second half of TE along the corresponding axis. (SX/SY/SZ) Slice selection gradient along the corresponding axis.

the mixing time. The sequence has an echo time of 20 ms, a mixing time of 10 ms, and δL is 20 mm along each axis.

The slice selection gradient in the x-direction is described by the three formulae $SX_1(t)$, $SX_2(t)$, and $SX_3(t)$. $SX_1(t)$, and $SX_3(t)$ are the ramps of the gradient. $SX_2(t)$ is the plateau of the gradient. This terminology applies to all subsequent gradients.

$$SX_1(t) = -7.14\,\frac{mT}{m \cdot ms}\,(t - 1\,ms) \qquad | \, 1.0\,ms < t < 1.8\,ms \tag{3.137}$$

$$SX_2(t) = -5.71\,\frac{mT}{m} \qquad | \, 1.8\,ms < t < 4.6\,ms \tag{3.138}$$

$$SX_3(t) = 7.14\,\frac{mT}{m \cdot ms}\,(t - 5.4\,ms) \qquad | \, 4.6\,ms < t < 5.4\,ms \tag{3.139}$$

The crusher gradient CX1 is described by the three formulae $CX1_1(t)$, $CX1_2(t)$, and $CX1_3(t)$.

$$CX1_1(t) = -12.06\,\frac{mT}{m \cdot ms}\,(t - 8\,ms) \qquad | 8.0\,ms < t < 8.8\,ms \qquad (3.140)$$

$$CX1_2(t) = -9.64\,\frac{mT}{m} \qquad | 8.8\,ms < t < 12.0\,ms \qquad (3.141)$$

$$CX1_3(t) = 12.06\,\frac{mT}{m \cdot ms}\,(t - 12.8\,ms) \qquad | 12.0\,ms < t < 12.8\,ms \qquad (3.142)$$

The crusher gradient CX2 is described by the three formulae $CX2_1(t)$, $CX2_2(t)$, and $CX2_3(t)$.

$$CX2_1(t) = -20.63\,\frac{mT}{m \cdot ms}\,(t - 14.6\,ms) \qquad | 14.6\,ms < t < 15.4\,ms \qquad (3.143)$$

$$CX2_2(t) = -16.5\,\frac{mT}{m} \qquad | 15.4\,ms < t < 18.6\,ms \qquad (3.144)$$

$$CX2_3(t) = 20.63\,\frac{mT}{m \cdot ms}\,(t - 19.4\,ms) \qquad | 18.6\,ms < t < 19.4\,ms \qquad (3.145)$$

The crusher gradient CX3 is described by the three formulae $CX3_1(t)$, $CX3_2(t)$, and $CX3_3(t)$.

$$CX3_1(t) = -14.38\,\frac{mT}{m \cdot ms}\,(t - 24.6\,ms) \qquad | 24.6\,ms < t < 25.4\,ms \qquad (3.146)$$

$$CX3_2(t) = -11.5\,\frac{mT}{m} \qquad | 25.4\,ms < t < 28.6\,ms \qquad (3.147)$$

$$CX3_3(t) = 14.38\,\frac{mT}{m \cdot ms}\,(t - 29.4\,ms) \qquad | 28.6\,ms < t < 29.4\,ms \qquad (3.148)$$

Gradients of the exemplary STEAM sequence along the y-direction

Here, all formulae are listed that describe the gradients of the STEAM sequence along the y-direction.

The crusher gradient number CY1 is described by the three formulae $CY1_1(t)$, $CY1_2(t)$, and $CY1_3(t)$.

$$CY1_1(t) = -12.06\,\frac{mT}{m \cdot ms}\,(t - 8.0\,ms) \qquad | 8.0\,ms < t < 8.8\,ms \qquad (3.149)$$

$$CY1_2(t) = -9.64\,\frac{mT}{m} \qquad | 8.8\,ms < t < 12.0\,ms \qquad (3.150)$$

$$CY1_3(t) = 4.92\,\frac{mT}{m \cdot ms}\,(t - 13.96\,ms) \qquad | 12.0\,ms < t < 12.8\,ms \qquad (3.151)$$

The slice selection gradient in the y-direction is described by the formula SY(t).

$$SY(t) = -5.71\frac{mT}{m} \qquad | 12.8\,ms < t < 14.6\,ms \qquad (3.152)$$

The crusher gradient number CY2 is described by the three formulae $CY2_1(t)$, $CY2_2(t)$,

and $CY2_3$(t).

$$CY2_1(t) = -13.49\,\frac{mT}{m \cdot ms}\,(t - 14.18\,ms) \quad | 14.6\,ms < t < 15.4\,ms \tag{3.153}$$

$$CY2_2(t) = -16.5\,\frac{mT}{m} \quad | 15.4\,ms < t < 18.6\,ms \tag{3.154}$$

$$CY2_3(t) = 20.63\,\frac{mT}{m \cdot ms}\,(t - 19.4\,ms) \quad | 18.6\,ms < t < 19.4\,ms \tag{3.155}$$

The crusher gradient number CY3 is described by the three formulae $CY3_1$(t), $CY3_2$(t), and $CY3_3$(t).

$$CY3_1(t) = -14.38\,\frac{mT}{m \cdot ms}\,(t - 24.6\,ms) \quad | 24.6\,ms < t < 25.4\,ms \tag{3.156}$$

$$CY3_2(t) = -11.5\,\frac{mT}{m} \quad | 25.4\,ms < t < 28.6\,ms \tag{3.157}$$

$$CY3_3(t) = 14.38\,\frac{mT}{m \cdot ms}\,(t - 29.4\,ms) \quad | 28.6\,ms < t < 29.4\,ms \tag{3.158}$$

Gradients of the exemplary STEAM sequence along the z-direction

Here, all formulae are listed that describe the gradients of the STEAM sequence along the z-direction.

The crusher gradient number CZ1 is described by the three formulae $CZ1_1$(t), $CZ1_2$(t), and $CZ1_3$(t).

$$CZ1_1(t) = -14.38\,\frac{mT}{m \cdot ms}\,(t - 8\,ms) \quad | 8.0\,ms < t < 8.8\,ms \tag{3.159}$$

$$CZ1_2(t) = -11.5\,\frac{mT}{m} \quad |8.8\,ms < t < \ 12.0\,ms \tag{3.160}$$

$$CZ1_3(t) = 14.38\,\frac{mT}{m \cdot ms}\,(t - 12.8\,ms) \quad | 12.0\,ms < t < 12.8\,ms \tag{3.161}$$

The crusher gradient number CZ2 is described by the three formulae $CZ2_1$(t), $CZ2_2$(t), and $CZ2_3$(t).

$$CZ2_1(t) = -20.63\,\frac{mT}{m \cdot ms}\,(t - 14.6\,ms) \quad | 14.6\,ms < t < 15.4\,ms \tag{3.162}$$

$$CZ2_2(t) = -16.5\,\frac{mT}{m} \quad | 15.4\,ms < t < 18.6\,ms \tag{3.163}$$

$$CZ2_3(t) = 20.63\,\frac{mT}{m \cdot ms}\,(t - 19.4\,ms) \quad | 18.6\,ms < t < 19.4\,ms \tag{3.164}$$

The slice selection gradient in the z-direction is described by the formulae $SZ(t)_1$ and

$SZ(t)_2$.

$$SZ_1(t) = -7.14\,\frac{mT}{m \cdot ms}(t - 22.0\,ms) \qquad | 22.0\,ms < t < 22.8\,ms \qquad (3.165)$$

$$SZ_2(t) = -5.71\,\frac{mT}{m} \qquad | 22.8\,ms < t < 24.6\,ms \qquad (3.166)$$

The crusher gradient number CZ3 is described by the three formulae $CZ3_1(t)$, $CZ3_2(t)$, and $CZ3_3(t)$.

$$CZ3_1(t) = -4.92\,\frac{mT}{m \cdot ms}\,(t - 23.44\,ms) \qquad | 24.6\,ms < t < 25.4\,ms \qquad (3.167)$$

$$CZ3_2(t) = -9.64\,\frac{mT}{m} \qquad | 25.4\,ms < t < 28.6\,ms \qquad (3.168)$$

$$CZ3_3(t) = 12.06\,\frac{mT}{m \cdot ms}\,(t - 29.4\,ms) \qquad | 28.6\,ms < t < 29.4\,ms \qquad (3.169)$$

3.1.4 Calculation of gradient-induced phase-shift effects in STEAM

Here, the way to calculate the change in phase of the flowing nuclei along a given direction for a STEAM sequence is shown. The exemplary STEAM sequence shown in Figure 3.5 is used for this purpose. When considering the STEAM sequence, it is crucial to notice that the two consecutive 90°-pulses act together like a single 180°-pulse and invert the dephasing previously created. Further, the crusher gradient during the mixing time does not create dephasing. The time between 13.7 and 23.7 ms corresponds to the mixing time in this example. Therefore, the crusher gradients along the x-axis (CX2), y-axis (CY2), and z-axis (CZ2) during the mixing time are irrelevant.

Gradient-induced phase-shift effects in STEAM along the x-direction

For the calculation, the Equations 3.50 and 3.51 were used. Those were presented above for the calculation of the dephasing of the PRESS sequence. The total dephasing of an ^1H nucleus moving along the x-axis depending on its velocity v is called $\Delta\varphi_{total,x}(v)$. It is the sum of the effect of the first crusher gradient (CX1), the third crusher gradient (CX3), and the slice selection gradient (SX). $\Delta\varphi(CX1)$ is the dephasing of the nucleus caused by the first crusher gradient CX1. This terminology is applied to all other gradients as well. Figure 3.6 shows the gradients responsible for the phase-shift effects.

$$\Delta\varphi_{total,x}(v) = \Delta\varphi(SX) + \Delta\varphi(CX1) + \Delta\varphi(CX3) \qquad (3.170)$$

Calculation of $\Delta\varphi$(SX) The 90°-pulse excites the nucleus 3.7 ms after the start of the sequence. Therefore, the effect of the gradient starts at 3.7 ms. $\Delta\varphi(SX_2)$ represents

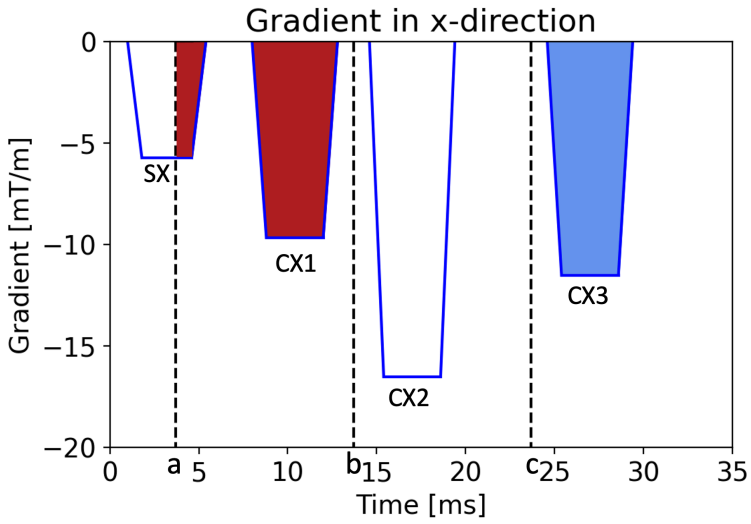

Figure 3.6: STEAM gradients in the x-direction and their impact on phase-shift effects. Sequence parameters: δL = 20 mm, TE = 20 ms, TM = 10 ms. (a) Timing of the initial 90°-pulse. (b) Timing of the second 90°-pulse. (c) Timing of the final 90°-pulse. (CX1) Crusher gradient during the first half of TE. (CX2) Crusher gradient during TM. (CX3) Crusher gradient during the second half of TE. (SX) Slice selection gradient. Notably, the pale blue colour of CX3 signifies its negative algebraic contribution to the gradient-induced phase shift. Conversely, the reddish colour of CX1 and the latter part of SX (after the initial 90°-pulse) represents their positive algebraic contribution to the gradient-induced phase shift. An important observation is that the initial part of SX does not contribute to the phase shift since no transverse magnetisation has been generated up to that point. CX2 does not influence the phase shift as it is applied during the mixing time.

the dephasing due to the plateau of the gradient described by the formula for SX_2(t) and $\Delta\varphi(SX_3)$ represents the dephasing due to the latter ramp of the gradient described by the formula SX_3(t). The contribution of the dephasing due to the slice selection gradient is calculated using Equation 3.50:

$$\Delta\varphi(SX_2) = 2.675 \cdot 10^8 \cdot \frac{rad}{s\,T} \cdot v \cdot \gamma \cdot \int_{0.0037s}^{0.0046s} -0.00571 \frac{T}{m} \cdot t \cdot dt \tag{3.171}$$

$$\Delta\varphi(SX_3) = v \cdot \gamma \cdot \int_{0.0046s}^{0.0054s} 7.14 \frac{T}{m \cdot s} \cdot (t - 0.0054s) \cdot t \cdot dt \tag{3.172}$$

Here, $\Delta\varphi(SX)$ is the sum of the inverse of both components. Because of the inversion of the dephasing due to both 90°-pulses, a negative algebraic sign is applied to both terms. Calculating the above integrals yields the following formula for the contribution of the

slice selection gradient.

$$\Delta\varphi(SX) = -(\Delta\varphi(SX_2) + \Delta\varphi(SX_3)) \tag{3.173}$$

$$\Delta\varphi(SX) = 8.68\,\frac{rad \cdot s}{m} \cdot v \tag{3.174}$$

Calculation of $\Delta\varphi$(CX1) The first crusher gradient along the x-axis is described by the three formulae $CX1_1$(t), $CX1_2$(t), and $CX1_3$(t). Their contributions to the dephasing of the nucleus are called $\Delta\varphi(CX1_1)$, $\Delta\varphi(CX1_2)$, and $\Delta\varphi(CX1_3)$ respectively. Here, Equation 3.50 is used again to determine the contributions of the components.

$$\Delta\varphi(CX1_1) = v \cdot \gamma \cdot \int_{0.0080s}^{0.0088s} -12.06\frac{T}{m \cdot s}(t - 0.008s) \cdot t \cdot dt \tag{3.175}$$

$$\Delta\varphi(CX1_2) = v \cdot \gamma \cdot \int_{0.0088s}^{0.0120s} -0.00964\frac{T}{m} \cdot t \cdot dt \tag{3.176}$$

$$\Delta\varphi(CX1_3) = v \cdot \gamma \cdot \int_{0.0120s}^{0.0128s} 12.06\frac{T}{m \cdot s} \cdot (t - 0.0128s) \cdot t \cdot dt \tag{3.177}$$

Here, $\Delta\varphi(CX1)$ is the sum of the inverse of the three components. Because of the inversion of the dephasing due to both 90°-pulses, a negative algebraic sign is applied to all three terms. Calculating of the above integrals yields the following formula for the contribution of the crusher gradient.

$$\Delta\varphi(CX1) = -(\Delta\varphi(CX1_1) + \Delta\varphi(CX1_2) + \Delta\varphi(CX1_3)) \tag{3.178}$$

$$\Delta\varphi(CX1) = 107.33\,\frac{rad \cdot s}{m} \cdot v \tag{3.179}$$

Calculation of $\Delta\varphi$(CX3) The third crusher gradient along the x-axis is described by the three formulae $CX3_1$(t), $CX3_2$(t), and $CX3_3$(t). Their contributions to the dephasing of the nuclei are called $\Delta\varphi(CX3_1)$, $\Delta\varphi(CX3_2)$, and $\Delta\varphi(CX3_3)$ respectively. Here, Equation 3.50 is used again to determine the contributions of the components.

$$\Delta\varphi(CX3_1) = v \cdot \gamma \cdot \int_{0.0246s}^{0.0254s} -14.38\frac{T}{m \cdot s} \cdot (t - 0.0246s) \cdot t \cdot dt \tag{3.180}$$

$$\Delta\varphi(CX3_2) = v \cdot \gamma \cdot \int_{0.0254s}^{0.0286s} -0.0115\frac{T}{m} \cdot t \cdot dt \tag{3.181}$$

$$\Delta\varphi(CX3_3) = v \cdot \gamma \cdot \int_{0.0286s}^{0.0294s} 14.38\frac{T}{m \cdot s} \cdot (t - 0.0294s) \cdot t \cdot dt \tag{3.182}$$

No pulse follows the third crusher gradient. Therefore, no inversion has to be taken into account. The value of $\Delta\varphi(CX3)$ is the sum of the above components.

$$\Delta\varphi(CX3) = \Delta\varphi(CX3_1) + \Delta\varphi(CX3_2) + \Delta\varphi(CX3_3) \tag{3.183}$$

$$\Delta\varphi(CX3) = -332.26\,\frac{rad \cdot s}{m} \cdot v \tag{3.184}$$

Calculation of $\Delta\varphi_{total,x}$ The value of $\Delta\varphi_{total,x}$ is given by the sum of the contribution of the above gradients.

$$\Delta\varphi_{total,x}(v) = \Delta\varphi(SX) + \Delta\varphi(CX1) + \Delta\varphi(CX3) \tag{3.185}$$

$$\Delta\varphi_{total,x}(v) = -216.25\,\frac{rad \cdot s}{m} \cdot v \approx -12390°\frac{s}{m} \cdot v \tag{3.186}$$

This formula can be utilised to determine the dephasing of an ^{1}H nucleus flowing or moving with the velocity v along the x-axis for the exemplary STEAM sequence.

Gradient-induced phase-shift effects in STEAM along the y-direction

Calculating the dephasing of a nucleus moving along the y-axis is similar to the above calculation. Figure 3.7 shows the gradients responsible for the phase-shift effects. The total dephasing along the y-axis is called $\Delta\varphi_{total,y}(v)$. Again, $\Delta\varphi(CY1)$ denotes the dephasing caused by the first crusher gradient along the y-axis CY1 and so on.

$$\Delta\varphi_{total,y}(v) = \Delta\varphi(CY1) + \Delta\varphi(SY) + \Delta\varphi(CY3) \tag{3.187}$$

$$\tag{3.188}$$

Calculation of $\Delta\varphi$(CY1) The first crusher gradient along the y-axis is described by the three formulae CY1$_1$(t), CY1$_2$(t), and CY1$_3$(t). Their contributions to the dephasing of the nuclei are called $\Delta\varphi(CY1_1)$, $\Delta\varphi(CY1_2)$, and $\Delta\varphi(CY1_3)$ respectively. Here, Equation 3.50 is used again to determine the contributions of the components.

$$\Delta\varphi(CY1_1) = v \cdot \gamma \cdot \int_{0.0080s}^{0.0088s} -12.06\frac{T}{m \cdot s} \cdot (t - 0.0080s) \cdot t \cdot dt \tag{3.189}$$

$$\Delta\varphi(CY1_2) = v \cdot \gamma \cdot \int_{0.0088s}^{0.0120s} -0.00964\frac{T}{m} \cdot t \cdot dt \tag{3.190}$$

$$\Delta\varphi(CY1_3) = v \cdot \gamma \cdot \int_{0.0120s}^{0.0128s} 4.92\frac{T}{m \cdot s} \cdot (t - 0.01396s) \cdot t \cdot dt \tag{3.191}$$

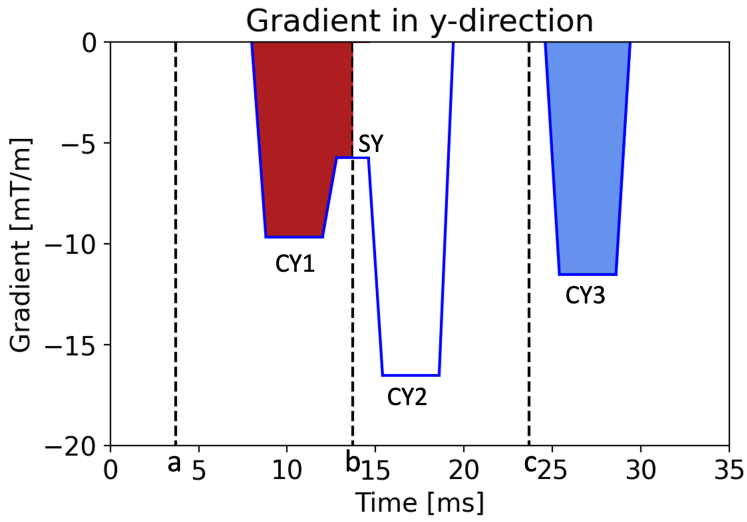

Figure 3.7: STEAM gradients in the y-direction and their impact on phase-shift effects. Sequence parameters: δL = 20 mm, TE = 20 ms, TM = 10 ms. (a) Timing of the initial 90°-pulse. (b) Timing of the second 90°-pulse. (c) Timing of the final 90°-pulse. (CY1) Crusher gradient during the first half of TE. (CY2) Crusher gradient during TM. (CY3) Crusher gradient during the second half of TE. (SY) Slice selection gradient. Notably, the pale blue colour of CY3 signifies its negative algebraic contribution to the gradient-induced phase shift. Conversely, the reddish colour of CY1 and the first half of SY represent their positive algebraic contribution to the gradient-induced phase shift. CY2 and the latter half of SY do not influence the phase shift as they are applied during the mixing time.

Here, $\Delta\varphi(CY1)$ is the sum of the inverse of the three components. Because of the inversion of the dephasing due to the two 90°-pulses following the gradient, a negative algebraic sign is applied to all three terms. Calculating the above integrals yields the following formula for the contribution of the crusher gradient.

$$\Delta\varphi(CY1) = -(\Delta\varphi(CY1_1) + \Delta\varphi(CY1_2) + \Delta\varphi(CY1_3)) \tag{3.192}$$

$$\Delta\varphi(CY1) = 114.99\,\frac{rad \cdot s}{m} \cdot v \tag{3.193}$$

Calculation of $\Delta\varphi$(SY) It has to be taken into account that the contribution of $\Delta\varphi(SY)$ must be inverted since the first half of the gradient is followed by two 90°-pulses. The second half of the slice selection gradient is applied during the mixing time, meaning the second half does not affect the dephasing.

$$\Delta\varphi(SY) = -(v \cdot \gamma \cdot \int_{0.0128s}^{0.0137s} -0.00571\frac{T}{m} \cdot t \cdot dt) \tag{3.194}$$

$$\Delta\varphi(SY) = 18.21\,\frac{rad \cdot s}{m} \cdot v \tag{3.195}$$

Calculation of $\Delta\varphi$(CY3) The third crusher gradient along the y-axis is described by the three formulae $CY3_1$(t), $CY3_2$(t), and $CY3_3$(t). Their contributions to the dephasing of the nuclei are called $\Delta\varphi(CY3_1)$, $\Delta\varphi(CY3_2)$, and $\Delta\varphi(CY3_3)$ respectively. Here, Equation 3.50 is used again to determine the contributions of the components.

$$\Delta\varphi(CY3_1) = v \cdot \gamma \cdot \int_{0.0246s}^{0.0254s} -14.38\frac{T}{m \cdot s} \cdot (t - 0.0246s) \cdot t \cdot dt \tag{3.196}$$

$$\Delta\varphi(CY3_2) = v \cdot \gamma \cdot \int_{0.0254s}^{0.0286s} -0.0115\frac{T}{m} \cdot t \cdot dt \tag{3.197}$$

$$\Delta\varphi(CY3_3) = v \cdot \gamma \cdot \int_{0.0286s}^{0.0294s} 14.38\frac{T}{m \cdot s} \cdot (t - 0.0294s) \cdot t \cdot dt \tag{3.198}$$

No pulse follows the third crusher gradient. Therefore, no inversion has to be taken into account. The value of $\Delta\varphi(CY3)$ is the sum of the above components.

$$\Delta\varphi(CY3) = \Delta\varphi(CY3_1) + \Delta\varphi(CY3_2) + \Delta\varphi(CY3_3) \tag{3.199}$$

$$\Delta\varphi(CY3) = -332.26\ \frac{rad \cdot s}{m} \cdot v \tag{3.200}$$

Calculation of $\Delta\varphi_{total,y}$ The value of $\Delta\varphi_{total,y}$ is given by the sum of the contribution of the above gradients.

$$\Delta\varphi_{total,y}(v) = \Delta\varphi(CY1) + \Delta\varphi(SY) + \Delta\varphi(CY3) \tag{3.201}$$

$$\Delta\varphi_{total,y}(v) = -199.06\ \frac{rad \cdot s}{m} \cdot v \approx -11405°\frac{s}{m} \cdot v \tag{3.202}$$

This formula can be utilised to determine the dephasing of an ^{1}H nucleus flowing or moving with the velocity v along the y-axis for the exemplary STEAM sequence.

Gradient-induced phase-shift effects in STEAM along the z-direction

The following shows the calculation of the dephasing of a nucleus moving along the z-axis. Figure 3.8 illustrates the gradients responsible for the phase-shift effects. The total dephasing along the z-axis is called $\Delta\varphi_{total,z}(v)$. Again, $\Delta\varphi(CZ1)$ denotes the dephasing caused by the first crusher gradient along the z-axis CZ1 and so on.

$$\Delta\varphi_{total,z}(v) = \Delta\varphi(CZ1) + \Delta\varphi(SZ) + \Delta\varphi(CZ3) \tag{3.203}$$

Calculation of $\Delta\varphi$(CZ1) The first crusher gradient along the y-axis is described by the three formulae $CZ1_1$(t), $CZ1_2$(t), and $CZ1_3$(t). Their contributions to the dephasing of the nuclei are called $\Delta\varphi(CZ1_1)$, $\Delta\varphi(CZ1_2)$, and $\Delta\varphi(CZ1_3)$ respectively. Here, Equation

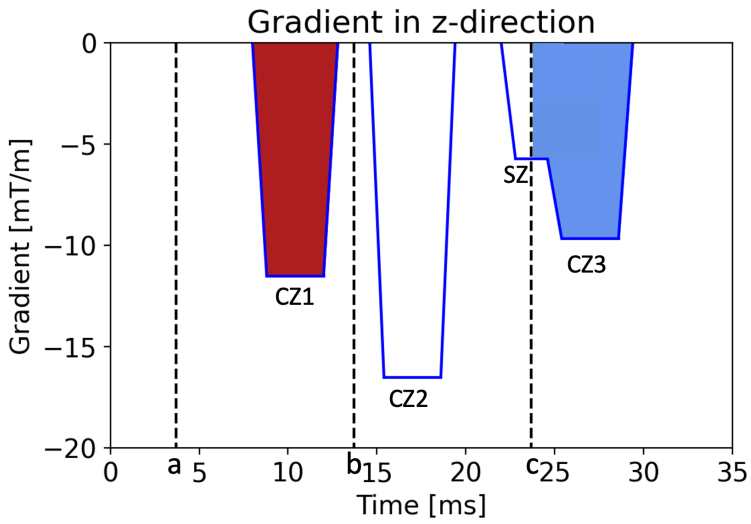

Figure 3.8: STEAM gradients in the z-direction and their impact on phase-shift effects. Sequence parameters: δL = 20 mm, TE = 20 ms, TM = 10 ms. (a) Timing of the initial 90°-pulse. (b) Timing of the second 90°-pulse. (c) Timing of the final 90°-pulse. (CZ1) Crusher gradient during the first half of TE. (CZ2) Crusher gradient during TM. (CZ3) Crusher gradient during the second half of TE. (SZ) Slice selection gradient. Notably, the pale blue colour of CZ3 and the latter part of SZ (after the final 90°-pulse) signifies their negative algebraic contribution to the gradient-induced phase shift. Conversely, the reddish colour of CZ1 represents its positive algebraic contribution to the gradient-induced phase shift. CZ2 and the former part of SY do not influence the phase shift as they are applied during the mixing time.

3.50 is used again to determine the contributions of the components.

$$\Delta\varphi(CZ1_1) = v \cdot \gamma \cdot \int_{0.0080s}^{0.0088s} -14.38\frac{T}{m \cdot s}(t - 0.008s) \cdot t \cdot dt \tag{3.204}$$

$$\Delta\varphi(CZ1_2) = v \cdot \gamma \cdot \int_{0.0088s}^{0.0120s} -0.0115\frac{T}{m} \cdot t \cdot dt \tag{3.205}$$

$$\Delta\varphi(CZ1_3) = v \cdot \gamma \cdot \int_{0.0120s}^{0.0128s} 14.38\frac{T}{m \cdot s} \cdot (t - 0.0128s) \cdot t \cdot dt \tag{3.206}$$

Here, $\Delta\varphi(CZ1)$ is the sum of the inverse of the three components. Because of the inversion of the dephasing due to the two 90°-pulses following the gradient, a negative algebraic sign is applied to all three terms. Calculating the above integrals yields the following formula for the contribution of the crusher gradient.

$$\Delta\varphi(CZ1) = -(\Delta\varphi(CZ1_1) + \Delta\varphi(CZ1_2) + \Delta\varphi(CZ1_3)) \tag{3.207}$$

$$\Delta\varphi(CZ1) = 127.98\,\frac{rad \cdot s}{m} \cdot v \tag{3.208}$$

Calculation of $\Delta\varphi$(SZ) The first half of the gradient is applied during the mixing time. Therefore, it can be ignored in the calculation. The second half of the slice selection

gradient is not followed by any pulse, so no inversion has to be considered.

$$\Delta\varphi(SZ) = v \cdot \gamma \cdot \int_{0.0237s}^{0.0246s} -0.00571\frac{T}{m} \cdot t \cdot dt \tag{3.209}$$

$$\Delta\varphi(SZ) = -33.19\ \frac{rad \cdot s}{m} \cdot v \tag{3.210}$$

Calculation of $\Delta\varphi$(CZ3) The third crusher gradient along the z-axis is described by the three formulae $CZ3_1$(t), $CZ3_2$(t), and $CZ3_3$(t). Their contributions to the dephasing of the nuclei are called $\Delta\varphi(CZ3_1)$, $\Delta\varphi(CZ3_2)$, and $\Delta\varphi(CZ3_3)$ respectively. Here, Equation 3.50 is used again to determine the contributions of the components.

$$\Delta\varphi(CZ3_1) = v \cdot \gamma \cdot \int_{0.0246s}^{0.0254s} -4.92\frac{T}{m \cdot s} \cdot (t - 0.02344s) \cdot t \cdot dt \tag{3.211}$$

$$\Delta\varphi(CZ3_2) = v \cdot \gamma \cdot \int_{0.0254s}^{0.0286s} -0.00964\frac{T}{m} \cdot t \cdot dt \tag{3.212}$$

$$\Delta\varphi(CZ3_3) = v \cdot \gamma \cdot \int_{0.0286s}^{0.0294s} 12.06\frac{T}{m \cdot s} \cdot (t - 0.0294s) \cdot t \cdot dt \tag{3.213}$$

No pulse follows the third crusher gradient. Therefore, no inversion has to be taken into account. The value of $\Delta\varphi(CZ3)$ is the sum of the above components.

$$\Delta\varphi(CZ3) = \Delta\varphi(CZ3_1) + \Delta\varphi(CZ3_2) + \Delta\varphi(CZ3_3) \tag{3.214}$$

$$\Delta\varphi(CZ3) = -293.85\ \frac{rad \cdot s}{m} \cdot v \tag{3.215}$$

Calculation of $\Delta\varphi_{total,z}$ The value of $\Delta\varphi_{total,y}$ is given by the sum of the contribution of the above gradients.

$$\Delta\varphi_{total,z}(v) = \Delta\varphi(CZ1) + \Delta\varphi(SZ) + \Delta\varphi(CZ3) \tag{3.216}$$

$$\Delta\varphi_{total,z}(v) = -199.06\ \frac{rad \cdot s}{m} \cdot v \approx -11405°\frac{s}{m} \cdot v \tag{3.217}$$

This formula can be utilised to determine the dephasing of an ^{1}H nucleus flowing or moving with the velocity v along the z-axis for the exemplary STEAM sequence.

3.1.5 Methods used for the simulation of gradient-induced phase-shift effects in ^{1}H spectroscopy

The exemplary PRESS sequence shown above has fixed values for TE and δL. Likewise, the exemplary STEAM sequence has set values for TE, TM, and δL. However, this study strives to give a more comprehensive insight into the influence of flow on PRESS and

STEAM sequences. Therefore, the author has written computer programs to simulate the influence of flow on PRESS and STEAM for various parameters. The programs have been written using Python (Version 3.9.7, 64 Bit) and the NumPy library. The results have been calculated in the same manner as shown above. Chapter 4 presents the results graphically. The Matplotlib library was used for the plots. Specifically, the flow sensitivity of the PRESS sequence was evaluated by varying TE and δL, and the flow sensitivity of the STEAM sequence was evaluated by varying TE, TM, and δL.

3.2 Phantom measurements

3.2.1 Aim of the experiments

As shown with the exemplary sequences in Section 3.1 (and the more detailed account of the simulations in Section 4.1), gradient-induced phase-shift effects influence spectra acquired with PRESS and STEAM sequences. Although the effects are expected to be most pronounced with flow velocities found in larger vessels, flow in smaller vessels can also affect the spectra in peripheral tissue. The experiments of this thesis aim to evaluate whether the effects of smaller flow velocities on the spectra are measurable.

To achieve this, the author constructed a flow phantom. The construction of the phantom is elucidated in Subsection 3.2.2. In essence, the phantom comprises an intraluminal flow-capable tube, enabling the adjustment of flow parameters. Acquisitions of spectra from both flowing and stationary fluids within the phantom were performed using PRESS and STEAM sequences. The author varied the flow between the measurements to evaluate whether the spectral signals intensities changed due to flow variations. The results are presented in Section 4.2 and discussed in Chapter 5.

A few conditions for a phantom experiment must be met to test whether flow indeed alters the signal behaviour of PRESS and STEAM measurements in a relevant manner. Firstly, it is essential to ensure that the flow velocity implemented in the phantom approximates the velocities observed in human tissue. This criterion allows for a simulation of flow dynamics encountered in different tissues. Additionally, it is crucial to maintain a laminar flow within the phantom, as arterioles, capillaries, and venules in human tissue also exhibit laminar flow characteristics. All conditions other than the mean flow velocity should be unchanged between measurements to make them comparable.

3.2.2 Experimental setup for the phantom measurements

The experiment aims to create a laminar flow with a variable flow velocity close to blood flow velocities in arterioles, capillaries, and venules. Spectra of a nickel sulfate solution

flowing through a tube were acquired. The flow was generated using a medical infusion set usually used for intravenous infusions. A nickel sulfate solution was filled into an IV bag. The infusion set is connected to the phantom using a three-way valve fixed to the tube. On the other side of the phantom, the solution is ejected through an extension for infusion lines. The solution is collected in a cup. Figure 3.9 shows the setup.

Instead of tap water, a nickel sulfate solution was used in the experiments as the shorter values of T_1 and T_2 helped to decrease testing times. Specifically, a solution of $NiSO_4 \cdot 6\ H_2O$ with a concentration of 3,8 mmol/L was used. Dr. Günter Steidle kindly provided the solution and information about its T_1 and T_2 values. T_1 is approximately 450 ms and T_2 approximately 350 ms.

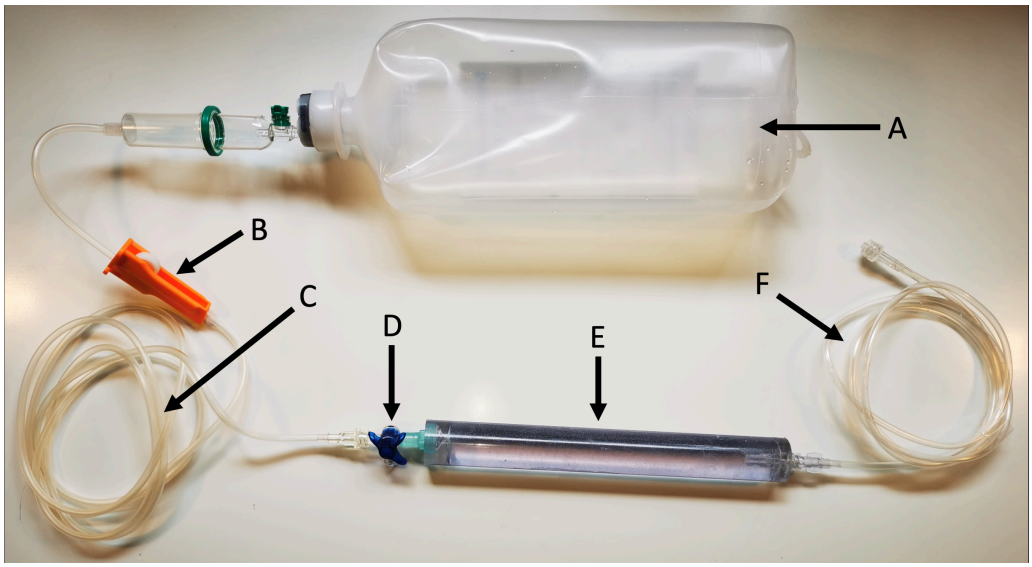

Figure 3.9: Scheme of the experimental setup for phantom measurements. (A) is the IV bag that serves as a reservoir for the fluid. (B) is the regulator of the infusion set used to vary the flow through the phantom. (C) is the infusion line that supplies the phantom with the fluid. (D) is the three-way valve used to switch the flow on and off in the preparation of the experiment. (E) is the tube of the phantom where the measurements are made. (F) is the Heidelberg extension line used to drain off the fluid. For the MR measurements, the IV bag was elevated. The weight of the fluid inside the IV bag created hydrostatic pressure and consecutively flow. The tube was placed inside a coil.

The flow variability is achieved through the regulator of the infusion system. The three-way valve was used to stop the flow during the preparation of the experiments. Further, the three-way valve facilitated the placement of the phantom inside the coil using the opening of the valve perpendicular to the tube.

The infusion set was a 1.8 m long Intrafix® SafeSet manufactured by B. Braun Melsungen AG (Melsungen, Germany). The IV bag holding the nickel sulfate solution was an empty Sterofundin® bag manufactured by B. Braun Melsungen AG (Melsungen, Ger-

many). A 6 mm hole was drilled into the top to fill it with the nickel sulfate solution. A 20 mL syringe manufactured by B. Braun Melsungen AG (Melsungen, Germany) was used for the filling.

The phantom tube is made of unplasticised polyvinyl chloride (PVC) and was manufactured by Georg Fischer AG (Schaffhausen, Switzerland). It is 201 mm long and has an inner diameter of 20 mm and an outer diameter of 25 mm (Figure 3.10). Both ends of the tube were sealed with epoxy resin manufactured by EPODEX GmbH (Krefeld, Germany). On the left side of the phantom, the layer of epoxy resin is 14 mm thick, and on the right side, it is 6 mm. A drill hole of 4 mm was made through the plate of epoxy resin on the left side. A second drill hole of 11.5 mm was made at the same location but only 8 mm deep into the plate. Into the drill hole of 11.5 mm, the end of a three-way valve was glued with the epoxy resin mentioned above. The three-way valve (Discofix®) was manufactured by B. Braun Melsungen AG (Melsungen, Germany). The inner diameter of the end of the three-way valve is 2 mm. A drill hole of 6 mm was made through the plate of epoxy resin on the right side. The end piece of a Heidelberg extension line (extension for infusion lines) was cut off and glued into the 6 mm drill hole with epoxy resin. Figure 3.11 shows a picture of the phantom.

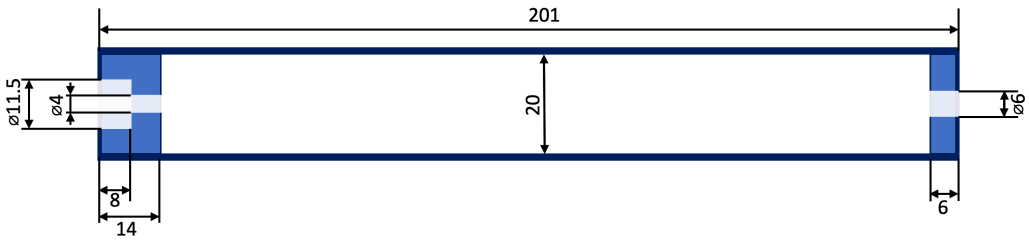

Figure 3.10: Dimensions of the phantom. All measurements are in mm. The dark blue outer rectangle represents the tube, and the two smaller pale blue rectangles represent the epoxy resin. The transparent cavities represent the drill holes in the epoxy resin.

The solution leaves the phantom through the truncated end piece of the Heidelberg extension line connected to another Heidelberg extension line measuring 1.40 m in length. Both Heidelberg extensions used were manufactured by Fresenius Kabi GmbH (Bad Homburg, Germany).

The scanner used to acquire the data was a 3 T Magnetom Prisma Fit whole-body MRI scanner by Siemens Healthcare GmbH (Erlangen, Germany). The coil used to obtain the spectra was a Head/Neck 20 3 T Tim coil manufactured by Siemens Healthcare GmbH (Erlangen, Germany). The tube of the phantom was placed vertically inside the coil. The vertical position was chosen to minimise the effects of gravity on the flow profile that might cause more turbulent or irregular flow. Foamed plastic cushions were used to hold

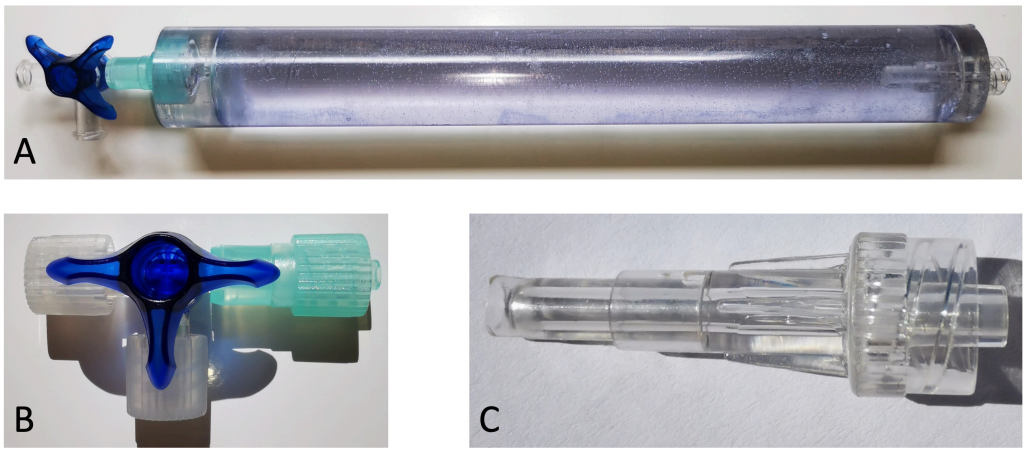

Figure 3.11: Pictures of the phantom, the three-way valve, and the end piece of the extension. [A] depicts the phantom. The three-way valve fixed to the tube can be seen on the left side. The truncated end piece of the Heidelberg extension line fixed to the tube is shown on the right side. The phantom is filled with the nickel sulfate solution, and the three-way valve is closed. [B] depicts the three-way valve used in constructing the phantom in detail. [C] depicts the end piece of the Heidelberg extension used in the construction of the phantom in detail.

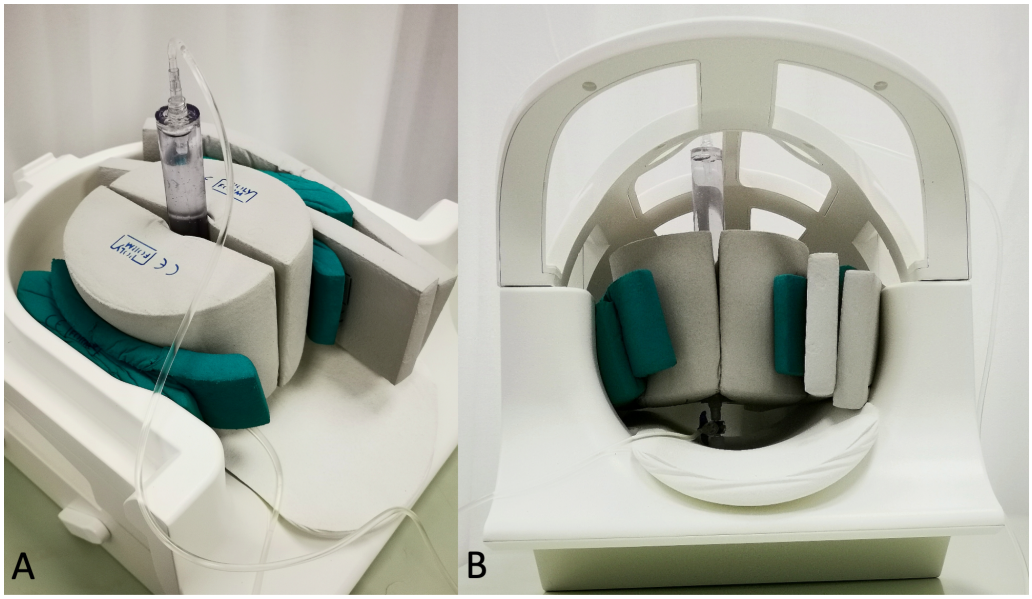

Figure 3.12: Positioning of the phantom inside the head coil. [A] shows the fixation of the phantom by cushions. The line on top of the phantom is the drain. The line that enters the phantom from the bottom is the infusion line supplying the fluid. [B] The phantom is placed vertically inside the coil, and the cap of the coil is mounted. The phantom is placed to the left to avoid the drain line being kinked by the central bar of the cap.

the phantom in place and to minimise artefacts. The positioning of the phantom inside the coil is shown in Figure 3.12.

A voxel with an edge length of 13 x 13 x 13 mm was used for all phantom measurements. The values were chosen for two reasons. Firstly, the in vivo and preliminary measurements were performed with the same voxel dimensions. Secondly, to maximise the signal, the voxel was chosen to be large but to fit inside the tube with an inner diameter of 20 mm. 13 x 13 x 13 mm is the middle ground, as can be seen in Figure 3.13.

The scale used for the weight measurements was a Page Comfort 300 Slim manufactured by Leifheit AG (Nassau, Germany). The stopwatch was imported by FL B.V. (Tiel, Netherlands); the producer is unknown.

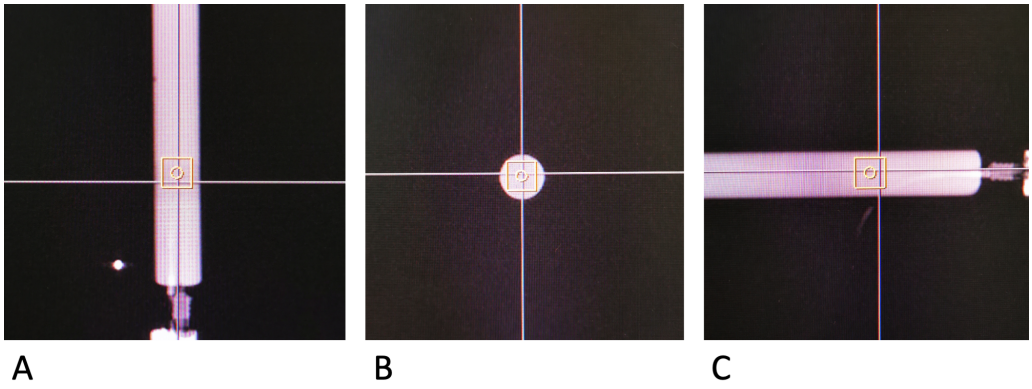

Figure 3.13: Positioning of the voxel inside the phantom. The yellow square represents the position of the voxel. The voxel was positioned centrally within the phantom. [A] depicts the transversal plane. [B] depicts the coronal plane. [C] depicts the sagittal plane.

3.2.3 Calculation of the Reynolds number expected in the phantom measurement

To ensure that the flow inside the phantom resembles the flow in arterioles, capillaries, and venules it should be laminar. To evaluate whether the flow through the phantom is laminar the Reynolds number is calculated using the following formula.

$$Re = \frac{\rho \, v_{flow} \, D_H}{\eta} \tag{3.218}$$

Here, ρ is the density of the fluid, v_{flow} is the mean velocity of the fluid, η is the fluid's dynamic viscosity, and D_H is the hydraulic diameter that is equal to the inner diameter of the tube. Due to the small concentration of nickel sulfate, the values for pure water are used here. However, this represents a simplification. The density of water is 998 $\frac{kg}{m^3}$ and

the dynamic viscosity is $1.00 \cdot 10^{-3}$ $\frac{kg}{m\,s}$ at 20 $°C$. The inner diameter of the phantom used is $2.0 \cdot 10^{-2}$ m. The mean velocity of the fluid did not exceed 2 mm/s or $2.00 \cdot 10^{-3}$ m/s. The Reynolds number is calculated using these values.

$$Re = \frac{998\ \frac{kg}{m^3} \cdot 2.00 \cdot 10^{-3}\ \frac{m}{s} \cdot 2.0 \cdot 10^{-2}\ m}{1.00 \cdot 10^{-3}\ \frac{kg}{m\,s}} \tag{3.219}$$

$$Re = 39.9 \tag{3.220}$$

The Reynolds number of 39.9 is far below the critical value (2300) for the transition from laminar to turbulent flow in a tube. Therefore, the flow through the phantom can be considered laminar.

3.2.4 Calculation of the flow velocity inside the phantom

The flow inside the phantom tube can be quantified in different ways. The maximum flow or average flow velocity can be used to quantify the flow. Here, the average flow velocity (v_{flow}) in m/s is used as it is easily and precisely calculable. The volumetric flow rate (Q) in $\frac{m^3}{s}$ is determined by the volume of the nickel solution (V) flowing through the phantom in the time interval called t_{flow}.

$$Q = \frac{V}{t_{flow}} \tag{3.221}$$

It is possible to calculate the flow velocity when the cross-sectional area (A) is known using the volumetric flow rate.

$$v_{flow} = \frac{Q}{A} \tag{3.222}$$

In the case of the tube, the cross-sectional area is calculated the following way (D denotes the inner diameter of the tube).

$$A = \left(\frac{D}{2}\right)^2 \cdot \pi \tag{3.223}$$

Further, it has to be considered that not the volume but the mass (m) of the nickel solution was determined experimentally. Therefore, the volume has to be calculated using the

density of the nickel solution.

$$V = \frac{m}{\rho} \tag{3.224}$$

The combination of all of the above formulae yields the following.

$$v_{flow} = \frac{m}{t_{flow} \cdot \rho \cdot \left(\frac{D}{2}\right)^2 \cdot \pi} \tag{3.225}$$

Although nickel sulfate solution has been used and not pure water, the density of pure water at 20°C is used for the calculation. The resulting error is neglectable as the density of nickel sulfate is 2.07 $\frac{g}{mL}$, and only 1 g of nickel sulfate per litre of water was used. Therefore, the error cannot be larger than 0.1%.

Measurements necessary for the calculation of the flow velocity inside the phantom

The following measurements were performed to determine the mean flow velocity used in the experiments. Before the spectra were acquired, the regulator was fixed to varying positions to enable different mean flow velocities. A plastic clip fixed to the infusion line blocked flow through the phantom during the regulator's adjustment. After the adjustment, the clip was opened. At that exact moment, a stopwatch was set to take the time. Then, the spectra were acquired. During the acquisition, a plastic cup collected the fluid.

After the measurements, the clip was closed, and the stopwatch was stopped. The measured time corresponds to t_{flow}. The cup holding the fluid was weighed to determine the mass of the liquid. The empty cup was weighed initially to subtract the weight from the previous measurement. Between each set of measurements, the cup was dried to ensure precise measurements.

3.3 In vivo measurements and measurements with flow-sensitised sequences

3.3.1 Aim of the experiments

This thesis evaluates whether the gradient-induced phase-shift effects in PRESS and STEAM sequences due to flow are relevant and how sequence parameters determine these effects. In addition to the previously introduced theoretical simulations, experiments were conducted to validate the simulation results. As a first step, measurements of a phantom containing flowing nickel sulfate solution were conducted (Subsection 3.2.2). The experiments investigated whether the gradient-induced phase-shift effects are observable for

flow velocities in peripheral tissue. The second step towards this goal was an in vivo measurement series outlined in this section. The measurement series was designed to investigate whether gradient-induced phase-shift effects can also be observed in vivo. For this purpose, spectra of red bone marrow in the third and fourth lumbar vertebral bodies in two subjects were acquired.

In contrast to the phantom measurements, the in vivo measurements of gradient-induced phase shifts cannot use variations in the flow velocity as the flow inside the bone marrow is not adjustable. Consequently, an alternative approach must be employed to evaluate the impact of gradients. A variation of the flow sensitivity of the PRESS and STEAM sequences is a feasible way to test the influence of flow on the spectra. For this reason, flow-sensitised PRESS and STEAM sequences have been developed. The following paragraph explains the idea behind the usage of the flow-sensitised sequences.

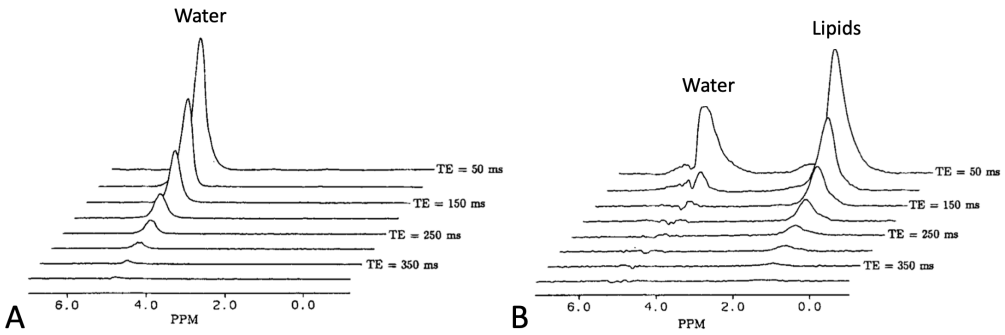

Figure 3.14: Comparison between two test series that show different T_2 relaxation dynamics. [A] shows a series of spectra acquired with a STEAM sequence. Note the gradual and orderly decay of the water signal with longer TE times. The spectrum was acquired in the bone marrow of a patient with acute lymphoblastic leukaemia. [B] depicts a similar test series acquired in the same patient after treating the disease. Note that the water signal decays more rapidly. This example illustrates that dephasing leads to shorter T_2 times and can be visualised in such a chart. Adapted from Schick et al. [116].

In the bone marrow, the complex arrangement of vessels and capillaries leads to a multitude of angles relative to the main magnetic field. Additionally, the flow velocities vary considerably in different vessels. Consequently, the dephasing of flowing nuclei occurs more chaotically than in phantom experiments.

The dephasing manifests as a form of T_2 decay, resulting in a fast decay of the signal originating from the bone marrow. Using a more flow-sensitive PRESS or STEAM sequence leads to stronger dephasing of the flowing nuclei than standard sequences. Therefore, the signal intensity of spectra acquired with flow-sensitised sequences is expected to be smaller. Further, longer echo times should lead to more pronounced differences between standard and flow-sensitised PRESS and STEAM sequences. As these processes are neither proven nor expected to be monoexponentially, the measurement of T_2 times is

unsuitable. Instead, a direct qualitative comparison of spectra obtained using sequences with different degrees of flow sensitivity was employed as the preferred approach. Thus, it was evaluated whether the effects of gradients are relevant for in vivo measurements without directly quantifying the dephasing.

In short, standard PRESS and STEAM sequences were compared to flow-sensitised sequences to elucidate the role of flow in the ^{1}H spectroscopy of peripheral tissue. If the effects of gradients on flow are relevant in vivo, a faster decrease in the signal intensity of the flow-sensitised sequences should occur with longer echo times compared to standard sequences (Figure 3.14). The crusher gradients were modified to achieve the increased flow sensitivity. Subsections 3.3.3 and 3.3.4 explain the details of the necessary modifications.

3.3.2 Experimental setup of the preliminary and in vivo measurements

Experimental setup of the preliminary measurements

Before conducting in vivo measurements, a comparison between the standard and flow-sensitised sequences was performed using phantom measurements. For this purpose, the phantom introduced in Subsection 3.2.2 was used. The aim of these comparative measurements was twofold: firstly, to verify the functionality of the flow-sensitised sequences and secondly, to assess their ability to demonstrate the effects of flow. By conducting these preliminary assessments in a phantom environment, the author aimed to prove the feasibility and reliability of the flow-sensitised sequences before conducting the in vivo investigations.

Firstly, the preliminary measurements compared a standard PRESS sequence with the flow-sensitised PRESS sequence. Secondly, a standard STEAM sequence was compared to the flow-sensitised STEAM sequence at a mixing time of 10 ms. Thirdly, a standard STEAM sequence was compared to the flow-sensitised STEAM sequence at a mixing time of 20 ms. In all cases, the flow-sensitised sequences had roughly double the flow sensitivity compared to the standard sequences.

Two test series were acquired for each pair of sequences (standard and flow-sensitised) that varied only in TE. The flow-sensitised sequences differed from the standard sequences only in the strength of their crusher gradients to achieve a high validity of the results. The dimension of the voxel, the positioning of the voxel, the mixing time and the echo time were identical in each pair of test series. Therefore, Subsection 3.2.2 lists all other information about the experimental setup of these preliminary measurements.

The manufacturer of the MRI scanner usually determines the strength of the crusher

gradients of PRESS and STEAM sequences. However, we reprogrammed the sequences to accommodate stronger crusher gradients to develop the flow-sensitised sequences. Subsections 3.3.3 and 3.3.4 demonstrate the modifications made to the PRESS and STEAM sequences, with separate presentations of the gradients along the x-, y-, and z-directions.

Experimental setup of the in vivo measurements

For the in vivo measurements, spectra of the red bone marrow of two subjects were acquired. The same 3 T Magnetom Prisma Fit scanner was used. The measurements were performed in the third or fourth lumbar vertebral body. Both subjects were placed on the table in a head-first supine position. The isocenter of the scanner was approximately 5 cm cranial to the iliac crest. For comfort, the heads of the volunteers were placed on a cushion. The spectra were acquired using the spine coil of the MRI scanner integrated into the table.

The first participant, Subject 1 from now on, was a 21-year-old male volunteer, while the second participant, referred to as Subject 2 from now on, was a 29-year-old female volunteer. Before the measurements, both subjects received detailed information about the potential risks associated with the measurements from a physician. The in vivo experiments were conducted as part of perfusion measurements, method development and tissue characterisation research at the Sektion für Experimentelle Radiologie, located at the University Hospital Tübingen. Before initiating, these projects obtained ethical approval from the ethics commission, ensuring adherence to established guidelines and regulations.

The voxel measuring 13 x 13 x 13 mm was placed inside the subjects' third or fourth lumbar vertebral body. Depending upon the images obtained by the localisers, the third or fourth vertebral body was chosen. The third vertebral body was preferred if both lumbar vertebral bodies were depicted sufficiently well to place the whole voxel inside them safely. Figure 3.15 shows the positioning of the voxel using the localiser.

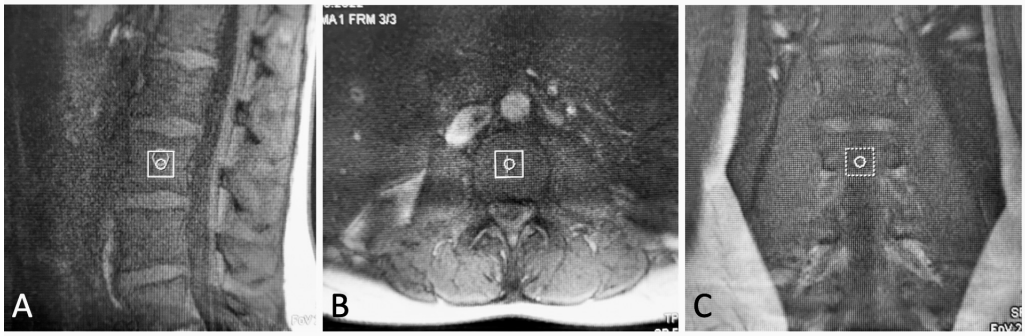

Figure 3.15: Positioning of the voxel in the bone marrow of the third vertebral body in Subject 2.

Experimental setup of the in vivo STEAM measurements with longer mixing times

Additionally, the sequences were used to investigate whether longer mixing times in STEAM sequences lead to stronger gradient-induced phase-shift effects. These experiments were motivated by the behaviour demonstrated in the simulations outlined in Sections 3.1 and 4.1. This investigation was done by conducting in vivo measurements with increasing mixing times using modified and standard sequences. By comparing the resulting spectra, the author aimed to investigate whether longer mixing times indeed contribute to stronger gradient-induced phase-shift effects, as suggested by the simulations.

3.3.3 Design of the flow-sensitised PRESS sequence

This section elucidates how the standard PRESS sequences were modified to create the flow-sensitised sequences. For the in vivo measurements, we chose a voxel size of 13 mm x 13 mm x 13 mm; therefore, these values were used in the following calculations. It is important to note that the results presented here only apply to this voxel size.

Firstly, it is evaluated how the gradients along the x-direction must be changed to roughly double the flow sensitivity of the sequence. There are two pairs of crusher gradients along the x-direction. However, since the first gradient of the first pair of crusher gradients depends on the strength of the slice selection gradient along the x-direction, it is more convenient to modify the second pair of crusher gradients (Figure 3.16). In the standard PRESS sequence of the MRI scanner used for the experiments, these crusher gradients have a magnitude of -16.5 mT/m. If the value is increased to -27.0 mT/m, the flow sensitivity is raised by a factor of 1.99 in theory. These results were determined using the approach introduced in Section 3.1. A comparison between the standard and flow-sensitised PRESS sequences is presented in Figure 3.16.

Along the y-direction, there are two pairs of crusher gradients as well. Both pairs can be flow-sensitised. Again, changing the second pair of gradients is more convenient, as the slice selection gradient connects the first pair (Figure 3.17). Modifying the first pair would make the sequence programming complex. In the standard PRESS sequence of the MRI scanner used for the experiments, the second pair of crusher gradients has a magnitude of -16.5 mT/m. An increase in value to -27.0 mT/m leads to an increase in flow sensitivity by a factor of 1.99.

The modification of gradients along the z-axis is more complex than along other axes. There are, again, two pairs of crusher gradients. A slice selection gradient connects the second pair. Therefore, the modification of the second pair is technically more complex than the modification of the first pair. However, an increase in the magnitude of the first pair of crusher gradients leads to decreased flow sensitivity. The option to decrease the

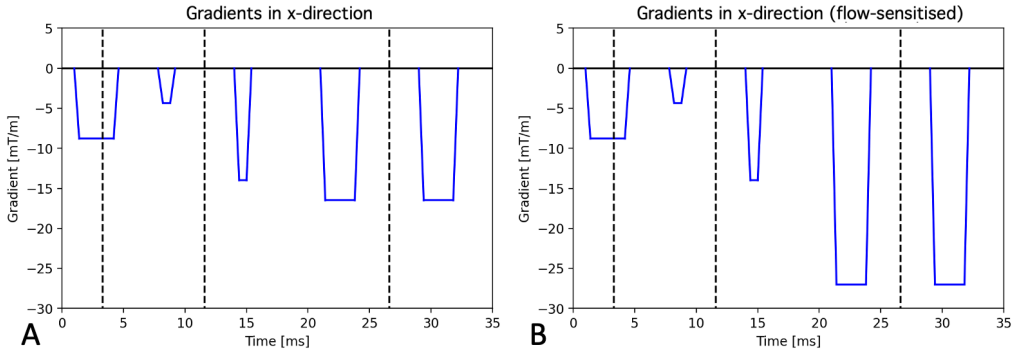

Figure 3.16: Comparison of the gradients in the x-direction between the standard and flow-sensitised PRESS sequence. Sequence parameters: TE = 30 ms, edge length of a voxel in a given direction (δL) = 13 mm. [A] shows the gradients along the x-axis used in the standard PRESS sequence. [B] shows the gradients used in the flow-sensitised sequence. The magnitudes of the second pair of crusher gradients focused around the third RF pulse (dashed line to the right) have been increased.

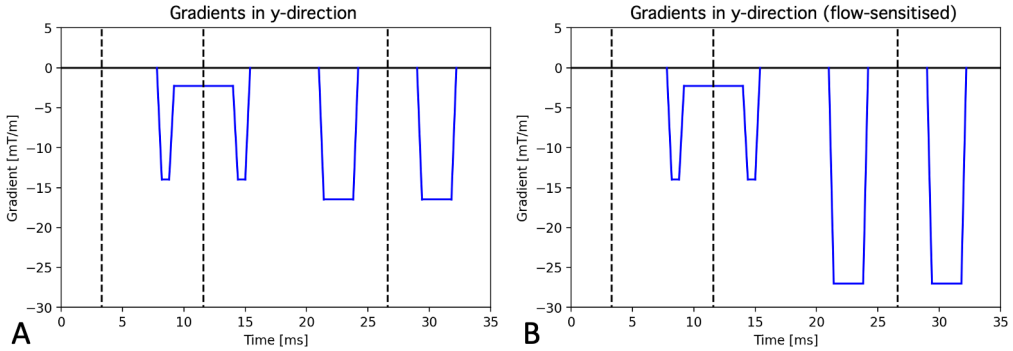

Figure 3.17: Comparison of the gradients in the y-direction between the standard and flow-sensitised PRESS sequences. Sequence parameters: TE = 30 ms, δL = 13 mm. [A] shows the gradients along the y-axis used in the standard PRESS sequence. [B] shows the gradients used in the flow-sensitised sequence. The magnitudes of the second pair of crusher gradients focused around the third RF pulse (dashed line to the right) were increased.

magnitude of the first pair of crusher gradients instead is not chosen since the usage of crusher gradients smaller than those implemented by the manufacturer might lead to unwanted signal components. Therefore, the option to increase the magnitude of the second pair of crusher gradients was chosen, although this is more complicated to implement (Figure 3.18). In the standard PRESS sequence of the MRI scanner used for the experiments, the second pair of crusher gradients has a magnitude of -16.5 mT/m. An increase in value to -27.0 mT/m leads to an increase in flow sensitivity by a factor of 1.79. Table 3.3 summarises the flow-sensitised PRESS sequence parameters.

As shown in Subsection 4.1.1, the flow sensitivity of PRESS sequences does not depend on the echo time. Therefore, the increase in flow sensitivity of the flow-sensitised

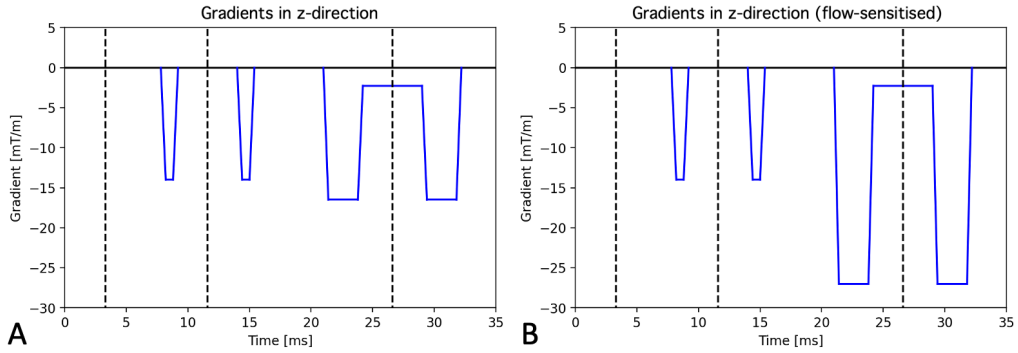

Figure 3.18: Comparison of the gradients in the z-direction between the standard and flow-sensitised PRESS sequences. Sequence parameters: TE = 30 ms, δL = 13 mm. [A] shows the gradients along the z-axis used in the standard PRESS sequence. [B] shows the gradients used in the flow-sensitised sequence. The magnitudes of the second pair of crusher gradients focused around the third RF pulse (dashed line to the right) were increased.

Table 3.3: Overview of the gradients used in the flow-sensitised PRESS sequence. The nomenclature of the gradients matches the nomenclature used in Chapter 3 (Figure 3.1). The row labelled "standard" lists the gradients used in the sequence provided by the manufacturer. The row labelled "flow-sensitised" lists the gradients used in the flow-sensitised sequence.

X-direction	SSG	CX1	CX2	CX3	CX4
Standard [mT/m]	−8.8	−4.3	−14.0	−16.5	−16.5
Flow-sensitised [mT/m]	−8.8	−4.3	−14.0	−27.0	−27.0
Y-direction	CY1	SSG	CY2	CY3	CY4
Standard [mT/m]	−14.0	−2.3	−14.0	−16.5	−16.5
Flow-sensitised [mT/m]	−14.0	−2.3	−14.0	−27.0	−27.0
Z-direction	CZ1	CZ2	CZ3	SSG	CZ4
Standard [mT/m]	−14.0	−14.0	−16.5	−2.3	−16.5
Flow-sensitised [mT/m]	−14.0	−14.0	−27.0	−2.3	−27.0

compared to the standard sequences is constant, and the factors do not change with varying echo times. This is not necessarily the case for changes in edge length of a voxel in a given direction (δL). However, δL is not varied during the experiments.

3.3.4 Design of the flow-sensitised STEAM sequence

For the modification of STEAM sequences, it is essential to notice that the crusher gradient applied during the mixing time is not a viable target for modification as it does not contribute to the flow sensitivity. The slice selection gradients should remain the same since they are reserved for volume selection, meaning that modifying the STEAM sequence's first and third crusher gradient is necessary. Alternatively, additional gradients could be added to the sequence. Again, the following calculations and values apply only for a voxel size of 13 mm x 13 mm x 13 mm. A mixing time of 10 ms is used for the calculations.

The first and third crusher gradients applied along the x-axis are not equally strong because the effect of the slice selection gradient must be taken into account to achieve complete rephasing at the end of the sequence (Figure 3.19). An increase in the magnitude of the third crusher gradient from -11.5 mT/m to -23.0 mT/m leads to an increase in flow sensitivity by a factor of 2.00 for an echo time of 20 ms. The magnitude of the flow-sensitised first crusher gradient for the chosen voxel size must be set to -20.1 mT/m to rephase the nuclei at the end of the sequence. In contrast to the gradients applied along the y- and z-axes in a STEAM sequence, the echo time changes the sensitivity for flow along the x-axis (Section 2.6). Consequently, the factor is not constant. For instance, it is reduced to 1.76 for an echo time of 50 ms and 1.13 for a very long echo time of 1000 ms. However, changing the mixing time influences the factor minutely. A maximum mixing time of 80 ms was used in the experiments, resulting in an increase of the factor to 2.04.

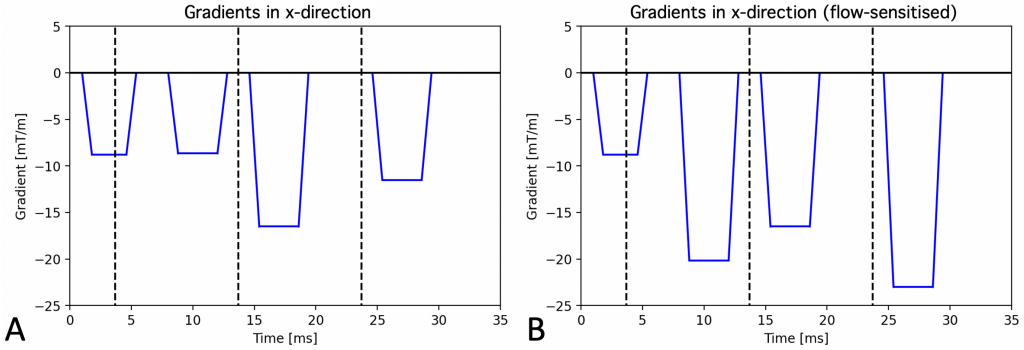

Figure 3.19: Comparison of the gradients in the x-direction between the standard and flow-sensitised STEAM sequences. Sequence parameters: TE = 20 ms, TM = 10 ms, δL = 13 mm. [A] shows the gradients along the x-axis used in the standard STEAM sequence. [B] shows the gradients used in the flow-sensitised sequence. The first and the final crusher gradients were increased in magnitude. Note that the first crusher gradient is smaller than the final gradient since it accounts for the effect of the slice selection gradient after the initial RF pulse.

The considerations for modifying the gradients applied along the y-axis are analogous to those applied along the x-axis. The first crusher gradient is smaller than the third since

the part of the slice selection gradient applied before the second RF pulse must be considered (Figure 3.20). An increase in the magnitude of the third crusher gradient from −11.5 mT/m to −23.0 mT/m leads to an increase in flow sensitivity by a factor of 2.04. The magnitude of the flow-sensitised first crusher gradient for the chosen voxel size must be set to −20.1 mT/m to rephase the nuclei at the end of the sequence. As mentioned above, the factor does not depend on the echo time. However, changing the mixing time has a minute influence on the factor. The factor decreases slightly to 2.01 for mixing times of 80 ms.

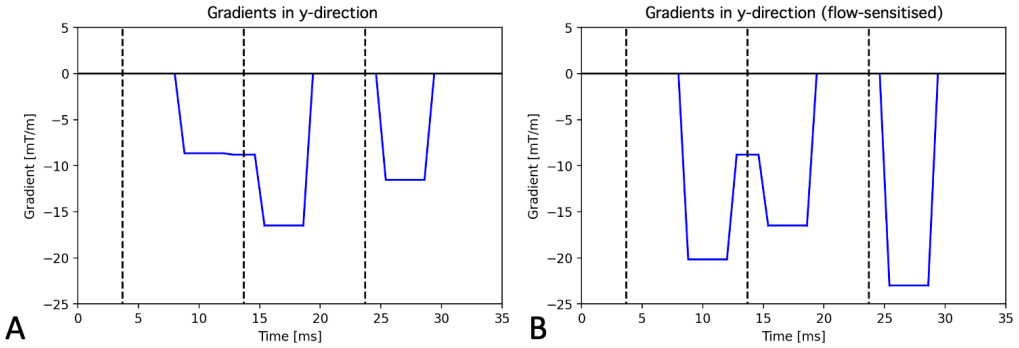

Figure 3.20: Comparison of the gradients in the y-direction between the standard and flow-sensitised STEAM sequences. Sequence parameters: TE = 20 ms, TM = 10 ms, δL = 13 mm. [A] shows the gradients along the y-axis used in the standard STEAM sequence. [B] shows the gradients used in the flow-sensitised sequence. The first and the final crusher gradients were increased in magnitude. The plateau between the first and second crusher gradient represents the slice selection gradient along the y-axis and is unchanged.

In the case of the gradients along the z-axis, an increase in the first crusher gradient from −11.5 mT/m to −23.0 mT/m and a corresponding increase in the third crusher gradient to −20.1 mT/m increases the flow sensitivity by a factor of 2.04 (Figure 3.21). Again, this factor is independent of the echo time and changing the mixing time influences the factor only slightly. As with the flow sensitivity along the y-axis, the factor decreases to 2.01 for mixing times of 80 ms.

Table 3.4 summarises the flow-sensitised STEAM sequence parameters.

3.4 Data analysis of the phantom and in vivo measurements

The following paragraphs show how the data acquired in the experiments was analysed. This account entails presenting the workflow employed and listing the computer programs used for data processing and analysis.

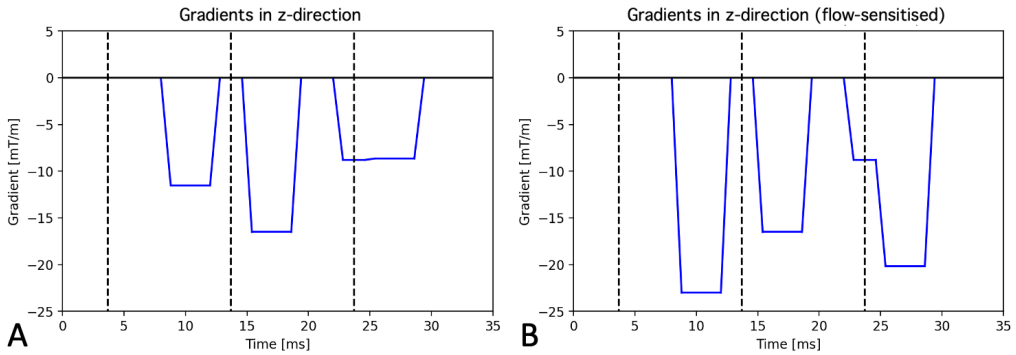

Figure 3.21: Comparison of the gradients in the z-direction between the standard and flow-sensitised STEAM sequences. Sequence parameters: TE = 20 ms, TM = 10 ms, δL = 13 mm. [A] shows the gradients along the z-axis used in the standard STEAM sequence. [B] shows the gradients used in the flow-sensitised sequence. The first and the final crusher gradients were increased in magnitude. The plateau attached to the left side of the third crusher gradient represents the slice selection gradient along the z-direction and remains unchanged.

Table 3.4: Overview of the gradients used in the flow-sensitised STEAM sequence. The nomenclature of the gradients matches the nomenclature used in Chapter 3 (Figure 3.5). The row labelled ”standard” lists the values for the gradients used in the sequence provided by the manufacturer. The row labelled ”flow-sensitised” lists the values of the gradients used in the flow-sensitised sequence.

X-direction	SSG	CX1	CX2	CX3
Standard [mT/m]	−8.8	−8.7	−16.5	−11.5
Flow-sensitised [mT/m]	−8.8	−20.1	−16.5	−23.0
Y-direction	CY1	SSG	CY2	CY3
Standard [mT/m]	−8.7	−8.8	−16.5	−11.5
Flow-sensitised [mT/m]	−20.1	−8.8	−16.5	−23.0
Z-direction	CZ1	CZ2	SSG	CZ3
Standard [mT/m]	−11.5	−16.5	−8.8	−8.7
Flow-sensitised [mT/m]	−23.0	−16.5	−8.8	−20.1

The data were exported from the MRI scanner in the Siemens DICOM format to determine the signal amplitudes. The files were imported into jMRUI (Version 5.2) running on a Windows 10 (64 Bit) computer [20]. For the quantification of the spectra, the AMARES

algorithm provided in jMRUI was used [132]. AMARES is a non-linear least-squares quantitation algorithm [132]. The algorithm also provided automatic zero- and first-order phase correction of the spectra. In rare cases, the phase correction was inaccurate and, therefore, performed manually.

Afterwards, the spectral data were exported in a plain text format using jMRUI. The conversion of the plain text into the Excel Workbook format was unreliable. Therefore, LibreOffice Calc (Version 4.2.3.3) was used for the conversion into the Excel Workbook format. The plots of the spectra were then created with Microsoft Excel for Mac (Version 16.0). As jMRUI did not correctly display the frequency corresponding to the peaks, the water peak was set to approximately 4.7 ppm (the usual position for water). Further, the MRI scanner console also showed the spectra' peaks at 4.7 ppm. The Matplotlib library of Python (Version 3.9.7, 64 Bit) was utilised to create graphs comparing peak amplitudes.

3.5 Simulation of BOLD-related phase-shift effects in ^{1}H spectroscopy

In addition to the gradient-induced phase-shift effects, the simulation of BOLD-related phase-shift effects represents the second large part of this thesis. Subsection 2.7.8 provided a comprehensive overview of the relationship between the BOLD effect and flow, laying the foundation for simulating the BOLD-related phase-shift effects. This section elucidates the methodology employed to model the susceptibility-induced phase shift in PRESS and STEAM sequences. For this purpose, two models were developed. Analogous to Section 3.1, exemplary PRESS and STEAM sequences serve to illustrate the approach. For the simulation, assumptions about the vessel geometry and flow velocity were made. In vivo, different vessel geometries and flow velocities occur, likely leading to highly variable BOLD-related phase-shift effects. Therefore, different conditions were simulated. The general results of the simulations are presented in Chapter 4 and discussed in Chapter 5.

Here, a brief account of the outline of this section is given. The first subsection presents a compilation of physiological parameters that serve as the foundation for the calculations. The two following subsections introduce Model 1 and 2. As Model 2 is more comprehensive than Model 1, Model 2 is used to simulate the BOLD-related phase-shift effects in ^{1}H spectroscopy. However, Model 1 plays a vital role in elucidating the underlying principles and serves as a basis for Model 2. Subsequently, Model 2 is applied to calculate the phase shift expected in an exemplary PRESS sequence. In the last subsection, Model 2 is applied to an exemplary STEAM sequence.

3.5.1 Parameters used to model BOLD-related phase-shift effects

Table 3.5 lists the parameters that are used for modelling the BOLD-related phase-shift effects. Some assumptions concerning the values for χ_{do} and Hct must be made to gain insight into the phenomenon. These two parameters are subject to variation in humans. Therefore, average values published in the literature were used [9, 56, 77, 139]. Values for the oxygenation level (SO_2) show huge variations depending on the vein under consideration. B_0 is assumed to be 3 T since a 3 T scanner was used to perform the experiments.

Table 3.5: Parameters used for modelling BOLD-related phase-shift effects in MRS. Note that the volume susceptibility in SI units is used for the calculations. In the literature, CGS units and molar susceptibilities are encountered frequently. The values for volume susceptibility published by Weisskoff [139] and Spees [122] were converted from CGS units to SI units using the factor of 4 π.

Parameter	Value	Reference
Hct	$0.40\ (40\%)$	Herold et al. [56]
SO_2	$0.65\ (65\%)$	Li et al. [77]
χ_{do}	$2.26 \cdot 10^{-6}$	Weisskoff et al. [139], Spees et al. [122]
B_0	$3.0\ T$	assumption
γ	$2.675 \cdot 10^8\ \frac{rad}{s\,T}$	Bloembergen et al. [9]

3.5.2 Model 1 – discrete bend

Basics of Model 1 A simplified scenario is considered at first to gain insight into the phenomenon. It is assumed that a curved vessel consists of two straight cylinders connected at a 45° angle. This angle is chosen arbitrarily. Figure 3.22 provides an example of such a geometry. A flowing ^{1}H nucleus (e.g. contained in a water molecule) will move through this system while a sequence is applied. In this simplified model, it is further assumed that a spin echo sequence with a 180°-pulse is used to refocus the nuclei. The flowing molecule will be at the junction of the cylinders the moment the refocusing 180°-pulse is applied (Figure 3.23). Further, the sequential movement of the nucleus is depicted in Figure 3.24.

Magnetic field and sequence design In Model 1, the average field difference between blood inside a curved vein and the surrounding tissue (ΔB) depends on the orientation of

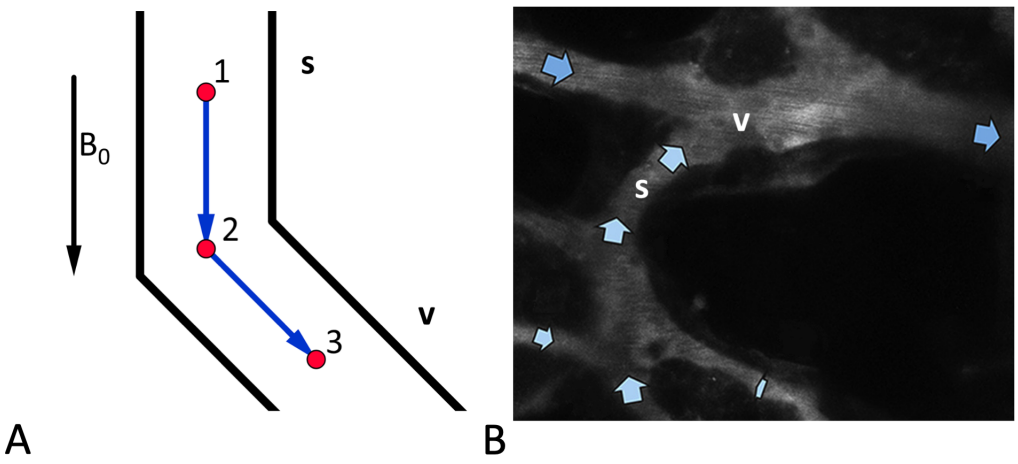

Figure 3.22: Geometry of Model 1. [A] The figure depicts the geometry of Model 1, where cylinders represent a vessel that is bent at an angle of 45°. However, this model is simplified as in vivo bends are more homogeneous. An ^{1}H nucleus (e.g. contained in a water molecule, red dot) flows through the bend. During the motion of the ^{1}H nucleus, a simple spin echo sequence is applied. It consists of an initial 90°-pulse and a refocusing 180°-pulse. At the time (1), the spin echo sequence starts with the 90°-pulse. At the time (2), the nucleus is at the level of the 45° bend. (2) is also when the refocusing 180°-pulse is applied. At the time (3), the FID is recorded. The upper part of the vessel is assumed to be aligned with B_0. Further, the two cylinders may also represent the flow of a peripheral vessel (like a sinusoid (s)) into a more central vessel (like a venule (v)) if they meet at an angle of 45°. [B] In vivo two-photon image of vessels in the bone marrow. Deoxygenated blood flows from a terminal sinusoid (s) into a venule (v). The arrows show the direction of flow. The angle between both is roughly 45°, representing a situation akin to the geometry used in Model 1. Adapted from Bixel et al. [7].

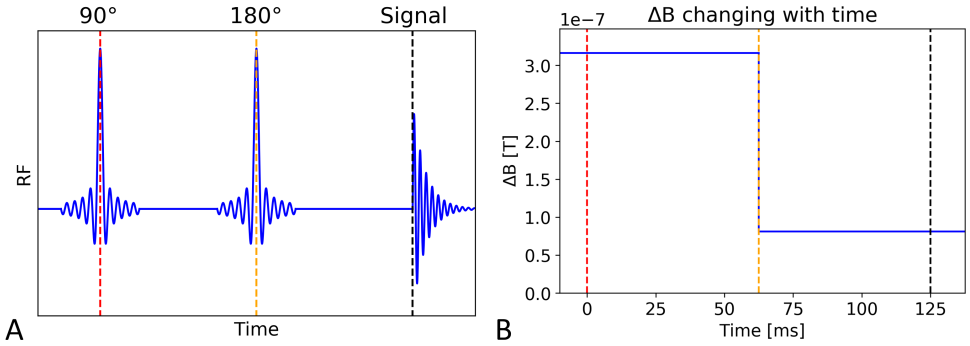

Figure 3.23: Spin echo sequence and magnetic field experienced by the ^{1}H nucleus in Model 1. [A] The simple design of the spin echo sequence consists of an initial 90°-pulse and a refocusing 180°-pulse. [B] The magnetic field the ^{1}H nucleus experiences in Model 1 is shown. Between the start of the sequence (dotted red line) and the 180°-pulse (dotted orange line), the ^{1}H nucleus flows in the upper part of the vessel, which is aligned with B_0. The ^{1}H nucleus flows through the lower part of the vessel in the interval between the 180°-pulse and the detection of the FID (dotted black line). Therefore, ΔB changes in the middle of the sequence from $3.16 \cdot 10^{-7}$ T to $8.11 \cdot 10^{-8}$ T assuming the parameters listed in Tables 3.5 and 3.6.

the cylinders relative to the main magnetic field (Subsection 2.7.7). It is assumed that the cylinder representing the upper/first part of the vessel is aligned with the main magnetic field. In Model 1, the nucleus experiences two fields depending on whether the nucleus is in the upper/first or lower/second part of the vessel. The magnetic fields can be calculated using Equation 2.28. In the middle of the sequence, when the nucleus is at the junction, and the 180°-pulse is applied, the dephasing will be inverted due to the 180°-pulse.

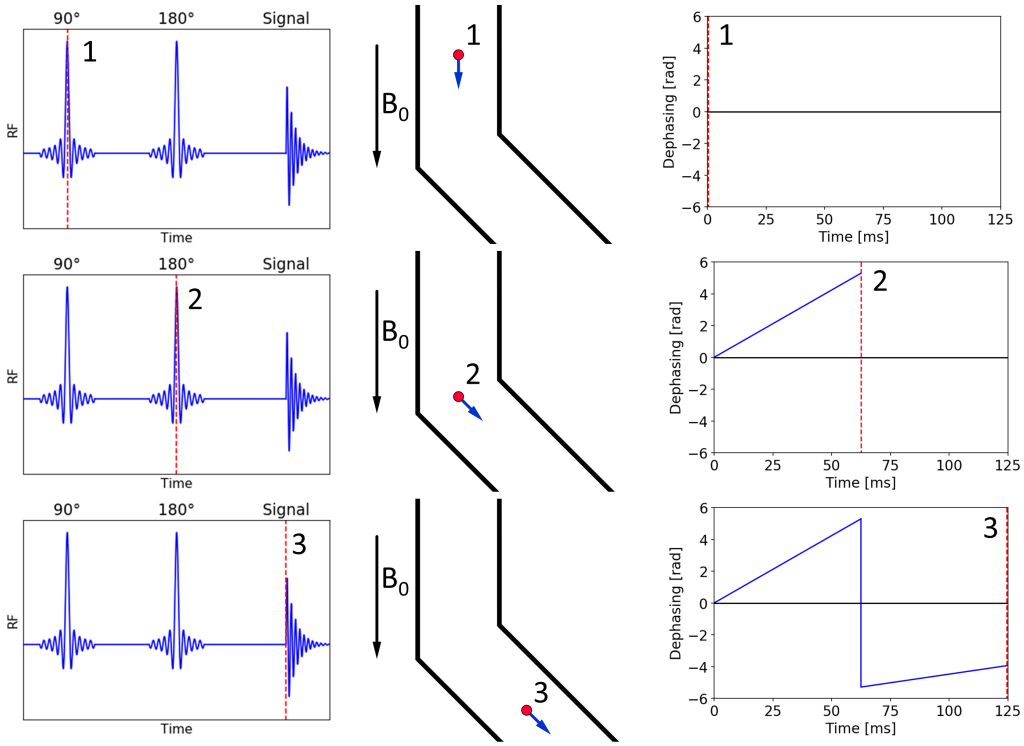

Figure 3.24: Dephasing occurring in Model 1. The situation is identical to the one depicted in Figures 3.22 and 3.23. The first column displays the spin echo sequence, with the dotted red line indicating the time point of the corresponding row. The second column represents the position of the nucleus at this time, while the third column shows the resulting dephasing during the sequence. At the time (1), the sequence starts, and the nucleus has a phase of zero. Between the 90°-pulse and the application of the 180°-pulse at the time (2), the nucleus has gained phase due to the strong magnetic field inside the sinusoid ($\Delta B = 3.16 \cdot 10^{-7}$ T, Figure 3.23). The 180°-pulse then reverses this phase gain. The phase gain between (2) and the measurement at the time (3) is smaller than the previous phase gain between (1) and (2) because of the weaker magnetic field ($\Delta B = 8.11 \cdot 10^{-8}$ T). As a result, a net phase shift occurs.

Parameters used in Model 1 With the above information and formulae, it is possible to evaluate the dephasing that is expected in Model 1. Further assumptions about the parameters and the flow velocity must be made. Those are listed in Table 3.6.

Table 3.6: Parameters used in Model 1. A flow velocity (0.5 mm/s) close to the average flow velocity in the venules of bone marrow was chosen (Subsection 2.5.2). The echo time and other corresponding parameters were chosen as they represent intermediately long values. *In the exemplary calculations performed in Model 1, an angle of $44.76°$ was used instead of $45°$ for technical reasons. Notably, Model 2 was designed with a vessel radius of curvature measuring 80 μm. It is reasonable to use the same echo time and flow velocity to ensure comparability between both models. Using the same echo time and flow velocity in Model 2 results in $44.76°$ of motion. Consequently, adopting the angle of $44.76°$ in Model 1 was a deliberate measure to enhance the comparability between the two models.

Parameter	Flow velocity	Angle	TE	t_{90}	t_{180}	$t_{measure}$
Value	$0.5\ \frac{mm}{s}$	$44.76°$ $(45°)$*	$125\ ms$	$0\ ms$	$62.5\ ms$	$125\ ms$

Calculation of the phase shift Here, the dephasing created in the example is calculated to illustrate Model 1. As shown in Figure 3.23, the upper and the lower part of the vessel differ in ΔB. Using Equations 2.27 and 2.28, ΔB can be determined the following way:

$$\Delta B = \frac{\chi_{do}\, Hct\, (1 - SO_2)\, B_0}{2} \left(\cos^2(\theta) - \frac{1}{3} \right) \tag{3.226}$$

Here, θ is the angle between the vessel and B_0. As described in the outline of Model 1, θ is assumed to be 0° for the upper part and 45° for the lower part of the vessel. ΔB inside the upper part of the vessel is called ΔB_1. In Model 1 ΔB_1 is:

$$\Delta B_1 = \frac{2.26 \cdot 10^{-6}\, 0.40\, (1 - 0.65)\, 3\, T}{2} \left(\cos^2(0°) - \frac{1}{3} \right) \tag{3.227}$$

$$\Delta B_1 = 3.16 \cdot 10^{-7}\, T \tag{3.228}$$

ΔB inside the lower part of the vessel is called ΔB_2. In Model 1 ΔB_2 is:

$$\Delta B_2 = \frac{2.26 \cdot 10^{-6}\, 0.40\, (1 - 0.65)\, 3\, T}{2} \left(\cos^2(44.76°) - \frac{1}{3} \right) \tag{3.229}$$

$$\Delta B_2 = 8.11 \cdot 10^{-8}\, T \tag{3.230}$$

Since the 180°-pulse is applied precisely in the middle of the sequence, and TE is 125 ms, an ^{1}H nucleus is subject to both values of ΔB for 62.5 ms. Notably, the phase gain acquired while the nucleus is in the upper part of the vessel is inverted by the 180°-pulse. The phase gain during the first half of the sequence $\Delta\varphi_1$ and during the latter half $\Delta\varphi_2$ are calculated below.

The nuclei inside the vessels gain phase because they experience higher Larmor frequencies than those not subject to BOLD-related phase-shift effects. The difference in Larmor frequencies between the interior and exterior of the vessel, $\Delta\omega_f$, is attributable to

the difference in ΔB, which can be evaluated using Equation 2.8:

$$\Delta\omega_f = \gamma \cdot \Delta B \tag{3.231}$$

Since the phase gain $\Delta\varphi$ is the product of angular (Larmor) frequency and time, it can be calculated:

$$\Delta\varphi = \Delta\omega_f \cdot t \tag{3.232}$$

With the combination of Equations 3.231 and 3.232 the values for $\Delta\varphi_1$ and $\Delta\varphi_2$ can be determined for Model 1.

$$\Delta\varphi_1 = \gamma \cdot \Delta B_1 \cdot (t_{180} - t_{90}) \tag{3.233}$$

$$\Delta\varphi_1 = 2.675 \cdot 10^8 \frac{rad}{s\,T}\, 3.16 \cdot 10^{-7}\, T \cdot (0.0625\, s - 0.0000\, s) \tag{3.234}$$

$$\Delta\varphi_1 = 5.28\, rad \tag{3.235}$$

$$\Delta\varphi_2 = \gamma \cdot \Delta B_2 \cdot (t_{measure} - t_{180}) \tag{3.236}$$

$$\Delta\varphi_2 = 2.675 \cdot 10^8 \frac{rad}{s\,T}\, 8.11 \cdot 10^{-8}\, T \cdot (0.1250\, s - 0.0625\, s) \tag{3.237}$$

$$\Delta\varphi_2 = 1.36\, rad \tag{3.238}$$

Taking into account the effect of the 180°-pulse, the total dephasing is:

$$\Delta\varphi_{total} = \Delta\varphi_2 - \Delta\varphi_1 \tag{3.239}$$

$$\Delta\varphi_{total} = 1.36\, rad - 5.28\, rad \tag{3.240}$$

$$\Delta\varphi_{total} = -3.92\, rad \tag{3.241}$$

Figure 3.24 illustrates this calculation. Model 1 predicts a significant phase shift for the chosen parameters. In the following subsection, a more refined model is developed (Model 2).

3.5.3 Model 2 – bend with a circular arc

Basics of Model 2 Model 2 is an extension of the previously introduced Model 1, but it aims to achieve a more realistic depiction of the phenomenon. In contrast to the abrupt bend in Model 1, Model 2 incorporates a smoothly curving bend that can be approximated using a circular arc (Figure 3.25). Specifically, the ^{1}H nucleus flowing through a bend

is assumed to rotate around a central axis outside the vein, requiring modifications to the formulae used in Model 1. In Model 2, the angle θ is no longer fixed but becomes a function of time due to the arc-like trajectory of the flowing nucleus. The new formula is given by:

$$\theta(t) = \omega_t \cdot t + \theta_0 \tag{3.242}$$

Here, θ_0 is the initial angle of the nucleus relative to B_0 and ω_t the angular velocity of the nucleus flowing through the bend.

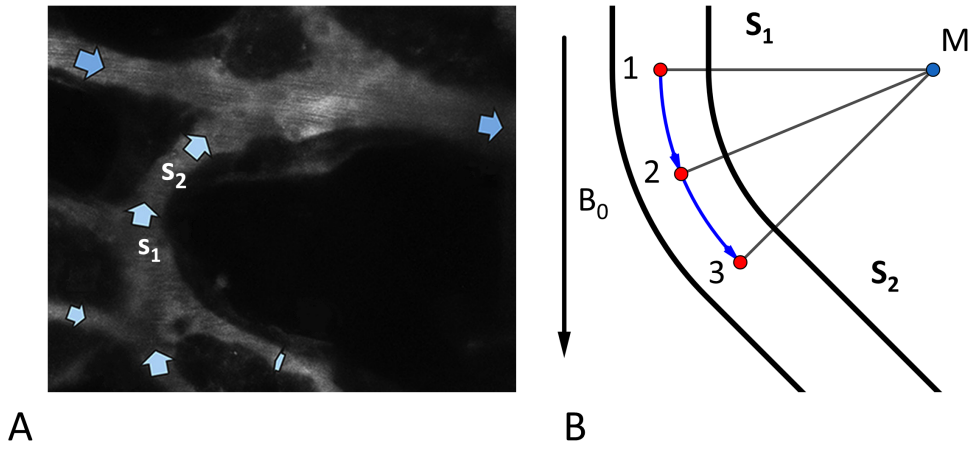

Figure 3.25: Geometry of Model 2. [A] A bend of a terminal sinusoid that delivers deoxygenated blood to a venule. The first part of the sinusoid (s_1) stands approximately at a 45° angle to the second part (s_2). The passage from (s_1) to (s_2) is not sudden but continuous. Adapted from Bixel et al. [7]. [B] A geometric representation of [A]. The bend between (s_1) and (s_2) is modelled by a circular arc. The centre of the arc is depicted and labelled (M). An ^{1}H nucleus (shown in red) moves on a circular path through the bend from position (1) to (2) and finally to (3). As in Model 1, the sequence will start at (1) and end at (3). The refocusing pulse is applied at the time (2). The magnetic field B_0 is aligned with s_1.

Flow and geometry in Model 2 The model assumes a revolving motion of the nucleus in the curve about a central axis associated with this curve. Equation 3.242 represents the equation of motion in Model 2. While θ_0 depends on the varying geometry of the vein under consideration, ω_t can be calculated when the flow velocity (v) and the radius of curvature (r) are known. The corresponding formula is:

$$\omega_t = \frac{v}{r} \tag{3.243}$$

Magnetic field and sequence design In Model 2, the magnetic field experienced by the nucleus changes due to the varying angle θ. This is the primary difference from Model 1. Although the magnetic field at the sequence's beginning and end are the same as in Model 1, the passage between those values is homogeneous. ΔB can be calculated by combining the Equations 3.226 and 3.242. This yields:

$$\Delta B = \frac{\chi_{do}\, Hct\, (1 - SO_2)\, B_0}{2} \left(\cos^2(\omega_t \cdot t + \theta_0) - \frac{1}{3} \right) \tag{3.244}$$

The sequence is not changed in Model 2 (compared to Model 1) and is depicted in Figure 3.26A. Figure 3.26B displays ΔB during the sequence used in Model 2.

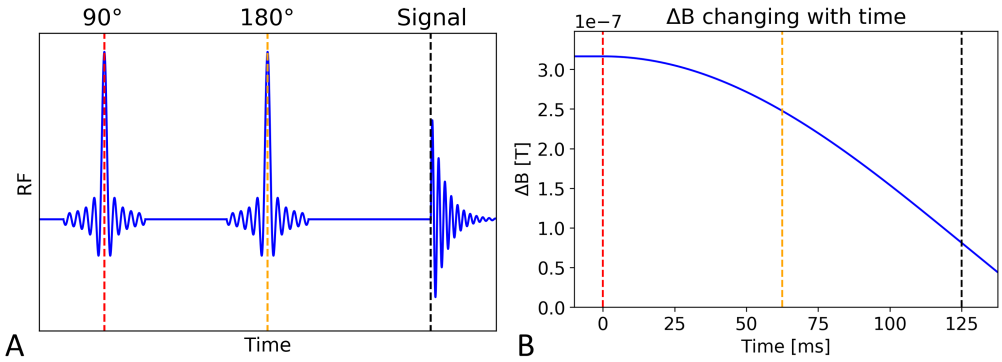

Figure 3.26: Spin echo sequence and magnetic field experienced by the ^{1}H nucleus in Model 2. [A] Design of the spin echo sequence for Model 2. The design is equal to the one used in Model 1, allowing a comparison between both models. [B] Magnetic field experienced by a flowing nucleus in Model 2. The coloured lines show the timing of corresponding elements of the sequence. The initial and terminal values of ΔB correspond to the values in Model 1. The curve itself is given by Equation 3.244.

Parameters used in Model 2 The radius of curvature was chosen to be 80 μm following the information about the microvasculature provided by Bixel et al. [7]. The flow velocity and all other conditions are equal to those listed in the corresponding section of Model 1 (Table 3.6). The otherwise identical conditions serve to make both models comparable.

Mathematical derivation Since the magnetic field changes with time in Model 2, the underlying mathematical framework is somewhat different. Equation 2.8 is the basis that allows relating the magnetic field inside the vein (ΔB) with an associated gain or loss in

phase ($\Delta\varphi$) when modified the following way:

$$\omega_L = \gamma\,\Delta B \qquad | \int dt \tag{3.245}$$

$$\int \omega_L\,dt = \gamma \int \Delta B\,dt \qquad | \int \omega_L\,dt = \Delta\varphi \tag{3.246}$$

$$\Delta\varphi = \gamma \int \Delta B\,dt \tag{3.247}$$

This transformation is possible because the integral of the Larmor frequency with respect to time is the phase gain. Subsequently, Equation 2.28 is used to model the magnetic field within the vein.

$$\Delta\varphi = \gamma \int \Delta B\,dt \mid \Delta B = \frac{\Delta\chi}{2}\left(\cos^2(\theta) - \frac{1}{3}\right) B_0 \tag{3.248}$$

$$\Delta\varphi = \gamma \int \frac{\Delta\chi}{2}\left(\cos^2(\theta) - \frac{1}{3}\right) B_0\,dt \tag{3.249}$$

Since the susceptibility inside the vein is known from Equation 2.27, Equation 3.249 can be modified as follows:

$$\Delta\varphi = \frac{\chi_{do}\,Hct\,(1 - SO_2)\,\gamma\,B_0}{2} \int \cos^2(\theta) - \frac{1}{3}\,dt \tag{3.250}$$

Equation 3.250 is the basis of Model 2. The parameters of this function can be changed according to the geometry of the vein. The maximal dephasing will occur when the bend lays within a plane that is parallel to B_0. This is the case in Model 2. Equation 3.242 can be used in conjunction with Equation 3.250 to yield the dephasing of the nucleus in Model 2.

$$\Delta\varphi = \frac{\chi_{do}\,Hct\,(1 - SO_2)\,\gamma\,B_0}{2} \int \cos^2(\omega_t \cdot t + \theta_0) - \frac{1}{3}\,dt \tag{3.251}$$

Assumptions and formalism In addition to the assumption that a vein can be modelled by an infinitely long cylinder for a straight segment of a vein, the above also assumes that this holds true within a bent vessel. The COMSOL simulations shown in Figure 3.27 and simulations done by Li et al. provide confidence in the validity of the assumption [77].

For simplicity, in Equation 3.251, the term in front of the integral can be summarised for a given set of initial conditions and will be called k. The term k is considered to be constant in this model. However, SO_2 can be subject to variations in capillaries where deoxygenation of haemoglobin occurs. B_0 and the haematocrit can be subject to minute

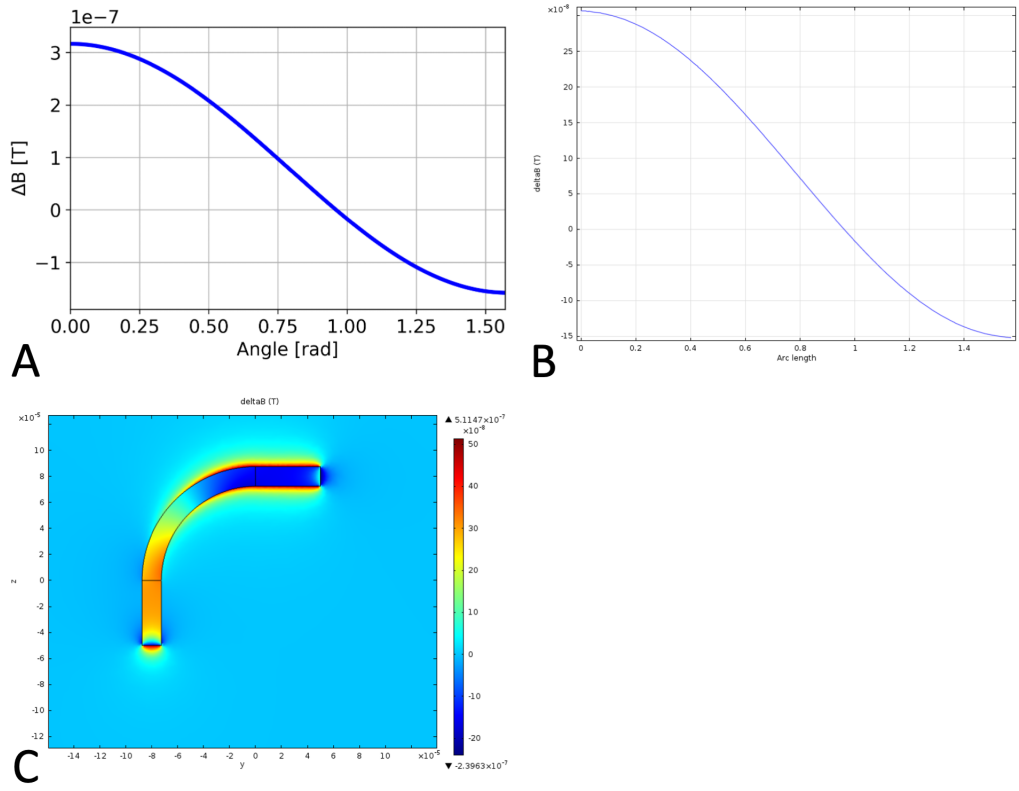

Figure 3.27: Simulation of the magnetic field inside a bent vein using COMSOL. Here, a vessel with a 90° bend, aligned with B_0 at one end, is considered. [A] depicts the local magnetic field of a specific point inside a vessel as a function of the angle relative to B_0. [A] is based on the assumption that each point can be modelled as part of an infinitely long cylinder, an assumption made in Model 2. A COMSOL simulation of the same scenario was performed to validate this assumption. Figure [B] depicts this simulation, which serves as a gold standard for the magnetic field inside the vessel. A comparison of [A] and [B] reveals a good agreement between both, confirming the validity of the assumption. [C] shows the rendering of the vessel and the magnetic field strengths along the vessel. All three diagrams use the same vessel geometry and parameters: diameter of the vessel = 15 μm, radius of curvature = 80 μm, $B_0 = 3.0$ T, $\Delta\chi = 3.164 \cdot 10^{-7}$. The author conducted the simulations in [A], while Sina Rück kindly provided the COMSOL simulations and the diagrams [B] and [C].

changes as well. Using k Equation 3.251 can be written as:

$$\Delta\varphi = k \int \cos^2(\omega_t \cdot t + \theta_0) - \frac{1}{3}\, dt \tag{3.252}$$

$$k = \frac{\chi_{do}\, Hct\, (1 - SO_2)\, \gamma\, B_0}{2} \tag{3.253}$$

Equation 3.243 is used to calculate ω_t.

Calculation of the phase-shift Here, the dephasing created in the example is calculated to illustrate Model 2 (Figure 3.28). Again, the contributions of each half of the sequence,

in this case, $\Delta\varphi_{s1}$ and $\Delta\varphi_{s2}$, will be calculated separately. Equations 3.252 and 3.253 will be used for this purpose. k is equal for both cases.

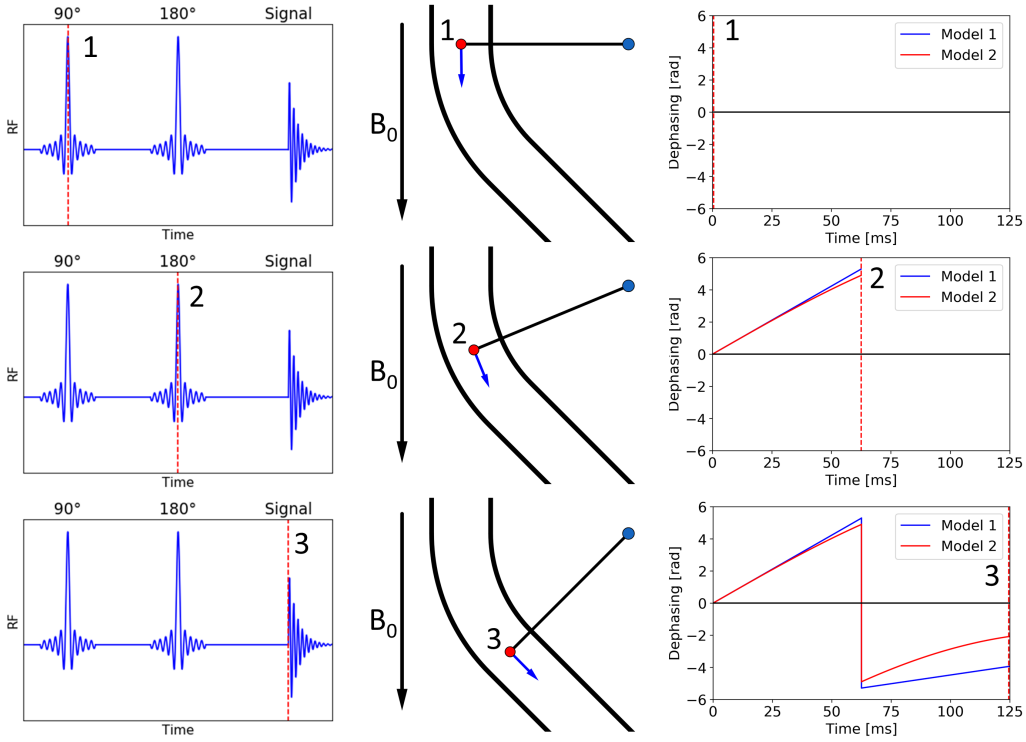

Figure 3.28: Dephasing occurring in Model 2. In the first column, the spin echo sequence is depicted. The numbers and the position of the dotted red line correspond to the time each picture in a given row shares. The second column depicts the position of the nucleus within the bend. In the third column, the associated dephasing is compared to the dephasing observed in Model 1. The nucleus starts moving at (1) and is subject to a 180°-pulse at (2). It continues to move to (3) when the measurement is performed. The 180°-pulse inverts the initial dephasing. During the first half of the sequence, Model 1 and 2 lead to comparable results (this can be explained by the slow decline in the cosine-squared function around t = 0 ms, Equation 2.28). In contrast, the difference between Model 1 and 2 is larger during the second half.

$$k = \frac{\chi_{do}\, Hct\, (1 - SO_2)\, \gamma\, B_0}{2} \tag{3.254}$$

$$k = \frac{2.26 \cdot 10^{-6}\, 0.40\, (1 - 0.65)\, 2.675 \cdot 10^{8}\, \frac{rad}{s\,T}\, 3\, T}{2} \tag{3.255}$$

$$k = 127\, \frac{rad}{s} \tag{3.256}$$

$$\Delta\varphi_{s1} = k \int_{t_{90}}^{t_{180}} \cos^2(\omega_t \cdot t + \theta_0) - \frac{1}{3}\, dt \tag{3.257}$$

$$\Delta\varphi_{s1} = 127\, \frac{rad}{s} \int_{0}^{62.5ms} \cos^2(6.25 \frac{rad}{s} \cdot t + 0°) - \frac{1}{3}\, dt \tag{3.258}$$

$$\Delta\varphi_{s1} = 4.90\, rad \tag{3.259}$$

$$\Delta\varphi_{s2} = k \int_{t_{180}}^{t_{measure}} \cos^2(\omega_t \cdot t + \theta_0) - \frac{1}{3}\, dt \tag{3.260}$$

$$\Delta\varphi_{s2} = 127\, \frac{rad}{s} \int_{62.5ms}^{125ms} \cos^2(6.25 \frac{rad}{s} \cdot t + 0°) - \frac{1}{3}\, dt \tag{3.261}$$

$$\Delta\varphi_{s2} = 2.83\, rad \tag{3.262}$$

Taking into account the effect of the 180°-pulse, the total dephasing in this scenario can be calculated to be:

$$\Delta\varphi_{total} = \Delta\varphi_{s2} - \Delta\varphi_{s1} \tag{3.263}$$

$$\Delta\varphi_{total} = 2.83\, rad - 4.90\, rad \tag{3.264}$$

$$\Delta\varphi_{total} = -2.07\, rad \tag{3.265}$$

3.5.4 BOLD-related phase-shift effects in PRESS

In the previous subsections, a simple spin echo sequence was used to show the basic principles of how BOLD-related phase-shift effects in a curved vein lead to signal dephasing. A central argument of this thesis is that this mechanism also affects ^{1}H spectroscopy. However, the mathematical framework must be modified as MRS sequences are more complex than the above spin echo sequence. Therefore, the calculations are adjusted to represent PRESS and STEAM sequences. In this subsection, a model for PRESS sequences is developed. Since Model 2 is more realistic than Model 1, it is used as a basis together with Equations 3.252 and 3.253. This model will be applied to an exemplary PRESS sequence to illustrate the method.

The following paragraphs delineate the application of Model 2 in the context of PRESS sequences. Figure 3.29 visualises the phase gain due to the BOLD-related phase-shift effects. In PRESS sequences, the two 180°-pulses act to invert the dephasing that has taken place before the pulses have been applied. The dephasing of the nuclei in a curved vein starts right after the initial 90°-pulse (at the time t_{90}) and continues until the first 180°-pulse inverts the dephasing at the time $t_{1,180}$. Between the first and the second 180°-pulse, the dephasing of the nuclei resumes. The second 180°-pulse again inverts the dephasing at the time $t_{2,180}$. In the time between the second 180°-pulse and the measurement at the

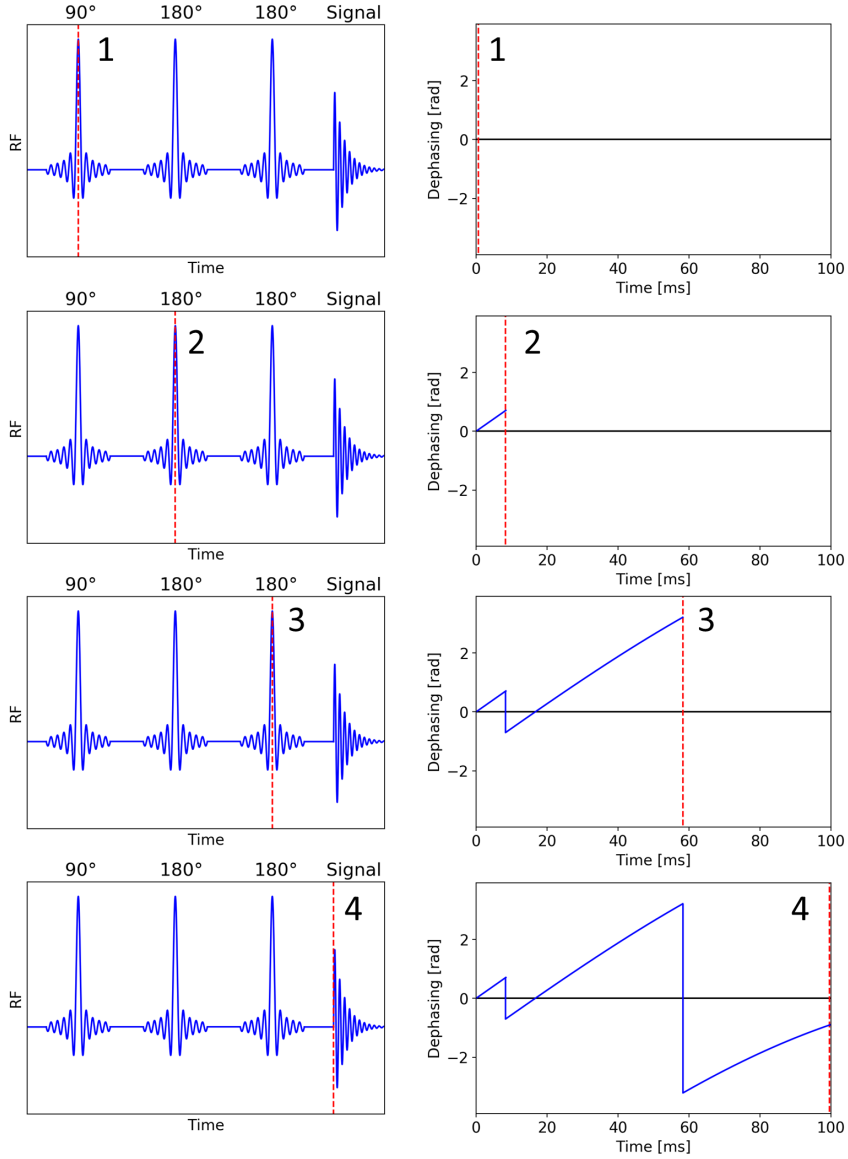

Figure 3.29: Simulation of BOLD-related phase-shift effects in PRESS using Model 2. In the left column, the RF pulses of the PRESS sequence are depicted. The right column shows the dephasing over time. From top to bottom, the sequence progresses. The dotted red line marks the point in time. At the time (1), the 90°-pulse is applied, and the dephasing starts. The first 180°-pulse inverts the dephasing at time (2). Between (2) and (3), the dephasing continues. The second 180°-pulse inverts the dephasing again at time (3). The final dephasing occurs between (3) and (4). The FID is recorded at time (4).

time $t_{measure}$, the nuclei continue to gain phase. Considering the combined effects of the inversions, the time between $t_{1,180}$ and $t_{2,180}$ diminishes the phase gain, and the other two

intervals increase the phase gain. Therefore, the total phase gain ($\Delta\varphi_{\text{total}}$) is given by:

$$\Delta\varphi_{total} = \Delta\varphi_{t_{90}-t_{1,180}} - \Delta\varphi_{t_{1,180}-t_{2,180}} + \Delta\varphi_{t_{2,180}-t_{measure}} \tag{3.266}$$

$\Delta\varphi_{t_{90}\text{-}t_{1,180}}$ represents the phase gain between t_{90} and $t_{2,180}$. $\Delta\varphi_{t_{1,180}\text{-}t_{2,180}}$ is the phase gain between $t_{1,180}$ and $t_{2,180}$. $\Delta\varphi_{t_{2,180}\text{-}t_{measure}}$ is the phase gain between $t_{2,180}$ and $t_{measure}$.

$$\Delta\varphi_{t_{90}-t_{1,180}} = k \cdot \int_{t_{90}}^{t_{1,180}} \cos^2(\omega_t \cdot t + \theta_0) - \frac{1}{3}\, dt \tag{3.267}$$

$$\Delta\varphi_{t_{1,180}-t_{2,180}} = k \cdot \int_{t_{1,180}}^{t_{2,180}} \cos^2(\omega_t \cdot t + \theta_0) - \frac{1}{3}\, dt \tag{3.268}$$

$$\Delta\varphi_{t_{2,180}-t_{measure}} = k \cdot \int_{t_{2,180}}^{t_{measure}} \cos^2(\omega_t \cdot t + \theta_0) - \frac{1}{3}\, dt \tag{3.269}$$

The following example will illustrate the method used to model the BOLD-related phase-shift effects in curved veins in PRESS (Figure 3.29). The effect a PRESS sequence has on flowing blood in a curved vein depends on the following: (1) the level of oxygenation (SO_2) and the haematocrit of the blood, (2) the geometry of the vessel, (3) the flow velocity of the blood, and (4) the PRESS sequence itself. However, the timing of the RF pulses is the only relevant parameter of the PRESS sequence because the RF pulses determine the timing of the spin echoes. Here, an exemplary PRESS sequence with an echo time of 100 ms is used for illustration. Table 3.7 shows the timing of the RF pulses in this sequence.

Table 3.7: Sequence parameters for the exemplary calculation of BOLD-related phase-shift effects in PRESS.

Parameter	TE	t_{90}	$t_{1,180}$	$t_{2,180}$	$t_{measure}$
Value	$100\ ms$	$0\ ms$	$8.3\ ms$	$58.3\ ms$	$100\ ms$

Several assumptions are made regarding vessel geometry and nucleus flow velocity. However, the values are chosen to approximate venules in bone marrow (Subsection 2.5.2) [7]. These assumptions are listed in Table 3.8.

Equation 3.243 was utilized to calculate ω_t based on the values of radius and flow velocity. θ_0 is chosen to be 0°, meaning that the part of the vessel where the nucleus flows at the start of the sequence is aligned with B_0. With these assumptions and the Equations

Table 3.8: Vessel geometry and flow velocity for the exemplary calculation of BOLD-related phase-shift effects in PRESS.

Parameter	Radius	Flow velocity	ω_t	θ_0
Value	$80\,\mu m$	$0.5\,\frac{mm}{s}$	$6.25\,\frac{rad}{s}$	$0\,rad$

3.266 to 3.269 the ansatz is:

$$\Delta\varphi_{t_{90}-t_{1,180}} = k \cdot \int_{0\,ms}^{8.3\,ms} \cos^2(6.25\,\frac{rad}{s} \cdot t + 0) - \frac{1}{3}\,dt \tag{3.270}$$

$$\Delta\varphi_{t_{1,180}-t_{2,180}} = k \cdot \int_{8.3\,ms}^{23.3\,ms} \cos^2(6.25\,\frac{rad}{s} \cdot t + 0) - \frac{1}{3}\,dt \tag{3.271}$$

$$\Delta\varphi_{t_{2,180}-t_{measure}} = k \cdot \int_{23.3\,ms}^{30\,ms} \cos^2(6.25\,\frac{rad}{s} \cdot t + 0) - \frac{1}{3}\,dt \tag{3.272}$$

Where k is determined with Equation 3.253:

$$k = \frac{\chi_{do}\,Hct\,(1 - SO_2)\,\gamma\,B_0}{2} \tag{3.273}$$

$$k = \frac{2.26 \cdot 10^{-6}\,0.40\,(1 - 0.65)\,2.675 \cdot 10^8\,\frac{rad}{s\,T}\,3\,T}{2} \tag{3.274}$$

$$k = 127\,\frac{rad}{s} \tag{3.275}$$

Thus, the individual phase shifts are:

$$\Delta\varphi_{t_{90}-t_{1,180}} = 0.702\,rad \tag{3.276}$$

$$\Delta\varphi_{t_{1,180}-t_{2,180}} = 3.914\,rad \tag{3.277}$$

$$\Delta\varphi_{t_{2,180}-t_{measure}} = 2.320\,rad \tag{3.278}$$

The total dephasing that occurred during the PRESS sequence is given by:

$$\Delta\varphi_{total} = \Delta\varphi_{t_{90}-t_{1,180}} - \Delta\varphi_{t_{1,180}-t_{2,180}} + \Delta\varphi_{t_{2,180}-t_{measure}} \tag{3.279}$$

$$\Delta\varphi_{total} = 0.702\,rad - 3.914\,rad + 2.320\,rad \tag{3.280}$$

$$\Delta\varphi_{total} = -0.892\,rad \approx -51^\circ \tag{3.281}$$

Hence, the BOLD-related phase shift leads to a phase shift of approximately 51° for a nucleus inside a curved vein compared to the surrounding tissue for this exemplary STEAM sequence. More general results are given in Section 4.5.

3.5.5 BOLD-related phase-shift effects in STEAM

This section shows how the BOLD-related phase-shift effects in STEAM can be modelled. The method is analogous to the method used to model PRESS sequences and also relies on Model 2 as a basis. Figure 3.30 visualises the phase gain due to the BOLD-related phase-shift effects. In STEAM, the dephasing is only inverted once by the combined effect of the second and third 90°-pulse. The dephasing starts after the initial 90°-pulse at the time $t_{1,90}$. The dephasing continues until the second 90°-pulse is applied at the time $t_{2,90}$. During TM, the nucleus does not gain phase. The third 90°-pulse acts to invert the initially acquired dephasing in combination with the second 90°-pulse. The inversion occurs at the time $t_{3,90}$. Between the application of the third 90°-pulse and the measurement (at the time $t_{measure}$), the nucleus gains phase again. Therefore, the initial phase gain counteracts the final phase gain and will be subtracted.

$$\Delta\varphi_{total} = -\Delta\varphi_{t_{1,90}-t_{2,90}} + \Delta\varphi_{t_{3,90}-t_{measure}} \tag{3.282}$$

$\Delta\varphi_{t_{1,90}\text{-}t_{2,90}}$ represents the phase gain between $t_{1,90}$ and $t_{2,90}$. $\Delta\varphi_{t_{3,90}\text{-}t_{measure}}$ is the phase gain between $t_{3,90}$ and $t_{measure}$. Both can be determined using Equation 3.252:

$$\Delta\varphi_{t_{1,90}-t_{2,90}} = k \cdot \int_{t_{1,90}}^{t_{2,90}} \cos^2(\omega_t \cdot t + \theta_0) - \frac{1}{3}\, dt \tag{3.283}$$

$$\Delta\varphi_{t_{3,90}-t_{measure}} = k \cdot \int_{t_{3,90}}^{t_{measure}} \cos^2(\omega_t \cdot t + \theta_0) - \frac{1}{3}\, dt \tag{3.284}$$

The following example will illustrate the method used to model BOLD-related phase-shift effects in curved veins in STEAM. The calculation of the phase shift for a STEAM sequence is structured like the example of the PRESS sequence above. The same flow velocity and geometry of the vessel are used (Table 3.8). A STEAM sequence with an echo time of 90 ms and a mixing time of 10 ms is used. Table 3.9 lists the corresponding parameters.

Table 3.9: Sequence parameters for the exemplary calculation of BOLD-related phase-shift effects in STEAM.

Parameter	TE	TM	$t_{1,90}$	$t_{2,90}$	$t_{3,90}$	$t_{measure}$
Value	90 ms	10 ms	0 ms	45 ms	55 ms	100 ms

The application of Equations 3.283 and 3.284 yields:

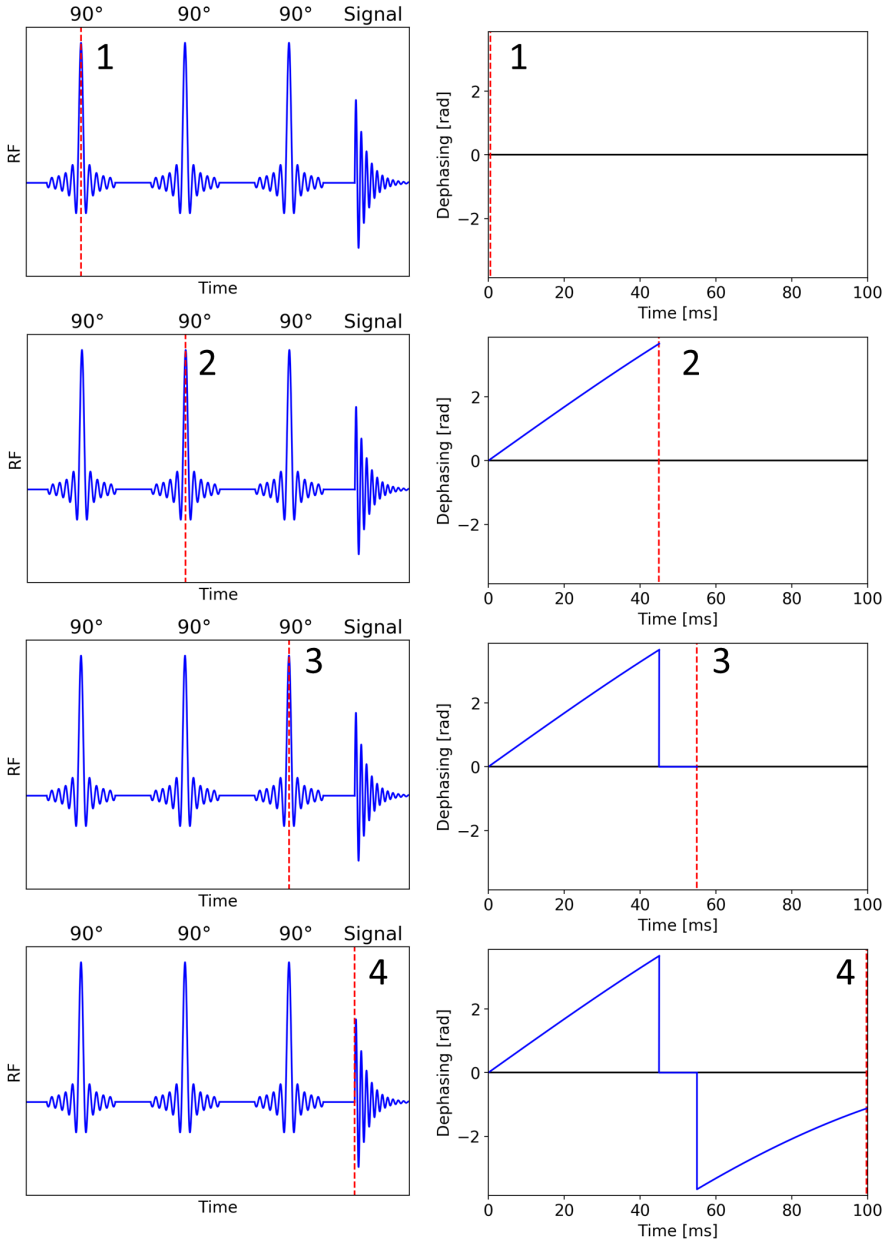

Figure 3.30: Simulation of BOLD-related phase-shift effects in STEAM using Model 2. In the left column, the RF pulses of the STEAM sequence are depicted. The right column shows the dephasing over time. From top to bottom, the sequence progresses. The dotted red line marks the point in time. At the time (1), the first 90°-pulse is applied, and the dephasing starts. The initial dephasing is built between (1) and (2). At the time (2), the mixing time begins, and no relevant dephasing occurs until it ends at (3). The initial dephasing is inverted at time (3) when the third 90°-pulse is applied. The nucleus experiences dephasing again between (3) and (4). The FID is recorded at time (4).

$$\Delta\varphi_{t_{1,90}-t_{2,90}} = k \cdot \int_{0\,ms}^{45\,ms} \cos^2(6.25\,\frac{rad}{s} \cdot t + 0) - \frac{1}{3}\,dt \tag{3.285}$$

$$\Delta\varphi_{t_{3,90}-t_{measure}} = k \cdot \int_{55\,ms}^{100\,ms} \cos^2(6.25\,\frac{rad}{s} \cdot t + 0) - \frac{1}{3}\,dt \tag{3.286}$$

The value of k does not change compared to the model for PRESS sequences (Equation 3.275). Thus, the individual phase shifts are:

$$\Delta\varphi_{t_{1,90}-t_{2,90}} = 3.661\,rad \tag{3.287}$$

$$\Delta\varphi_{t_{3,90}-t_{measure}} = 2.549\,rad \tag{3.288}$$

The total dephasing is:

$$\Delta\varphi_{total} = -\Delta\varphi_{t_{1,90}-t_{2,90}} + \Delta\varphi_{t_{3,90}-t_{measure}} \tag{3.289}$$

$$\Delta\varphi_{total} = -1.11\,rad \approx -64^\circ \tag{3.290}$$

Hence, the BOLD-related phase shift leads to a phase shift of approximately 64° for a nucleus inside a curved vein compared to the surrounding tissue in this example. More general results are given in Section 4.5.

Chapter 4

Results

4.1 Gradient-induced phase-shift effects in ^{1}H spectroscopy

This section presents the results obtained from the simulation of gradient-induced phase-shift effects in PRESS and STEAM sequences. Section 3.1 illustrated the sequences and the methodology used. The following subsection shows the impact of different sequence parameters in PRESS sequences on their flow sensitivity according to the simulations. Furthermore, it provides an estimation of the magnitude of the gradient-induced phase-shift effects for physiological flow velocities, thereby elucidating the significance of these effects in a more clinical context. Similarly, Subsection 4.1.2 is concerned with the impact of different sequence parameters and the magnitude of gradient-induced phase-shift effects in STEAM.

4.1.1 Gradient-induced phase-shift effects in PRESS

Firstly, the effects of varying sequence parameters on the flow sensitivity of PRESS sequences are shown. The results are depicted in Figure 4.1. For illustrative purposes, specific values for the fixed parameter were selected, enabling a visual representation of the findings.

Dependence of the flow sensitivity on voxel size in PRESS

Changing the edge length of the voxel (δL) along each axis had different effects on the flow sensitivity. The effects are illustrated in Figure 4.1A. The flow sensitivity along the x-axis got stronger with increasing edge length in the x-direction. The flow sensitivity for the minimum edge length of 3 mm was $-23.6\ \frac{rad \cdot s}{m}$. The flow sensitivity for the maximum edge length of 40 mm was $-71.8\ \frac{rad \cdot s}{m}$, representing more than a threefold increase in the

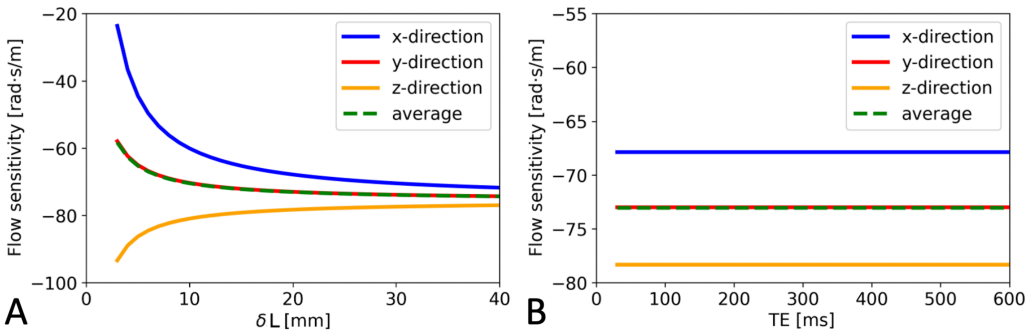

Figure 4.1: Dependence of the flow sensitivity on voxel size and TE in PRESS. [A] shows the flow sensitivity depending on δL for each axis (TE = 30 ms). [B] shows the flow sensitivity depending on TE for each axis (δL = 20 mm).

flow sensitivity. However, for edge lengths of more than 10 mm, the change was only gradual compared to the interval between 3 and 10 mm.

The flow sensitivity along the y-axis with increasing edge length in the y-direction behaved similarly. The longer the edge length of the voxel was, the stronger was the phase shift. The flow sensitivity for the minimum edge length of 3 mm was $-57.9\ \frac{rad \cdot s}{m}$. The flow sensitivity for the maximum edge length of 40 mm was $-74.3\ \frac{rad \cdot s}{m}$. However, the increase in phase shift was much smaller than the alteration of the edge length along the x-direction and amounted to only 29%.

The flow sensitivity along the z-axis diminished when the edge length of the voxel in the z-direction increased. This was different from increasing the edge length along the other two axes. For the minimum edge length of 3 mm, the flow sensitivity was $-93.4\ \frac{rad \cdot s}{m}$. The flow sensitivity for the maximum edge length of 40 mm was $-77.0\ \frac{rad \cdot s}{m}$. However, this amounted only to a 21% change in flow sensitivity.

Alongside the presentation of flow sensitivity along individual axes, Figure 4.1A also shows the average flow sensitivity across the x-, y-, and z-axes. The average was calculated assuming the edge lengths along each axis are equal, offering insights into the influence of isotropic flow within a voxel.

Dependence of the flow sensitivity on TE in PRESS

It can be seen from Figure 4.1B that changing the echo time of a PRESS sequence did not change its flow sensitivity along any axis, provided all other parameters are constant. However, it can be observed that the flow sensitivity for flow along each axis was different when δL was unchanged. In this specific example, where δL was set to 20 mm, the flow sensitivity was $-67.9\ \frac{rad \cdot s}{m}$ for flow along the x-axis, $-73.0\ \frac{rad \cdot s}{m}$ for flow along the y-axis, and $-78.3\ \frac{rad \cdot s}{m}$ for flow along the z-axis. The difference between the flow sensitivity in

the x- and z-direction amounted to 15%.

Phase shift in PRESS for physiological flow velocities

Based upon the results presented above, this paragraph shows how large the expected phase shift of an ^{1}H nucleus due to gradient-induced phase-shift effects is for different physiological flow velocities. Here, the phase shift is also given in degrees as this is more intuitive than radians. While TE did not influence the sequence's flow sensitivity, the flow sensitivity was influenced by changes of δL. Two different flow ranges are presented in the following. Firstly, the range of flow velocities in the microvasculature, i.e., capillaries, arterioles, and venules, is investigated. As discussed in Section 2.5, those flow velocities are primarily below 2.5 mm/s. Secondly, the range of flow velocities in larger arteries and veins is considered. These flow velocities are between 10 cm/s and 100 cm/s. The phase shifts for both ranges are shown for different edge lengths of the voxel in Figure 4.2.

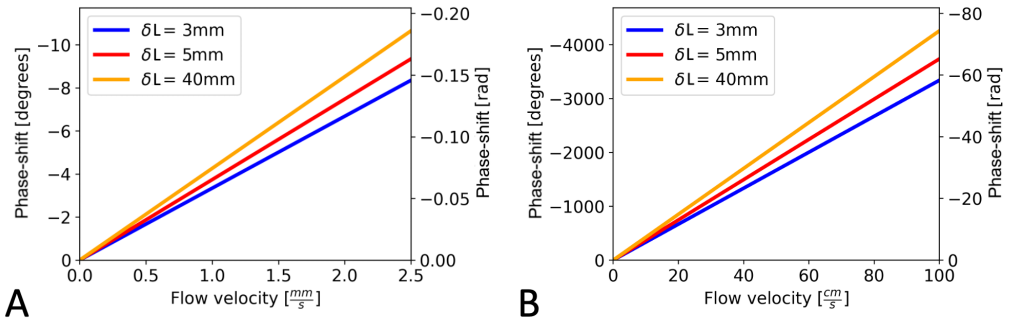

Figure 4.2: Phase shift in PRESS at different flow velocities depending on voxel size. Here, the phase shift at different flow velocities is shown for three distinct PRESS sequences with varying voxel sizes: δL = 3mm, δL = 5mm, and δL = 40mm. All PRESS sequences share an echo time of 30 ms. As degrees are more intuitive than radiants, the phase shift in degrees is provided on the left axis. [A] shows the phase shift for flow velocities in the microvasculature (up to 2.5 mm/s). [B] shows the phase shift for flow velocities of larger vessels (up to 100 cm/s).

The phase shift was calculated by multiplying the flow sensitivity of three exemplary PRESS sequences (δL = 3 mm, δL = 5 mm, δL = 40 mm) with the flow velocities. The average flow sensitivity (Figure 4.1) was used for this purpose rather than the flow sensitivity along any particular axis. However, differences along the axes existed (see above). In Figure 4.2A, it can be seen that the phase shift of an ^{1}H nucleus for flow velocities in the microvasculature is small. Even for 2.5 mm/s, it amounted to only about 10°. Considering flow velocities occurring in larger vessels, the resulting phase shift exceeded 180° for flow velocities above 4.2 cm/s (sequence parameters: δL = 40 mm, TE = 30 ms). The difference between the flow sensitivity at an edge length of 3 mm compared to an edge

length of 40 mm amounted to 22% equally along each axis.

4.1.2 Gradient-induced phase-shift effects in STEAM

Here, the effects of varying sequence parameters on the flow sensitivity of STEAM sequences are shown. The results are depicted in Figure 4.3. For illustrative purposes, specific values for the fixed parameter were selected, enabling a visual representation of the findings. Alongside the presentation of flow sensitivity along individual axes, Figure 4.3 also shows the average flow sensitivity across the x-, y-, and z-axes. The average was calculated assuming the edge lengths along each axis are equal, offering insights into the influence of isotropic flow within a voxel.

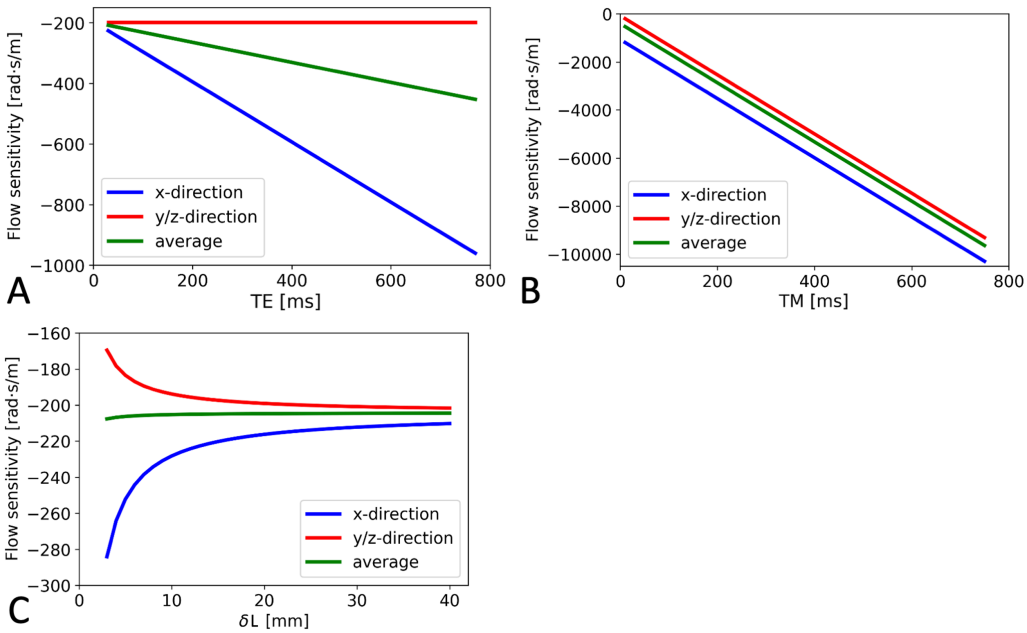

Figure 4.3: Dependence of the flow sensitivity on TE, TM, and voxel size in STEAM. [A] shows the flow sensitivity depending on TE for each axis (sequence parameters: δL = 20 mm, TM = 10 ms). [B] shows the flow sensitivity depending on TM for each axis (sequence parameters: δL = 20 mm, TE = 1000 ms). For short echo times, the three lines shown are indistinguishable. Therefore, a long echo time was chosen for the illustration. [C] shows the flow sensitivity depending on δL for each axis (sequence parameters: TE = 20 ms, TM = 10 ms).

Dependence of the flow sensitivity on voxel size in STEAM

Changing the edge length of the voxel along any axis led to changes in the flow sensitivity for STEAM sequences. This principle is illustrated in Figure 4.3C. The flow sensitivity along the x-axis decreased when the edge length of the voxel in the x-direction increased.

The flow sensitivity for the minimum edge length of 3 mm was $-284.1\ \frac{rad \cdot s}{m}$. The flow sensitivity for the maximum edge length of 40 mm was $-210.3\ \frac{rad \cdot s}{m}$. However, for edge lengths of more than 10 mm along the x-axis, the change was only gradual compared to the interval between 3 and 10 mm.

The flow sensitivity along the y- and z-axis increased with longer edge lengths in the y- and z-direction, respectively. The flow sensitivity for the minimum edge length of 3 mm was $-169.5\ \frac{rad \cdot s}{m}$. The flow sensitivity for the maximum edge length of 40 mm was $-201.7\ \frac{rad \cdot s}{m}$. However, this represented a smaller percentage difference (16.0 % versus 35.1 %) compared to the variation observed along the x-axis.

Dependence of the flow sensitivity on TE in STEAM

While increasing the echo time led to a higher flow sensitivity along the x-direction, it did not change the flow sensitivity along the y- or z-direction. This can be seen from Figure 4.3A. The flow sensitivities along the y- and z-axis were independent of TE. Consequently, Figure 4.3A shows only one function representing both. For the sequence parameters δL = 20 mm and TM = 10 ms, the flow sensitivity along the y- and z-direction was $-199.0\ \frac{rad \cdot s}{m}$ for every echo time. The flow sensitivity along the x-direction increased from $-226.2\ \frac{rad \cdot s}{m}$ for TE = 30 ms to $-960.8\ \frac{rad \cdot s}{m}$ for TE = 770 ms. The increase in flow sensitivity for flow along the x-direction led to an increase in the average flow sensitivity (Figure 4.3A) of the STEAM sequence; this is relevant for isotropic flow within a voxel.

Dependence of the flow sensitivity on TM in STEAM

Longer mixing times led to a substantial increase in flow sensitivity along each axis. The flow sensitivities along the y- and z-axis were equal. However, independent of the mixing time, the flow sensitivity along the x-axis consistently exceeded that along the y- and z-axis. This can be seen from Figure 4.3B. For the following example, the values are δL = 20 mm and TM = 100 ms. The flow sensitivity along the y- and z-axis (regardless of TE) was $-1307\ \frac{rad \cdot s}{m}$, while the flow sensitivity along the x-axis reached $-2297\ \frac{rad \cdot s}{m}$. These results highlight the impact of longer mixing times in STEAM sequences, which led to significantly higher flow sensitivities, particularly when compared to the flow sensitivities observed in PRESS.

Phase shift in STEAM for physiological flow velocities

As with the PRESS sequences above, this paragraph shows how large the expected phase shift of an ^{1}H nucleus due to gradient-induced phase-shift effects is for different physiological flow velocities. Again, the phase shift is given in degrees as this is more intuitive than

radians. The two ranges of flow velocities mentioned above were investigated. In general, STEAM sequences led to stronger gradient-induced phase shifts than PRESS sequences. The results are illustrated in the Figures 4.4, 4.5, and 4.6.

Phase shift in STEAM for physiological flow velocities depending on voxel size

As can be seen from Figure 4.4, the absolute effect of changing δL on the phase shift was nearly neglectable. The difference amounted to only 1.5% when comparing an edge length along every axis of 3mm to an edge length of 40 mm. This held true regardless of the flow velocity.

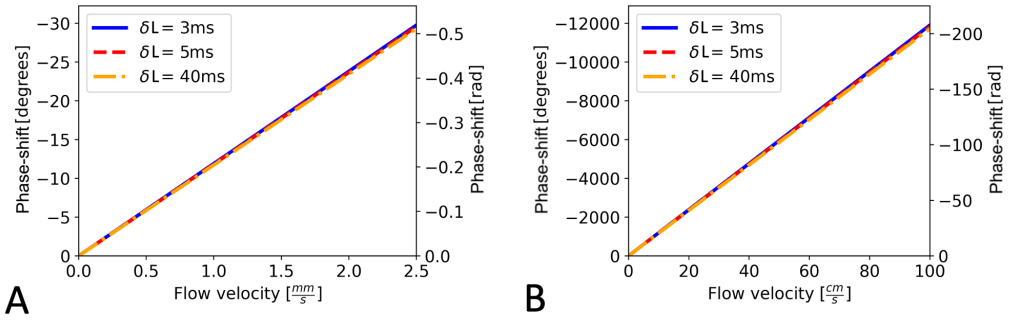

Figure 4.4: Phase shift in STEAM for different flow velocities depending on voxel size. Here, the phase shift at different flow velocities is shown for three distinct STEAM sequences with varying δL values: δL = 3 mm, δL = 5 mm, and δL = 40 mm. Fixed sequence parameters: TE = 20ms, TM = 10 ms. [A] shows the phase shift for flow velocities in the microvasculature (up to 2.5 mm/s). [B] shows the phase shift for flow velocities of larger vessels (up to 100 cm/s).

Phase shift in STEAM for physiological flow velocities depending on TE

Again, the average flow sensitivity along all three axes was used for the calculation. Therefore, changing the echo time of a STEAM sequence influenced the phase shift because the flow sensitivity along the x-direction depends on the echo time (see above).

Figure 4.5 depicts the gradient-induced phase shift for physiological flow velocities depending on the echo time. The phase shifts were calculated by multiplying the flow sensitivity of three exemplary STEAM sequences (TE = 20 ms, TE = 300 ms, TE = 600 ms) with the flow velocities. The sequences depicted in Figure 4.5 led to a considerably larger phase shift than the PRESS sequences investigated, even at short mixing times. With an echo time of 600 ms, the phase shift for a flow velocity of 2.2 mm/s exceeded 50°. In the range of flow velocities found in larger vessels, the phase shift of the ^{1}H nuclei exceeded 180° in every case.

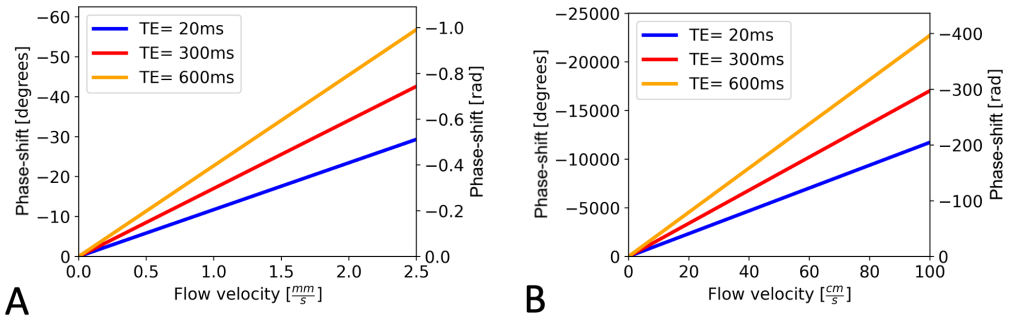

Figure 4.5: Phase shift in STEAM for different flow velocities depending on TE. Here, the phase shift at different flow velocities is shown for three distinct STEAM sequences with varying TE values: TE = 20 ms, TE = 300 ms, and TE = 600 ms. Fixed sequence parameters: TM = 10 ms, δL = 20mm. [A] shows the phase shift for flow velocities in the microvasculature (up to 2.5 mm/s). [B] shows the phase shift for flow velocities of larger vessels (up to 100 cm/s).

Phase shift in STEAM for physiological flow velocities depending on TM

Long mixing times led to a strong phase shift of flowing ^{1}H nuclei (Figure 4.6). With a mixing time of 200 ms, even a flow velocity of 1.2 mm/s led to a phase shift of 180°. However, for short mixing times, the phase shift was much smaller. For the same velocity, only a phase shift of 14° was observed when the mixing time was 10 ms. Regarding the range of flow velocities found in larger vessels, with a short mixing time of 10 ms, the phase shift was considerable and amounted to 1174° when the flow velocity equalled 10 cm/s.

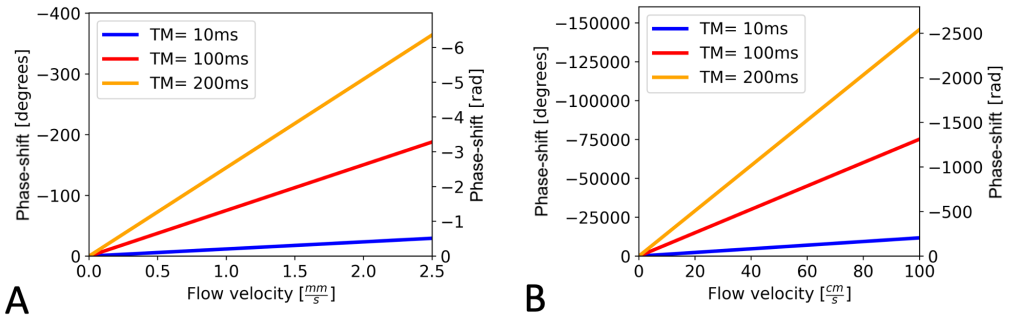

Figure 4.6: Phase shift in STEAM for different flow velocities depending on TM. Here, the phase shift at different flow velocities is shown for three distinct STEAM sequences with varying TM values: TM = 10 ms, TM = 100 ms, and TM = 200 ms. Fixed sequence parameters: TE = 20 ms, δL = 20 mm. [A] shows the phase shift for flow velocities in the microvasculature (up to 2.5 mm/s). [B] shows the phase shift for flow velocities of larger vessels (up to 100 cm/s).

4.2 Phantom measurements with standard sequences

This section presents the results of the experimental flow measurements with the phantom using the standard sequences. Firstly, the results of PRESS measurements are presented. Secondly, the results of the STEAM measurements are presented. In both cases, the flow created by the phantom is calculated first. The acquired spectra are shown in the following. Lastly, the signal amplitudes of the spectra obtained by the AMARES algorithm are presented.

4.2.1 Phantom measurements using standard PRESS sequences

Calculation of the flow velocity inside the phantom

The three flows created for the phantom measurements with PRESS sequences are denoted by ”Flow 1”, ”Flow 2”, and ”Flow 3”. This subsection shows the calculation of these flow velocities. Table 4.1 shows the results of the weight measurements performed to calculate the mean flow velocity.

Table 4.1: Weight measurements used to calculate the mean flow velocity in the phantom measurements using PRESS. The numbers 1, 2, and 3 denote three separate weight measurements. The last column of the table shows the averages for the measurements. The same cup was used for the measurements of Flows 1–3. m_{e1} denotes the mass of the empty cup. m_1–m_3 denote the masses of the cups holding the fluid in the cases of Flows 1–3.

	1	2	3	average
m_1	0.137 kg	0.138 kg	0.137 kg	0.137 kg
m_2	0.288 kg	0.288 kg	0.288 kg	0.288 kg
m_3	0.424 kg	0.424 kg	0.424 kg	0.424 kg
m_{e1}	0.006 kg	0.006 kg	0.006 kg	0.006 kg

Table 4.2 lists the time intervals of the flow measurements, the average mass of the fluid, as well as the resulting mean flow velocity in each case. Subsection 3.2.4 lists the formulae necessary for these calculations.

Table 4.2: Flow velocities in the phantom measurements using PRESS. This table lists the measurements necessary for the calculation of the flow velocities as well as the resulting flow velocities. The mass of the empty cup was subtracted from the mass of the cup holding the fluid to calculate the mass of the fluid. Equation 3.225 was used to determine the mean flow velocities (Flows 1–3).

Flow	t_{flow}	Mass	Mean flow velocity
Flow 1	900 s	0.131 kg	0.46 $\frac{mm}{s}$
Flow 2	900 s	0.282 kg	1.00 $\frac{mm}{s}$
Flow 3	720 s	0.418 kg	1.85 $\frac{mm}{s}$

Measurement conditions and sequence parameters

The author chose a repetition time of 2000 ms. The voxel had an edge length of 13 x 13 x 13 mm. One measurement consisted of 10 scans. The coil described in Subsection 3.2.2 was used. The position of the voxel was equal for all measurements. For all test series, spectra with various echo times were acquired. The echo times were 30, 100, 200, 300, 400, 500, 600, 700, 800, 900, 1000, and 1100 ms.

Spectra acquired in the phantom measurements with standard PRESS sequences

Figure 4.7 shows the spectra acquired with PRESS sequences for the varying flow velocities. Figure 4.7A shows the PRESS spectra that were acquired with no flow inside the phantom. A gradual decline in the signal amplitude can be seen with an increase in echo time. The exception is the spectrum acquired with an echo time of 30 ms. The amplitude of this spectrum is smaller than the amplitude acquired with an echo time of 100 ms. However, the width of the spectrum's peak with an echo time of 30 ms is larger than that of the spectrum with an echo time of 100 ms. Figure 4.7B shows the spectra acquired with a flow velocity of 0.46 mm/s. Here, the gradual decline in the amplitudes with increasing echo time can also be seen. In this case, the spectrum acquired with an echo time of 30 ms is no exception. Figure 4.7C shows the spectra obtained with a flow velocity of 1.00 mm/s. The decline in the amplitudes is as regular as in Figure 4.7B. In Figure 4.7D, the spectra acquired with a flow velocity of 1.85 mm/s are shown. Here, far smaller amplitudes can be seen. The peaks are broader than the peaks for smaller flow velocities, and the spectra are also more irregular. The spectra acquired with an echo time of 30 ms and an echo time of 100 ms show nearly identical shapes and amplitudes.

The spectrum acquired with an echo time of 30 ms and no flow showed another irreg-

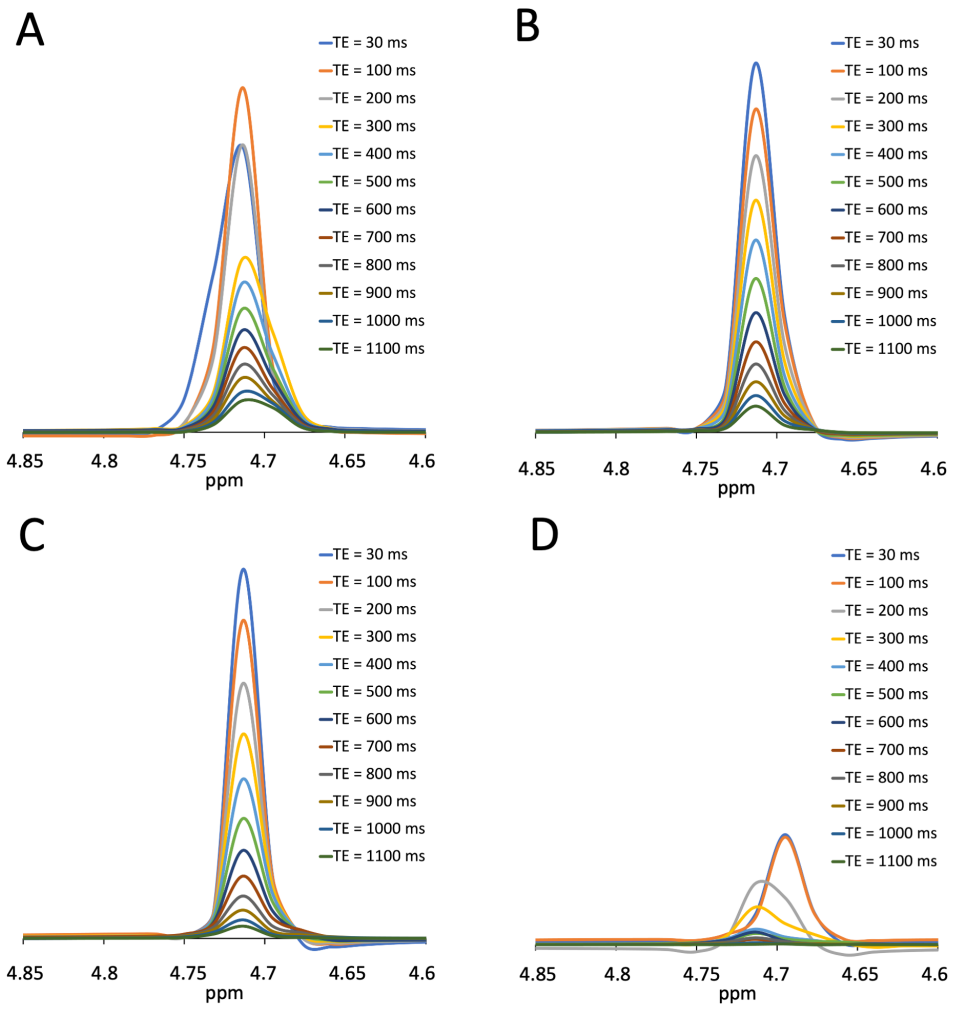

Figure 4.7: Comparison of the spectra acquired in the phantom measurements with standard PRESS sequences. [A] shows the spectra acquired without flow. [B] shows the spectra acquired with a flow velocity of 0.46 mm/s. [C] shows the spectra acquired with a flow velocity of 1.00 mm/s. [D] shows the spectra acquired with a flow velocity of 1.85 mm/s.

ularity. While the peaks of the spectra with longer echo times lined up at around 4.7 ppm, the peak of the spectrum with an echo time of 30 ms and no flow was at about 4.85 ppm. This difference must be spurious as the signal comes from ^{1}H nuclei of water molecules of the same nickel sulfate solution. Therefore, the spectrum was aligned with the other spectra in Figure 4.7A.

Amplitudes of the spectra acquired with standard PRESS sequences

Table 4.3 shows the amplitudes determined using the AMARES algorithm.

Table 4.3: Maximal amplitudes in the phantom measurements using PRESS.

TE [ms]	No flow	Flow 1, 0.46 $\frac{mm}{s}$	Flow 2, 1.00 $\frac{mm}{s}$	Flow 3, 1.85 $\frac{mm}{s}$
30	368000	362000	275000	106000
100	331000	321000	242000	99700
200	274000	268000	204000	98900
300	228000	221000	172000	52700
400	190000	179000	144000	23900
500	158000	144000	116000	18400
600	130000	112000	90400	14600
700	108000	86000	65600	6380
800	88900	65300	46800	9980
900	73300	49400	31100	4320
1000	59900	36200	20100	2510
1100	49200	24900	13500	776

Figure 4.8 compares the amplitudes of the measurements with varying flow velocities determined with AMARES. With longer echo times, a decline in amplitudes can be observed. Further, it can be seen that the higher the mean flow velocity, the smaller the amplitudes. While the difference between the measurements without flow and those with 0.46 mm/s is relatively small for echo times of up to 400 ms, it becomes more pronounced at an echo time of 500 ms and above. The measurements done with a mean flow velocity of 1.00 mm/s differ considerably from the measurements with 0.46 mm/s, even at echo times as small as 30 ms. The measurements with a mean flow velocity of 1.85 mm/s show a more irregular decay of amplitudes. Their amplitudes are far smaller than those of the previously mentioned measurements with smaller flow velocities.

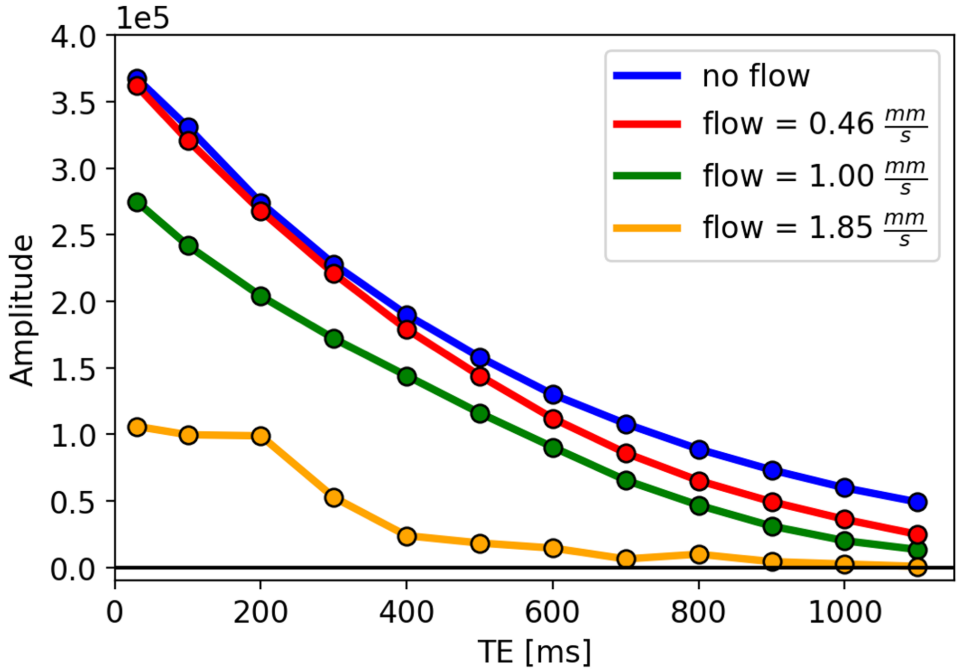

Figure 4.8: Change of signal intensity with different flow velocities in PRESS. This figure shows the decline in signal amplitudes with increasing echo times determined using the AMARES algorithm. The legend on the upper right shows the colours corresponding to the flow velocities. Note the scaling factor of $1 \cdot 10^5$ for the amplitudes.

4.2.2 Phantom measurements using standard STEAM sequences

Calculation of the flow velocity inside the phantom

The three flows created for the phantom measurements with STEAM sequences are denoted by ”Flow 4”, ”Flow 5”, and ”Flow 6”. This subsection shows the calculation of these flow velocities. Table 4.4 shows the results of the weight measurements performed to calculate the mean flow velocity.

Table 4.4: Weight measurements used to calculate the mean flow velocity in the phantom measurements using STEAM. The numbers 1, 2, and 3 denote three separate weight measurements. The last column of the table shows the averages for the measurements. The same cup was used for the measurements of Flows 4–6. m_{e2} denotes the mass of the empty cup. m_4–m_6 denote the masses of the cups holding the fluid in the cases of Flows 4–6.

	1	2	3	Average
m_4	0.097 kg	0.098 kg	0.098 kg	0.098 kg
m_5	0.364 kg	0.363 kg	0.363 kg	0.363 kg
m_6	0.371 kg	0.371 kg	0.370 kg	0.371 kg
m_{e2}	0.006 kg	0.006 kg	0.006 kg	0.006 kg

Table 4.5 lists the time intervals of the flow measurements, the average mass of the fluid, as well as the resulting mean flow velocity in each case. Subsection 3.2.4 lists the formulae necessary for these calculations.

Table 4.5: Flow velocities in the phantom measurements using STEAM. This table lists the measurements necessary for the calculation of the flow velocities as well as the resulting flow velocities. The mass of the empty cup was subtracted from the mass of the cup holding the fluid to calculate the mass of the fluid. Equation 3.225 was used to evaluate the mean flow velocities (Flows 4–6).

Flow	Time	Mass	Flow velocity
Flow 4	990 s	0.092 kg	0.29 $\frac{mm}{s}$
Flow 5	1032 s	0.357 kg	1.10 $\frac{mm}{s}$
Flow 6	960 s	0.365 kg	1.21 $\frac{mm}{s}$

In contrast to the PRESS measurements, where the mean flow velocities (Flows 1–3) were further apart, Flows 5 and 6 were closer to each other. The smaller difference was not planned but is due to the difficulty of predicting the resulting flow caused by different positions of the regulator of the phantom.

Measurement conditions and sequence parameters

A repetition time of 2300 ms was used. The voxel had an edge length of 13 x 13 x 13 mm. One measurement consisted of 12 scans. The coil described in Subsection 3.2.2 was used.

The position of the voxel was equal for all measurements. For all test series, spectra with various echo times were acquired. The echo times were 20, 100, 200, 300, 400, 500, 600, 700, 800, 900, 1000, and 1100 ms. Here, the mixing time was fixed to 10 ms.

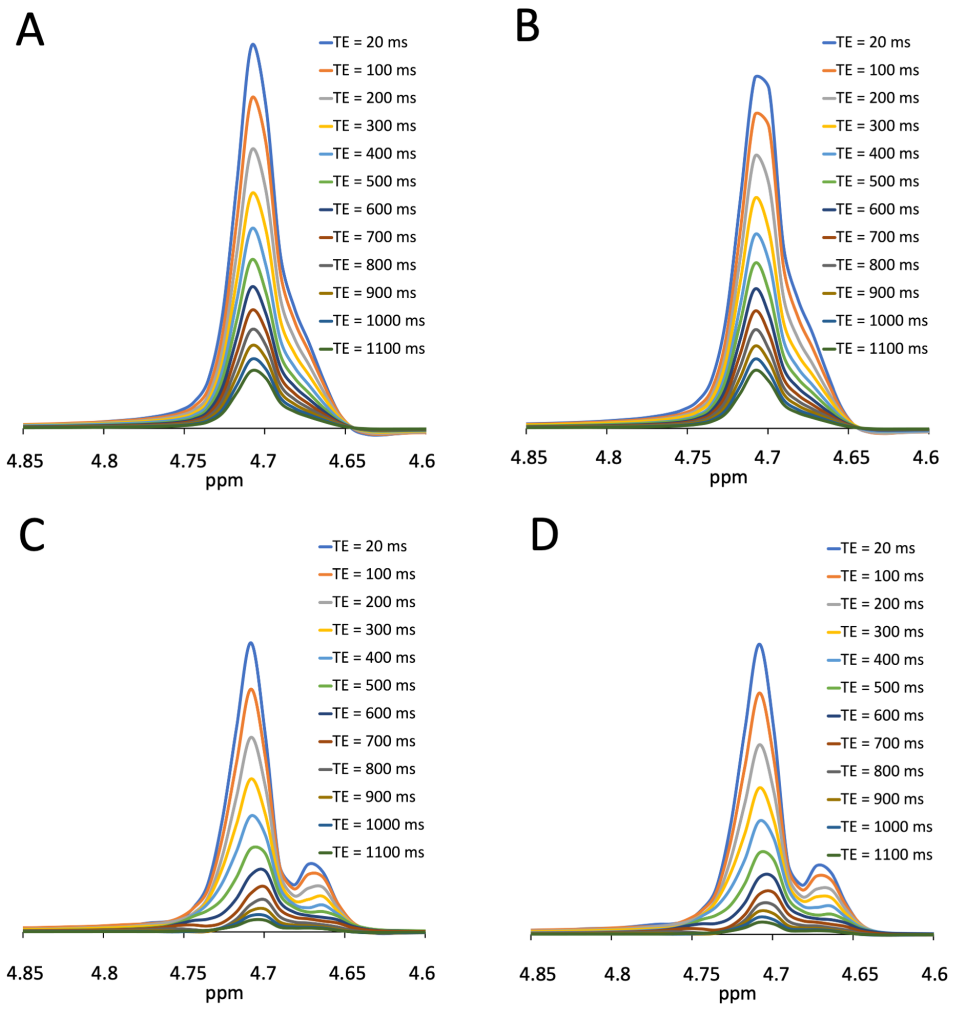

Figure 4.9: Comparison of the spectra acquired in the phantom measurements with standard STEAM sequences. [A] shows the spectra acquired without flow. [B] shows the spectra acquired with a flow velocity of 0.29 mm/s. [C] shows the spectra acquired with a flow velocity of 1.10 mm/s. [D] shows the spectra acquired with a flow velocity of 1.21 mm/s.

Spectra acquired in the phantom measurements with standard STEAM sequences

Figure 4.9 shows the spectra acquired with STEAM sequences for the varying flow velocities. Figure 4.9A shows the STEAM spectra that were acquired with no flow inside the phantom. A gradual decline in the signal amplitude can be seen with an increase in echo

time. The shape of the peaks shows a more gradual decline on the right side than on the left. Figure 4.9B shows the spectra acquired with a flow velocity of 0.29 mm/s. The shape of the peaks is similar to the shapes in Figure 4.9A. However, the peaks for the echo times 20 and 100 ms are not as pointed as those of the spectra that were acquired without flow. Figure 4.9C shows the spectra obtained with a flow velocity of 1.10 mm/s.

The decline in the amplitudes can be seen again. In contrast to the previous spectra, the signal pattern of the spectra acquired at a flow velocity of 1.10 mm/s is different. To the right side of the peak, an indentation appears for echo times between 20 and 400 ms. For longer echo times, the peak's left flank declines more slowly than the right flank. In Figure 4.9D, the spectra with a flow velocity of 1.21 mm/s are shown. Here, the signal pattern shown in Figure 4.9C recurs. Generally, the spectra acquired without flow and with a flow velocity of 0.29 mm/s on the one side and those obtained with the flow velocities of 1.10 mm/s and 1.21 mm/s on the other side appear very similar.

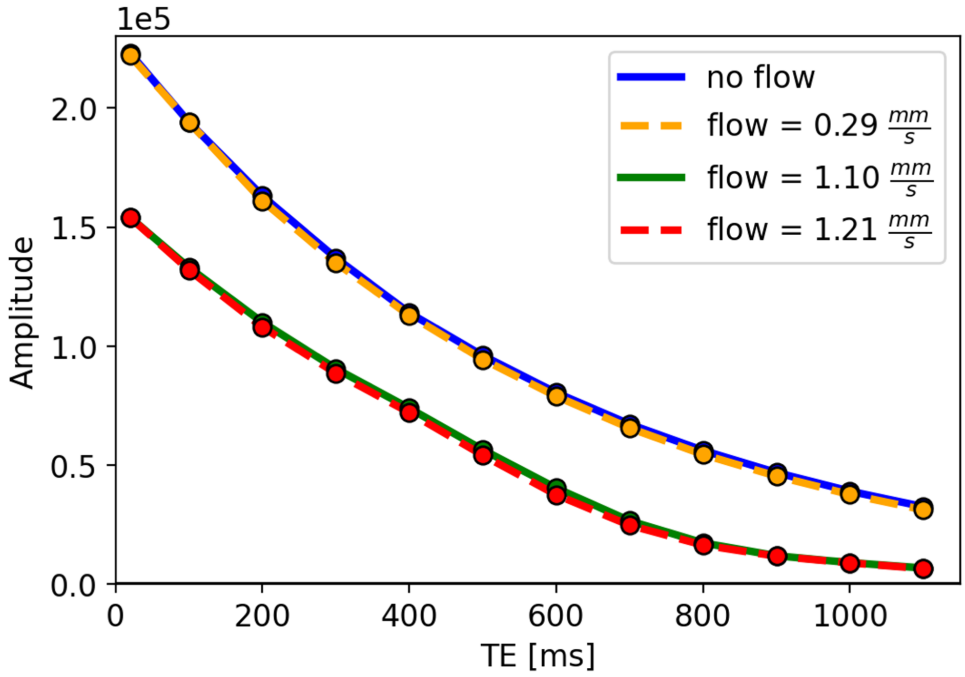

Figure 4.10: Change of signal intensity with different flow velocities in STEAM. This figure shows the decline in signal amplitudes with increasing echo times determined using the AMARES algorithm. The legend on the upper right shows the colours corresponding to the flow velocities.

Amplitudes of the spectra acquired with standard STEAM sequences

The amplitudes determined using the AMARES algorithm are shown in Table 4.6.

Table 4.6: Maximal amplitudes in the phantom measurements using STEAM.

TE [ms]	No flow	Flow 4, 0.29 $\frac{mm}{s}$	Flow 5, 1.10 $\frac{mm}{s}$	Flow 6, 1.21 $\frac{mm}{s}$
20	223000	222000	154000	154000
100	194000	194000	133000	132000
200	163000	161000	110000	108000
300	137000	135000	90500	88600
400	114000	113000	73900	72100
500	96000	94400	56500	54200
600	80400	78900	40400	37600
700	67200	65600	26700	24800
800	56200	54500	17400	16500
900	46900	45400	12000	11800
1000	39100	37700	9090	8980
1100	32600	31300	6830	6600

In Figure 4.10, the amplitudes determined by the AMARES algorithm are depicted. With longer echo times, a decline in amplitudes can be observed. It can be seen that the amplitudes of the spectra acquired without flow and with a flow velocity of 0.29 mm/s are very close to each other. On the other hand, the amplitudes of the spectra acquired with the flow velocities of 1.10 mm/s and 1.21 mm/s are close to each other as well. In absolute terms, these amplitudes are smaller than those determined for the measurement sets without flow and with a flow velocity of 0.29 mm/s.

4.2.3 Phantom measurements comparing standard STEAM sequences with varying mixing times

As the model developed in Section 3.1 predicts that the mixing time strongly influences gradient-induced phase-shift effects in STEAM spectra, further measurements were made

to test this. For this purpose, three sets of measurements were performed. The three measurement sets varied in their mixing time. In the first set, a mixing time of 10 ms was used; in the second set, a mixing time of 50 ms was used; in the third set, a mixing time of 75 ms was used. Each set consisted of a measurement series without flow and a measurement series with a flow of 0.94 mm/s. The model developed predicts that the difference between the amplitudes of the spectra with and without flux should increase with increasing mixing times.

Calculation of the flow velocity inside the phantom

The flow created for the phantom measurements with STEAM sequences and varying mixing times is denoted by ”Flow 7”. This subsection shows the calculation of the flow velocity. Table 4.7 shows the results of the weight measurements performed to calculate the mean flow velocity.

Table 4.7: Weight measurements used to calculate the mean flow velocity in the phantom measurements using STEAM with varying TM. The numbers 1, 2, and 3 denote three separate weight measurements. The last column of the table shows the averages for the measurements. m_7 denotes the mass of the cup holding the fluid in the case of Flow 7. The cup previously used for measuring Flows 4–6 was used for the weight measurements. Therefore, the cup was not weighted again.

	1	2	3	Average
m_7	0.420 kg	0.420 kg	0.420 kg	0.420 kg

Table 4.8 lists the time interval of the flow measurement, the average mass of the fluid, as well as the resulting mean flow velocity. Subsection 3.2.4 lists the formulae necessary for these calculations.

Table 4.8: Flow velocity in the phantom measurements using STEAM with varying TM. This table lists the measurements necessary for the calculation of the flow velocity as well as the resulting flow velocity. The mass of the empty cup was subtracted from the mass of the cup holding the fluid to calculate the mass of the fluid. Equation 3.225 was used to evaluate the mean flow velocity (Flow 7).

Flow	Time	Mass	Flow velocity
Flow 7	1410 s	0.414 kg	0.94 $\frac{mm}{s}$

Measurement conditions and sequence parameters

A repetition time of 2300 ms was used. The voxel had an edge length of 13 x 13 x 13 mm. One measurement consisted of 12 scans. The coil described in Subsection 3.2.2 was used. The position of the voxel was equal for all measurements. For all test series, spectra with various echo times were acquired. The echo times were 20, 100, 200, 300, 400, 500, 600, 700, 800, 900, 1000, and 1100 ms.

Spectra acquired in the phantom measurements comparing standard STEAM sequences with varying mixing times

Figure 4.11 shows the spectra with a mixing time of 10 ms that were acquired to investigate the influence of the mixing time on the spectra. While Figure 4.11A shows the spectra acquired without flow, Figure 4.11B shows the spectra acquired with a flow velocity of 0.94 mm/s. It can be seen that the peaks in Figure 4.11B are not as pointed as in Figure 4.11A. A decline in the amplitudes with longer echo times can be appreciated for both measurement sets.

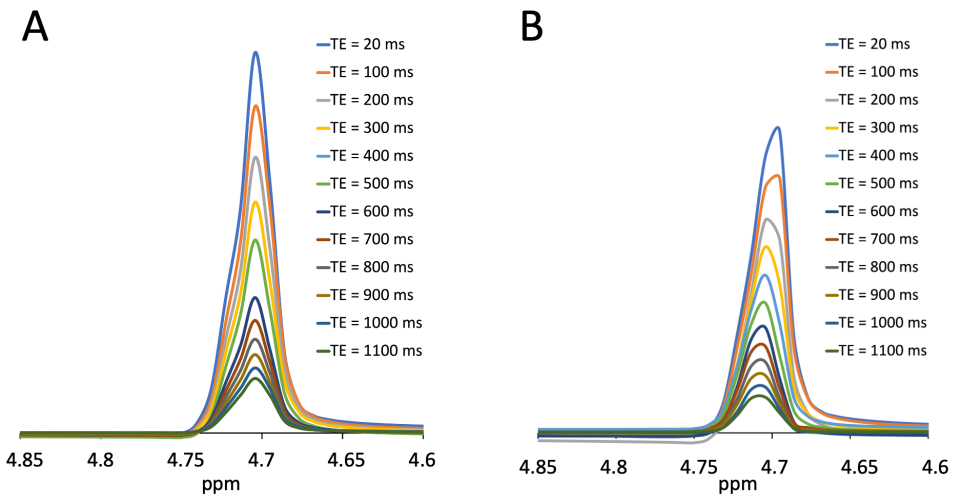

Figure 4.11: Comparison of the spectra acquired in the phantom measurements with standard STEAM sequences and varying TM (TM = 10 ms). [A] shows the spectra acquired without flow. [B] shows the spectra acquired with a flow velocity of 0.94 mm/s.

Figure 4.12 shows the spectra with a mixing time of 50 ms that were acquired to investigate the influence of the mixing time on the spectra. While Figure 4.12A shows the spectra obtained without flow, Figure 4.12B shows the spectra acquired with a flow velocity of 0.94 mm/s. It can be seen that the peaks in Figure 4.12B have an irregular shape compared to the peaks in Figure 4.12A. An indentation on the right side of the peak can

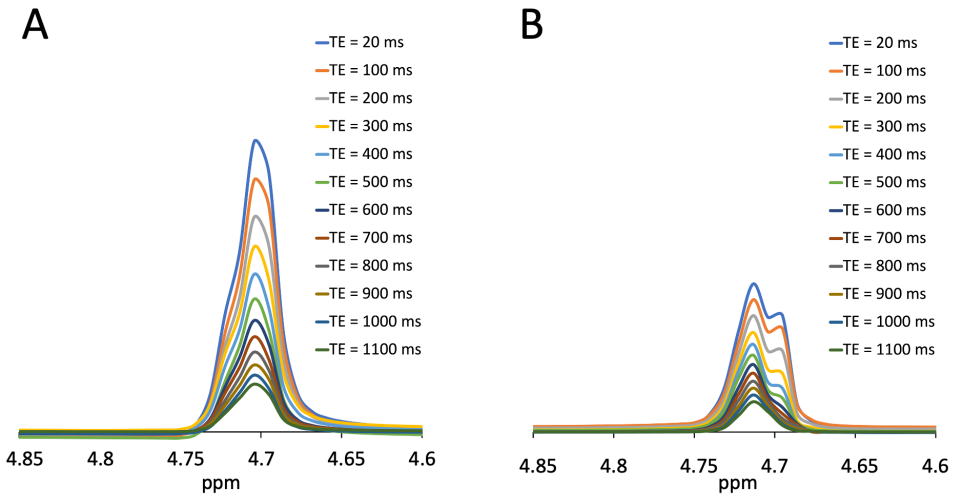

Figure 4.12: Comparison of the spectra acquired in the phantom measurements with standard STEAM sequences and varying TM (TM = 50 ms). [A] shows the spectra acquired without flow. [B] shows the spectra acquired with a flow velocity of 0.94 mm/s.

be seen for the echo times of 20 to 200 ms. For echo times between 300 and 600 ms, the same region of the peak shows a plateau. For longer echo times, these features cannot be seen. A decline in the amplitudes with longer echo times can be appreciated for both measurement sets.

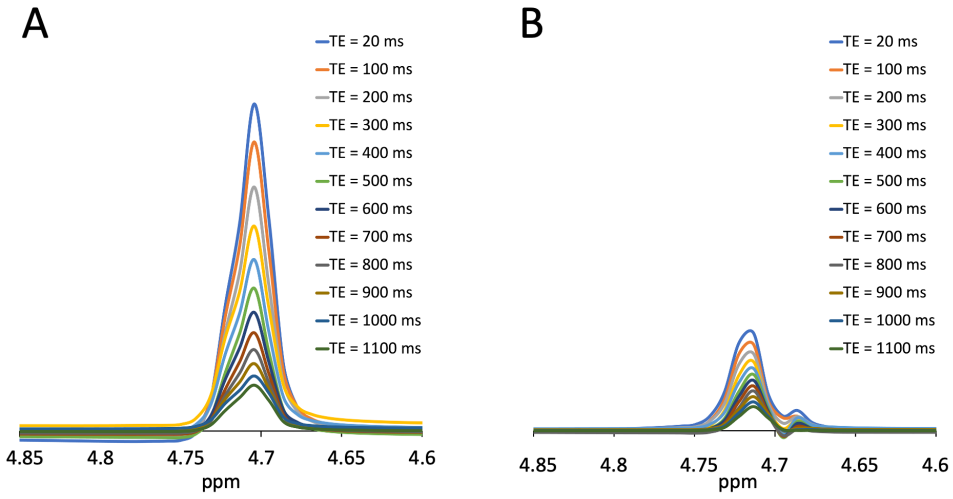

Figure 4.13: Comparison of the spectra acquired in the phantom measurements with standard STEAM sequences and varying TM (TM = 75 ms). [A] shows the spectra acquired without flow. [B] shows the spectra acquired with a flow velocity of 0.94 mm/s.

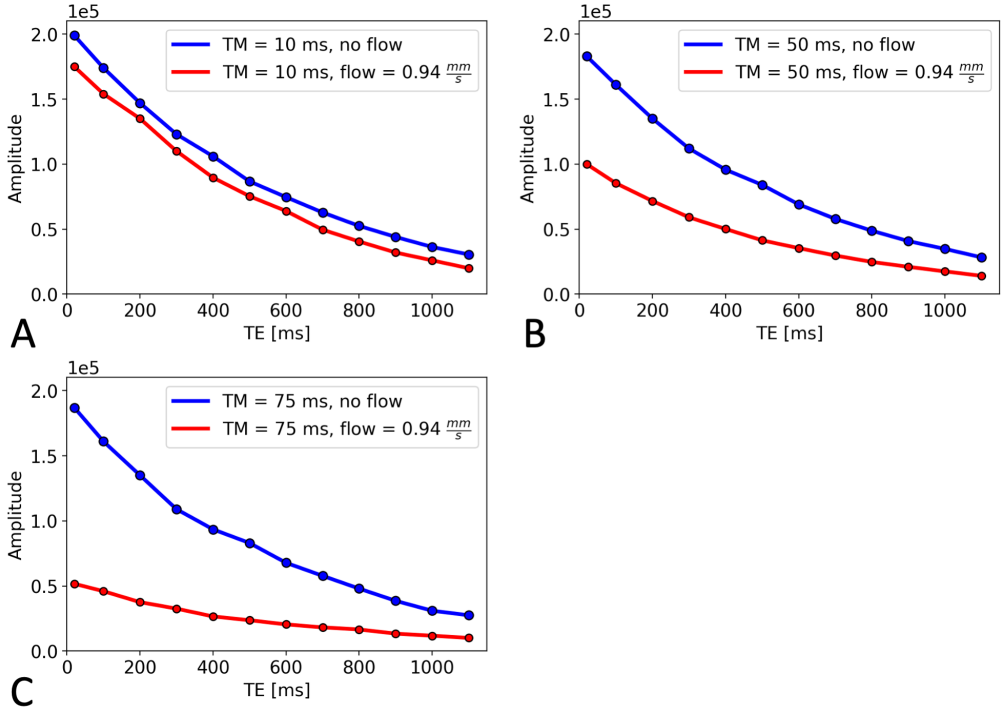

Figure 4.14: Results of the phantom measurements with standard STEAM sequences and varying TM. Here, a comparison between three measurement sets with varying TM is shown. These measurements aimed to evaluate whether an increase in TM leads to a decrease in signal intensity when the fluid flows through the phantom. Each set consists of a series acquired without flow and one acquired with a flow of 0.94 mm/s. [A] Here, the two series of the first set are shown. TM was 10 ms. [B] depicts the two series of the second measurement set acquired with a TM of 50 ms. [C] Here, the two series of the third set are shown. TM was 75 ms in this case.

Figure 4.13 shows the spectra with a mixing time of 75 ms that were acquired to investigate the influence of the mixing time on the spectra. While Figure 4.13A shows the spectra acquired without flow, Figure 4.13B shows the spectra obtained with a flow velocity of 0.94 mm/s. It can be seen that the peaks in Figure 4.13B have an irregular shape compared to the peaks in Figure 4.13A. An indentation on the right side of the peak can be seen for all echo times measured. A decline in the amplitudes with longer echo times can be appreciated for both measurement sets.

Amplitudes of the spectra acquired with standard STEAM sequences and varying mixing times

AMARES was used to determine the amplitudes of the spectra. The amplitudes of the measurement sets with a mixing time of 10 and 50 ms are shown in Table 4.9, while the amplitudes of the measurement set with a mixing time of 75 ms are shown in Table 4.10.

Table 4.9: Maximal amplitudes in the phantom measurements using STEAM with varying TM (TM = 10 ms, TM = 50 ms).

TE [ms]	TM = 10 ms	TM = 50 ms	Flow 7, TM = 10 ms	Flow 7, TM = 50 ms
20	199000	183000	175000	100000
100	174000	161000	154000	85300
200	147000	135000	135000	71600
300	123000	112000	110000	59100
400	106000	95700	89600	50100
500	86700	84000	75300	41400
600	74600	69000	63900	35400
700	62800	57900	49600	29700
800	52500	48800	40500	24800
900	44000	40800	32000	21000
1000	36300	34800	26000	17500
1100	30500	28300	19900	14100

In Figure 4.14, the amplitudes determined with AMARES are illustrated. Figure 4.14A shows the measurements with a mixing time of 10 ms for both no flow and a flow velocity of 0.94 mm/s. It can be seen that the amplitudes are smaller for the spectra with flow compared to the spectra without flow.

Figure 4.14B shows the measurements with a mixing time of 50 ms for both no flow and a flow velocity of 0.94 mm/s. Akin to the measurements with a mixing time of 10 ms, the amplitudes are smaller for the spectra with flow than those without flow. However, the difference in amplitudes is more pronounced.

Figure 4.14C shows the measurements with a mixing time of 50 ms for both no flow and a flow velocity of 0.94 mm/s. Here, the amplitudes of the spectra acquired with a flow are smaller than in the previous measurement sets. Therefore, the difference between the spectra with flow and those without flow is even more significant.

Table 4.10: Maximal amplitudes in the phantom measurements using STEAM with varying TM (TM = 75 ms).

TE [ms]	TM = 75 ms	Flow 7, TM = 75 ms
20	187000	51700
100	161000	46000
200	135000	37600
300	109000	32600
400	93500	26600
500	83000	23700
600	67800	20500
700	57800	18200
800	48000	16600
900	38600	13400
1000	31000	11800
1100	27500	10100

In general, all measurement sets seem to decay exponentially with increased the echo time. While the amplitudes of the spectra acquired with flow become progressively smaller with an increase in the mixing time, the effect of an increase in mixing time is less pronounced for the spectra without flow.

4.3 Phantom measurements with the flow-sensitised sequences

As stated above, the aim of the preliminary phantom measurements was twofold. The first aim was to compare the standard and flow-sensitised sequences without flow to investigate whether the spectra obtained by the sequences were comparable. As both sequences differ

only in the crusher gradients, signal amplitudes should be comparable. The second aim was to test whether the flow-sensitised sequences were more susceptible to flow than the standard sequences in phantom measurements, as this is the prerequisite for the in vivo measurements to be meaningful.

The experimental setup of the phantom measurements was the same as for the measurements depicted in Section 4.2. The measurements were performed in the same setting.

4.3.1 Phantom measurements comparing standard and flow-sensitised PRESS sequences

The measurements presented here compared the standard PRESS sequence to the flow-sensitised sequence. In addition to measurements without flow, measurements with flowing nickel sulfate solution were made.

Measurement conditions and sequence parameters

The mean flow velocities were 0.46, 1.00, and 1.85 mm/s. These were the same conditions presented in Section 4.2, where the calculation of the flow velocities is shown. A repetition time of 2000 ms was used. The voxel had an edge length of 13 x 13 x 13 mm. One measurement consisted of 10 scans. The head coil described in Section 2.6 was used. The voxel's position was equal for the standard and flow-sensitised PRESS sequence measurements. For all test series, spectra with various echo times were acquired. The echo times were 30, 100, 200, 300, 400, 500, 600, 700, 800, 900, 1000, and 1100 ms.

Spectra acquired in the phantom measurements comparing standard and flow-sensitised PRESS sequences

Figure 4.15 shows the spectra of the PRESS measurements without flow obtained to compare the standard and flow-sensitised sequences. Figure 4.15A shows the spectra acquired using the standard PRESS sequence (identical to the spectra presented in Figure 4.7A, where the features of the spectra are discussed). These are shown for comparison. Figure 4.15B shows the spectra acquired using the flow-sensitised PRESS sequence. The spectra show progressively smaller amplitudes with an increase in echo times. The spectrum with an echo time of 30 ms in Figure 4.15B has its peak at approximately 4.85 ppm (akin to the spectrum shown in Figure 4.7A with a TE of 30 ms). For the reasons explained above, the position of the spectrum has been corrected.

Figure 4.16 shows the spectra of the PRESS measurements with a flow velocity of 0.46 mm/s obtained to compare the standard and flow-sensitised sequences. Figure 4.16A shows the spectra acquired using the standard PRESS sequence (identical to the spectra

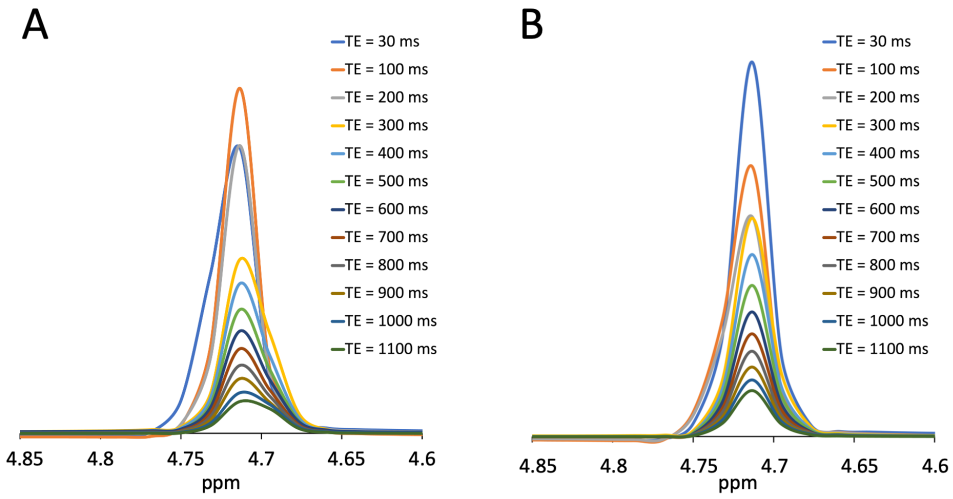

Figure 4.15: Comparison of the standard and flow-sensitised PRESS sequences without flow. [A] shows the spectra acquired with the standard PRESS sequence. [B] shows the spectra acquired with the flow-sensitised PRESS sequence.

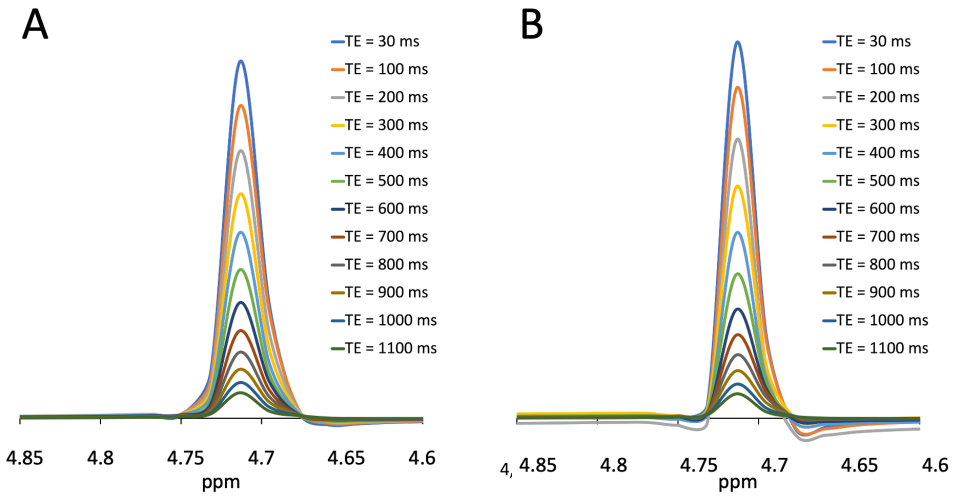

Figure 4.16: Comparison of the standard and flow-sensitised PRESS sequences with a flow velocity of 0.46 mm/s. [A] shows the spectra acquired with the standard PRESS sequence. [B] shows the spectra acquired with the flow-sensitised PRESS sequence.

presented in Figure 4.7B, where the features of the spectra are discussed). These are shown for comparison. Figure 4.16B shows the spectra acquired using the flow-sensitised PRESS sequence. The spectra show progressively smaller amplitudes with an increase in echo times.

Figure 4.17 shows the spectra of the PRESS measurements with a flow velocity of

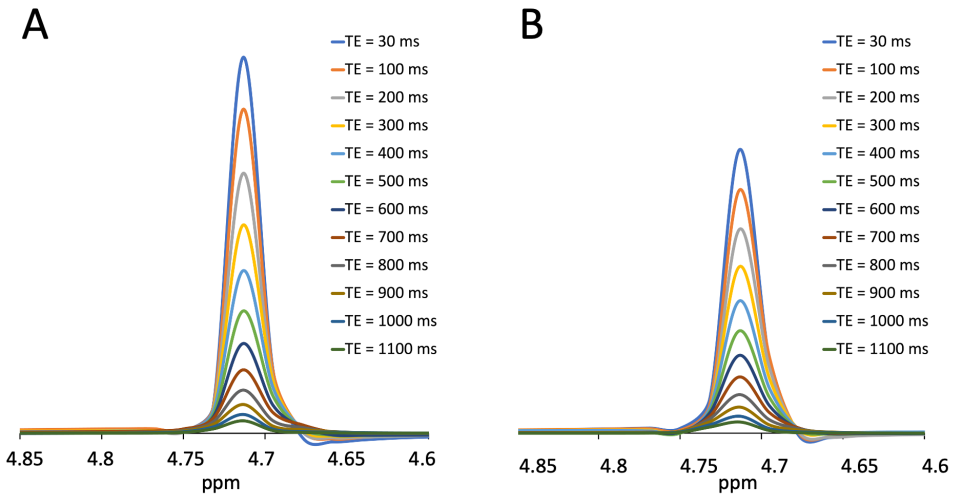

Figure 4.17: Comparison of the standard and flow-sensitised PRESS sequences with a flow velocity of 1.00 mm/s. [A] shows the spectra acquired with the standard PRESS sequence. [B] shows the spectra acquired with the flow-sensitised PRESS sequence.

1.00 mm/s obtained to compare the standard and flow-sensitised sequences. Figure 4.17A shows the spectra acquired using the standard PRESS sequence (identical to the spectra presented in Figure 4.7C, where the features of the spectra are discussed). These are shown for comparison. Figure 4.17B shows the spectra acquired using the flow-sensitised PRESS sequence. The spectra show progressively smaller amplitudes with an increase in echo times.

Figure 4.18 shows the spectra of the PRESS measurements with a flow velocity of 1.85 mm/s obtained to compare the standard and flow-sensitised sequences. Figure 4.18A shows the spectra acquired using the standard PRESS sequence (identical to the spectra presented in Figure 4.7D, where the features of the spectra are discussed). These are shown for comparison. Figure 4.18B shows the spectra acquired using the flow-sensitised PRESS sequence. The peaks of the spectra in Figure 4.18B are broad and irregular. A tendency can be seen that longer echo times lead to smaller amplitudes. Apparent exceptions are the spectra with echo times of 30 and 200 ms, as the latter has a larger amplitude than the former.

Amplitudes of the spectra acquired in the phantom measurements comparing standard and flow-sensitised PRESS sequences

The amplitudes of the spectra were evaluated with AMARES and are listed in Table 4.11. As the corresponding measurements using the standard PRESS sequence were already presented in Table 4.3, the amplitudes are not listed again. Figure 4.15 compares the

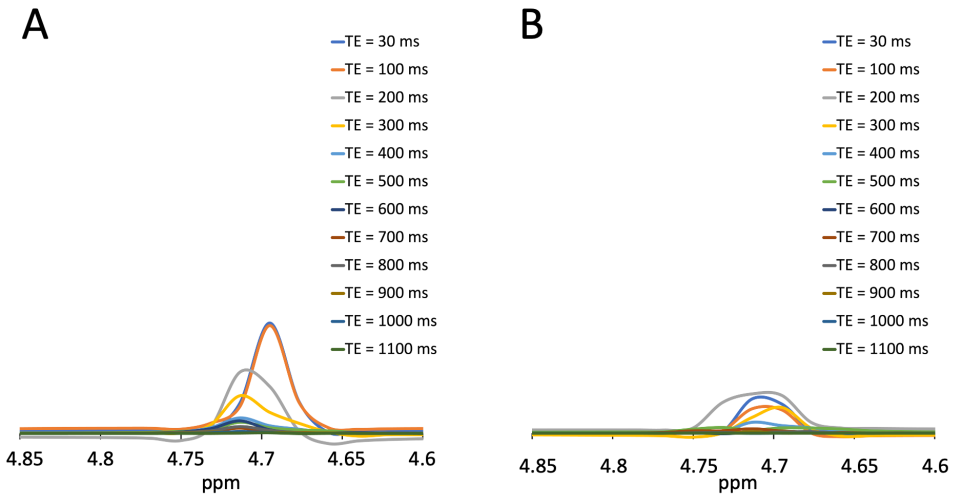

Figure 4.18: Comparison of the standard and flow-sensitised PRESS sequences with a flow velocity of 1.85 mm/s. [A] shows the spectra acquired with the standard PRESS sequence. [B] shows the spectra acquired with the flow-sensitised PRESS sequence.

standard and flow-sensitised PRESS sequence without flow. It can be seen in Figure 4.15 that the amplitudes of both sequences are nearly equal for all echo times investigated.

Figure 4.19 shows the amplitudes determined by the AMARES algorithm for the measurements done with the standard and flow-sensitised PRESS sequence.

Figure 4.19A compares the standard and flow-sensitised PRESS sequence with no flow inside the phantom. It can be seen that the amplitudes for all echo times are nearly identical.

Figure 4.19B compares the standard and flow-sensitised PRESS sequence with a mean flow velocity of 0.46 mm/s. For echo times between 30 and 600 ms, the amplitudes of both sequences are markedly different. This is not the case for the above measurements without flow. However, the difference is not as pronounced for echo times of 700 ms and above. The amplitudes for both the standard and flow-sensitised PRESS sequences are smaller than for measurements without flow.

Figure 4.19C compares the standard and flow-sensitised PRESS sequence with a mean flow velocity of 1.00 mm/s. It can be seen that for echo times between 30 and 500 ms, the amplitudes of both sequences are markedly different. However, the difference is not as pronounced for echo times of 600 ms and above. The amplitudes for both the standard and flow-sensitised PRESS sequences are smaller than in the measurements with a flow of 0.46 mm/s.

Figure 4.19D compares the standard and flow-sensitised PRESS sequence with a mean flow velocity of 1.85 mm/s It can be seen that for echo times between 30 and 400 ms,

Table 4.11: Maximal amplitudes in the phantom measurements using flow-sensitised PRESS.

TE [ms]	No flow	Flow 1, 0.46 $\frac{mm}{s}$	Flow 2, 1.00 $\frac{mm}{s}$	Flow 3, 1.85 $\frac{mm}{s}$
30	370000	320000	239000	49200
100	331000	285000	218000	41000
200	277000	244000	184000	62900
300	229000	191000	152000	41000
400	191000	158000	125000	14200
500	158000	123000	104000	16600
600	131000	97500	83800	630
700	108000	76200	64100	8350
800	89000	61100	47100	2440
900	73400	46700	32800	647
1000	60000	33500	22000	112
1100	49300	23400	14600	88.6

the amplitudes of both sequences are markedly different. However, the differences vary for echo times of 500 ms and above, and for an echo time of 700 ms, the flow-sensitised PRESS sequence shows an even larger amplitude than the standard PRESS sequence. The amplitudes are smaller than in the measurements with a flow of 1.00 mm/s. Compared to the measurements with no flow, a flow velocity of 0.46, and 1.00 mm/s, the amplitudes decline more chaotically. The amplitude of the flow-sensitised sequence for an echo time of 200 ms is larger than that for 30 and 100 ms.

Figure 4.20 shows the signal amplitudes of all the above measurements using the flow-sensitised PRESS sequence. It can be seen that the amplitudes decrease with increasing flow velocity. The decay for the test series with a flow of 1.85 mm/s is not as continuous as for the other three test series. The test series with a flow of 1.85 mm/s shows small absolute amplitudes compared to measurements without flow and smaller flow velocities.

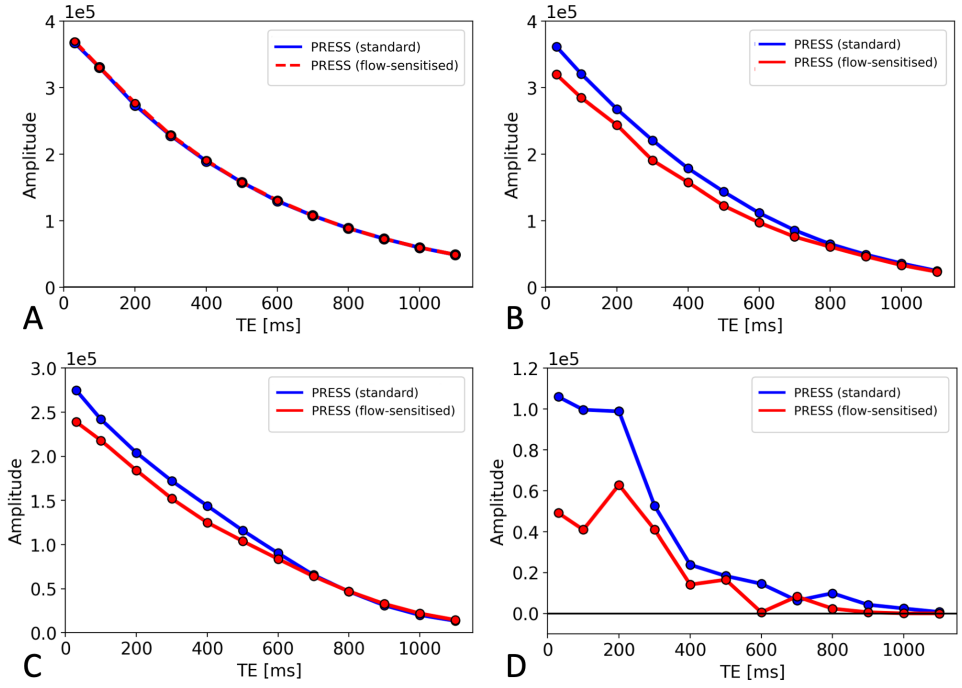

Figure 4.19: Comparison of the amplitudes of the standard and flow-sensitised PRESS sequences. [A] Comparison between the standard and flow-sensitised PRESS sequence with no flow. [B] Comparison between the standard and flow-sensitised PRESS sequence with a flow velocity of 0.46 mm/s. [C] Comparison between the standard and flow-sensitised PRESS sequence with a flow velocity of 1.00 mm/s. [D] Comparison between the standard and flow-sensitised PRESS sequence with a flow velocity of 1.85 mm/s.

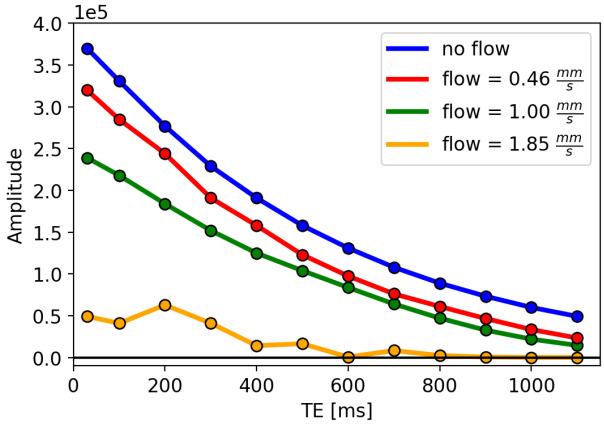

Figure 4.20: Illustration of the signal decay of different flow velocities using the flow-sensitised PRESS sequence. This figure shows the decline in signal amplitudes with increasing echo times determined using the AMARES algorithm. The legend on the upper right shows the colours corresponding to the flow velocities.

4.3.2 Phantom measurements comparing the standard and flow-sensitised STEAM sequences

The measurements presented here compared the standard STEAM sequence to the flow-sensitised sequence. In addition to measurements without flow, measurements with flowing nickel sulfate solution were made.

Measurement conditions and sequence parameters

The mean flow velocities were 0.26, 1.10, and 1.21 mm/s. These were the same conditions that are presented in Section 2.6, where the calculation of the flow velocities is shown. As mentioned in Section 2.6, it was planned that flow velocities 5 and 6 are further apart.

A repetition time of 2300 ms was used. The voxel had an edge length of 13 x 13 x 13 mm. One measurement consisted of 12 scans. The mixing time was 10 ms in every measurement. The head coil described in Section 2.6 was used. The voxel's position was equal for the standard and flow-sensitised STEAM sequence measurements. For all test series, spectra for various echo times were acquired. The echo times were 20, 100, 200, 300, 400, 500, 600, 700, 800, 900, 1000, and 1100 ms.

Spectra acquired in the phantom measurements comparing standard and flow-sensitised STEAM sequences

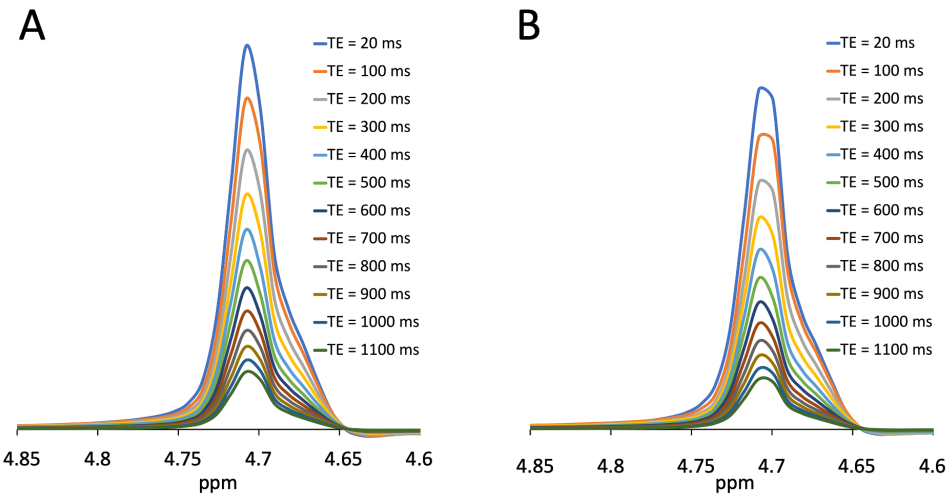

Figure 4.21: Comparison of the standard and flow-sensitised STEAM sequences without flow. [A] shows the spectra acquired with the standard STEAM sequence. [B] shows the spectra acquired with the flow-sensitised STEAM sequence.

Figure 4.21 shows the spectra of the STEAM measurements without flow obtained to compare the standard and flow-sensitised sequences. Figure 4.21A shows the spectra acquired using the standard STEAM sequence (identical to the spectra presented in Figure 4.9A, where the features of the spectra are discussed). These are shown for comparison. Figure 4.21B shows the spectra acquired using the flow-sensitised STEAM sequence. The spectra show progressively smaller amplitudes with an increase in echo times. The shape of the peaks is similar in Figure 4.21A and B. However, the peaks of the spectra that were acquired with the flow-sensitised sequences are less pointed than the ones acquired with the standard STEAM sequence.

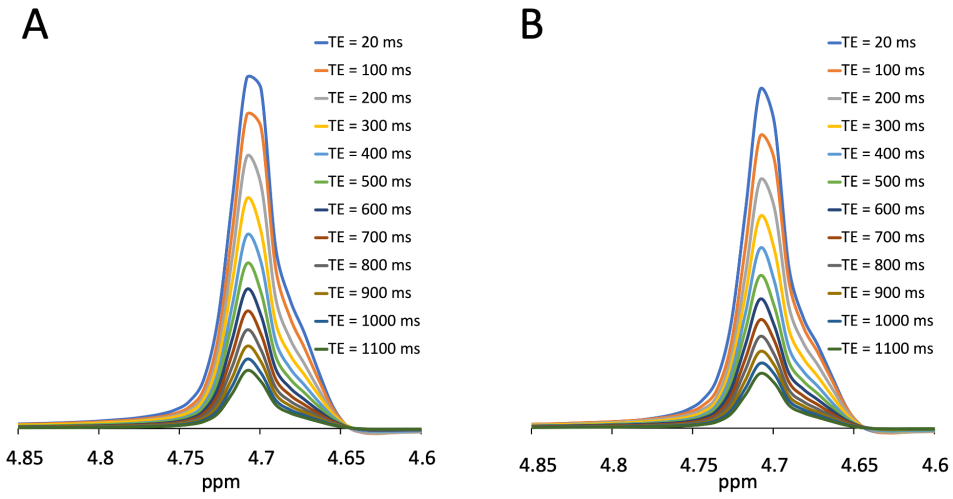

Figure 4.22: Comparison of the standard and flow-sensitised STEAM sequences with a flow velocity of 0.29 mm/s. [A] shows the spectra acquired with the standard STEAM sequence. [B] shows the spectra acquired with the flow-sensitised STEAM sequence.

Figure 4.22 shows the spectra of the STEAM measurements with a flow velocity of 0.29 mm/s obtained to compare the standard and flow-sensitised sequences. Figure 4.22A shows the spectra acquired using the standard STEAM sequence (identical to the spectra presented in Figure 4.9B, where the features of the spectra are discussed). These are shown for comparison. Figure 4.22B shows the spectra acquired using the flow-sensitised STEAM sequence. The spectra show progressively smaller amplitudes with an increase in echo times. The shape of the peaks is similar in Figure 4.22A and B.

Figure 4.23 shows the spectra of the STEAM measurements with a flow velocity of 1.10 mm/s obtained to compare the standard and flow-sensitised sequences. Figure 4.23A shows the spectra acquired using the standard STEAM sequence (identical to the spectra presented in Figure 4.9C, where the features of the spectra are discussed). These are shown for comparison. Figure 4.23B shows the spectra acquired using the flow-sensitised

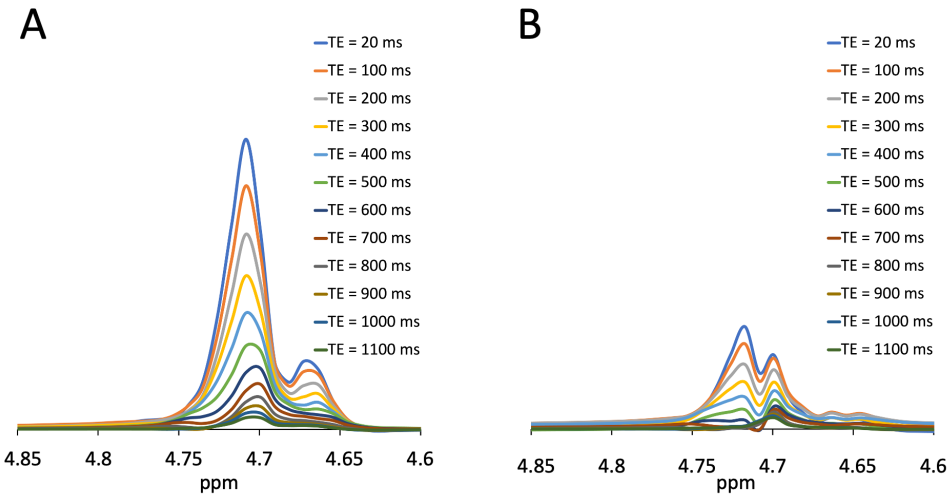

Figure 4.23: Comparison of the standard and flow-sensitised STEAM sequences with a flow velocity of 1.10 mm/s. [A] shows the spectra acquired with the standard STEAM sequence. [B] shows the spectra acquired with the flow-sensitised STEAM sequence.

STEAM sequence. The spectra show progressively smaller amplitudes with an increase in echo times. As in Figure 4.23A, an indentation can be seen in Figure 4.23B. Relative to the height of the peak, the indentation is more prominent in the spectra acquired with the flow-sensitised sequence.

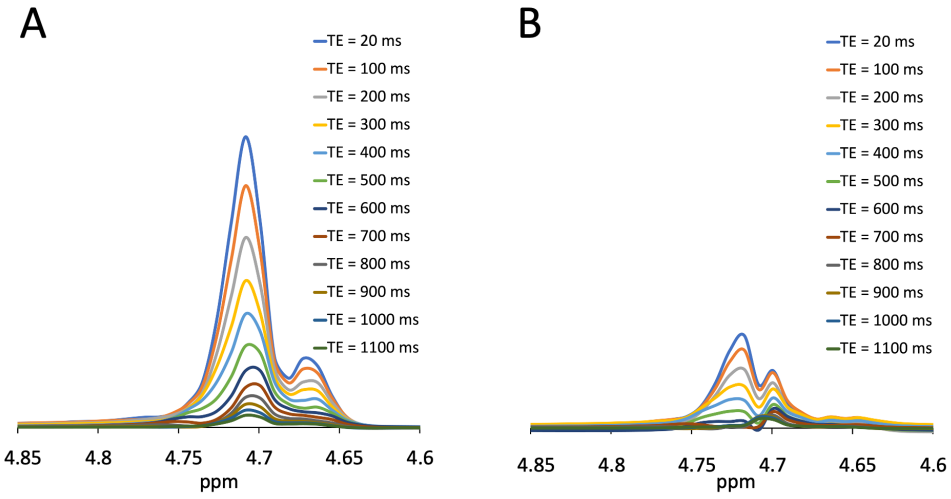

Figure 4.24: Comparison of the standard and flow-sensitised STEAM sequences with a flow velocity of 1.21 mm/s. [A] shows the spectra acquired with the standard STEAM sequence. [B] shows the spectra acquired with the flow-sensitised STEAM sequence.

Figure 4.24 shows the spectra of the STEAM measurements with a flow velocity of 1.21 mm/s obtained to compare the standard and flow-sensitised sequences. Figure 4.24A shows the spectra acquired using the standard STEAM sequence (identical to the spectra presented in Figure 4.9D, where the features of the spectra are discussed). These are shown for comparison. Figure 4.24B shows the spectra acquired using the flow-sensitised STEAM sequence. The spectra show progressively smaller amplitudes with an increase in echo times. As in Figure 4.24A, an indentation can be seen in Figure 4.24B. Relative to the height of the peak, the indentation is more prominent in the spectra acquired with the flow-sensitised sequence. The pattern is similar to the one shown for a flow velocity of 1.10 mm/s.

Table 4.12: Maximal amplitudes in the phantom measurements using flow-sensitised STEAM.

TE [ms]	No flow	Flow 4, 0.29 $\frac{mm}{s}$	Flow 5, 1.10 $\frac{mm}{s}$	Flow 6, 1.21 $\frac{mm}{s}$
20	210000	206000	74000	67000
100	182000	180000	60500	58400
200	153000	150000	49100	53000
300	127000	126000	42400	38300
400	107000	106000	30100	31900
500	89100	88200	29700	30500
600	74400	73800	18400	23600
700	62100	61800	6390	5650
800	51900	51700	4750	4420
900	43300	43300	4870	4690
1000	35900	36200	4900	4680
1100	29800	30100	4390	4070

Amplitudes of the spectra acquired in the phantom measurements comparing standard and flow-sensitised PRESS sequences

AMARES was used to determine the amplitudes of the spectra. The amplitudes are listed in Table 4.12. The corresponding amplitudes of the standard STEAM measurements are listed in Table 4.6.

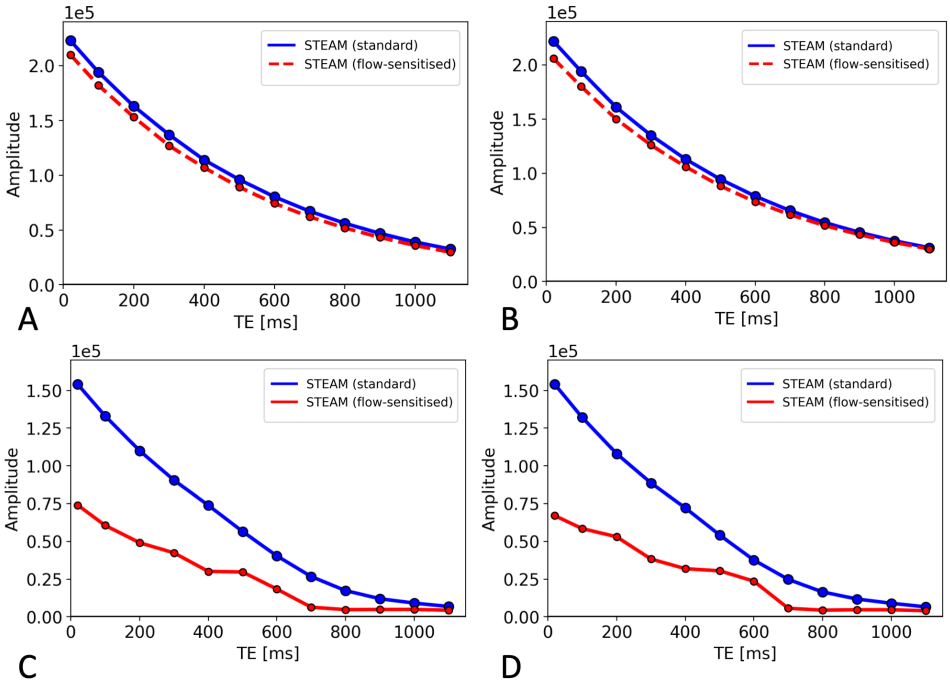

Figure 4.25: Comparison of the amplitudes of the standard and flow-sensitised STEAM sequences. [A] Comparison between the standard and flow-sensitised STEAM sequence with no flow. [B] Comparison between the standard and flow-sensitised STEAM sequence with a flow velocity of 0.29 mm/s. [C] Comparison between the standard and flow-sensitised STEAM sequence with a flow velocity of 1.10 mm/s. [D]Comparison between the standard and flow-sensitised STEAM sequence with a flow velocity of 1.21 mm/s.

Figure 4.25 shows the amplitudes determined by the AMARES algorithm for the measurements done with the standard and flow-sensitised STEAM sequence.

Figure 4.25A compares the standard and flow-sensitised STEAM sequence with no flow inside the phantom. It can be seen that the amplitudes for all echo times are smaller in the case of the flow-sensitised STEAM sequence. However, the difference is comparatively small. The amplitudes of both measurement sets decline with an increase in the echo time.

Figure 4.25B compares the standard and flow-sensitised STEAM sequence with a mean flow velocity of 0.29 mm/s. It can be seen that the amplitudes for all echo times

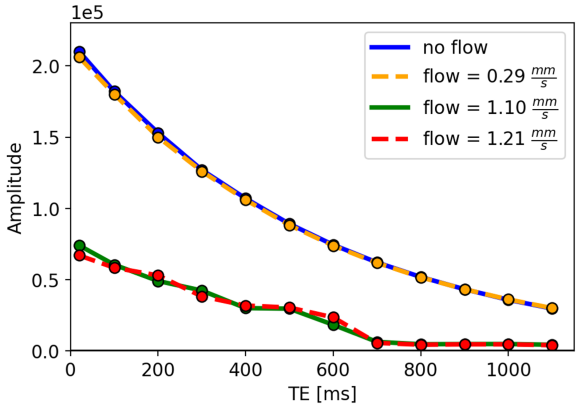

Figure 4.26: Illustration of the signal decay of different flow velocities using the flow-sensitised STEAM sequence. This figure shows the decline in signal amplitudes with increasing echo times determined using the AMARES algorithm. The legend on the upper right shows the colours corresponding to the flow velocities.

are smaller in the case of the flow-sensitised STEAM sequence. However, the difference is comparatively small. The amplitudes of both measurement sets decline with an increase in the echo time.

Figure 4.25C compares the standard and flow-sensitised STEAM sequence with a mean flow velocity of 1.10 mm/s. Here, the difference between the amplitudes is much more pronounced. The amplitudes of the spectra acquired with the flow-sensitised STEAM sequence are approximately half as large as the ones obtained with the standard STEAM sequence. The amplitudes of both measurement sets decline with an increase in the echo time.

Figure 4.25D compares the standard and flow-sensitised STEAM sequence with a mean flow velocity of 1.21 mm/s. The difference between both sets of amplitudes is as pronounced as in the case of a flow velocity of 1.10 mm/s. The amplitudes of both measurement sets decline with an increase in the echo time.

Figure 4.26 shows the signal amplitudes of all the above measurements using the flow-sensitised STEAM sequence. It can be seen that the amplitudes of the measurements with a flow velocity of 0.29 mm/s are very similar to the amplitudes of the measurements without flow. On the other hand, the measurements with flow velocities of 1.10 mm/s and 1.21 mm/s show very similar amplitudes as well. However, the difference between both groups is pronounced. The measurements with flow velocities of 1.10 mm/s and 1.21 mm/s show far smaller amplitudes than the former measurements.

4.4 In vivo measurements

Here, the results of the in vivo measurements are presented. The in vivo measurements using the PRESS sequences are presented in the first subsection. The results of the in vivo measurements using the STEAM sequences are shown in the second subsection.

4.4.1 In vivo measurements comparing standard and flow-sensitised PRESS sequences

Measurement conditions and sequence parameters

The author chose a repetition time of 2000 ms. The voxel had an edge length of 13 x 13 x 13 mm. One measurement consisted of 32 scans. The position of the voxel was equal for all measurements. For all test series, spectra with various echo times were acquired. The echo times were 35, 50, 65, 80, 95, 110, 125, and 150 ms in Subject 1. Because the signal amplitudes in Subject 2 were smaller, shorter echo times were used. The echo times were 35, 42, 50, 57, 65, 72, 80, and 95 ms in Subject 2. Subsection 3.3.2 lists all other information about the experimental setup.

Spectra acquired in the in vivo measurements comparing standard and flow-sensitised PRESS sequences

Figure 4.27 shows the spectra acquired with PRESS sequences in Subject 1. Figure 4.27A shows the measurement series that was performed with the standard PRESS sequence. It can be seen that the peak corresponding to the water molecules at around 4.7 ppm is higher than the peak corresponding to the lipids at about 1 ppm. The amplitudes of the peaks diminish with rising echo times. The decline in the amplitudes is more pronounced for the water peak than the lipid peak. At an echo time of 150 ms, only a tiny water signal is noticeable, while the peak of the lipids can be seen easily. Figure 4.27B shows the measurement series performed with the flow-sensitised PRESS sequence. No significant differences in shape can be observed comparing both series.

Figure 4.28 shows the spectra acquired with PRESS sequences in Subject 2. Figure 4.28A shows a measurement series performed with the standard PRESS sequence. It can be seen that the peak corresponding to the water molecules at around 4.7 ppm is smaller than the peak corresponding to the lipids at about 1 ppm. This is not the case for Subject 1. The amplitudes of the peaks diminish with rising echo times. The decline in the amplitudes is more pronounced for the water peak than the lipid peak. At an echo time of 95 ms, only a tiny water signal is noticeable, while the peak of the lipids is still large. Figure 4.28B

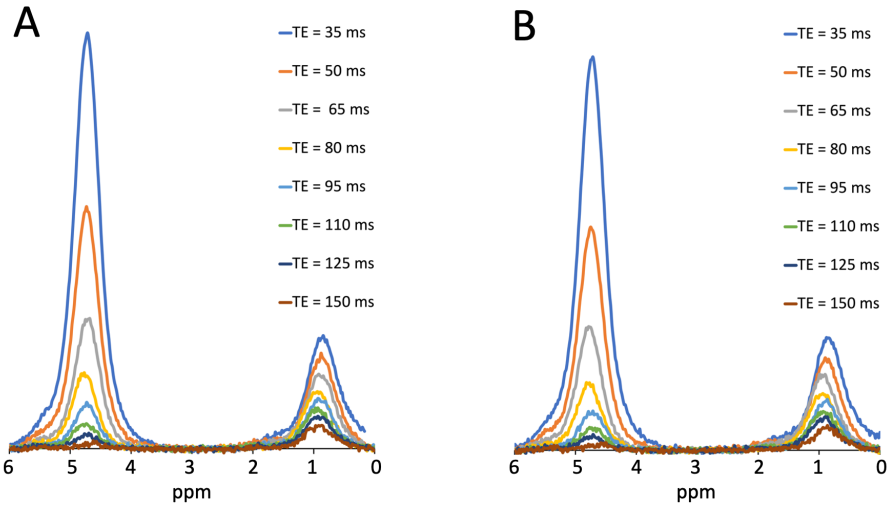

Figure 4.27: Comparison of the standard and flow-sensitised PRESS sequences in Subject 1. [A] shows the spectra acquired with the standard PRESS sequence. [B] shows the spectra acquired with the flow-sensitised PRESS sequence. The peak at around 4.7 ppm corresponds to the water molecules, while the peak at about 1 ppm corresponds to the lipids.

shows the measurement series performed with the flow-sensitised PRESS sequence in Subject 2. No significant differences in shape can be observed comparing both series.

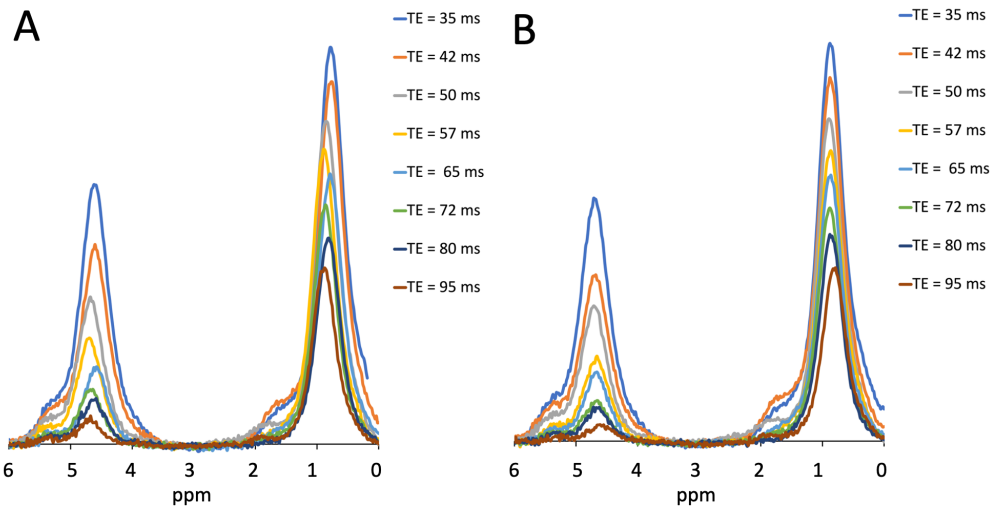

Figure 4.28: Comparison of the standard and flow-sensitised PRESS sequences in Subject 2. [A] shows the spectra acquired with the standard PRESS sequence. [B] shows the spectra acquired with the flow-sensitised PRESS sequence.

Amplitudes of the spectra acquired in the in vivo measurements comparing standard and flow-sensitised PRESS sequences

Table 4.13 shows the amplitudes determined for the PRESS spectra in Subject 1. These were determined using the AMARES algorithm. The amplitudes are significantly smaller than the amplitudes determined in the phantom measurements.

Table 4.13: Maximal amplitudes in the in vivo measurements using standard and flow-sensitised PRESS, Subject 1.

TE [ms]	Subject 1 standard	Subject 1 flow-sensitised
35	13500	12900
50	7880	7380
65	4230	3990
80	2390	2150
95	1360	1230
110	789	703
125	433	434
150	171	186

Table 4.14 shows the amplitudes determined for the PRESS spectra in Subject 2. These were determined using the AMARES algorithm.

The amplitudes listed in Tables 4.13 and 4.14 are shown graphically in Figure 4.29. While Figure 4.29A depicts the amplitudes for Subject 1, Figure 4.29B depicts the amplitudes for Subject 2. The decline in the amplitudes with rising echo times can be seen in both cases. For Subject 1, a tendency can be seen that the flow-sensitised PRESS sequences yield slightly smaller amplitudes than the standard PRESS sequences. However, this was not the case for echo times of 125 and 150 ms, as can be appreciated in Table 4.13. The same tendency can be seen for Subject 2. However, the trend is more pronounced for Subject 2. As can be seen from Table 4.14, the amplitude obtained by the standard PRESS sequence is larger than the amplitude obtained by the flow-sensitised PRESS sequence in every case.

Table 4.14: Maximal amplitudes in the in vivo measurements using standard and flow-sensitised PRESS, Subject 2.

TE [ms]	Subject 2 standard	Subject 2 flow-sensitised
35	9360	8830
42	6980	6230
50	4970	4750
57	3460	2830
65	2360	2150
72	1700	1290
80	1310	1030
95	707	491

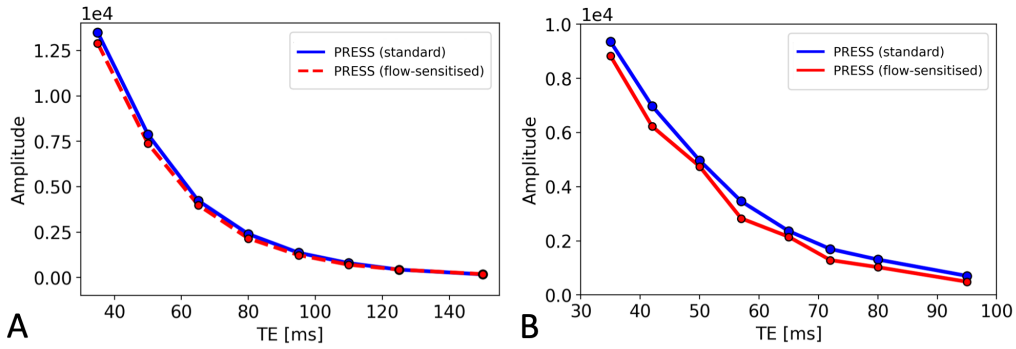

Figure 4.29: Water peak amplitudes of the spectra acquired using standard and flow-sensitised PRESS sequences in vivo. [A] depicts the amplitudes of the spectra acquired in Subject 1. [B] depicts the amplitudes acquired in Subject 2.

4.4.2 In vivo measurements comparing standard and flow-sensitised STEAM sequences

Measurement conditions and sequence parameters

The author chose a repetition time of 2000 ms. The voxel had an edge length of 13 x 13 x 13 mm. One measurement consisted of 32 scans. The position of the voxel was equal

for all measurements. For all test series, spectra with various echo times were acquired. The echo times were 20, 27, 35, 50, 65, 80, and 100 ms in Subject 1. Because the signal amplitudes in Subject 2 were smaller, shorter echo times were used. The echo times were 20, 27, 35, 42, 50, 57, and 65 ms in Subject 2. Subsection 3.3.2 lists all other information about the experimental setup.

Spectra acquired in the in vivo measurements comparing standard and flow-sensitised STEAM sequences

STEAM measurements in Subject 1 Figure 4.30 shows the spectra acquired with STEAM sequences in Subject 1. The mixing time used was 10 ms in all cases. Figure 4.30A shows the measurement series that was performed with the standard STEAM sequence. It can be seen that the peak corresponding to the water molecules at around 4.7 ppm is larger than the peak corresponding to the lipids at about 1 ppm. The amplitudes of the peaks diminish with rising echo times. The decline in the amplitudes is more pronounced for the water peak than the lipid peak. Figure 4.30B shows the measurement series performed with the flow-sensitised STEAM sequence. No significant differences in shape can be observed comparing both series.

There was a slight difference in the positioning of the voxel between the measurements of the standard and flow-sensitised STEAM sequences in Subject 1 due to technical issues. The positioning was approximately 2 mm different along all axes.

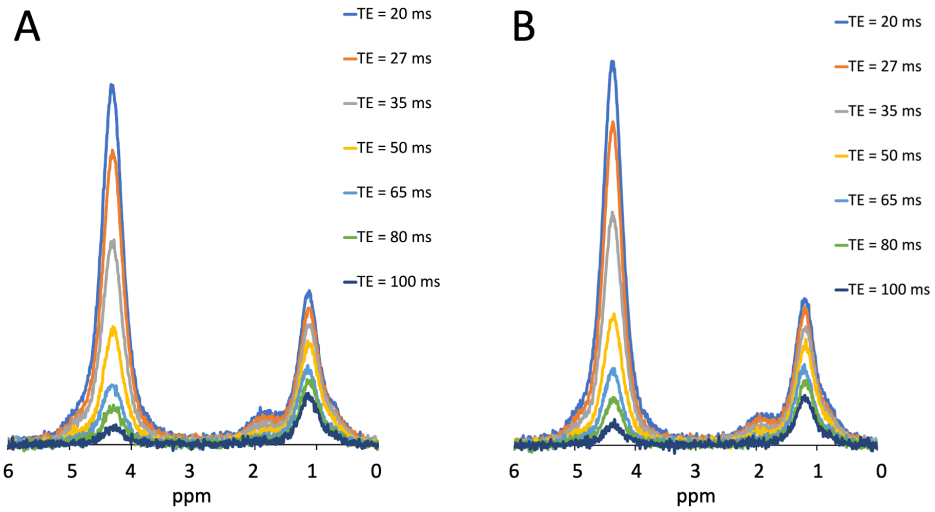

Figure 4.30: Comparison of the standard and flow-sensitised STEAM sequences in Subject 1. [A] shows the spectra acquired with the standard STEAM sequence. [B] shows the spectra acquired with the flow-sensitised STEAM sequence.

STEAM measurements in Subject 2 with a mixing time of 10 ms Figure 4.31 shows the spectra acquired with STEAM sequences in Subject 2 using a mixing time of 10 ms. Figure 4.31A shows the measurement series that was performed with the standard STEAM sequence. It can be seen that the peak corresponding to the water molecules at around 4.7 ppm is smaller than the peak corresponding to the lipids at about 1 ppm. This was not the case for Subject 1. The amplitudes of the peaks diminish with rising echo times. The decline in the amplitudes is more pronounced for the water peak than the lipid peak. Figure 4.31B shows the measurement series performed with the flow-sensitised STEAM sequence in Subject 2. No significant differences in shape can be observed comparing both series.

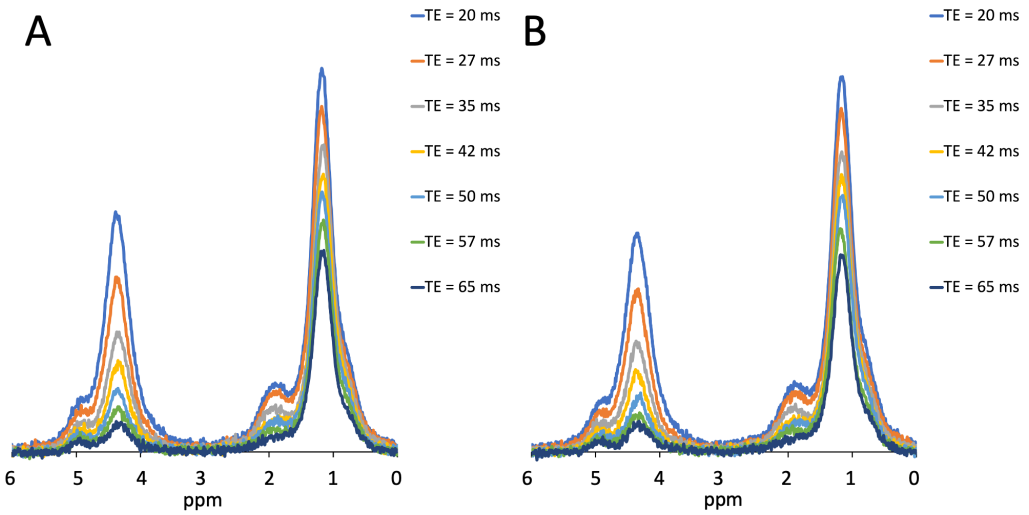

Figure 4.31: Comparison of the standard and flow-sensitised STEAM sequences in Subject 2 with TM = 10 ms. [A] shows the spectra acquired with the standard STEAM sequence. [B] shows the spectra acquired with the flow-sensitised STEAM sequence.

STEAM measurements in Subject 2 with a mixing time of 50 ms Figure 4.32 shows the spectra acquired with STEAM sequences in Subject 2 using a mixing time of 50 ms. Figure 4.32A shows the measurement series that was performed with the standard STEAM sequence. It can be seen that the peak corresponding to the water molecules at around 4.7 ppm is smaller than the peak corresponding to the lipids at about 1 ppm.

Comparing the water peak in Figure 4.31 to the water peak here, it can be noticed that the water peak is smaller compared to the peak corresponding to the lipids. The amplitudes of the peaks diminish with rising echo times. The decline in the amplitudes is more pronounced for the water peak than the lipid peak.

Figure 4.32B shows the measurement series performed with the flow-sensitised STEAM

sequence in Subject 2. No significant differences in shape can be observed comparing both series.

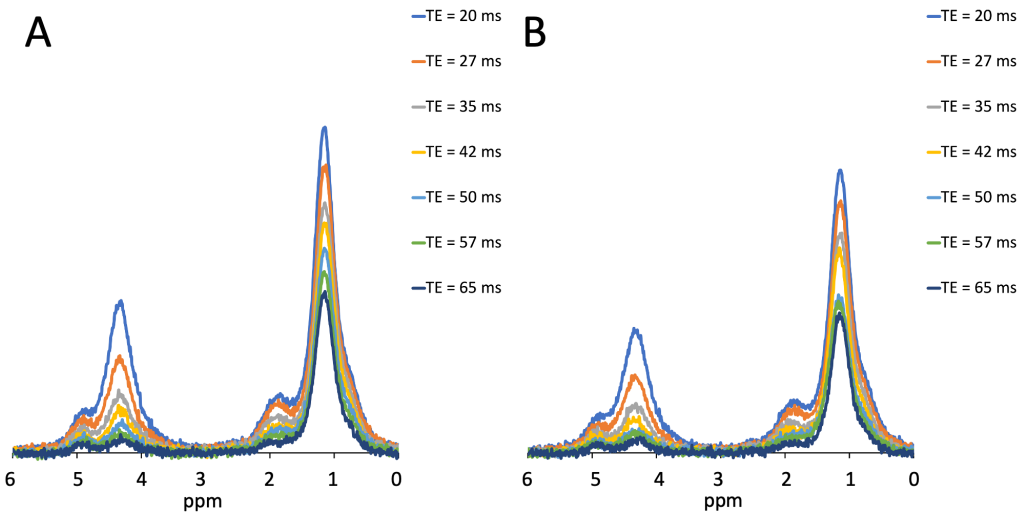

Figure 4.32: Comparison of the standard and flow-sensitised STEAM sequences in Subject 2 with TM = 50 ms. [A] shows the spectra acquired with the standard STEAM sequence. [B] shows the spectra acquired with the flow-sensitised STEAM sequence.

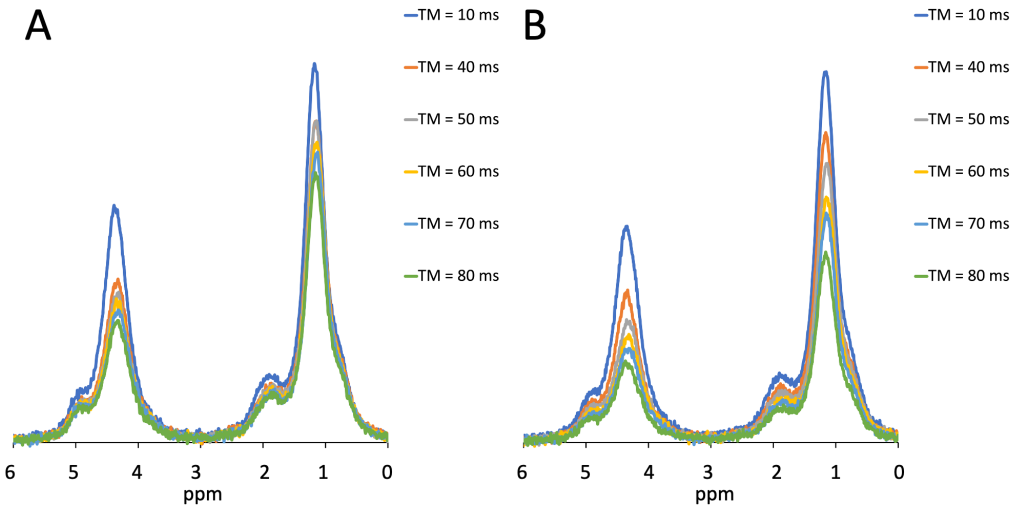

Figure 4.33: Comparison of the standard and flow-sensitised STEAM sequences in Subject 2 with various mixing times. [A] shows the spectra acquired with the standard STEAM sequence. [B] shows the spectra acquired with the flow-sensitised STEAM sequence.

STEAM measurements in Subject 2 with varying mixing times Figure 4.33 shows the spectra acquired with STEAM sequences in Subject 2 with an echo time of 20 ms

and various mixing times. In Figure 4.33A, the measurement series is illustrated that was performed with the standard STEAM sequence. Figure 4.33B shows the measurements performed with the flow-sensitised STEAM sequence. The spectra with mixing times of 10 and 50 ms are identical to the ones shown in Figure 4.31 and 4.32. All other spectra shown in Figure 4.33 stem from a separate set of measurements with the same conditions. Figure 4.33 shows that the water peak declines more rapidly with rising echo times than the lipid peak. This tendency is more prominent for the flow-sensitised sequences than for the standard sequences.

Amplitudes of the spectra acquired in the in vivo measurements comparing standard and flow-sensitised STEAM sequences

STEAM measurements in Subject 1 Table 4.15 shows the amplitudes determined for the STEAM spectra in Subject 1 with a mixing time of 10 ms. These were determined using the AMARES algorithm.

Table 4.15: Maximal amplitudes in the in vivo measurements using standard and flow-sensitised STEAM, Subject 1. The mixing time was 10 ms.

TE [ms]	Standard, TM=10	Flow-sensitised, TM=10
20	9770	10200
27	7820	8090
35	5490	5930
50	3000	3290
65	1600	1870
80	921	1110
100	433	490

STEAM measurements in Subject 2 with mixing times of 10 and 50 ms Tables 4.16 and 4.17 show the amplitudes determined for the STEAM spectra in Subject 2. These were determined using the AMARES algorithm. The amplitudes for both measurement series (TM = 10 ms, TM = 50 ms) are listed.

Table 4.16: Maximal amplitudes of the in vivo measurements with the standard and flow-sensitised STEAM sequence in Subject 2 (TM = 10 ms).

TE [ms]	Standard, TM=10	Flow-sensitised, TM=10
20	7320	6980
27	5060	4830
35	3450	3220
42	2420	2210
50	1800	1510
57	1230	1090
65	828	802

Table 4.17: Maximal amplitudes in the in vivo measurements using standard and flow-sensitised STEAM, Subject 2 (TM = 50 ms).

TE [ms]	Standard, TM=50	Flow-sensitised, TM=50
20	4870	4180
27	3090	2600
35	1930	1630
42	1340	1100
50	926	757
57	622	587
65	430	411

STEAM measurements in Subject 2 with varying mixing times Table 4.18 shows the amplitudes determined for the STEAM spectra in Subject 2 with varying mixing times. These were determined using the AMARES algorithm.

Table 4.18: Maximal amplitudes in the in vivo measurements using standard and flow-sensitised STEAM with varying TM, Subject 2. STEAM sequence with TE = 20 ms. The values denoted by " * " originate from the data in Table 4.16. Those values are comparable as they were acquired under the same conditions in the same examination.

Mixing time [ms]	Standard	Flow-sensitised
10*	7320	6980
40	5270	4890
50*	4870	4180
60	4670	3650
70	4420	3310
80	4060	2770

Comparison of the in vivo measurements with standard and flow-sensitised STEAM sequences The amplitudes listed in Tables 4.15, 4.16, and 4.18 are shown graphically in Figure 4.34. Figure 4.34A depicts the amplitudes for Subject 1. Figure 4.34B depicts the amplitudes for Subject 2 with a mixing time of 10 ms. Figure 4.34C depicts the amplitudes for Subject 2 with a mixing time of 50 ms. The decline in the amplitudes with rising echo times can be seen in all three cases.

In the case of Subject 1, it can be seen that the spectra acquired with the flow-sensitised sequences yield amplitudes larger than the amplitudes of the spectra acquired with the standard STEAM sequences. In the case of Subject 2, the opposite is the case for mixing times of 10 and 50 ms. The flow-sensitised STEAM sequence yields smaller amplitudes in every case. The difference between the standard and flow-sensitised STEAM sequence seems to be larger at a mixing time of 50 ms compared to a mixing time of 10 ms.

Figure 4.35 shows the amplitudes of the water peaks of the spectra acquired with STEAM sequences depending on the mixing time used. It can be seen that the amplitudes of the water peaks of the spectra obtained with the standard STEAM sequence decline with an increase in echo time. The same can be seen for the amplitudes of the water peaks of the spectra acquired with the flow-sensitised STEAM sequence. The amplitudes of the water peaks are smaller in the case of the flow-sensitised sequence for the shortest mixing time of 10 ms compared to the standard STEAM sequence. However, this tendency becomes more pronounced with an increase in mixing time. For a mixing time of 80 ms,

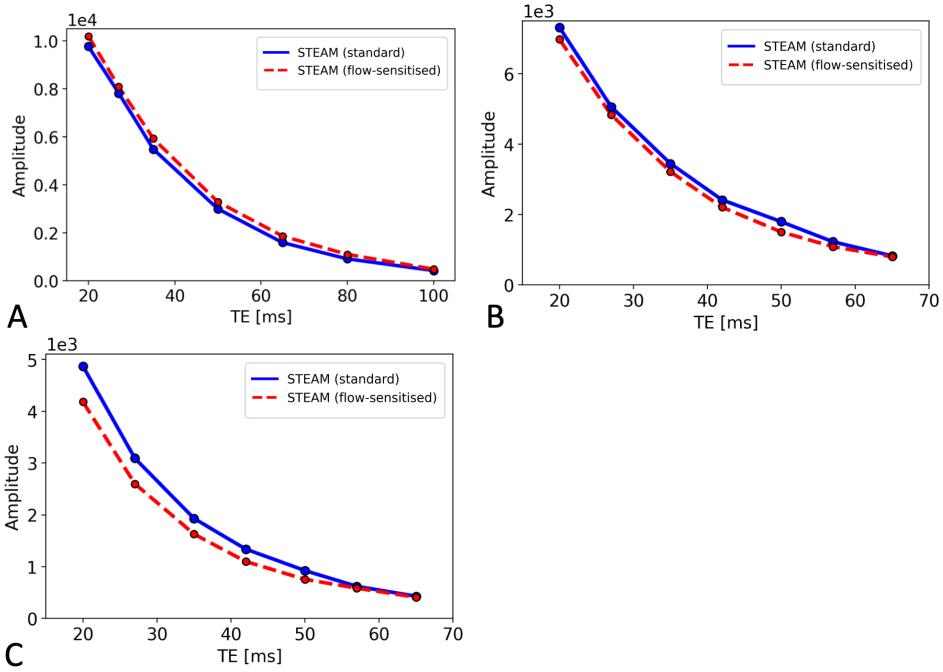

Figure 4.34: Comparison of the water peak amplitudes of the spectra acquired using STEAM sequences in both subjects. [A] compares the water peak amplitudes in Subject 1 using standard and flow-sensitised STEAM sequences. [B] compares the water peak amplitudes in Subject 2 using standard and flow-sensitised STEAM sequences with TM = 10 ms. [C] compares the water peak amplitudes in Subject 2 using standard and flow-sensitised STEAM sequences with TM = 50 ms.

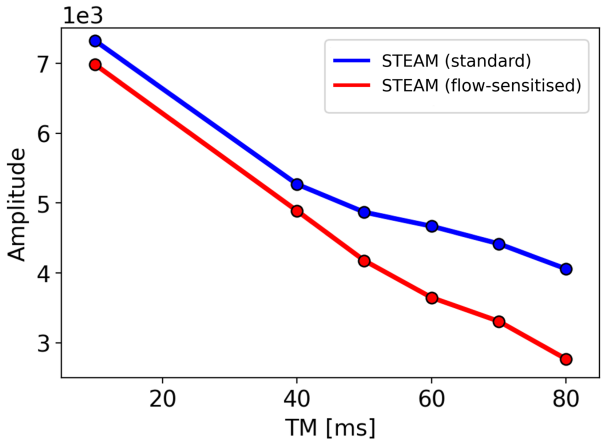

Figure 4.35: Comparison between the water peak amplitudes of the standard and flow-sensitised STEAM sequence with varying TM in Subject 2. STEAM sequence with TE = 20 ms.

the difference in the amplitudes of the water peaks is most noticeable.

Table 4.19 shows the difference in per cent between the amplitudes of the water peak for different mixing times between the standard and flow-sensitised STEAM sequence. This illustrates the tendency for the difference to become larger with increased mixing time. Figure 4.35 illustrates this trend.

Table 4.19: Difference in per cent between the signal amplitudes of the standard and flow-sensitised STEAM measurements with varying TM.

TM [ms]	10	40	50	60	70	80
Difference in per cent (water)	5%	8%	17%	28%	34%	47%

4.5 BOLD-related phase-shift effects in ^{1}H spectroscopy

This section presents the simulation results of the BOLD-related phase-shift effects in PRESS and STEAM sequences. The results provide insights into the magnitude of BOLD-related phase-shift effects encountered in peripheral tissue during MRS. The methods used for the simulation were introduced in Section 3.5. The influence of different parameters on the phase shift of individual ^{1}H nuclei was analysed. The investigated parameters included both sequence-specific factors, such as TE and TM, as well as the tissue-specific parameter flow velocity. As the angle of a vessel relative to B_0 varies and leads to different phase shifts, this parameter was investigated as well.

4.5.1 BOLD-related phase-shift effects in PRESS

BOLD-related phase shift in PRESS for varying flow velocities

Figure 4.36 depicts the influence of different flow velocities on the phase shift generated in PRESS sequences. A short value for TE was chosen (50 ms). The haematocrit, oxygen saturation, and B_0 listed in Table 3.5 were used. A range of flow velocities between 0 and 2.5 mm/s was chosen as this represents the flow velocities encountered in the microvasculature of bone marrow (Subsection 2.5.2). For the curvature of the vessel, a radius of 80 μm was chosen (Subsection 2.5.2). The six different diagrams in Figure 4.36 consider the varying vessel geometry. θ_0 represents the angle of the vessel containing the ^{1}H nucleus at the beginning of the sequence relative to B_0. As the vessels are distributed isotropically in most tissues, θ_0 is highly variable.

The phase shift varied significantly with different flow velocities. Depending on the flow velocity and more strongly on θ_0, the algebraic sign of the phase shift was either positive or negative. For the range of flow velocities considered, higher flow velocities led to stronger absolute phase shifts in most cases. However, for specific geometries, this was not the case (Figure 4.36B and C). The largest phase shifts observed are close to 60° and occurred for flow velocities of 2.5 mm/s when θ_0 equalled 54° and 72°. A flow velocity of 2.5 mm/s corresponds to the upper range of flow within the microvasculature (Subsection 2.5.2). For flow velocities observed in small vessels such as sinusoidal capillaries (0.23 ± 0.22 mm/s), phase shifts were smaller than 10°.

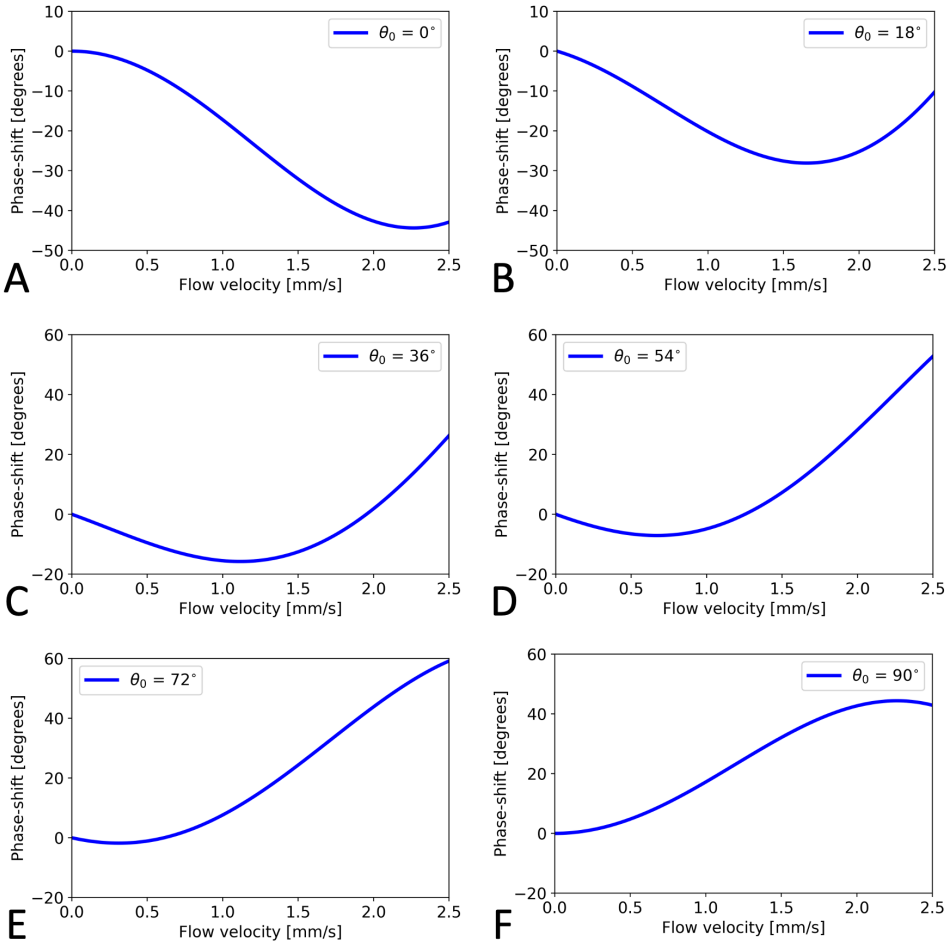

Figure 4.36: BOLD-related phase shift in PRESS for different flow velocities. Here, the phase shifts for flow velocities between 0 and 2.5 mm/s are shown. Different scenarios for the vessel geometry are depicted. θ_0 represents the angle of the vessel that contains the nucleus at the start of the sequence relative to B_0. θ_0 is varied as follows: [A] $\theta_0 = 0°$, [B] $\theta_0 = 18°$, [C] $\theta_0 = 36°$, [D] $\theta_0 = 54°$, [E] $\theta_0 = 72°$, [F] $\theta_0 = 90°$. In all cases, TE was 50 ms.

BOLD-related phase shift in PRESS for varying echo times

Further, the effects of increasing echo times on BOLD-related phase-shift effects were investigated. The results are shown in Figure 4.37. A fixed flow velocity of 0.5 mm/s was chosen, representing flow in capillaries and venules. All other parameters remained constant compared to the investigation of changing flow velocities (see above). The four diagrams in Figure 4.37 differ in θ_0 to take into account the varying vessel geometry. Echo times between 30 and 150 ms were studied because longer echo times led to phase shifts exceeding 180°.

Depending on θ_0 and, to a lesser extent, the echo time (Figure 4.37C), the algebraic sign of the phase shift was either positive or negative. When θ_0 equalled 0°, 30°, and 90°, longer echo times led to stronger dephasing. In case θ_0 equalled 60°, the phase shift decreased for echo times longer than approximately 110 ms. With echo times of 150 ms, phase shifts exceeded 150° when θ_0 equalled 0°, 30°, and 90°. In general, echo times firmly determined the phase shifts.

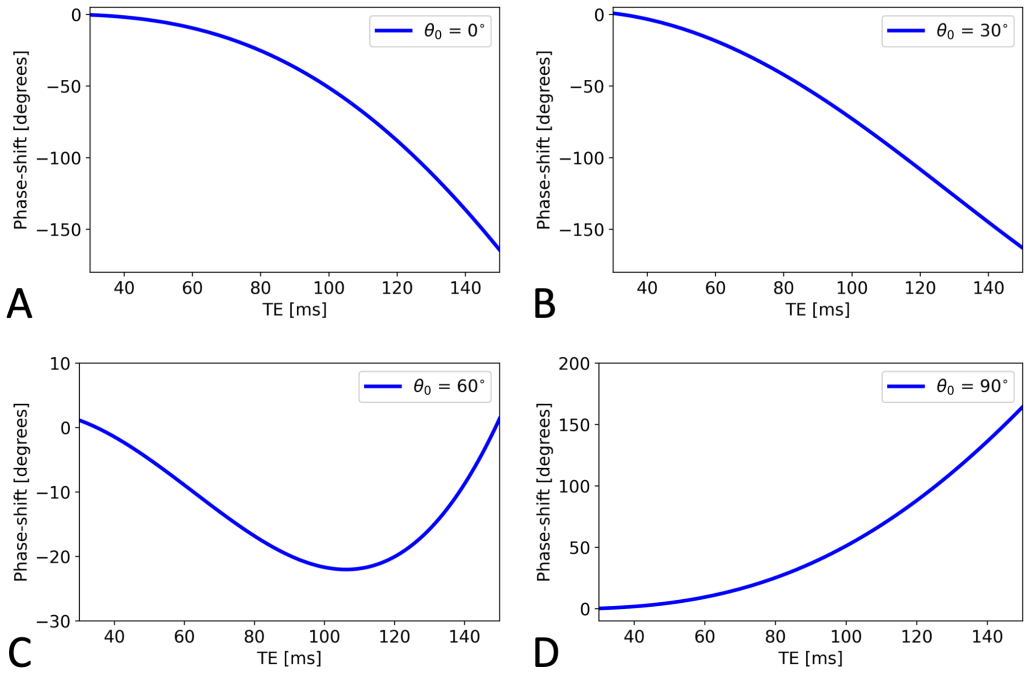

Figure 4.37: BOLD-related phase shift in PRESS for varying echo times. Here, the echo time of the PRESS sequence is varied between 30 and 150 ms. [A]–[D] show the corresponding phase shifts. Note that the plots vary in θ_0 as follows: [A] $\theta_0 = 0°$, [B] $\theta_0 = 30°$, [C] $\theta_0 = 60°$, [D] $\theta_0 = 90°$. In all cases, the flow velocity was 0.5 mm/s.

BOLD-related phase shift in PRESS for varying vessel geometries

As stated above, θ_0 is highly variable in most tissues. Therefore, the influence of θ_0 on BOLD-related phase-shift effects was investigated. θ_0 can assume values between 0° (vessel aligned with B_0) and 180° (vessel antiparallel to B_0). In addition to θ_0, other geometrical parameters can also vary. An ^1H nucleus can either flow through a vessel that bends towards B_0 or that bends away from B_0. So far, only scenarios have been considered where the nucleus flows through a vessel that bends away from B_0. A positive value for θ_0 denotes such a scenario. In Figure 4.38, negative algebraic signs for θ_0 are shown. These represent cases where the vessel bends away from B_0. However, note that $-\theta_0$ still denotes a case in which the absolute angle of the vessel relative to B_0 at the start of the sequence is θ_0.

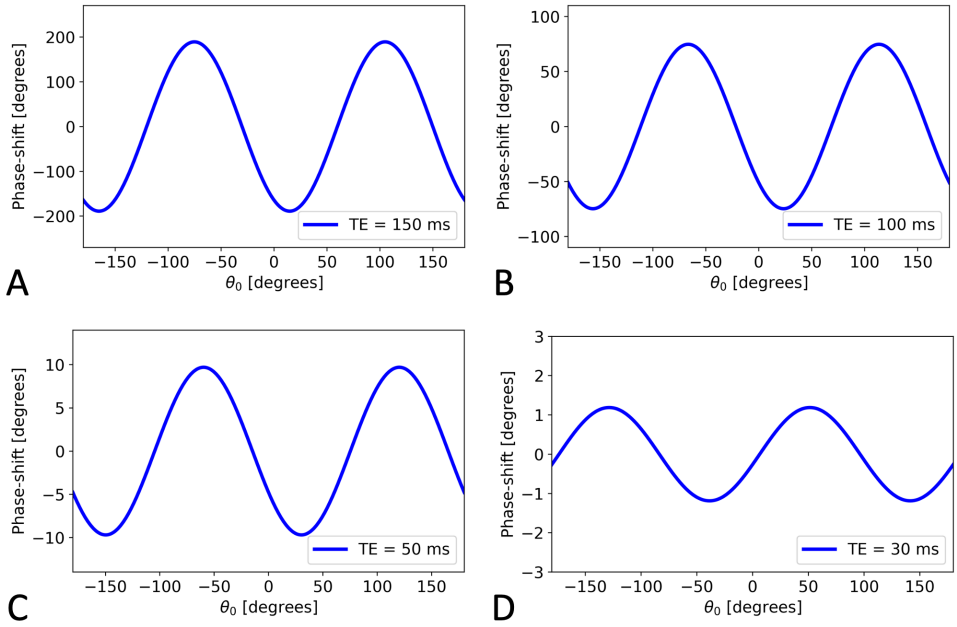

Figure 4.38: BOLD-related phase shift in PRESS for varying vessel geometries. Here, the vessel's geometry is varied, and the resulting phase shifts are shown. Specifically, θ_0 is subject to variations between 0° and 180°. Positive algebraic signs represent a nucleus flowing through a bend that curves away from B_0 (θ gets larger over time). Negative algebraic signs represent a nucleus flowing through a bend that curves towards B_0. This is shown for different echo times: [A] TE = 150 ms, [B] TE = 100 ms, [C] TE = 50 ms, [D] TE = 30 ms. In all cases, the flow velocity was 0.5 mm/s.

In Figure 4.38, the four diagrams differ in the echo times used (30, 50, 100, and 150 ms). θ_0 largely determined the algebraic sign of the resulting phase shift. Generally, the resulting phase shift fluctuated in a sinusoidal fashion depending on θ_0. For echo times of 30 ms, the phase shift fluctuated between 0 and approximately 1.2° depending on θ_0. For echo times of 150 ms, the phase shift fluctuated between 0 and approximately 200°

depending on θ_0. On average, θ_0 significantly influenced the phase shift, meaning that the orientation of the vessels relative to B_0 is relevant in PRESS.

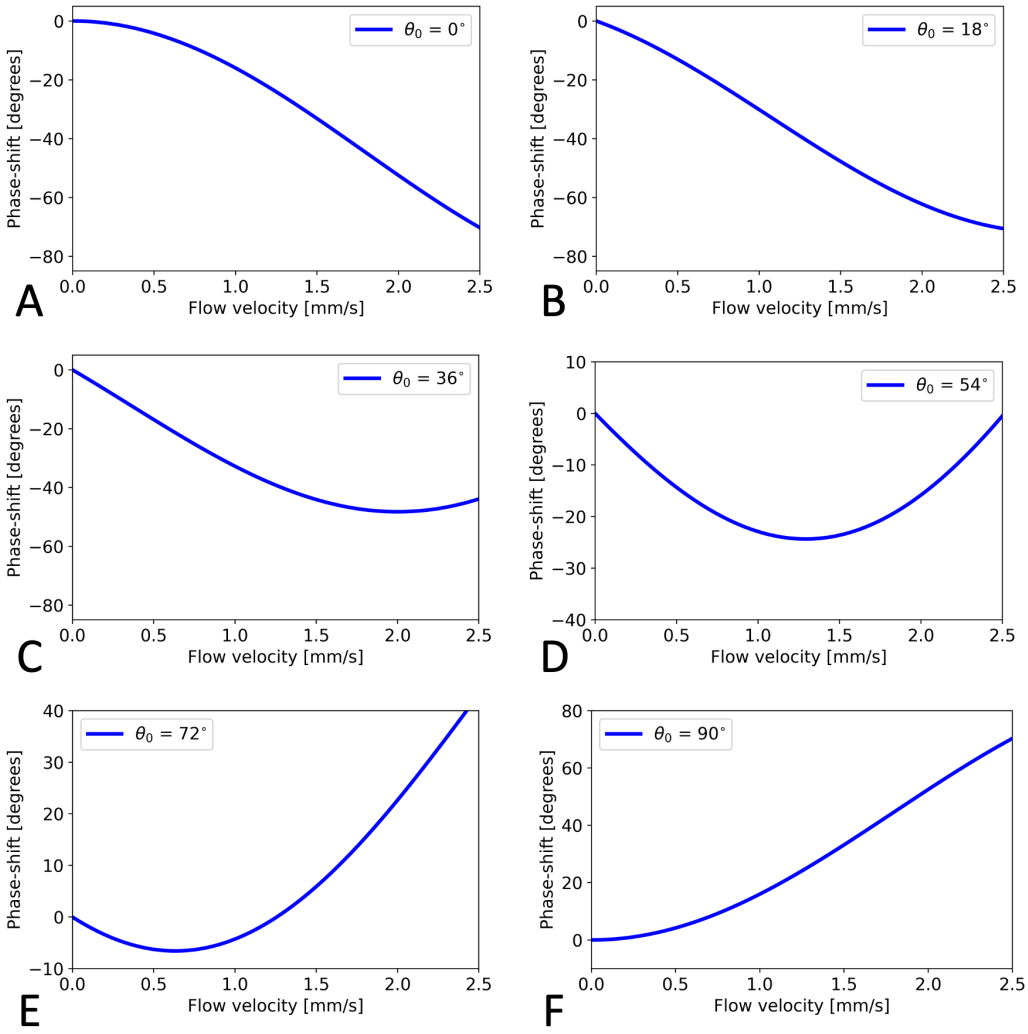

Figure 4.39: BOLD-related phase shift in STEAM for different flow velocities. Here, the phase shifts for flow velocities between 0 and 2.5 mm/s are shown. Further, different scenarios for the vessel geometry are considered. θ_0 represents the angle of the vessel that contains the nucleus relative to B_0 at the start of the sequence. θ_0 is varied as follows: [A] $\theta_0 = 0°$, [B] $\theta_0 = 18°$, [C] $\theta_0 = 36°$, [D] $\theta_0 = 54°$, [E] $\theta_0 = 72°$, [F] $\theta_0 = 90°$. In all cases, TE was 30 ms, and TM was 10 ms.

4.5.2 BOLD-related phase-shift effects in STEAM

BOLD-related phase shift in STEAM for varying flow velocities

Figure 4.39 depicts the influence of different flow velocities on the phase shift generated in STEAM sequences. Short echo times (30 ms) and mixing times (10 ms) were chosen.

The haematocrit, oxygen saturation, and B_0 listed in Table 3.5 were used. Again, a range of flow velocities between 0 and 2.5 mm/s was chosen as this represents the flow velocities encountered in the microvasculature of bone marrow. For the curvature of the vessel, a radius of 80 μm was chosen. The six different diagrams in Figure 4.39 take into account the varying vessel geometry (see Subsection 4.5.1).

The phase shift varied significantly with different flow velocities (Figure 4.39). Depending on the flow velocity and more strongly on θ_0, the algebraic sign of the phase shift was either positive or negative. For the range of flow velocities considered, higher flow velocities led to stronger absolute phase shifts in most cases. However, for specific geometries, this was not the case (Figure 4.39C–E). The strongest phase shifts observed were 70.3° and −70.3° and occurred for flow velocities of 2.5 mm/s when θ_0 equalled 90° and 0°, respectively. For flow velocities observed in small vessels such as sinusoidal capillaries, phase shifts were smaller than 15°.

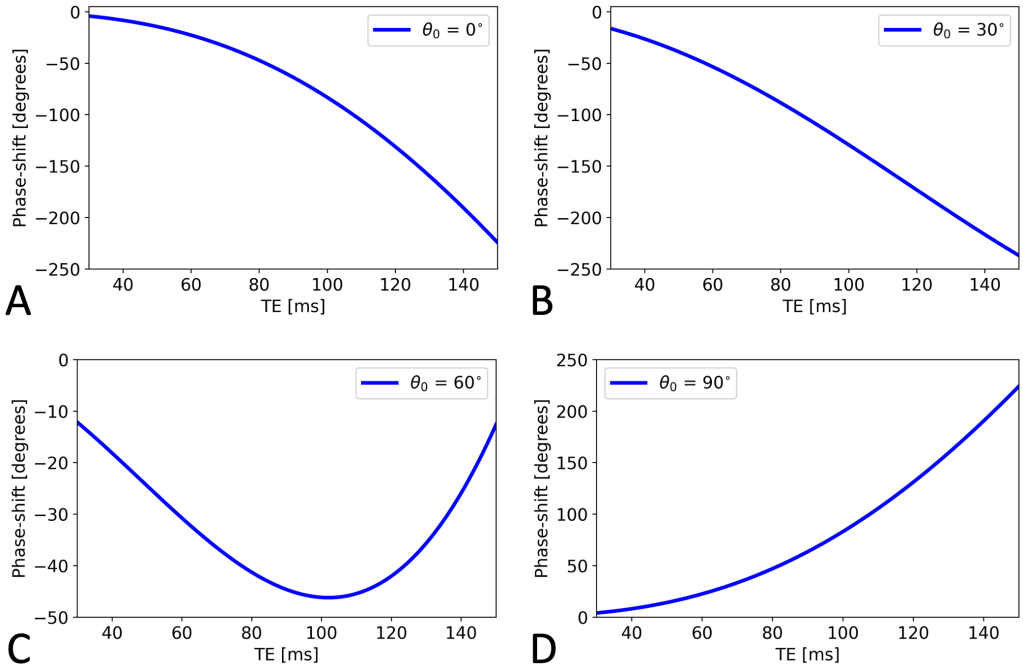

Figure 4.40: BOLD-related phase shift in STEAM for varying echo times. Here, the echo time of the STEAM sequence is varied between 30 and 150 ms. [A]–[D] show the corresponding phase shifts. Note that the plots vary in θ_0 as follows: [A] $\theta_0 = 0°$, [B] $\theta = 30°$, [C] $\theta_0 = 60°$, [D] $\theta_0 = 90°$. In all cases, the flow velocity was 0.5 mm/s, and TM was 10 ms.

BOLD-related phase shift in STEAM for varying echo times

Further, the effects of increasing echo times on BOLD-related phase-shift effects were investigated. The results are shown in Figure 4.40. A fixed flow velocity of 0.5 mm/s

was chosen, representing flow in capillaries and venules. All other parameters remained constant compared to the investigation of changing flow velocities (see above). The four diagrams in Figure 4.40 differ in θ_0 to take into account the varying vessel geometry. Echo times between 30 and 150 ms were studied.

Depending on θ_0, the algebraic sign of the phase shift was either positive or negative. When θ_0 equalled 0°, 30°, and 90°, longer echo times led to stronger dephasing. In case θ_0 equalled 60°, the absolute phase shift decreased for echo times longer than approximately 105 ms. With echo times of 100 ms and above, phase shifts exceeded 180° in most cases when θ_0 equalled 0°, 30°, and 90°. In general, echo times strongly determined the phase shifts.

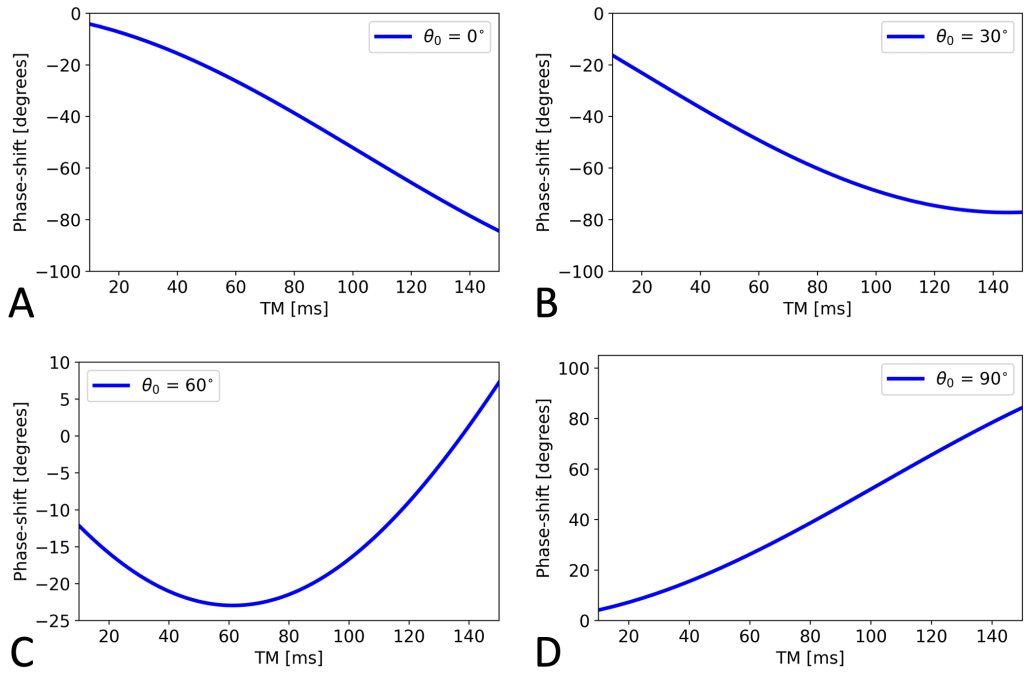

Figure 4.41: BOLD-related phase shift in STEAM for varying mixing times. Here, the mixing time of the STEAM sequence is varied between 10 and 150 ms. [A]–[D] show the corresponding phase shifts. Note that the plots vary in θ_0 as follows: [A] $\theta_0 = 0°$, [B] $\theta = 30°$, [C] $\theta_0 = 60°$, [D] $\theta_0 = 90°$. In all cases, the flow velocity was 0.5 mm/s, and TE was 30 ms.

BOLD-related phase shift in STEAM for varying mixing times

Additionally, the effects of increasing mixing times on BOLD-related phase-shift effects were investigated. The results are shown in Figure 4.41. A fixed flow velocity of 0.5 mm/s was chosen, representing flow in capillaries and venules. All other parameters remained constant compared to the investigation of changing flow velocities (see above). The four

diagrams in Figure 4.41 differ in θ_0 to take into account the varying vessel geometry. Mixing times between 10 and 150 ms were studied.

Depending on θ_0, the algebraic sign of the phase shift was either positive or negative when θ_0 equalled 0°, 30°, and 90°. However, when θ_0 equalled 60°, the phase shift was positive when mixing times exceeded approximately 135 ms and was negative below this threshold. In case θ_0 equalled 0°, 30°, and 90°, longer echo times led to stronger dephasing. However, when θ_0 equalled 60°, the phase shift decreased in absolute terms for mixing times between approximately 60 ms and 135 ms. The strongest phase shifts observed were $-84.3°$ and 84.3° and occurred for mixing times of 150 ms when θ_0 equalled 0° and 90° respectively. In general, mixing times firmly determined the phase shifts.

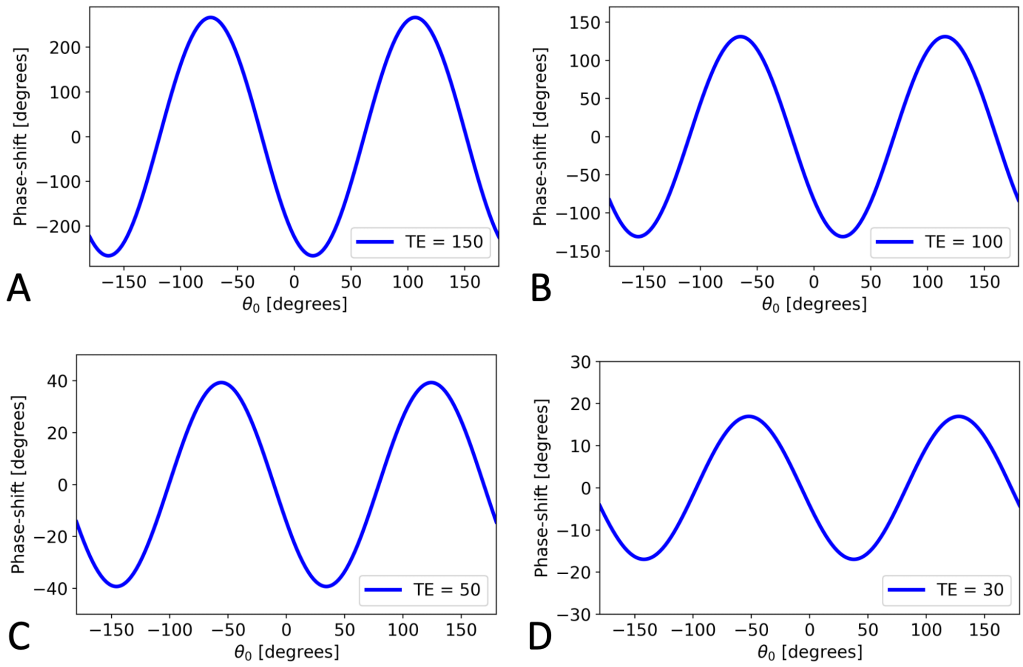

Figure 4.42: BOLD-related phase shift in STEAM for varying vessel geometries. Here, the vessel's geometry is varied, and the resulting phase shift is shown. θ_0 is subject to variations between $-180°$ and 180°. Positive values represent a nucleus flowing through a bend that curves away from B_0 (θ gets larger over time). Negative values represent a nucleus flowing through a bend that curves towards B_0. This is shown for different echo times: [A] TE = 150 ms, [B] TE = 100 ms, [C] TE = 50 ms, [D] TE = 30 ms. In all cases, the flow velocity was 0.5 mm/s, and the mixing time was 10 ms.

BOLD-related phase shift in STEAM for varying vessel geometries

As stated above, θ_0 is highly variable in most tissues. Therefore, the influence of θ_0 on BOLD-related phase-shift effects was investigated. In Figure 4.42, negative algebraic signs for θ_0 are shown. These represent cases where the vessel bends away from B_0. How-

ever, note that $-\theta_0$ still denotes a case in which the absolute angle of the vessel relative to B_0 at the start of the sequence is θ_0.

In Figure 4.42, the four diagrams differ in the echo times used (30, 50, 100, and 150 ms). θ_0 largely determined the algebraic sign of the resulting phase shift. In general, the resulting phase shift fluctuated in a sinusoidal fashion depending on θ_0. For echo times of 30 ms, the phase shift fluctuated between 0 and approximately 20° depending on θ_0. For echo times of 150 ms, the phase shift fluctuated between 0 and approximately 260° depending on θ_0. On average, θ_0 significantly influenced the phase shift, meaning that the orientation of the vessels relative to B_0 is relevant in STEAM.

Chapter 5

Discussion

5.1 Simulation of gradient-induced phase-shift effects

This section discusses the results obtained by the simulation of gradient-induced phase-shift effects in PRESS and STEAM sequences. The first subsection discusses the gradient-induced phase-shift effects in PRESS. This discussion entails the effects of changing the echo time and voxel size on the flow sensitivity. The second subsection discusses the gradient-induced phase-shift effects in STEAM. The effects of changing the echo time, mixing time, and voxel size on the flow sensitivity are debated. If the effects differ according to the axis along which the gradients are applied, they are discussed separately in both subsections.

Further, this section delineates why specific parameters alter the flow sensitivity while others do not. Sequence plots are shown to visualize why changes in the sequence parameters alter the flow sensitivity. This analysis serves to make the results obtained from the simulations explainable. At the end of both subsections, a brief summary will be provided.

5.1.1 Simulation of gradient-induced phase-shift effects in PRESS

Changing TE in PRESS sequences

As shown in Chapter 4, changing the echo time of a PRESS sequence does not alter its sensitivity to flow. This fact can be explained by an effect known as even echo rephasing, first described by Waluch and Bradley [136]. Increasing the echo time in a PRESS sequence is achieved by elongating TE_2 while TE_1 stays constant (Figure 2.10). Consequently, the crusher gradients during TE_2 are the only gradients that change their position. Although longer echo times postpone these crusher gradients, the time interval between both gradients stays constant. Since only the interval between the crusher gradients during TE_2 is responsible for the flow sensitivity created by them, and this interval is unchanged, the

flow sensitivity of the PRESS sequence stays constant with increasing echo times. Figure 5.1 illustrates the crusher gradients' position change during TE_2.

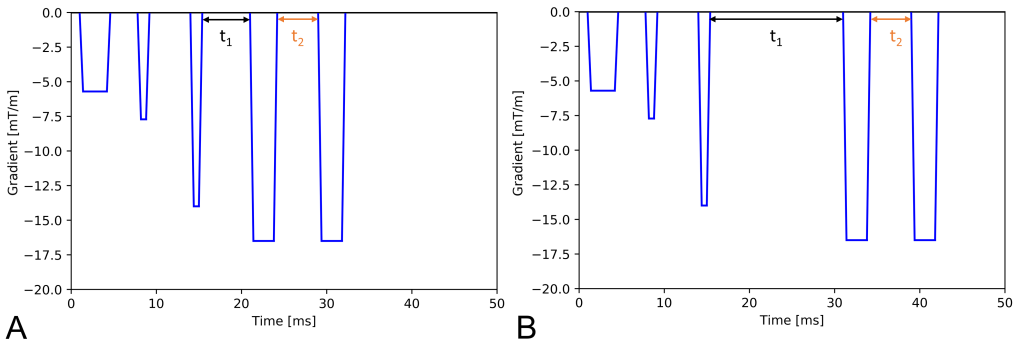

Figure 5.1: Effects of changing TE in PRESS. This figure visualises why changing the echo time does not affect the flow sensitivity of a PRESS sequence. Here, the gradients along the x-axis of two PRESS sequences are depicted. [A] Sequence parameters: TE = 30 ms, δL = 20 mm. The time interval t_1 is the interval between the crusher gradients applied during TE_1 and those applied during TE_2. t_2 is the time interval between both crusher gradients applied during TE_2. [B] Sequence parameters: TE = 50 ms, δL = 20 mm. Compared to [A], [B] has a longer echo time, and the interval t_1 increases due to the increase of TE_2. However, the crucial interval t_2 remains constant. As only the interval t_2 is responsible for the flow sensitivity, the flow sensitivity remains unchanged.

Changing voxel size in PRESS sequences

Changing the edge length of the voxel (δL) along any axis has different effects on the flow sensitivity depending on whether the x-, y-, or z-axis is considered. The simulations delineated in Chapter 4 showed this.

The following paragraphs explain the reasons for these differences in PRESS. For these explanations, three principles are vital. 1) The edge length of the voxel determines the magnitude of the slice selection gradients. The smaller the edge length, the steeper the slice selection gradients. 2) If a gradient is applied before the first or after the second 180°-pulse, its overall contribution to the flow sensitivity is with a negative algebraic sign. If such a gradient steepens, the phase shift increases. 3) A gradient between both 180°-pulses contributes with a positive algebraic sign to the flow sensitivity. Consequently, the phase shift decreases if such a gradient steepens.

Changing voxel size along the x-direction

The example provided in Figure 5.2 explains why small edge lengths lead to a higher flow sensitivity. Figure 5.2A depicts a PRESS sequence with an edge length of 30 mm along the x-direction, and Figure 5.2B depicts a PRESS sequence with an edge length of 10 mm

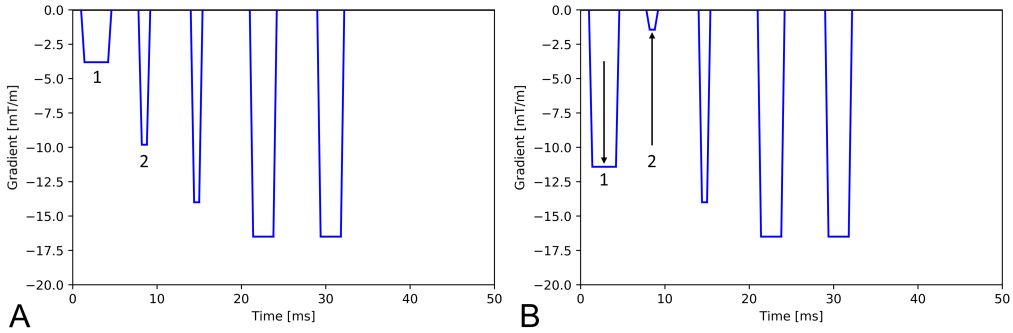

Figure 5.2: Effects of changing δL along the x-direction in PRESS. [A] A PRESS sequence with δL = 30 mm along the x-axis has a flow sensitivity of $-70.5\ \frac{rad \cdot s}{m}$ for flow along the x-axis. [B] A PRESS sequence with δL = 10 mm along the x-axis has a flow sensitivity of $-60.5\ \frac{rad \cdot s}{m}$ for flow along the x-axis. The slice selection gradient (1) grows at the expense of the first crusher gradient (2) during TE_1 when the edge length is decreased. Thus, the combined effect of both gradients to increase the flow sensitivity gets weaker.

along the x-direction. In the latter case, the slice selection gradient is steeper to select ^{1}H nuclei along a shorter edge length. When the edge length is 10 mm, a steeper slice selection gradient requires a weaker first crusher gradient. This is because the second crusher gradient balances the slice selection gradient and the first crusher gradient. Otherwise, no spin echo would form.

The slice selection gradient contributes less to the flow sensitivity than the first crusher gradient (Subsection 3.1.2). This paragraph explains this fact. When the first crusher gradient is applied, the ^{1}H nucleus has moved further away from its initial position and thus experiences a stronger local magnetic field during the crusher gradient than during the previous slice selection gradient. The decrease in the first crusher gradient for shorter edge lengths has a more significant effect on the flow sensitivity than the increase in the slice selection gradient. Their combined effect diminishes when the edge length decreases. Both gradients contribute to the flow sensitivity with a negative algebraic sign since they are applied before the first 180°-pulse. Thus, the flow sensitivity of a PRESS sequence diminishes if the edge lengths are shortened along the x-axis.

Changing voxel size along the y-direction

Figure 5.3 shows the impact of decreasing the edge length along the y-axis on PRESS sequences. The consequence of decreasing edge lengths is the increase in the magnitude of the slice selection gradient. The SSG is the only gradient affected significantly. In general, the effect of the slice selection gradient along the y-axis diminishes the flow sensitivity of the sequence because the second half of the slice selection gradient dominates and is applied after the first 180°-pulse (Chapter 3). Since the slice selection gradient

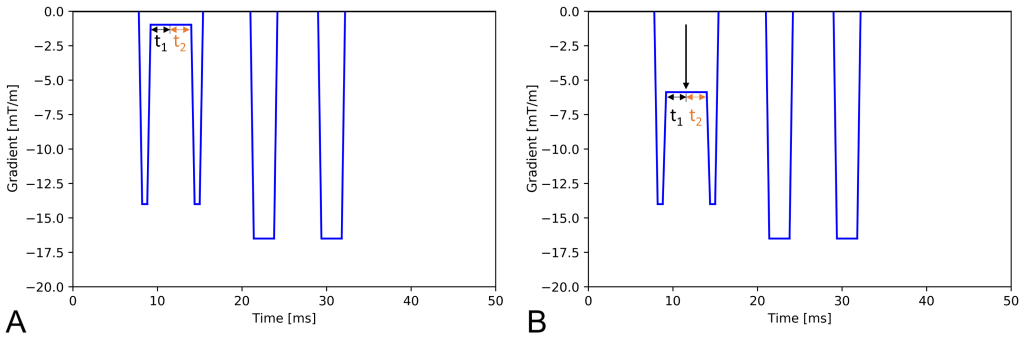

Figure 5.3: Effects of changing δL along the y-direction in PRESS. [A] A PRESS sequence with δL = 30 mm along the y-axis has a flow sensitivity of $-73.9\ \frac{rad \cdot s}{m}$ for flow along the y-axis. [B] A PRESS sequence with δL = 5 mm along the y-axis has a flow sensitivity of $-65.0\ \frac{rad \cdot s}{m}$ for flow along the y-axis. The slice selection gradient gets steeper for small edge lengths (arrow). While the first half of the slice selection gradient during t_1 increases the flow sensitivity, the second half during t_2 decreases the flow sensitivity. However, the effect of the second half dominates. Therefore, the effect of the slice selection gradient to diminish the flow sensitivity is increased for smaller edge lengths.

gets stronger when δL is small, its contribution to diminishing the flow sensitivity of the PRESS sequence is more pronounced. Therefore, the flow sensitivity of a PRESS sequence diminishes if the edge lengths are shortened along the y-axis.

Changing voxel size along the z-direction

Figure 5.4 shows the impact of decreasing the edge length along the z-axis on PRESS sequences. As with the slice selection gradient along the y-axis, only the slice selection gradient along the z-axis is affected by a change in the edge length along the z-axis. The smaller the edge length, the stronger the slice selection gradient along the z-axis.

In general, the slice selection gradient along the z-axis increases the flow sensitivity of the sequence (Chapter 3) due to the dominating effect of the second half of the slice selection gradient (applied after the final 180°-pulse). Since the slice selection gradient gets stronger when δL is small, its contribution to increasing the flow sensitivity of the PRESS sequence is strengthened. Therefore, the flow sensitivity of a PRESS sequence increases if the edge lengths are shortened along the z-axis.

Summary

The simulations showed that the PRESS sequences behave as follows. The flow sensitivity along each axis differs in PRESS. When assuming equal edge lengths, the flow sensitivity is the largest along the z-axis and the smallest along the x-axis. The echo time does not influence the flow sensitivity. However, the edge length along each axis influences the

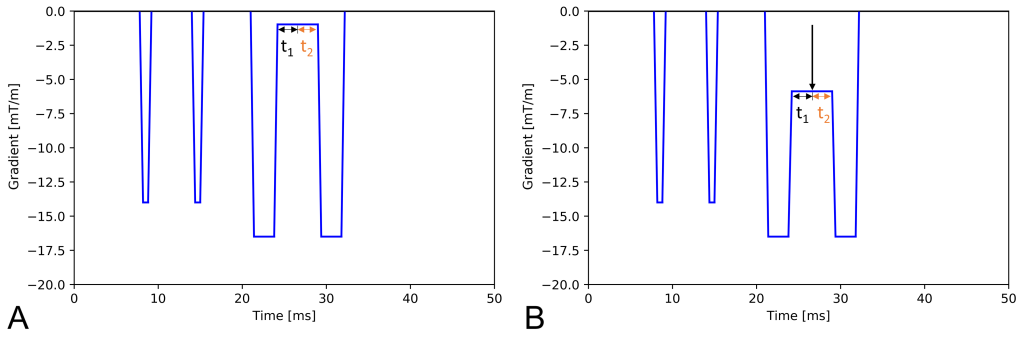

Figure 5.4: Effects of changing δL along the z-direction in PRESS. [A] A PRESS sequence with δL = 30 mm along the z-axis has a flow sensitivity of $-77.4\ \frac{rad \cdot s}{m}$ for flow along the z-axis. [B] A PRESS sequence with δL = 5 mm along the z-axis has a flow sensitivity of $-86.3\ \frac{rad \cdot s}{m}$ for flow along the z-axis. The slice selection gradient gets steeper for small edge lengths (arrow). While the first half of the slice selection gradient during t_1 decreases the flow sensitivity, the second half during t_2 increases the flow sensitivity. However, the effect of the second half dominates. Therefore, the effect of the slice selection gradient to increase the flow sensitivity is more pronounced for small edge lengths.

flow sensitivity. The shorter the edge lengths along the x- and y-axis, the smaller the flow sensitivity. The shorter the edge lengths along the z-axis, the larger the flow sensitivity. The analysis above shows that the simulation results align with theoretical considerations. The implications are discussed in Section 5.4.

5.1.2 Simulation of gradient-induced phase-shift effects in STEAM

Changing TE along the x-direction

Figure 5.5 shows the effect of changing the echo time of the STEAM sequence on the gradients along the x-axis. In STEAM, the slice select gradient counteracts the effect of the third crusher gradient along the x-axis to produce a stimulated echo (Figure 3.6). Note that the third crusher gradient also counteracts the effects of the first crusher gradient. When the echo time is increased, the position of the slice selection gradient stays constant, whereas all crusher gradients are postponed. While the interval between the first and the third crusher gradient is unchanged with increasing echo times, the interval between the slice select gradient and the third crusher gradient is elongated significantly.

When the third crusher is applied, the ^{1}H nucleus has moved further away from its initial position and thus experiences a relatively stronger local magnetic field during the crusher gradient than during the initial slice selection gradient. The slice select gradient contributes to the flow sensitivity with a positive algebraic sign, while the third crusher gradient contributes to the flow sensitivity with a negative algebraic sign (Subsection 3.1.2). The contribution to the flow sensitivity due to the slice select gradient stays equal when

the interval is elongated – however, the contribution of the third crusher gradient increases. Therefore, longer echo times lead to a higher flow sensitivity for flow along the x-axis in STEAM.

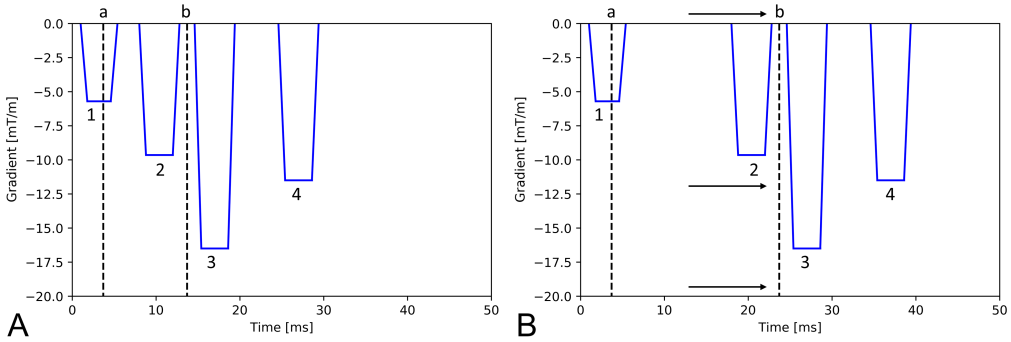

Figure 5.5: Effects of changing TE along the x-direction in STEAM. Sequence parameters: δL = 20 mm, TM = 10 ms. [A] A STEAM sequence with TE = 20 ms has a flow sensitivity of $-216.2\ \frac{rad \cdot s}{m}$ for flow along the x-axis. The label (a) marks the beginning of the sequence, while (b) marks the timing of the second 90°-pulse. [B] A STEAM sequence with TE = 40 ms has a flow sensitivity of $-236.1\ \frac{rad \cdot s}{m}$ for flow along the x-axis. The increase in echo time from [A] to [B] postpones all crusher gradients (arrows) as the second 90°-pulse is applied later. The separation of the slice select gradient from the third crusher gradient increases the flow sensitivity when echo times increase.

Changing TE along the y- and z-direction

Increasing the echo time in a STEAM sequence alters the y- and z-direction gradients similarly. Figure 5.6 shows this for the gradients along the y-axis. A shift in the gradients relative to the start of the sequence is the only effect of increasing the echo time. Such a change neither affects the relative position of the gradients to each other nor the strength of the gradients. Therefore, the sensitivity to flow along a STEAM sequence's y- and z-axis does not depend on the echo time.

Changing TM in STEAM sequences

Longer mixing times in STEAM sequences lead to stronger gradient-induced phase-shift effects for flow in every direction. The third crusher gradient along every direction is applied later when the mixing time is elongated. In contrast, all other gradients do not change their position (except the slice selection gradient along the z-axis). The longer time interval between the first and the third crusher gradient means that the ^{1}H nuclei experience a stronger local magnetic field due to the third crusher gradient when the mixing time is long. Therefore, the flow sensitivity is higher the longer the mixing time. Along the z-axis, a later application of the slice selection gradient further contributes to the effect. Figure 5.7

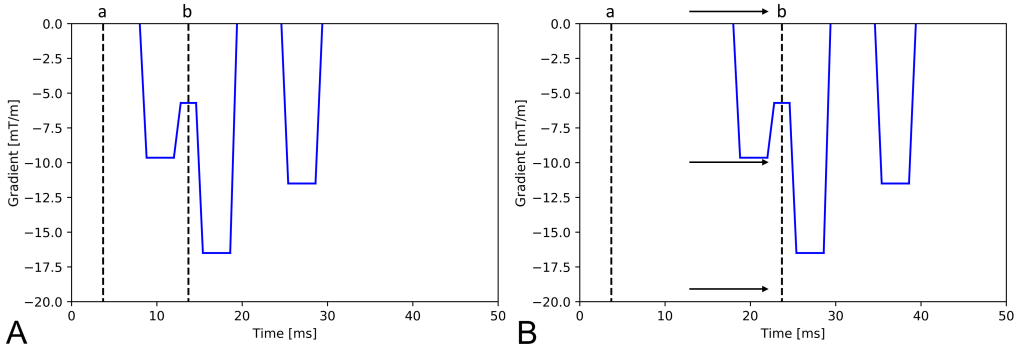

Figure 5.6: Effects of changing TE along the y-direction in STEAM. Sequence parameters: δL = 20 mm for all axes, TM = 10 ms. [A] A STEAM sequence with TE = 20 ms has a flow sensitivity of $-199.1\ \frac{rad \cdot s}{m}$ for flow along the y- and z-axis. The label (a) marks the beginning of the sequence, while (b) marks the timing of the second 90°-pulse. [B] A STEAM sequence with TE = 40 ms. When the echo time is elongated and the second 90°-pulse postponed, the only effect on the gradients along the y- and z-axis is that they are applied later (arrows). Their relative timing to each other is not affected. Therefore, the flow sensitivity is equal for [A] and [B].

depicts the sequence change due to longer mixing times with the example of the gradients along the x-axis.

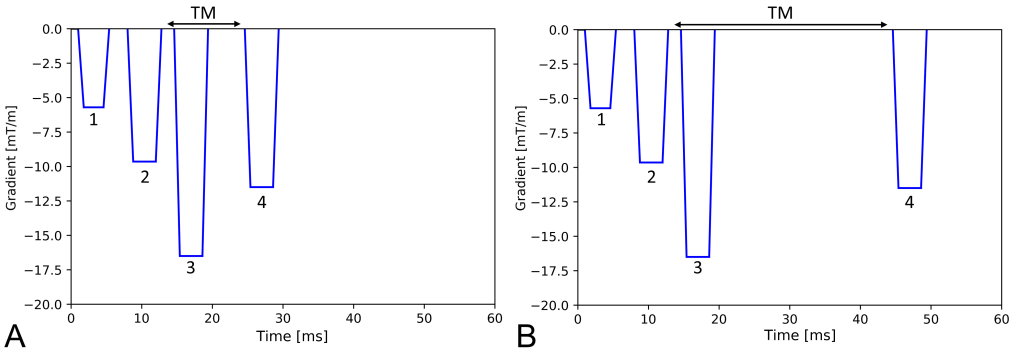

Figure 5.7: Effects of changing TM in STEAM. The gradients of a STEAM sequence along the x-axis are shown. Sequence parameters: TE = 20 ms, δL = 20 mm. [A] With TM = 10 ms, the sequence has a flow sensitivity of $-216.3\ \frac{rad \cdot s}{m}$ for flow along the x-axis. [B] With TM = 30 ms, the sequence has a flow sensitivity of $-462.4\ \frac{rad \cdot s}{m}$ for flow along the x-axis. (1) denotes the slice selection gradient, (2) the first crusher gradient, (3) the second crusher gradient, and (4) the third crusher gradient. The gradients (1) and (2) counterbalance the effect of the gradient (4) for stationary nuclei, while (3) does not influence the flow sensitivity. If TM is increased, the contributions of (1) and (2) do not change. However, the effect of (4) becomes stronger, leading to an overall increase in flow sensitivity.

Changing voxel size along the x-direction

The effect of the gradients between the initial 90°-pulse and the second 90°-pulse is to reduce the flow sensitivity in STEAM sequences (Figure 3.6). The slice selection gradient along the x-axis and the first crusher gradient are applied during this interval. The slice selection gradient must be steeper when the edge length is shortened. Consequently, the first crusher gradient is decreased to form a stimulated echo. Figure 5.8 illustrates this. While the higher amplitude of the slice selection gradients leads to less flow sensitivity, the lower amplitude of the first crusher gradient increases the flow sensitivity and has a more significant effect overall. Thus, if the edge length is shortened along the x-axis, a STEAM sequence gets more sensitive for flow along the x-axis.

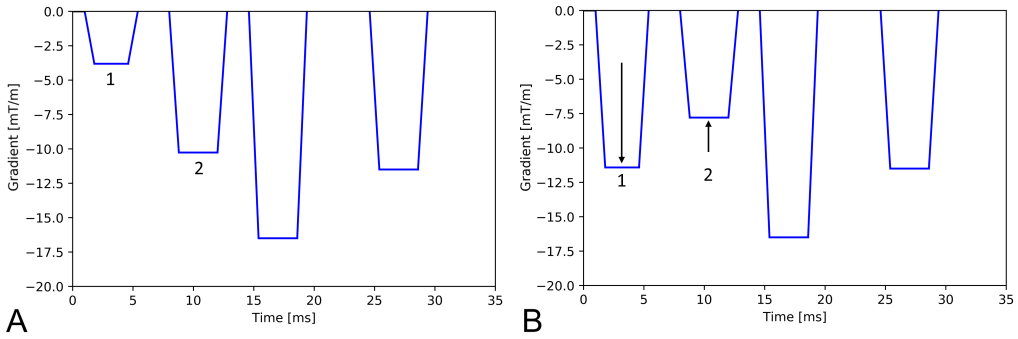

Figure 5.8: Effects of changing δL along the x-direction in STEAM. Sequence parameters: TE = 20 ms, TM = 10 ms. [A] shows a sequence with δL = 30 mm along the x-axis. Its flow sensitivity is $-212.3\ \frac{rad \cdot s}{m}$ for flow along the x-axis. [B] shows a sequence with δL = 10 mm. Its flow sensitivity is $-228.2\ \frac{rad \cdot s}{m}$. (1) denotes the slice selection gradient, and (2) is the first crusher gradient. As edge lengths shorten, (1) increases and (2) decreases in amplitude. Both gradients contribute with a positive algebraic sign to the flow sensitivity, while the third crusher gradient contributes negatively (Subsection 3.1.4). As the effect of the former two gradients is weakened by the shortening of the edge length along the x-axis, the effect of the third crusher gradient dominates, and the flow sensitivity is increased.

Changing voxel size along the y-direction

For stationary ^{1}H nuclei, the dephasing created by the slice selection gradient and the first crusher gradient equalises the third crusher gradient. Small edge lengths along the y-direction lead to steeper slice selection gradients. A decrease in the strength of the first crusher gradient must compensate for the steeper slice selection gradient (Figure 5.9). As the slice selection gradient is applied later than the crusher gradient, the ^{1}H nuclei are further away from their initial position during the slice selection gradient. Therefore, they experienced a relatively stronger local magnetic field during the slice selection gradient, and the combined effect of both gradients increases for flowing ^{1}H nuclei. This increase

means that the overall flow sensitivity will be smaller for shorter edge lengths as the effect of the third crusher gradient is counterbalanced by the first two gradients to a greater extent (Figure 3.7).

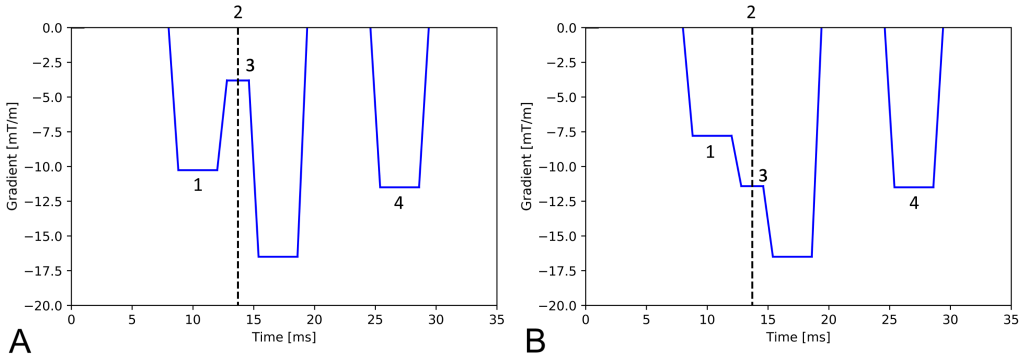

Figure 5.9: Effects of changing δL along the y-direction in STEAM. Sequence parameters: TE = 20 ms, TM = 10 ms. [A] shows a sequence with δL = 30 mm. Its flow sensitivity is $-200.8\ \frac{rad \cdot s}{m}$ for flow along the y-axis. [B] shows a sequence with δL = 10 mm. Its flow sensitivity is $-193.8\ \frac{rad \cdot s}{m}$ for flow along the y-axis. (1) denotes the first crusher gradient, (2) the timing of the second 90°-pulse, (3) the first crusher gradient, and (4) the third crusher gradient. In STEAM, shorter edge lengths along the y-axis are achieved by increasing the slice select gradient along the y-axis. This increase makes a decrease in the first crusher gradient necessary. Overall, the changes lead to stronger dephasing of ^{1}H nuclei prior to the second 90°-pulse. However, as the effect of the third crusher gradient dominates, this leads to smaller overall flow sensitivity for shorter edge lengths.

Changing voxel size along the z-direction

Along the z-direction, the increase in the strength of the slice selection gradient for shorter edge lengths means that the final crusher gradient must be decreased in amplitude (Figure 5.10). Although the increase in the strength of the slice selection gradient leads to more flow sensitivity, the decrease in the strength of the crusher gradient leads to an overall reduction in flow sensitivity. This is because the ^{1}H nuclei are further away from their initial position during the third crusher gradient compared to the position of the ^{1}H nuclei during the slice selection gradient.

Summary

The simulations showed that STEAM sequences behave as follows. The flow sensitivity along the x-axis is larger than the flow sensitivity along the y- and z-axis independent of the echo time. However, the larger the echo time, the larger the flow sensitivity along the x-axis. The flow sensitivity along the y- and z-axis does not depend on the echo time. Further, the edge length along each axis influences the flow sensitivity. The shorter the

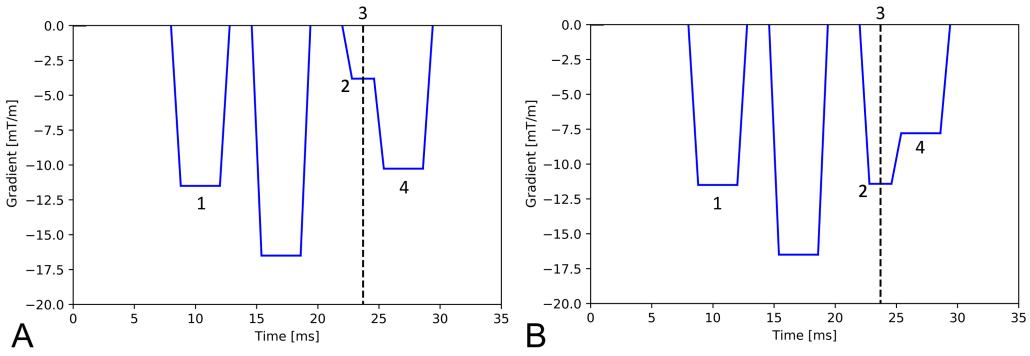

Figure 5.10: Effects of changing δL along the z-direction in STEAM. Sequence parameters: TE = 20 ms, TM = 10 ms. [A] shows a sequence with δL = 30 mm. Its flow sensitivity is $-200.8\ \frac{rad \cdot s}{m}$ for flow along the z-axis. [B] shows a sequence with δL = 10 mm. Its flow sensitivity is $-193.8\ \frac{rad \cdot s}{m}$ for flow along the z-axis. (1) denotes the first crusher gradient, (2) denotes the slice selection gradient, (3) denotes the third 90°-pulse, and (4) denotes the third crusher gradient. The third crusher gradient diminishes for shorter edge lengths while the slice selection gradient increases. This leads to an overall decrease in the flow sensitivity of the STEAM sequence for flow along the z-axis.

edge lengths along the y- and z-axis, the smaller the flow sensitivity. The shorter the edge lengths along the x-axis, the larger the flow sensitivity. Elongating the mixing time leads to increased flow sensitivity along each axis. The analysis above shows that the simulation results align with theoretical considerations. The implications are discussed in Section 5.4.

5.2 Experiments on gradient-induced phase-shift effects

The phantom measurements were the first step to evaluate whether gradient-induced phase-shift effects lead to measurable changes in the spectra acquired by PRESS and STEAM sequences. These are discussed in the first subsection. The second subsection discusses the phantom measurements using the flow-sensitised sequences. These measurements were essential to validate the flow-sensitised sequences as their comparability to the standard sequences is vital for the in vivo measurements. The third subsection discusses the results of the in vivo measurements. These measurements represent an integral part of this thesis, as one of the principal aims was to assess whether gradient-induced phase-shift effects are detectable in vivo.

5.2.1 Phantom measurements

The flowing water molecules inside the phantom have different flow velocities. The molecules close to the centre are the fastest, while the molecules close to the tube wall

move more slowly. This velocity profile means that not all molecules flowing through the tube experience the same gradient-induced phase-shift effects because the effects depend on the molecule's velocity. In theory, the signal amplitude of the water peak should decrease when the fluid flows through the phantom as the water molecules get dephased from each other due to the gradient-induced phase-shift effects. The phantom measurements sought to evaluate whether such a decrease in signal amplitudes is detectable.

An increase in the mean flow velocity inside the phantom was associated with smaller amplitudes of the water peak for PRESS measurements. Figure 4.8 shows this. While the tendency was weak for the comparatively small flow velocity of 0.46 mm/s, the trend was more significant for higher flow velocities (1.00 and 1.85 mm/s), in line with the theory that suggests such behaviour.

The phantom measurements performed for this purpose with STEAM sequences showed similar results. For flow velocities of 1.10 and 1.21 mm/s, the amplitudes of the peaks were significantly smaller compared to the measurements without flow (Figure 4.10). However, the spectra acquired with a flow velocity of 0.29 mm/s (the lowest flow velocity in all experiments) showed no significant difference from the spectra acquired without flow. This can be explained in the following way. Since the flow velocity was small, the phase-shift effect was likely too small to be measurable in the experiment.

Further, the phantom experiments sought to validate whether increasing the STEAM sequences' mixing times is associated with signal alterations. The calculations presented in Subsection 4.1.2 suggest that stronger dephasing should occur for longer mixing times. Thus, the signal amplitudes should be smaller for longer mixing times. Figure 4.14 shows that elongating the mixing time without a change in any other parameter led to smaller amplitudes of the water peaks for a flow velocity of 0.94 mm/s. An increase in mixing time without flow through the phantom was not associated with a significant change in the signal amplitudes (Table 4.9 and 4.10). Therefore, the experiments seem to validate the mathematical findings.

Both PRESS and STEAM measurements align with theory. In the experiments, flow velocities of around 1.00 mm/s yield measurable differences in the spectra acquired with PRESS and STEAM sequences. This velocity is in the order of blood flow velocities in arterioles and post-arterial capillaries (Section 2.5) [7]. Therefore, gradient-induced phase-shift effects in PRESS and STEAM might be detectable in human tissue when a significant amount of such vessels is present.

It is important to note that the vessels in the human body point in various directions, a clear difference from the experimental setting, where the flow was unidirectional. This circumstance constitutes a limitation of the study. However, the random orientation of the capillaries in the human body likely yields an even stronger distribution of different flow

velocities compared to the phantom measurements. This should lead to stronger gradient-induced phase-shift effects in the totality of vessels within a voxel than in the experiment, provided the flow velocities are comparable.

5.2.2 Preliminary measurements using the flow-sensitised sequences

The preliminary phantom measurements using the flow-sensitised sequences were made to evaluate whether flow-sensitised sequences were directly comparable to the standard sequences provided by Siemens Healthcare. A quantitative comparison of both types of sequences is only sensible if the spectra and their amplitudes are comparable. Further, the effects shown in the previous phantom measurements should be more pronounced in the flow-sensitised sequences. The decline in signal amplitudes with flow due to gradient-induced phase-shift effects should be more prominent in the flow-sensitised sequences as the crusher gradients are larger (Subsection 3.3.1).

The comparison between the standard and flow-sensitised PRESS sequence without flow shows that the shape of the spectra is very similar and the differences in amplitudes are slight (Figures 4.19A and 4.15). The measurements comparing standard and flow-sensitised STEAM sequences without flow show similar shapes of the spectra as well (Figure 4.21). However, a slight difference in amplitudes is observable (Figure 4.25). The standard and flow-sensitised sequences show similar behaviour for PRESS and STEAM when no flow is present. This is in line with the theory, as the increase in the strength of the crusher gradients should not alter the signal behaviour when no flow is present.

A pattern of declining amplitudes with increased flow velocity was observed in the measurements with the flow-sensitised PRESS sequence and varying flow velocities. Table 4.11 shows that the amplitudes get progressively smaller for larger flow velocities. Further, Figure 4.19 illustrates that flow-sensitised PRESS sequences show even smaller amplitudes than the standard PRESS sequence when a flow is present in most cases. This tendency is most pronounced for echo times of 500 ms and below. That the difference is not as impressive for longer echo times can be explained by the small absolute amplitudes that make differences harder to detect. The fact that the flow-sensitised PRESS sequences show smaller amplitudes when a flow is present compared to the standard PRESS sequences is expected due to the more potent gradient-induced phase-shift effects created by the altered crusher gradients.

The measurements with the flow-sensitised STEAM sequence and varying flow velocities show similar results to the PRESS measurements. The amplitude of the water peak declines with an increase in mean flow velocity (Table 4.12). Again, this is expected due to the stronger crusher gradients. However, the decline is minor for the small mean flow velocity of 0.29 mm/s and is only apparent for echo times of up to 800 ms. The small mean

flow velocity likely leads to only weak gradient-induced phase-shift effects and might be an explanation for this. For higher flow velocities (1.10 and 1.21 mm/s), the decline in peak amplitudes is very pronounced without exception. In Figure 4.25, a comparison of the amplitudes of the peaks acquired with the standard and flow-sensitised sequences is shown. It can be seen clearly that the amplitudes of the flow-sensitised sequences are far smaller for the higher flow velocities of 1.10 and 1.21 mm/s compared to the standard STEAM sequence. Again, the differences for the measurements with a flow velocity of 0.29 mm/s are small.

The measurements with flow-sensitised PRESS and STEAM sequences behave as expected. Without flow, the flow-sensitised sequences behave very similarly to the standard sequences under the conditions studied. Again, the flow-sensitised PRESS and STEAM sequences show smaller signal amplitudes of the water peaks when the water molecules flow through the phantom. This can be explained by the stronger dephasing of water molecules due to the gradient-induced phase-shift effects. The development of the sequences aimed to create PRESS and STEAM sequences with a stronger sensitivity to flow. The experimental data suggest this aim was achieved.

Further, the spectra showed an indentation or second peak in the STEAM measurements with standard and flow-sensitised sequences at higher flow velocities. Collenbusch has already described this second peak based on experiments with cation exchange resins [23]. She postulated that one peak corresponds to bound water molecules and the other to free water molecules. However, only free water molecules were present in the experiments described here. The acquired spectra suggest that the indentation/second peak has a different cause. Further experiments are needed to elucidate the cause of these signal alterations.

5.2.3 In vivo measurements

The in vivo measurements were conducted to evaluate whether gradient-induced phase-shift effects are measurable in vivo for PRESS and STEAM sequences. The red bone marrow was chosen for the measurements because Schick et al. already demonstrated signal alterations in the red bone marrow, likely caused by phase-shift effects [116].

A comparison between the standard and flow-sensitised sequences was chosen to examine for gradient-induced phase-shift effects. Standard and flow-sensitised sequences differ only in the strength of their crusher gradients, meaning that gradient-induced phase-shift effects should be more pronounced in the spectra acquired with the flow-sensitised sequences. If the flow-sensitised sequences show alterations in the signal, gradient-induced phase-shift effects should also be relevant but smaller for standard sequences. Susceptibility-induced and BOLD-related phase-shift effects should not depend on the crusher gradients.

Therefore, the method is specific to gradient-induced phase-shift effects.

As seen with the phantom measurements, gradient-induced phase-shift effects should lead to the dephasing of water molecules moving with different velocities inside the red bone marrow's vessels. In theory, this dephasing leads to smaller signal amplitudes of the water peak. As shown in the calculations in Subsection 4.1.2, the effects should be more pronounced for STEAM measurements and explicitly the STEAM measurements with longer mixing times. The peak associated with the lipids should be unaffected by the flow-sensitised sequence, as the lipids are primarily stationary in human tissue.

The in vivo measurements using the PRESS sequences showed a slight tendency of the flow-sensitised sequence to yield smaller amplitudes than the standard PRESS sequence. The difference was tiny in Subject 1 and somewhat more pronounced in Subject 2. This might be due to different ratios of stationary and flowing water molecules in the red bone marrow of the subjects studied. As noted above, the PRESS sequence is expected to be less sensitive to gradient-induced phase-shift effects than the STEAM sequence. The comparatively minor differences between the standard and flow-sensitised PRESS sequence might signify that gradient-induced phase-shift effects in spectra acquired with PRESS sequences are minor in the red bone marrow.

The initial in vivo measurements with the STEAM sequences and a mixing time of 10 ms must be interpreted cautiously. While the experimental setup was accurate in Subject 2, it could have been more optimal for Subject 1. For technical reasons, placing the voxel at precisely the same position for both the standard and flow-sensitised STEAM sequence was impossible. The result was a difference in positioning of the voxels of about 2 mm along all axes. The more reliable measurements in Subject 2 show a slight decline in the amplitude of the water peak for the flow-sensitised sequence compared to the standard sequence. However, the measurements in Subject 1 showed the opposite. A likely explanation for this is the inaccurate positioning of the voxel. In conclusion, the effect observed with Subject 2 was small, while the expected effect did not show in Subject 1.

As the STEAM measurements presented above are inconclusive, further measurement sets were acquired. Because the gradient-induced phase-shift effects are supposed to be stronger with longer mixing times, a measurement series with a mixing time of 50 ms has been conducted. As can be seen in Figure 4.34C, the flow-sensitised STEAM sequence shows peak amplitudes that are smaller than the amplitudes in the measurements with the standard STEAM sequence at a mixing time of 50 ms. This difference is significantly larger than the difference at 10 ms. In this respect, the measurements with a mixing time of 50 ms behave as expected. The longer mixing time seems to increase the gradient-induced phase-shift effects.

A final measurement set with multiple different mixing times was acquired to validate

the above finding. As can be seen from Figure 4.35 and Table 4.19, an inverse correlation between the mixing time and the peak amplitude of the water signal is observable.

In summary, the gradient-induced phase-shift effects in the PRESS sequences were shown to be small in the subjects studied. The same holds true for the STEAM measurements at short mixing times. However, the measurements showed that the signal alterations due to gradient-induced phase-shift effects were more pronounced at longer mixing times. This is consistent with the mathematical models developed. An explicit limitation of the study is that only two subjects were studied. As the subjects' ages were 21 and 29, different results might be obtainable when studying older adults.

5.3 Simulation of BOLD-related phase-shift effects

The simulation of BOLD-related phase-shift effects in PRESS and STEAM sequences showed that the resulting phase shifts are highly dependent on vessel geometry, flow velocity, echo times, and, in the case of STEAM, the mixing time. Long echo times led to significant changes in phase shifts as the ^{1}H nuclei continue to flow during the echo time and transition between two positions in the vessel with vastly different local magnetic fields. The exact mechanism affects long mixing times, even though the nuclei are not subject to phase shifts during the mixing time. When echo times exceeded approximately 150 ms, the consecutive phase shifts surpassed 180° in most cases for PRESS and STEAM.

In conclusion, BOLD-related phase-shift effects led to relevant phase shifts for PRESS and STEAM sequences with long echo times. The effects of long mixing times were also strong but smaller than the effects of long echo times. The orientation of the vessels relative to the main magnetic field also firmly determined the excepted phase shifts. The results show that BOLD-related phase-shift effects were larger for higher flow velocities, meaning that these effects should be more pronounced in larger venules and veins.

Although STEAM sequences showed slightly larger phase shifts than comparable PRESS sequences, these differences were minor compared to those seen in gradient-induced phase-shift effects. This can be explained by the fact that the sequence parameters that influence BOLD-related phase-shift effects are only echo and mixing times. The differences in the gradients between PRESS and STEAM do not affect BOLD-related phase-shift effects.

Limitations of the simulation

A few assumptions had to be made to simulate the BOLD-related phase-shift effects. These paragraphs discuss the assumptions to evaluate the study's potential limitations and

identify further determining factors.

The models calculated the magnetic field inside the vein by assuming the vein is an infinitely long, straight cylinder. This simplification leads to inaccuracies in the results. However, the COMSOL simulations presented in Figure 3.27 and the data published by Li et al. show that these inaccuracies are minor [77].

Further, Model 2 assumes the vessels bend perfectly circular, which represents another simplification. For irregularly bent vessels, phase shifts might be different. However, the order of magnitude of the phase shifts should be similar.

The calculations also assume that the oxygenation level stays constant during a spectroscopy sequence. In the case of capillaries, where oxygen is transferred to the surrounding tissue, oxygen levels decrease during the sequence. The drop in the oxygenation level might lead to stronger phase shifts if the echo time (or mixing time) is sufficiently long.

The simulations were performed with a venous oxygenation level of 0.65. Note that organs differ in their oxygen extraction ratio, meaning that the results of the simulations might over- or underestimate phase-shift effects in some organs. Additionally, diseases or metabolic factors might change venous oxygenation levels and, consequently, the magnitude of BOLD-related phase-shift effects.

5.4 Conclusion and outlook

5.4.1 Relevance of flow effects in vivo

This subsection delineates the conditions in which different phase-shift effects are relevant. Furthermore, this subsection discusses which phase-shift effects dominate depending on organ-specific parameters.

Gradient-induced phase-shift effects In theory, gradient-induced phase-shift effects become relevant when flow velocities are high, or the microvasculature is dense in a given organ. Therefore, organs with above-average perfusion, such as the brain, heart, lungs and kidneys, should be prone to gradient-induced phase-shift effects. Note that high flow velocities/above-average perfusion will also increase the magnitude of other phase-shift effects. As mentioned above, STEAM sequences are prone to gradient-induced phase-shift effects, especially with long mixing times. Measurements obtained by PRESS sequences are more resistant to such phase-shift effects.

BOLD-related phase-shift effects Organs with a tortuous microvasculature, such as red bone marrow and the spleen, might be prone to BOLD-related phase-shift effects. Additionally, as the BOLD-related phase-shift effects depend on the oxygenation level, organs

with a high oxygen extraction ratio, such as the brain or heart, are more likely to be affected than others. Both PRESS and STEAM sequences are affected by BOLD-related phase-shift effects. However, as with gradient-induced phase-shift effects, STEAM sequences with long mixing times are affected most.

Other susceptibility-induced phase-shift effects Although this study discussed susceptibility-induced phase-shift effects other than BOLD-related phase-shift effects only in Section 2.7, they are expected to contribute significantly to signal alterations due to flow in some organs. When the microvasculature is close to substances like iron, fat, or air, microscopic field gradients arise, leading to significant phase shifts. Lungs with numerous air-tissue boundaries and organs where iron is deposited are especially prone to susceptibility-induced phase-shift effects. This effect is particularly pronounced in diseases such as haemochromatosis.

Comparison of phase-shift effects In the simulations, the BOLD-related phase-shift effects led to more significant phase shifts when compared to gradient-induced phase-shift effects, assuming equal flow velocities and sequence parameters. However, gradient-induced phase-shift effects are encountered in every vessel, while BOLD-related phase-shift effects only occur in bent vessels where deoxygenated blood has accumulated. Therefore, BOLD-related phase-shift effects are not generally more relevant than gradient-induced phase-shift effects. Depending on the organ in question, one or the other might dominate. Other susceptibility-induced phase-shift effects are likely a significant contributor in organs with above-average iron deposits or many susceptibility interfaces. In some organs, these effects are expected to be the primary source of signal alterations due to flow, e.g., the lungs.

5.4.2 Organs affected by flow effects

The overall flow effects encountered in a specific organ are expected to be the sum of gradient-induced, BOLD-related, and other susceptibility-induced phase-shift effects. The individual contribution of these effects is presumed to vary vastly between different orangs. Depending on the tissue under consideration, the vessel anatomy, flow velocities, and susceptibility interfaces vary and might favour one effect. This subsection evaluates organs in regard to the anticipated magnitude of different phase-shift effects and discusses whether they are promising targets for future experiments.

Bone marrow The interest of our research group in signal alterations due to flow originated from observations made in red bone marrow [116]. Alterations of the water signal

observed in patients with acute lymphoblastic leukaemia were suspected to arise from changes in the ratio of flowing to stationary water molecules. Phase distortions and structured signals were observed in individuals with a suspected high percentage of flowing water molecules, presumably caused by phase-shift effects [116].

BOLD-related and gradient-induced phase-shift effects likely contribute to signal alterations as red bone marrow has a tortuous microvasculature and above-average perfusion [7]. A study by Spencer et al. found low oxygen saturations in the microvasculature of bone marrow in mice [123]. The low oxygen saturation indicates strong BOLD-related phase-shift effects relative to organs with lower or average oxygen extraction ratios.

However, susceptibility-induced phase-shift effects are likely responsible for most of the observed signal alterations. The proximity of bone trabeculae, iron deposits and fat vacuoles to sinusoids in red bone marrow leads to strongly inhomogeneous magnetic fields next to flowing blood, representing a potentially significant source of susceptibility-induced phase-shift effects.

The results of this study indicate that gradient-induced phase-shift effects are insignificant in red bone marrow. Even though the effects were observable in flow-sensitised STEAM sequences with long mixing times, they were minor. Therefore, gradient-induced phase-shift effects should be negligible when using standard sequences and sequence parameters.

Brain As the brain has above-average perfusion, phase-shift effects are expected to be significant [121]. Further, the brain has a high oxygen extraction ratio, favouring BOLD-related phase-shift effects [38]. This fact is intuitive as fMRI was established in brain imaging based on the BOLD effect [96]. However, susceptibility-induced phase-shift effects could also be relevant in iron-rich brain regions such as the basal ganglia and the dentate nucleus (Subsection 2.7.4).

As brain tumours are an established clinical use of MR spectroscopy, the barrier to implementing phase-shift effects as a diagnostic tool in brain imaging might be lower than elsewhere [19]. A potential application in differentiating response and pseudoresponse in malignant glioma patients treated with antiangiogenic therapies is conceivable as the ratio of stationary to flowing water nuclei is expected to change in case of a proper response. The differentiation between response and pseudoresponse still represents a diagnostic challenge [22].

Heart The high oxygen extraction ratio of the heart muscle likely leads to strong BOLD-related phase-shift effects [38]. The above-average perfusion facilitates gradient-induced and BOLD-related phase-shift effects. However, the heart is likely no viable target for

measurements of signal alterations due to flow as the movements during the heart cycle and the nearby flow of blood in the heart cavities would lead to considerable artefacts.

Liver The liver is expected to be strongly affected by susceptibility-induced phase-shift effects as it is the primary location of haemosiderin and ferritin deposits. Further, in liver steatosis, additional fat-water interfaces near vessels should increase these effects [14]. In haemochromatosis, these effects are expected to be even more pronounced. However, the evaluation of hepatic steatosis and haemochromatosis by other MR techniques is already well established [11, 31]. The liver's dense microvasculature facilitates BOLD-related and gradient-induced phase-shift effects. BOLD-related phase-shift effects are likely further increased as two-thirds of the blood is supplied by the portal vein that carries blood with comparatively low oxygen saturation [53].

Spleen As the mononuclear phagocyte system inside the spleen contains ferritin and haemosiderin, susceptibility-induced phase shift effects are expected to occur [95]. Further, the tortuous microvasculature benefits BOLD-related phase-shift effects. However, a low oxygen extraction ratio counteracts BOLD-related phase-shift effects. Gradient-induced phase-shift effects are also expected as the spleens perfusion is substantial [121]. Lymphoma cells frequently infiltrate the spleen [39]. The consecutive change in the ratio of stationary to flowing water molecules might be detectable by flow-sensitised MR spectroscopy sequences.

Kidneys Kidneys have above-average perfusion and a dense microvasculature [121]. Therefore, gradient-induced and BOLD-related phase-shift effects could be significant. However, considering BOLD-related phase-shift effects, the low oxygen extraction ratio of the kidneys likely minimises the effects [76]. Therefore, gradient-induced phase-shift effects might dominate in kidneys. Further, no significant susceptibility-induced phase-shift effects are expected as no relevant air or bone interfaces exist, and significant renal iron deposits are seldom [64].

Skeletal muscles Skeletal muscles have an average oxygen extraction ratio at rest and an average perfusion [121]. Therefore, both gradient-induced and BOLD-related phase-shift effects could be measurable. However, muscle tissue has only minute variations of susceptibility compared to other organs. Hence, susceptibility-induced phase-shift effects should be minor.

5.4.3 Potential diagnostic use of flow effects in ^{1}H spectroscopy

In contrast to MR angiography sequences in MR imaging, MR spectroscopy can potentially evaluate flow on the microvasculature level and, thereby, in peripheral tissue. This study showed that signal alterations due to flow in peripheral tissue are measurable in MR spectroscopy. Specific sequence parameters that can be used to maximise phase shifts/signal alterations due to flow in the microvasculature were identified. Further, we developed PRESS and STEAM sequences with increased flow sensitivity.

Using these flow-sensitised sequences and long mixing (and echo) times enables the detection of such signal alterations with increased sensitivity. Thereby, PRESS and STEAM sequences show potential diagnostic use for diseases where blood flow in peripheral tissue is increased/decreased or with an altered ratio of flowing to stationary water molecules. Diseases involving neoangiogenesis, cell proliferation, oedema or ischaemia are candidates for diagnostic uses. Inflammation, in particular, could be detected by the increased blood flow and the altered ratio of stationary to flowing water molecules.

As shown by the results of this study, STEAM sequences with long echo and mixing times are especially prone to signal alterations due to gradient-induced and BOLD-related phase-shift effects. Note that an increase in the mixing time usually leads to less signal decay and a more significant increase in flow sensitivity than an equal increase in the echo time. Therefore, flow-sensitised STEAM sequences with long mixing times are ideal candidates for clinical applications.

Schick et al. have already shown the potential for clinical applications in bone marrow [116]. However, the applications are not limited to bone marrow. Subsection 5.4.2 discussed organs that are viable targets for future use cases.

5.4.4 How to avoid signal alterations due to flow effects

Applications that make deliberate use of phase-shift effects are conceivable. However, in other situations, phase-shift effects might lead to unwanted signal alterations. This study shows various possibilities to minimise such effects in practice. One option is to prefer PRESS over STEAM measurements to avoid gradient-induced phase-shift effects. The mathematical and experimental data suggest that PRESS is less prone to gradient-induced phase-shift effects.

Further, when using STEAM sequences, gradient-induced phase-shift effects can be reduced by using short mixing times. Additionally, the mathematical model suggests that a smaller edge length along the x-axis can be chosen to decrease gradient-induced phase-shift effects in PRESS measurements. However, this and the previously mentioned approaches might only be feasible in some cases.

Preferring PRESS over STEAM sequences to avoid signal alterations due to flow is also supported by the results of the simulations of the BOLD-related phase-shift effects. These simulations showed that phase shifts in STEAM sequences tend to be stronger than in PRESS sequences. Likewise, reducing the echo time (and mixing time for STEAM sequences) was shown to reduce BOLD-related phase-shift effects.

In conclusion, gradient-induced and BOLD-related phase-shift effects can be minimised using PRESS sequences with short echo times. If STEAM sequences cannot be avoided and signal alterations due to flow are unwanted, the echo and mixing times should be kept to a minimum.

Chapter 6

Summary

Flow measurements using MR imaging are established in clinical routine as they offer added value for many indications. Thus, flow effects in MR imaging are well studied. However, flow effects also occur in MR spectroscopy. Schick et al. showed that flow effects in red bone marrow are measurable and potentially diagnostically relevant. Nevertheless, literature about the underlying mechanisms of flow effects in MR spectroscopy and their implications for spectra is scarce. This thesis aimed to identify the causative mechanisms and evaluate the relevance of the flow effects. Another objective was to elucidate which sequence parameters affect the flow effects in PRESS and STEAM.

Two groups of mechanisms likely constitute most of the observable flow effects in MR spectroscopy: susceptibility- and gradient-induced phase-shift effects. The thesis studied both groups of mechanisms using PRESS and STEAM sequences. The effects were studied primarily on the level of flow velocities in the microvasculature, as this is most relevant for spectroscopy of peripheral tissue. Mathematical simulations aimed to evaluate the magnitude of the gradient-induced phase-shift effects. Phantom and in vivo measurements were conducted to study the gradient-induced phase-shift effects experimentally. The experiments compared standard and flow-sensitised sequences. The flow-sensitised sequences were developed as a part of this project.

One of the effects constituting the BOLD effect leads to inhomogeneities in the magnetic field along the curvature of veins and capillaries. Blood flowing through bent veins and capillaries thus experiences dephasing and likely also signal alterations if a spectrum is acquired. This mechanism was deducted theoretically, and models for simulating this mechanism in PRESS and STEAM sequences were developed. Further, materials like iron, bone, air and fat lead to phase shifts of neighbouring flowing blood and may influence signal characteristics in MR spectroscopy. The thesis explored this group of susceptibility-induced phase-shift effects theoretically.

The simulations showed that gradient-induced flow effects have larger magnitudes in

STEAM than in PRESS sequences. In PRESS, the echo time does not affect the expected phase shift, while the size of the chosen voxel does so. In STEAM, the mixing time has the greatest influence on the magnitude of the phase shift. Phantom measurements verified these findings. The in vivo measurements were performed in the red bone marrow of lumbar vertebral bodies. The in vivo experiments could not demonstrate significant flow effects due to gradient-induced phase-shift effects for STEAM sequences with short mixing times and PRESS sequences. However, STEAM sequences with longer mixing times led to relevant alterations in the spectra.

Further, the simulation of the flow effects caused by the susceptibility-induced (BOLD-related) magnetic field inhomogeneities in small vessels revealed factors influencing the magnitude of these effects. Vessel geometry, flow velocity, and sequence parameters significantly influenced the expected phase shifts. The simulations demonstrated that high flow velocities, long echo and mixing times lead to strong phase-shift effects in theory.

This thesis contributes to the research on flow effects in MR spectroscopy. Starting with the theoretic delineation of the relevant mechanisms leading to phase-shift effects, factors that determine the magnitude of these effects were identified. Additionally, phantom and in vivo measurements showed that gradient-induced phase-shift effects are measurable and relevant under certain conditions. The results can be used to suppress signal alterations to reduce artefacts. Further, modifying sequence parameters allows the maximisation of phase-shift effects and shows potential for future diagnostic use of modified MR spectroscopy sequences.

Chapter 7

German Summary

Flussmessungen mittels MR-Bildgebung sind in der klinischen Routine etabliert, da sie für viele Indikationen einen Mehrwert bieten. Ergo sind Flusseffekte in der MR-Bildgebung gut erforscht. Flusseffekte lassen sich jedoch auch in der MR-Spektroskopie beobachten. Schick et al. konnten zeigen, dass sich Flusseffekte in vivo im roten Knochenmark messen lassen und diese potenziell diagnostisch relevant sind. Allerdings existiert kaum Literatur über die zugrunde liegenden Mechanismen und die Auswirkungen der Flusseffekte auf die Spektren. Ziel dieser Dissertation ist es, die ursächlichen Mechanismen zu identifizieren und die Relevanz der einzelnen Effekte zu evaluieren. Ein weiteres Ziel war es zu eruieren, welche Sequenzparameter die Flusseffekte beeinflussen.

Es lassen sich zwei mechanistische Hauptgruppen identifizieren, von denen anzunehmen ist, dass sie das Gros der beobachtbaren Flusseffekte bedingen. Zum einen sind dies suszeptibilitätsbedingte und zum anderen durch Gradientenschaltungen hervorgerufene Effekte. Beide Gruppen wurden in der Dissertation erforscht. PRESS und STEAM Sequenzen wurden bezüglich beider Effektgruppen untersucht. Dabei wurden diese Effekte vor allem im Bereich der Flussgeschwindigkeiten der Mikrozirkulation untersucht, da dies für die Spektroskopie von Organgewebe am relevantesten ist. Mittels mathematischer Simulationen wurde zunächst abgeschätzt, wie groß die Gradienten-assoziierten Flusseffekte sind. Zusätzlich wurden Phantommessungen und In-vivo-Messungen an zwei Probanden durchgeführt, um den tatsächlichen Einfluss der Flusseffekte auf die Spektren zu bestimmen. Dazu wurden reguläre und Fluss-sensitivierte PRESS und STEAM Sequenzen verglichen. Die Fluss-sensitivierten Sequenzen wurden im Rahmen des Projektes entwickelt.

Einer der den BOLD-Effekt konstituierenden Mechanismen führt dazu, dass sich das Magnetfeld entlang des Verlaufs der Krümmung einer kleinen Vene, Venole oder Kapillare unterscheidet. Fließt Blut während einer Spektroskopiesequenz durch solch ein Gefäß, ist eine Dephasierung zu erwarten und damit eine Alteration des resultierenden Spektrums.

Dieser Flusseffekt wurde theoretisch hergeleitet und Modelle zur Simulation dieses Effektes entwickelt. Eines der Modelle wurde auf PRESS und STEAM Sequenzen angewendet. Darüber hinaus führen Eisen, Knochentrabekel, Luft und Fett über Suszeptibilitätseffekte ebenfalls zur Dephasierung von benachbartem fließendem Blut und haben damit ebenfalls Einfluss auf die Spektren. Die Suszeptibilitätseffekte durch diese Materialien wurden theoretisch abgehandelt.

Hinsichtlich der durch Gradienten bedingten Flusseffekte konnte anhand der Simulationen gezeigt werden, dass bei STEAM Sequenzen stärkere Signalalterationen zu erwarten sind als durch PRESS Sequenzen. Bei PRESS wirkt sich die Echozeit nicht auf die zu erwartende Effektgröße aus, jedoch hat die Größe des gewählten Voxels einen Einfluss. Bei STEAM hat die Mischzeit den größten Einfluss auf die Stärke der Flusseffekte. Diese Erkenntnisse konnten mittels Phantommessungen verifiziert werden. Die In-vivo-Messungen wurden im roten Knochenmark von Lendenwirbelkörpern durchgeführt. Für STEAM Sequenzen mit kurzen Mischzeiten und PRESS Sequenzen konnten sich in vivo Flusseffekte durch Gradienten nicht eindeutig demonstrieren lassen. Jedoch führten STEAM Sequenzen mit längeren Mischzeiten zu relevanten Signalalterationen in den Spektren.

Die Simulation der Flusseffekte, die durch die suszeptibilitätsbedingten Magnetfeldinhomogenitäten in kleinen Gefäßen zustande kommen, zeigte eine Reihe von Einflussfaktoren auf die Effektstärke. Die Gefäßgeometrie, Flussgeschwindigkeiten und Sequenzparameter hatten einen relevanten Einfluss auf die zu erwartenden Dephasierungen und damit potenziell auf die resultierenden Spektren. Es ließ sich zeigen, dass besonders bei höheren Flussgeschwindigkeiten sowie längeren Echo- und Mischzeiten starke Dephasierungen zu erwarten sind.

Die Dissertation leistet einen Beitrag zur Erforschung von Flusseffekten in der MR-Spektroskopie. Ausgehend von der theoretischen Aufarbeitung relevanter Mechanismen, die zu Flusseffekten führen, konnten anhand von Simulationen Einflussfaktoren identifiziert werden, die die Effektstärke determinieren. Darüber hinaus konnte mittels Phantommessungen und In-vivo-Messungen etabliert werden, dass Gradienten-assoziierte Flusseffekte messbar sind und damit relevant sein können. Diese Erkenntnisse können dazu verwendet werden, unerwünschte Flusseffekte in der MR-Spektroskopie im Sinne einer Artefaktreduktion zu minimieren. Weiter können Flusseffekte durch Anpassung der Sequenzparameter maximiert werden und somit potenziell für diagnostische Zwecke nutzbar gemacht werden.

Chapter 8

Student Contribution

The study was conducted at the Sektion für Experimentelle Radiologie at the Clinic of Radiology of the University Hospital Tübingen under the supervision of Prof. Dr. Dr. Fritz Schick. The conceptual design was developed with Prof. Dr. Dr. Schick, head of the Institute and Dr. Günter Steidle, research associate. After initial skill adaptation training provided by Dr. Steidle, I conducted all experiments myself. The experimental design was developed with the counsel of Prof. Dr. Dr. Schick, Dr. Steidle and Dr. Petros Martirosian. Statistical analysis was unnecessary as the results represent numerical calculations or proof of concept experiments.

I developed the design of the flow-sensitised sequences. Dr. Steidle did the necessary programming for implementing the flow-sensitised PRESS and STEAM sequences. The nickel sulfate solution used in the phantom measurements was made and provided by Dr. Günter Steidle. He also provided the parameters of the PRESS and STEAM sequences for calculating the gradient-induced and BOLD-related phase-shift effects. I did the calculations myself. The simulations presented in Figures 3.27B and C were conducted by Sina Rück, a student at the institute. Furthermore, Ms. Rück played a pivotal role in the design of Figures 3.27B and C.

I hereby declare that the manuscript was written by myself. Prof. Dr. Dr. Schick and Dr. Steidle provided suggestions for improvement. I only used the references provided in the list of references. I further declare that I declared all assistance received by other people above.

Tübingen, 2 December 2024

Moritz Oberparleiter

Bibliography

[1] *Allen PD, St. Pierre TG, Chua-Anusorn W, Ström V, Rao KV*. Low-frequency low-field magnetic susceptibility of ferritin and hemosiderin. Biochim Biophys Acta. 2000; 1500(2):186–96. doi:10.1016/s0925-4439(99)00104-0.

[2] *Baliyan V, Das CJ, Sharma R, Gupta AK*. Diffusion weighted imaging: Technique and applications. World journal of radiology. 2016;8(9):785–798. doi:10.4329/wjr.v8.i9.785

[3] *Barker PB, Golay X, Zaharchuk G*. Clinical Perfusion MRI: Techniques and Applications. Cambridge University Press; 2013.

[4] *Benninghoff A, Drenckhahn D*. Anatomie (German). 16th ed. Urban & Fischer; 2008.

[5] *Bertholdo D, Watcharakorn A, Castillo M*. Brain proton magnetic resonance spectroscopy: introduction and overview. Neuroimaging Clin N Am. 2013;23(3):359–80. doi:10.1016/j.nic.2012.10.002

[6] *Biederer J, Beer M, Hirsch W, et al.* MRI of the lung (2/3). Why … when … how? Insights Imaging. 2012;3(4):355–71. doi:10.1007/s13244-011-0146-8

[7] *Bixel MG, Kusumbe AP, Ramasamy SK, et al.* Flow Dynamics and HSPC Homing in Bone Marrow Microvessels. Cell Rep. 2017;18(7):1804–1816. doi:10.1016/j.celrep.2017.01.042

[8] *Bloch F*. Nuclear Induction. Phys. Rev. 1946;70:460–474. doi:10.1103/PhysRev.70.460.

[9] *Bloembergen N, Purcell EM, Pound RV*. Relaxation Effects in Nuclear Magnetic Resonance Absorption. Phys. Rev. 1948;73:679–712. doi:10.1103/PhysRev.73.679.

[10] *Bonavita S, Di Salle F, Tedeschi G*. Proton MRS in neurological disorders. Eur J Radiol. 1999;30(2):125–31. doi:10.1016/s0720-048x(99)00051-0

[11] *Bonkovsky HL, Rubin RB, Cable EE, Davidoff A, Rijcken TH, Stark DD*. Hepatic iron concentration: noninvasive estimation by means of MR imaging techniques. Radiology. 1999;212(1):227–34. doi:10.1148/radiology.212.1.r99jl35227.

[12] *Boxerman JL, Bandettini PA, Kwong KK, et al.* The intravascular contribution to fmri signal change: monte carlo modeling and diffusion-weighted studies in vivo. Magn Reson Med. 1995;34(1):4-10. doi:10.1002/mrm.1910340103.

[13] *Brown GT, Kleiner DE*. Histopathology of nonalcoholic fatty liver disease and nonalcoholic steatohepatitis. Metabolism. 2016;65(8):1080–6. doi:10.1016/j.metabol.2015.11.008.

[14] *Brown RW, Cheng YC, Haacke EM, Thompson MR, Venkatesan R*. Magnetic Resonance Imaging. 2nd ed. John Wiley Sons; 2014.

[15] *Bryant DJ, Payne JA, Firmin DN, Longmore DB*. Measurement of flow with NMR imaging using a gradient pulse and phase difference technique. J Comput Assist Tomogr. 1984;8(4):588–93. doi:10.1097/00004728-198408000-00002.

[16] *Burstein D*. Stimulated echoes: Description, applications, practical hints. Concepts in Magnetic Resonance. 1996;8(4):269–278. doi:10.1002/(sici)1099-0534(1996)8:4<269::Aid-cmr3>3.0.Co;2-x.

[17] *Caprihan A, Davis JG, Altobelli SA, Fukushima E*. A new method for flow velocity measurement: frequency encoded NMR. Magn Reson Med. 1986;3(2):352–62. doi:10.1002/mrm.1910030223

[18] *Carr H*. Field gradients in early MRI. Physics Today. 2004;57:83–83. doi:10.1063/1.1784322.

[19] *Cecil KM*. Proton magnetic resonance spectroscopy: technique for the neuroradiologist. Neuroimaging Clin N Am. 2013;23(3):381–92. doi:10.1016/j.nic.2012.10.003.

[20] *Cesare F, Andrasescu A, Popa E, et al.* Quantitation of magnetic resonance spectroscopy signals: The jMRUI software package. Measurement Science and Technology. 2009;20:104035. doi:10.1088/0957-0233/20/10/104035.

[21] *Chavhan GB, Babyn PS, Thomas B, Shroff MM, Haacke EM*. Principles, techniques, and applications of T2*-based MR imaging and its special applications. Radiographics. 2009;29(5):1433–49. doi:10.1148/rg.295095034.

[22] *Clarke JL, Chang S*. Pseudoprogression and pseudoresponse: challenges in brain tumor imaging. Curr Neurol Neurosci Rep. 2009;9(3):241–6. doi:10.1007/s11910-009-0035-4.

[23] *Collenbusch JR*. Auswirkungen von Fluidbewegungen auf die Signale bei der volumenselektiven 1H-MR-Spektroskopie: Untersuchungen in-vitro für eine verbesserte Interpretation von Ergebnissen in-vivo (German). Dissertation, University of Tübingen; 2016.

[24] *Crichton R*. Inorganic Biochemistry of Iron Metabolism. 2nd ed. John Wiley Sons; 2001.

[25] *Damadian R*. Tumor detection by nuclear magnetic resonance. Science. 1971;171(3976):1151-1153. doi:10.1126/science.171.3976.1151.

[26] *Demirkaya S, Uluc K, Bek S, Vural O*. Normal blood flow velocities of basal cerebral arteries decrease with advancing age: a transcranial doppler sonography study. The Tohoku journal of experimental medicine. 2008;214:145–9. doi:10.1620/tjem.214.145.

[27] *Demtröder W*. Experimentalphysik, Band 2 (German). 3rd ed. Springer; 2004.

[28] *Demtröder W*. Experimentalphysik, Band 1 (German). 4th ed. Springer; 2006.

[29] *Drewes LR*. Molecular architecture of the brain microvasculature: perspective on blood-brain transport. J Mol Neurosci. 2001;16(2-3):93-157. doi:10.1385/JMN:16:2-3:93.

[30] *Elster AD*. Gradient-echo MR imaging: techniques and acronyms. Radiology. 1993;186(1):1-8. doi:10.1148/radiology.186.1.8416546.

[31] *Erden A, Kuru D, Peker E, et al.* MRI quantification techniques in fatty liver: the diagnostic performance of hepatic T1, T2, and stiffness measurements in relation to the proton density fat fraction. Diagn Interv Radiol. 2021;27(1):7-14. doi:10.5152/dir.2020.19654.

[32] *Faghihi R, Zeinali-Rafsanjani B, Mosleh-Shirazi MA, et al.* Magnetic resonance spectroscopy and its clinical applications: a review. Ther Adv Cardiovasc Dis. 2022;16:17539447221119624. doi:10.1177/17539447221119624.

[33] *Ford JC, Wehrli FW, Chung HW*. Magnetic field distribution in models of trabecular bone. Magn Reson Med. 1993;30(3):373-379. doi:10.1002/mrm.1910300316.

[34] *Fox PT, Raichle ME*. Focal physiological uncoupling of cerebral blood flow and oxidative metabolism during somatosensory stimulation in human subjects. Proc Natl Acad Sci U S A. 1986;83(4):1140-1144. doi:10.1073/pnas.83.4.1140.

[35] *Friebolin H*. Ein- und zweidimensionale NMR-Spektroskopie: Eine Einführung (German). 5th ed. John Wiley Sons; 2013.

[36] *Gallagher TA, Nemeth AJ, Hacein-Bey L*. An introduction to the Fourier transform: relationship to MRI. AJR Am J Roentgenol. 2008;190(5):1396-1405. doi:10.2214/AJR.07.2874.

[37] *Garcia J, van der Palen RLF, Bollache E, et al.* Distribution of blood flow velocity in the normal aorta: effect of age and gender. J Magn Reson Imaging. 2018;47(2):487-498. doi:10.1002/jmri.25773.

[38] *Gilbert-Kawai ET, Wittenberg MD*. Essential Equations for Anaesthesia: Key Clinical Concepts for the FRCA and EDA. Cambridge University Press; 2014.

[39] *Giovagnoni A, Giorgi C, Goteri G*. Tumours of the spleen. Cancer Imaging. 2005;5(1):73-77. doi:10.1102/1470-7330.2005.0002.

[40] *Glielmi CB, Xu Q, Craddock RC, Hu X.* Simultaneous acquisition of gradient echo/spin echo BOLD and perfusion with a separate labeling coil. Magn Reson Med. 2010;64(6):1827-1831. doi:10.1002/mrm.22554.

[41] *Glunde K, Jiang L, Moestue SA, Gribbestad IS.* MRS and MRSI guidance in molecular medicine: targeting and monitoring of choline and glucose metabolism in cancer. NMR Biomed. 2011;24(6):673-690. doi:10.1002/nbm.1751.

[42] *Goldman M.* Formal theory of spin–lattice relaxation. J Magn Reson. 2001;149(2):160-187. doi:10.1006/jmre.2000.2239.

[43] *Greve JM.* In vivo NMR imaging. Humana Press; 2011.

[44] *Griffiths DJ.* Quantenmechanik (German, translation). 2nd ed. Pearson; 2012.

[45] *Gruber B, Froeling M, Leiner T, Klomp DWJ.* RF coils: a practical guide for nonphysicists. J Magn Reson Imaging. doi:10.1002/jmri.26187.

[46] *Guo Y, Chen Y, Zhang X, et al.* Magnetic susceptibility and fat content in the lumbar spine of postmenopausal women with varying bone mineral density. J Magn Reson Imaging. 2019;49(4):1020-1028. doi:10.1002/jmri.26279.

[47] *Gutierrez-Jimenez E, Cai C, Mikkelsen IK, et al.* Effect of electrical forepaw stimulation on capillary transit-time heterogeneity (CTH). J Cereb Blood Flow Metab. 2016;36(12):2072-2086. doi:10.1177/0271678X16631560.

[48] *Gutiérrez L, Vujić Spasić M, Muckenthaler MU, Lázaro FJ.* Quantitative magnetic analysis reveals ferritin-like iron as the most predominant iron-containing species in the murine Hfe-haemochromatosis. Biochim Biophys Acta. 2012;1822(7):1147-1153. doi:10.1016/j.bbadis.2012.03.008.

[49] *Hahn EL.* Spin Echoes. Phys. Rev. 1950;80(4):580-594. doi:10.1103/PhysRev.80.580.

[50] *Hahn EL.* Free Nuclear Induction. Physics Today. 1953;6(11):4–9. doi:10.1063/1.3061075.

[51] *Hallgren B, Sourander P.* The effect of age on the non-haemin iron in the human brain. J Neurochem. 1958;3(1):41-51. doi:10.1111/j.1471-4159.1958.tb12607.x.

[52] *Hanson LG.* Is quantum mechanics necessary for understanding magnetic resonance? Magn. Reson. 2008;32A:329-340. doi:10.1002/cmr.a.20123.

[53] *Hardin RA, Shumacker HB, Su CS.* Studies on portal venous oxygen saturation. Arch Surg. 1963;87:831-835. doi:10.1001/archsurg.1963.01310170117019.

[54] *Harris RK, Becker ED, Cabral de Menezes SM, Goodfellow R, Granger P.* NMR nomenclature: nuclear spin properties and conventions for chemical shifts. IUPAC recommendations 2001. Solid State Nucl Magn Reson. 2002;22(4):458-483. doi:10.1006/snmr.2002.0063.

[55] *Haynes H, Holmes W*. The Emergence of Magnetic Resonance Imaging (MRI) for 3D Analysis of Sediment Beds. In: Geomorphological Techniques (Online Edition). British Society for Geomorphology; 2013. Accessed February 18, 2024.

[56] *Herold G*. Innere medizin (German). Herold, Gerd (Publisher); 2017.

[57] *Hoogenraad FG, Pouwels PJ, Hofman MD, Reichenbach JR, Sprenger M, Haacke EM*. Quantitative differentiation between BOLD models in fMRI. Magn Reson Med. 2001;45(2):233-246. doi:10.1002/1522-2594(200102)45:2<233::aid-mrm1032>3.0.co;2-w.

[58] *Hopkins JA, Wehrli FW*. Magnetic susceptibility measurement of insoluble solids by NMR: magnetic susceptibility of bone. Magn Reson Med. 1997;37(4):494-500. doi:10.1002/mrm.1910370404.

[59] *Iima M, Honda M, Sigmund EE, Kishimoto A, Kataoka M, Togashi K*. Diffusion MRI of the breast: current status and future directions. J Magn Reson Imaging. 2020;52(1):70-90. doi:10.1002/jmri.26908.

[60] *Ismail A, Ademola BL, Yusuf L, Abdulmalik MA*. Renal arterial doppler velocimetric indices among healthy subjects in north west nigeria (French). J West Afr Coll Surg. 2018;8(1):40-49.

[61] *Ivanov KP, Kalinina MK, Levkovich-Yu I*. Blood flow velocity in capillaries of brain and muscles and its physiological significance. Microvasc Res. 1981;22(2):143-155. doi:10.1016/0026-2862(81)90084-4.

[62] *Jackson GD, Kuzniecky RI, Pell GS*. Principles of magnetic resonance imaging. In: Magnetic Resonance in Epilepsy. 2nd ed. Academic Press;2005:17-28.

[63] *Jensen KE, Jensen M, Grundtvig P, Thomsen C, Karle H, Henriksen O*. Localized in vivo proton spectroscopy of the bone marrow in patients with leukemia. Magn Reson Imaging. 1990;8(6):779-789. doi:10.1016/0730-725x(90)90014-s.

[64] *Jeong JY, Kim SH, Lee HJ, Sim JS*. Atypical low-signal-intensity renal parenchyma: causes and patterns. Radiographics. 2002;22(4):833-846. doi:10.1148/radiographics.22.4.g02jl04833.

[65] *Jordan EC, Balmain KG*. Electromagnetic waves and radiating systems. 2nd ed. TBS; 1968.

[66] *Kaunitz JD*. Magnetic resonance imaging: the nuclear option. Dig Dis Sci. 2018;63(5):1100-1101. doi:10.1007/s10620-018-4992-9.

[67] *Kindig CA, Poole DC*. A comparison of the microcirculation in the rat spinotrapezius and diaphragm muscles. Microvasc Res. 1998;55(3):249-259. doi:10.1006/mvre.1998.2075.

[68] *Kindig CA, Richardson TE, Poole DC*. Skeletal muscle capillary hemodynamics from rest to contractions: implications for oxygen transfer. J Appl Physiol (1985). 2002;92(6):2513-2520. doi:10.1152/japplphysiol.01222.2001.

[69] *Klitzman B, Duling BR*. Microvascular hematocrit and red cell flow in resting and contracting striated muscle. Am J Physiol. 1979;237(4):H481-H490. doi:10.1152/ajpheart.1979.237.4.H481.

[70] *Klose U*. Measurement sequences for single voxel proton MR spectroscopy. Eur J Radiol. 2008;67(2):194-201. doi:10.1016/j.ejrad.2008.03.023.

[71] *Latroche C, Gitiaux C, Chretien F, Desguerre I, Mounier R, Chazaud B*. Skeletal muscle microvasculature: a highly dynamic lifeline. Physiology (Bethesda). 2015;30(6):417-427. doi:10.1152/physiol.00026.2015.

[72] *Lauterbur PC*. Image formation by induced local interactions: examples employing nuclear magnetic resonance. 1973. Clin Orthop Relat Res. 1989;(244):3-6.

[73] *Leupold J, Hennig J, Scheffler K*. Moment and direction of the spoiler gradient for effective artifact suppression in RF-spoiled gradient echo imaging. Magn Reson Med. 2008;60(1):119-127. doi:10.1002/mrm.21614.

[74] *Leupold J, Neubauer J, Bock M*. Spin echo and gradient echo : methodological duo of MRI. Radiologe. 2018;58(8):769-784. doi:10.1007/s00117-018-0422-4.

[75] *Levitt MH*. Spin dynamics : basics of nuclear magnetic resonance. 2nd ed. John Wiley Sons; 2008.

[76] *Levy NM*. Effect of variations of blood flow on renal oxygen extraction. Am J Physiol. 1960;199:13-18. doi:10.1152/ajplegacy.1960.199.1.13.

[77] *Li C, Langham MC, Epstein CL, et al.* Accuracy of the cylinder approximation for susceptometric measurement of intravascular oxygen saturation. Magn Reson Med. 2012;67(3):808-813. doi:10.1002/mrm.23034.

[78] *Li D, Wang Y, Waight DJ*. Blood oxygen saturation assessment in vivo using T2* estimation. Magn Reson Med. 1998;39(5):685-690. doi:10.1002/mrm.1910390503.

[79] *Libertiny G, Hands L*. Lower limb deep venous flow in patients with peripheral vascular disease. J Vasc Surg. 1999;29(6):1065-1070. doi:10.1016/s0741-5214(99)70247-8.

[80] *Luissint AC, Artus C, Glacial F, Ganeshamoorthy K, Couraud PO*. Tight junctions at the blood brain barrier: physiological architecture and disease-associated dysregulation. Fluids Barriers CNS. 2012;9(1):23. doi:10.1186/2045-8118-9-23.

[81] *Lüllmann-Rauch R, Asan E*. Taschenlehrbuch histologie (German). 6th ed. Thieme; 2019.

[82] *Machann J, Raible A, Schnatterbeck P, Lutz O, Claussen CD, Schick F*. Osteodensitometry of human heel bones by MR spin-echo imaging: comparison with MR gradient-echo imaging and quantitative computed tomography. J Magn Reson Imaging. 2001;14(2):147-155. doi:10.1002/jmri.1165.

[83] *Machann J, Stefan N, Schick F*. 1H MR spectroscopy of skeletal muscle, liver and bone marrow. Eur J Radiol. 2008;67(2):275-284. doi:10.1016/j.ejrad.2008.02.032.

[84] *Mahesh M*. The essential physics of medical imaging. 3rd ed. Med Phys. 2013;40(7):10.1118/1.4811156. doi:10.1118/1.4811156.

[85] *Mansfield P*. Multi-planar image formation using NMR spin echoes. J. Phys. C: Solid State Phys. 1977;10(3):L55-L58. doi:10.1088/0022-3719/10/3/004.

[86] *Markl M, Leupold J*. Gradient echo imaging. J Magn Reson Imaging. 2012;35(6):1274-1289. doi:10.1002/jmri.23638.

[87] *Markl M, Schnell S, Wu C, et al.* Advanced flow MRI: emerging techniques and applications. Clin Radiol. 2016;71(8):779-795. doi:10.1016/j.crad.2016.01.011.

[88] *Marques JP, Bowtell RW*. Using forward calculations of the magnetic field perturbation due to a realistic vascular model to explore the BOLD effect. NMR Biomed. 2008;21(6):553-565. doi:10.1002/nbm.1224.

[89] *Meguro R, Asano Y, Odagiri S, Li C, Shoumura K*. Cellular and subcellular localizations of nonheme ferric and ferrous iron in the rat brain: a light and electron microscopic study by the perfusion-Perls and -Turnbull methods. Arch Histol Cytol. 2008;71(4):205-222. doi:10.1679/aohc.71.205.

[90] *Mekkaoui C, Reese TG, Jackowski MP, Bhat H, Sosnovik DE*. Diffusion MRI in the heart. NMR Biomed. 2017;30(3):e3426. doi:10.1002/nbm.3426.

[91] *Merboldt KD, Hanicke W, Frahm J*. Diffusion imaging using stimulated echoes. Magn Reson Med. 1991;19(2):233-239. doi:10.1002/mrm.1910190208.

[92] *Moonen CT, von Kienlin M, van Zijl PC, Cohen J, Gillen J, Daly P, Wolf G*. Comparison of single-shot localization methods (STEAM and PRESS) for in vivo proton NMR spectroscopy. NMR Biomed. 1989;2(5-6):201-208. doi:10.1002/nbm.1940020506.

[93] *Mountford C, Ramadan S, Stanwell P, Malycha P*. Proton MRS of the breast in the clinical setting. NMR Biomed. 2009;22(1):54-64. doi:10.1002/nbm.1301.

[94] *Negendank W*. Studies of human tumors by MRS: a review. NMR Biomed. 1992;5(5):303–24. doi:10.1002/nbm.1940050518.

[95] *Oertel J*. Das Eisen im Knochenmark (German). Folia Haematol Int Mag Klin Morphol Blutforsch. 1982;109(5):697-715.

[96] *Ogawa S, Lee TM, Kay AR, Tank DW*. Brain magnetic resonance imaging with contrast dependent on blood oxygenation. Proc Natl Acad Sci U S A. 1990;87(24):9868-9872. doi:10.1073/pnas.87.24.9868.

[97] *Ogawa S, Tank DW, Menon R, et al.* Intrinsic signal changes accompanying sensory stimulation: functional brain mapping with magnetic resonance imaging. Proc Natl Acad Sci U S A. 1992;89(13):5951-5955. doi:10.1073/pnas.89.13.5951.

[98] *Papula L*. Mathematik für ingenieure und naturwissenschaftler (German). 12th ed. Vieweg+Teubner; 2009.

[99] *Parkes LM, Schwarzbach JV, Bouts AA, Deckers RH, Pullens P, Norris DG*. Quantifying the spatial resolution of the gradient echo and spin echo BOLD response at 3 Tesla. Magn Reson Med. 2005;54(6):1465-1472. doi:10.1002/mrm.20712.

[100] *Pauling L*. Magnetic properties and structure of oxyhemoglobin. Proc Natl Acad Sci U S A. 1977;74(7):2612-2613. doi:10.1073/pnas.74.7.2612.

[101] *Pauling L, Coryell CD*. The Magnetic Properties and Structure of Hemoglobin, Oxyhemoglobin and Carbonmonoxyhemoglobin. Proc Natl Acad Sci U S A. 1936;22(4):210-216. doi:10.1073/pnas.22.4.210.

[102] *Peci F, Dekker L, Pagliaro A, et al.* The cellular composition and function of the bone marrow niche after allogeneic hematopoietic cell transplantation. Bone Marrow Transplant. 2022;57(9):1357-1364. doi:10.1038/s41409-022-01728-0.

[103] *Plays M, Müller S, Rodriguez R*. Chemistry and biology of ferritin. Metallomics. 2021;13(5):mfab021. doi:10.1093/mtomcs/mfab021.

[104] *Poser BA, Norris DG*. Fast spin echo sequences for BOLD functional MRI. MAGMA. 2007;20(1):11-17. doi:10.1007/s10334-006-0063-x.

[105] *Rabi II, Zacharias JR, Millman S, Kusch P*. A new method of measuring nuclear magnetic moment. Phys. Rev. 1938;53:318–318. doi:10.1103/PhysRev.53.318.

[106] *Rogler G, Vavricka S*. Anemia in inflammatory bowel disease: an underestimated problem? Front Med (Lausanne). 2015;1:58. doi:10.3389/fmed.2014.00058.

[107] *Ropele S, Langkammer C*. Iron quantification with susceptibility. NMR Biomed. 2017;30(4):10.1002/nbm.3534. doi:10.1002/nbm.3534.

[108] *Ruschke S, Syväri J, Dieckmeyer M, et al.* Physiological variation of the vertebral bone marrow water T2 relaxation time. NMR Biomed. 2021;34(2):e4439. doi:10.1002/nbm.4439.

[109] *Russell JA, Kindig CA, Behnke BJ, Poole DC, Musch TI*. Effects of aging on capillary geometry and hemodynamics in rat spinotrapezius muscle. Am J Physiol Heart Circ Physiol. 2003;285(1):H251-H258. doi:10.1152/ajpheart.01086.2002.

[110] *Schenck JF*. The role of magnetic susceptibility in magnetic resonance imaging: MRI magnetic compatibility of the first and second kinds. Med Phys. 1996;23(6):815-850. doi:10.1118/1.597854.

[111] *Schick F*. Bone marrow NMR in vivo. Progress in Nuclear Magnetic Resonance Spectroscopy. 1996,29(3)169–227. doi:10.1016/S0079-6565(96)01030-8.

[112] *Schick F*. Grundlagen der Magnetresonanztomographie (MRT) (German). Radiologe. 2005;45(1):69-88. doi:10.1007/s00117-004-1146-1.

[113] *Schick F*. Sequenzen in der MRT. Teil II (German). Radiologe. 2006;46(9):803-819. doi:10.1007/s00117-006-1377-4.

[114] *Schick F*. Bildkontraste bei statischen Aufnahmen in der klinischen Magnetresonanztomographie (German). Radiologe. 2013;53(8):709-722. doi:10.1007/s00117-013-2534-1.

[115] *Schick F*. Wechselwirkungen mit magnetisch aktivem und elektrisch leitfähigem Material (German). Radiologe. 2019;59(10):860-868. doi:10.1007/s00117-019-0514-9.

[116] *Schick F, Bongers H, Jung WI, et al.* Proton relaxation times in human red bone marrow by volume selective magnetic resonance spectroscopy. Appl. Magn. Reson. 1992;3:947–963. doi:10.1007/BF03166165.

[117] *Schulte ML, Wood JD, Hudetz AG*. Cortical electrical stimulation alters erythrocyte perfusion pattern in the cerebral capillary network of the rat. Brain Res. 2003;963(1-2):81-92. doi:10.1016/s0006-8993(02)03848-9.

[118] *Sharma U, Baek HM, Su MY, Jagannathan NR*. In vivo 1H MRS in the assessment of the therapeutic response of breast cancer patients. NMR Biomed. 2011;24(6):700-711. doi:10.1002/nbm.1654.

[119] *Sharma U, Jagannathan NR*. Metabolism of prostate cancer by magnetic resonance spectroscopy (MRS). Biophys Rev. 2020;12(5):1163-1173. doi:10.1007/s12551-020-00758-6.

[120] *Shellock FG, Karacozoff AM*. Detection of implants and other objects using a ferromagnetic detection system: implications for patient screening before MRI. AJR Am J Roentgenol. 2013;201(4):720-725. doi:10.2214/AJR.12.10332.

[121] *Sidhu P, Peng HT, Cheung B, Edginton A*. Simulation of differential drug pharmacokinetics under heat and exercise stress using a physiologically based pharmacokinetic modeling approach. Can J Physiol Pharmacol. 2011;89(5):365-382. doi:10.1139/y11-030.

[122] *Spees WM, Yablonskiy DA, Oswood MC, Ackerman JJ*. Water proton MR properties of human blood at 1.5 Tesla: Magnetic susceptibility, T1, T2, T, and non-Lorentzian signal behavior. Magn Reson Med. 2001;45(4):533-542. doi:10.1002/mrm.1072.

[123] *Spencer JA, Ferraro F, Roussakis E, et al.* Direct measurement of local oxygen concentration in the bone marrow of live animals. Nature. 2014;508(7495):269-273. doi:10.1038/nature13034.

[124] *Stecco A, Saponaro A, Carriero A*. Patient safety issues in magnetic resonance imaging: state of the art. Radiol Med. 2007;112(4):491-508. doi:10.1007/s11547-007-0154-4.

[125] *Stejskal EO, Tanner JE*. Spin diffusion measurements: spin echoes in the presence of a time-dependent field gradient. J. Chem. Phys. 1965;42(1):288–292. doi:10.1063/1.1695690.

[126] *Tanner JE*. Use of the stimulated echo in NMR diffusion studies. J. Chem. Phys. 1970;52(5):2523-2526. doi:10.1063/1.1673336.

[127] *Teitelbaum GP, Yee CA, van Horn D, Kim HS, Colletti PM*. Metallic ballistic fragments: MR imaging safety and artifacts. Radiology. 1990;175(3):855-859. doi:10.1148/radiology.175.3.2343136.

[128] *The CMS Collaboration*. Constraints on anomalous Higgs boson couplings using production and decay information in the four-lepton final state. Physics Letters B. 2017,775:1–24. doi:10.1016/j.physletb.2017.10.021.

[129] *Thulborn KR, Waterton JC, Matthews PM, Radda G*. Oxygenation dependence of the transverse relaxation time of water protons in whole blood at high field. Biochim Biophys Acta. 1982;714(2):265-270. doi:10.1016/0304-4165(82)90333-6.

[130] *Tognarelli JM, Dawood M, Shariff MIF et al.* Magnetic resonance spectroscopy: principles and techniques: lessons for clinicians. J Clin Exp Hepatol. 2015;5(4):320-328. doi:10.1016/j.jceh.2015.10.006.

[131] *Van der Graaf M*. In vivo magnetic resonance spectroscopy: basic methodology and clinical applications. Eur Biophys J. 2010;39(4):527-540. doi:10.1007/s00249-009-0517-y.

[132] *Vanhamme L, van den Boogaart A, van Huffel S*. Improved method for accurate and efficient quantification of MRS data with use of prior knowledge. J Magn Reson. 1997;129(1):35-43. doi:10.1006/jmre.1997.1244.

[133] *Vignaud A, Maître X, Guillot G, et al.* Magnetic susceptibility matching at the air–tissue interface in rat lung by using a superparamagnetic intravascular contrast agent: Influence on transverse relaxation time of hyperpolarized helium-3. Magn Reson Med. 2005;54(1):28-33. doi:10.1002/mrm.20576.

[134] *Villringer A, Them A, Lindauer U, Einhaupl K, Dirnagl U*. Capillary perfusion of the rat brain cortex. An in vivo confocal microscopy study. Circ Res. 1994;75(1):55-62. doi:10.1161/01.res.75.1.55.

[135] *Vymazal J, Urgosík D, Bulte JW*. Differentiation between hemosiderin- and ferritin-bound brain iron using nuclear magnetic resonance and magnetic resonance imaging. Cell Mol Biol (Noisy-le-grand). 2000;46(4):835-842.

[136] *Waluch V, Bradley WG*. NMR even echo rephasing in slow laminar flow. J Comput Assist Tomogr. 1984;8(4):594-598. doi:10.1097/00004728-198408000-00003.

[137] *Wang Y, Yu Y, Li D, et al.* Artery and vein separation using susceptibility-dependent phase in contrast-enhanced MRA. J Magn Reson Imaging. 2000;12(5):661-670. doi:10.1002/1522-2586(200011)12:5<661::aid-jmri2>3.0.co;2-l.

[138] *Wehrli FW, Ford JC, Chung HW, et al.* Potential role of nuclear magnetic resonance for the evaluation of trabecular bone quality. Calcif Tissue Int. 1993;53 Suppl 1:S162-S169. doi:10.1007/BF01673429.

[139] *Weisskoff RM, Kiihne S.* MRI susceptometry: Image-based measurement of absolute susceptibility of MR contrast agents and human blood. Magn Reson Med. 1992;24(2):375-383. doi:10.1002/mrm.1910240219.

[140] *Wexler L, Bergel DH, Gabe IT, Makin GS, Mills CJ.* Velocity of blood flow in normal human venae cavae. Circ Res. 1968;23(3):349-359. doi:10.1161/01.res.23.3.349.

[141] *Wild JM, Marshall H, Bock M, et al.* MRI of the lung (1/3): methods. Insights Imaging. 2012;3(4):345-353. doi:10.1007/s13244-012-0176-x.

[142] *Wymer DT, Patel KP, Burke WF, Bhatia VK.* Phase-contrast MRI: physics, techniques, and clinical applications. Radiographics. 2020;40(1):122-140. doi:10.1148/rg.2020190039.

[143] *Yokoo T, Bae WC, Hamilton G.* A quantitative approach to sequence and image weighting. J Comput Assist Tomogr. 2010;34(3):317-331. doi:10.1097/RCT.0b013e3181d3449a.

[144] *Zhang L, Zou X, Zhang B, et al.* Label-free imaging of hemoglobin degradation and hemosiderin formation in brain tissues with femtosecond pump-probe microscopy. Theranostics. 2018;8(15):4129-4140. doi:10.7150/thno.26946.

Acknowledgements

Firstly, I would like to thank Prof. Dr. Dr. Fritz Schick very much for allowing me to write the thesis at the Sektion für Experimentelle Radiologie. It gave me a unique opportunity to learn about research and MR physics. The knowledge I gained serves me greatly in my career as a radiologist. Further, I appreciate the many talks that made the advancement of the thesis possible, the proofreading, and the suggestions for improvement.

Secondly, I thank my supervisor, Dr. Günter Steidle, who taught me the skills to perform the experiments, reprogrammed the spectroscopy sequences and helped me with the experimental design. I am grateful for the sound supervision and the proofreading.

Further, I thank Dr. Petros Martirosian, who supported me with technical issues and gave me input concerning the experimental design. Additionally, I thank Sina Rück for performing the COMSOL simulation. I want to thank the whole Sektion für Experimentelle Radiologie team, which was professional and companionable.

As the finalisation of the thesis marks the endpoint of my studies in Tübingen, I would like to thank all the good friends and acquaintances I had the pleasure of getting to know during my studies. It was an exquisite time that leaves fond memories and constitutes the cornerstone for more to come. Florian, Simon, Max, Nik, Theo, and Nikita, thank you for the profound talks and eventful evenings. Finally, Dorothea, meeting you was the most meaningful event for me. Thank you very much for the true companionship, exciting adventures, and enduring support.

After all the technicalities, I reserve the right to use a few letters for something belletristic, a haiku dedicated to everyone mentioned above.

Reading and writing
Hours innumerable spent
Wiser in the end?